



UNIVERSIDAD EUROPEA DE MADRID

**ESCUELA DE ARQUITECTURA, INGENIERÍA Y DISEÑO
DEGREE IN AEROSPACE ENGINEERING**

FINAL PROJECT REPORT

**Preliminary Design of a Stealth Air Superiority
Fighter: EXF “Estadea”**

By GABRIEL MANTILLA LÓPEZ

Academic Year 2022-23





TITLE: Preliminary Design of a Stealth Air Superiority Fighter: EXF “Estadea”.

AUTHOR: Gabriel Mantilla López.

SUPERVISOR: Rafael Pax Dolz del Castellar.

DEGREE: Bachelor’s Degree in Aerospace Engineering.

DATE: June 9th, 2023.

G.M.L.



(This page has been intentionally left blank)

G.M.L.

ABSTRACT

This final degree project was centered around the preliminary design phase of the EXF “Estadea” air superiority fighter, intended to act as the primary striker in the European theater against all enemy aircraft present in a given airspace where air dominance has not yet been achieved. Estadea was designed with all-around stealth and thrust vectoring in mind, featuring a clipped and cropped delta wing for low wing loading and high fuel capacity, all-movable ruddervators for reduced RCS and added authority, an internal weapons storage and a lightweight, simple and reliable structural design and actuation mechanisms. This design, due to the combination of two powerful F-135 engines and its sleek profile, has demonstrated to be superior in many key metrics (specifically turn rate, initial climb rate, absolute ceiling and combat radius) against current fighters (F-22, F-35, Eurofighter, etc.) when compared with the publicly available specifications of the latter. Other considerations included the ability to use short runways, alternative runways such as highways and standardize equipment, therefore reducing the economic impact in constrained military budgets.

RESUMEN

Este trabajo final de grado se centró en la fase de diseño preliminar del caza de superioridad aérea EXF “Estadea”, destinado a actuar como principal atacante en el teatro europeo contra todas las aeronaves enemigas presentes en un espacio aéreo determinado donde aún no se ha logrado el dominio aéreo. Estadea se diseñó teniendo en cuenta el sigilo y el empuje vectorial, con un ala delta recortada para bajas cargas alares y alta capacidad de combustible, timones totalmente móviles para RCS reducido y mayor autoridad, un almacenamiento interno de armas y un diseño estructural ligero y sencillo. Este diseño, debido a la combinación de dos potentes motores F-135 y su suave perfil, ha demostrado ser superior en muchas métricas clave (específicamente tasa de giro, velocidad de ascenso inicial, techo de vuelo y radio de combate) frente a los cazas actuales (F-22, F-35, Eurofighter, etc.) en comparación con las especificaciones disponibles públicamente de estos últimos. Otras consideraciones incluyen la capacidad de usar pistas cortas, pistas alternativas como autopistas y equipos estandarizados, reduciendo así el impacto económico en presupuestos militares limitados.

ACKNOWLEDGEMENTS

The author of this Final Degree Project would like to personally acknowledge the invaluable assistance of:

- Professor Rafael Pax Dolz del Castellar for both his weekly oversee, doubt resolution and reference provision throughout the months.

G.M.L.

Contents

ABSTRACT.....	4
RESUMEN.....	4
List of Figures.....	8
List of Tables.....	16
Abbreviations.....	17
CHAPTER 1. INTRODUCTION.....	19
1.1. The Reason Behind Estadea.....	19
1.2. State of the Art.....	21
1.3. Mission, Objectives & Top Level Requirements.....	25
CHAPTER 2. GENERAL DESIGN CONSIDERATIONS.....	28
2.1. Airworthiness & Certification Regulations.....	28
2.2. Supersonic Flight.....	30
2.3. Stall Characteristics, Control Surfaces, High Lift Devices & Maneuverability.....	56
2.4. Armament Compatibility.....	75
2.5. Ground Interface Considerations.....	80
CHAPTER 3. STEALTH DESIGN CONSIDERATIONS.....	82
3.1. Passive Camouflage.....	82
3.2. Active Camouflage.....	92
CHAPTER 4. AIRCRAFT GENERAL ARRANGEMENT.....	96
CHAPTER 5. ENGINE SELECTION.....	99
5.1. Candidate Selection.....	99
5.2. Engine Performance Assessment.....	102
CHAPTER 6. 3D Design & Weight Estimation.....	103
6.1. Wing and Ruddervators:.....	104
6.2. Fuselage.....	105
6.3. Major Internal Components & Systems.....	107
6.4. Weight Estimation.....	117

CHAPTER 7. AERODYNAMIC ANALYSIS.....	126
7.1. Airfoil Selection.....	126
7.2. Subsonic Characteristics.....	130
7.3. Stability.....	139
7.4. Supersonic Characteristics.....	143
7.5. Total Drag Coefficient vs. Airspeed (Steady and Level Flight).....	147
7.6. c_L Requirements and Stall Speed (Steady and Level Flight).....	150
7.7. Thrust Required vs. Airspeed (Steady and Level Flight).....	152
Chapter 8. STRUCTURAL DESIGN PROPOSITION.....	155
8.1. Wing.....	155
8.2. Ruddervators.....	158
8.3. Control Surfaces.....	160
8.4. Fuselage.....	162
8.5. Landing Gear.....	164
8.6. Thrust Vectoring Mechanism.....	166
8.7. Missile Pylons.....	167
Chapter 9. GENERAL PERFORMANCE & COMPARISON.....	169
9.1. Maximum Velocity and Supercruise Capabilities.....	169
9.2. Climb Performance.....	170
9.3. Absolute Ceiling, Service Ceiling, Cruise Ceiling.....	172
9.4. General Maneuvering Performance.....	174
9.5. Mission Range & Endurance, Payload-Range Diagram.....	181
9.8. Summary of Estadea’s Specifications.....	198
Chapter 10. CONCLUSIONS AND FUTURE WORK.....	200
REFERENCES.....	202

List of Figures

Fig. 1. Artistic representation of early aerial combat.....	20
Fig. 2. Lockheed Martin F-22 Raptor.....	21
Fig. 3. Lockheed Martin F-35 Lightning.....	21
Fig. 4. Sukhoi SU-57.....	21
Fig. 5. Chengdu J-20.....	21
Fig. 6. BAE Systems Tempest.....	21
Fig. 8. Boeing F/A-XX.....	21
Fig. 9. FCAS system.....	21
Fig. 10. F-35 advanced helmet design.....	22
Fig. 11. General Electric XA-100, an adaptive cycle engine.....	23
Fig. 12. Artistic representation of a direct energy weapon system in action.....	23
Fig. 13. Formation of shock waves over an airfoil at the critical Mach number.....	29
Fig. 14. Cp distribution on conventional low speed and supercritical airfoils.....	30
Fig. 15. Relative thickness vs. Mach number trend.....	30
Fig. 16. Basic supersonic airfoil shapes.....	31
Fig. 17. Lift generation in a supersonic airfoil.....	31
Fig. 18. Subsonic airfoil at supersonic speeds & supersonic airfoil at subsonic speeds at 0° AoA.....	31
Fig. 19. Effect of wing sweep on the critical Mach number.....	32
Fig. 20. Sound wave topography at subsonic and supersonic speeds.....	33
Fig. 21. Relation between the oblique shock-wave angle and the Mach angle.....	33
Fig. 22. Attached and detached shocks.....	34
Fig. 23. θ - β -M relation courtesy of Wikipedia.....	35
Fig. 24. Shock wave distribution over a fighter.....	35
Fig. 25. Accommodation of wing planform through sweep angle inside the Mach cone..	36
Fig. 26. Geometric calculation of the MAC and wing A.C.....	37
Fig. 27. Wing Magnitudes.....	37
Fig. 28. Examples of delta, trapezoidal and sweptback wings.....	39

Fig. 29. Examples of stabilators, tailerons and ruddervators.....	40
Fig. 30. Wave drag reduction due to fuselage waisting.....	41
Fig. 31. Cross-sectional distribution through mach plane references.....	42
Fig. 32. F-35 side view.....	42
Fig. 33. Typical nose cone geometries for aerospace applications.....	43
Fig. 34. Variation of drag coefficient with Mach number and fineness ratio for a conical nose design.....	44
Fig. 35. Quantitative comparison between nose cone geometries at transonic and supersonic speeds.....	44
Fig. 36. Von Karman nose cone shape.....	44
Fig. 37. Legacy fighter’s inlet and nozzle systems.....	45
Fig. 38. Example of a variable geometry inlet design.....	46
Fig. 39. Caret Inlet design and example.....	47
Fig. 40. Diverterless inlet or “bump” inlet design of the YF-23.....	47
Fig. 41. Various types of intake geometry and their effect on pressure recovery.....	48
Fig. 42. F-22 overpressure relief doors.....	48
Fig. 43. Sketch of the whole inlet system with on-design shock positions, courtesy of the Georgia Institute of Technology.....	49
Fig. 44. Optimized inlet sketch.....	49
Fig. 45. Effects of ambient pressure in C-D nozzles at subsonic and supersonic conditions.....	50
Fig. 46. C-D nozzle subsonic configuration.....	51
Fig. 47. C-D nozzle supersonic configuration.....	51
Fig. 48. Energy balance in the afterburner.....	52
Fig. 49. Turbojet and low bypass turbofan simplified installation sketches.....	52
Fig. 50. Sears-Haack body drop tank design.....	53
Fig. 51. A fighter’s “hot points”.....	54
Fig. 52. Thin airfoil c_l vs. α curves.....	55
Fig. 53. Stall progression (blue) in various wing planforms.....	55

Fig. 54. Effects of negative tip twist in spanwise lift distribution.....	56
Fig. 55. Effects of AR in stall angle and $cL_{, max}$	57
Fig. 56. Lift enhancement via LERX addition at intermediate and high AoA.....	57
Fig. 57. The three aircraft DOFs.....	58
Fig. 58. Flaperon positioning and functioning.....	58
Fig. 59. Roll, pitch and yaw moments.....	59
Fig. 60. SU57 thrust vectoring mechanism.....	59
Fig. 61. LE Flap and Flaperon mechanism examples.....	60
Fig. 62. Effects of non-extending flaps and LE flap on cl curves.....	61
Fig. 63. F-16 LE and TE flap configuration for its different flight regimes.....	61
Fig. 64. The concept of static stability.....	62
Fig. 65. The concept of dynamic stability.....	63
Fig. 66. Effects of pushing CoG aft.....	64
Fig. 67. Wing mounting options.....	64
Fig. 68. Fighter tail and CoG placement comparison in terms of net lift and trim drag....	65
Fig. 69. Tail placement and extent of the tail wake at high AoA maneuvers for various fighters.....	66
Fig. 70. Pugachev’s Cobra maneuver performed by a SU-27.....	66
Fig. 71. Herbst maneuver performed by a X-31, courtesy of NASA.....	66
Fig. 72. Example of a flight envelope or “V-n Diagram”.....	67
Fig. 73. Variation of turn rate and turn radius with altitude and speed.....	69
Fig. 74. Engine thrust variation with airspeed.....	70
Fig. 75. Example of a jet fighter climb profile.....	70
Fig. 76. Variation of roll rate with speed.....	71
Fig. 77. Static stability analogy.....	72
Fig. 78. Mauser BK-27 revolver cannon and feeding system.....	74
Fig. 79. AIM-120 AMRAAM and MBDA Meteor missiles.....	75
Fig. 80. AIM-9X Sidewinder and IRIS-T missiles.....	76
Fig. 81. JDAM kit installed in a free-fall Mk83 bomb.....	77

Fig. 82. Example of disruptive camouflage, courtesy of National Geographic.....	81
Fig. 83. Types of radar reflection.....	83
Fig. 84. RCS factors and main sources of radar detection in fighters.....	83
Fig. 85. Effect of edge serrations.....	84
Fig. 86. Edge diffraction from the TE of a straight and serrated wing.....	84
Fig. 87. Creeping wave return and geometric countermeasure.....	85
Fig. 88. Edge scattering and effects of edge alignment.....	85
Fig. 89. Stealth edge treatment.....	86
Fig. 90. F-22 canopy glass showing stealth coating.....	86
Fig. 91. Types of radar assembly radar return and solutions.....	87
Fig. 92. F-35 inlet countermeasures for short, medium and long radar wavelengths.....	88
Fig. 93. F-35 method of IR signature reduction.....	89
Fig. 94. F-22 rectangular nozzle design.....	89
Fig. 95. Maintenance operations in the F-22’s stealth coating.....	90
Fig. 96. F-35 flare dispenser trap door detail.....	91
Fig. 97. Electronic warfare modules and their position within the F-35 airframe.....	92
Fig. 98. General USAF jamming procedure to close-in radar and SAM sites.....	93
Fig. 99. F-35 front view. Top:IRST module part of Nothrop Grumman’s AN/AAQ-37 360° view system. Bottom: Lockheed Martin’s EOTS, intended for ground targets.....	93
Fig. 100. Estadea’s General Arrangement.....	95
Fig. 101. Cutout of the F135-100 turbofan engine, courtesy of Gandoza.com.....	99
Fig. 102. Estadea’s simplified inlet design (dimensions given in meters).....	99
Fig. 103. Pratt & Whitney F135-100 engine performance assessment.....	101
Fig. 104. 3D wing and ruddervator planforms.....	103
Table 9: Wing and Ruddervator planforms’ general characteristics.....	103
Fig. 105. 3D Fuselage Design.....	104
Fig. 106. Fuselage sections (scaled).....	104
Fig. 107. Simplified 3D model.....	105
Fig. 108. General internal components arrangement.....	106

Fig. 109. Weapon systems arrangement.....	106
Fig. 110. Propulsion & auxiliary power systems arrangement.....	107
Fig. 111. Landing gear arrangement.....	108
Fig. 112. Countermeasures arrangement.....	109
Fig. 113. Fuel probe arrangement.....	109
Fig. 114. AESA radar antenna arrangement.....	110
Fig. 115. Estadea vs. Airbus A319/A320/A321 and Aerospace standard 580B visibility patterns.....	111
Fig. 116. Estadea cockpit design.....	112
Fig. 117. Estadea’s cockpit ergonomics.....	113
Fig. 118. Lockheed Martin F-35 Power-by-Wire architecture.....	114
Fig. 119. VSCF electrical system diagramm.....	115
Fig. 120. Estadea’s primary systems arrangement.....	115
Fig. 121. Weight estimation statistical correlations.....	117
Fig. 122. Estadea and F-22’s front view (scaled).....	118
Fig. 123. Estadea’s fuel tank distribution.....	120
Fig. 124. F-22 external fuel tanks.....	121
Fig. 125. Drop tanks arrangement.....	122
Fig. 126. Drag penalty per drop tank.....	122
Fig. 127. CoG computation.....	123
Fig. 128. NACA 6-series airfoils aerodynamic results.....	126
Fig. 129. NACA 64A-006 and NACA 64A-204 airfoils.....	126
Fig. 130. Area plots.....	127
Fig. 131. Evolution of wave drag coefficient vs. Mach n°.....	128
Fig. 132. Wave drag coefficient vs. Mach n° of several legacy fighters.....	128
Fig. 133. cL vs AoA, clean configuration, subsonic conditions.....	130
Fig. 134. F-16 clean configuration cL vs. AoA curve.....	130
Fig. 135. cL vs. AoA, takeoff configuration.....	131
Fig. 136. cL vs. AoA, maneuver configuration.....	131

Fig. 137. Polar graph, clean configuration, subsonic conditions.....	132
Fig. 138. Oswald Factor, subsonic conditions.....	133
Fig. 139. Evolution of c_L distribution over the span with AoA, clean configuration.....	134
Fig. 140. L/D vs. AoA, clean configuration, subsonic conditions.....	135
Fig. 141. L/D vs. AoA, takeoff configuration.....	135
Fig. 142. L/D vs. AoA, maneuver configuration.....	136
Fig. 143. c_{My} vs. AoA at $CoG=10.274m$, clean configuration, subsonic conditions.....	137
Fig. 144. Ruddervators c_L vs. AoA, subsonic conditions.....	138
Fig. 145. NP, MP and Fwd Limit Determination, subsonic conditions.....	139
Fig. 146. c_{Fz} vs. Beta at 0° AoA, clean configuration, subsonic conditions.....	140
Fig. 147. Pressure contour at $Beta=20.625^\circ$, 0° AoA, clean configuration, subsonic conditions.....	140
Fig. 148. c_{Mx} vs. Beta at 0° AoA, clean configuration, subsonic conditions.....	141
Fig. 149. Ruddervators c_{Lmax} evolution at different Mach (ignore transonic speeds)...	142
Fig. 150. Wing c_{Lmax} evolution at different Mach (ignore transonic speeds).....	143
Fig. 151. c_L vs. AoA, clean configuration, supersonic conditions.....	143
Fig. 152. e vs. AoA, clean configuration, supersonic conditions.....	144
Fig. 153. L/D vs. AoA, clean configuration, supersonic conditions.....	145
Fig. 154. OpenVSP parasite drag tab.....	146
Fig. 155. Parasite drag evolution with airspeed and altitude, clean configuration.....	147
Fig. 156. Lift induced drag evolution with airspeed and altitude at combat weight.....	147
Fig. 157. Total drag evolution with airspeed and altitude at combat weight, clean configuration.....	148
Fig. 158. c_L required evolution. airspeed at MTOW.....	149
Fig. 159. Stall speed evolution with weight, altitude and temperature.....	150
Fig. 160. Thrust required and thrust available vs. airspeed.....	152
Fig. 161. F-35 wing structure.....	154
Fig. 162. F-22 wing structural design overview.....	154
Fig. 163. Ti-6Al-4V and carbon epoxy AS4 3501-6 properties.....	155

Fig. 164. I spar section description.....	155
Fig. 165. Estadea’s wing structure.....	156
Fig. 166. “T” section beam dimensions.....	156
Fig. 167. F-15 taileron structure.....	157
Fig. 168. Estadea’s ruddervator structure.....	157
Fig. 169. Ruddervator actuation mechanism.....	158
Fig. 170. Flaperon and aileron actuation mechanism.....	159
Fig. 171. LE flap actuation mechanism.....	160
Fig. 172. Estadea’s fuselage structure.....	161
Fig. 173. Canopy actuation mechanism.....	162
Fig. 174. Door actuation mechanism.....	162
Fig. 175. Estadea’s main landing gear design.....	163
Fig. 176. Estadea’s nose landing gear design.....	164
Fig. 177. Estadea’s thrust vectoring mechanism.....	165
Fig . 178. From top to bottom: LAU-128/A, LAU-141/A and LAU-142/A missile launchers.....	166
Fig. 179. Estadea’s climb performance.....	169
Fig. 180. Estadea’s thrust to weight ratio vs. altitude.....	170
Fig. 181. Estadea’s H-M envelope.....	172
Fig. 182. Jet fighters service ceiling comparison	
Fig. 183. Conditions for a coordinated turn.....	173
Fig. 184. Pull-up and pull-down maneuver, respectively.....	174
Fig. 185. Maximum bank angle in a coordinated turn at combat weight.....	175
Fig. 186. Minimum turn radius in a coordinated turn at combat weight.....	176
Fig. 187. Maximum turn rate in a coordinated turn at combat weight.....	177
Fig. 188. Sustained Pull-up and Pull-down rate at combat weight.....	178
Fig. 189. Sustained Pull-up and Pull-down radius at combat weight.....	179
Fig. 190. Range and endurance for mission configuration over the speed range.....	181
Fig. 191. Estadea’s area of operations (combat radius).....	182

Fig. 192. Estadea’s air patrol range.....	182
Fig. 193. F-35 internal fuel, ranges and weapons arrangement.....	183
Fig. 194. Estadea’s Payload-Range diagram.....	184
Fig. 195. Estadea’s V-n diagram adjusted for MTOW at 33,000 feet, ISA+0 conditions.....	185
Fig. 196. V _{mcg} determination at S.L., ISA+0 conditions.....	186
Fig. 197. Effects of thrust vectoring in the take-off run.....	187
Fig. 198. Estadea’s takeoff ground roll approximation.....	188
Fig. 199. Estadea’s landing ground roll approximation.....	189
Fig. 200. General aircraft clearance radiuses.....	190
Fig. 201. Center of Rotation calculation.....	191
Fig. 202. Spanish roads transversal dimensions.....	192
Fig. 203. Autovía del Noroeste Airfield (Castilla y León).....	193
Fig. 204. LZ-1 Airfield (Lanzarote).....	193
Fig. 205. BL-3 weapons loader by Advanced Ground Support Systems LTD.....	194
Fig. 206. Linkless ammunition loading vehicle by Meggitt Defense Systems.....	194
Fig. 207. Kovatch R-11-6000 fuel truck.....	195
Fig. 208. Mototok 6500 towing vehicle.....	195
Fig. 209. TLD 401 ACU unit.....	195
Fig. 210. Estadea ground interface.....	196

List of Tables

Table 1. Normalized inlet dimensions.....	50
Table 2. BK-27 Specifications, courtesy of Rheinmetall.....	75
Table 3. MBDA Meteor Specifications, courtesy of MBDA.....	76
Table 4. AIM-120 AMRAAM Specifications, courtesy of Raytheon.....	76
Table 5. AIM-9X Sidewinder Specifications, courtesy of Raytheon.....	77
Table 6. IRIS-T Specifications, courtesy of Diehl.....	77
Table 7. Mk83 bomb Specifications, courtesy of the USAF.....	78
Table 8. Modern NATO and European fighter’s engine public data.....	98
Table 10: Weight estimation statistical samples.....	116
Table 11: Weight estimation results.....	118
Table 12: Crew and Payload weight calculations.....	119
Table 13: Estadea Weight Configurations.....	123
Table 14: Control surfaces’ deflection angles.....	129
Table 15: Mission configuration landing weights.....	180
Table: 16. Weight configuration take-off and landing weights.....	184
Table 17: Summary of Estadea’s Specifications.....	197

Abbreviations

AESA	Active Electronically Scanned Radar
AoA	Angle of Attack
A.C.	Aerodynamic Center
Aft	After
AMRAAM	Advanced Medium-Range Air-to-Air Missile
APU	Auxiliary Power Unit
AR	Aspect Ratio
AWACS	Airborne Warning and Control System
BVR	Beyond Visual Range
cl	Lift Coefficient
cd	Drag Coefficient
CoG	Center of Gravity
CS	Certification Specifications
Def-Stan	Defense Standard
DOF	Degree of Freedom
EDA	European Defense Agency
EMAAC	European Military Airworthiness Certification Criteria
EW	Empty Weight
FAR	Federal Aviation Regulations
FL	Flight Level
Fwd	Forward
HTP	Horizontal Tail Plane
IAS	Indicated Airspeed
ISA	International Standard Atmosphere
IR	Infrared
IRST	Infrared Search and Track
ISA	International Standard Atmosphere
JDAM	Joint Direct Attack Munition
LCD	Liquid Crystal Display
LE	Leading Edge
LERX	Leading Edge Root Extension

MAC	Mean Aerodynamic Chord
MAW	Missile Approach Warning
MTOW	Maximum Takeoff Weight
MP	Maneuver Point
NATO	North Atlantic Treaty Organization
NEZ	No-Escape Zone
NMAA	National Military Airworthiness Authorities
NP	Neutral Point
OWS	Overload Warning System
PGM	Precision Guided Munitions
Radar	Radio Detection and Ranging
RAM	Radar Absorbent Material
RCS	Radar Cross-Section
RWR	Radar Warning Receiver
SAM	Surface to Air Missile
STANAG	Standardization Agreement
STOL	Short Take-off and Landing
TAS	True Airspeed
TE	Trailing Edge
VTP	Vertical Tail Plane
WVR	Within Visual Range

CHAPTER 1. INTRODUCTION

1.1. The Reason Behind Estadea

Air was transformed into a battlefield centuries ago, it began with man-carrying kites in ancient China and progressed to balloon warfare in the third century. The air medium had been relegated to reconnaissance and signaling purposes with manned and unmanned balloons (being the French Aerostatic Corps the first dedicated unit to this purpose, in the midst of the War of the First Coalition, 1791-98). In the American Civil War (1861-65), their usage was greatly expanded in the form of the Union Army Balloon Corps which used tethered flight to observe the confederates' positions.

The first powered, controlled, sustained flight of a heavier-than-air aircraft achieved on December 17th, 1903, by the Wright brothers gave way to the dawn of the airplane. This new invention was extensively introduced in the aerial battlefields in World War I (1914-18) first as a reconnaissance medium to then the role of bombing, strafing, maritime reconnaissance, anti-submarine warfare and propaganda throwing; it was in the skies over the European Front where the first aerial jousts will take place. Rapid technological advancements during the war such as the gun synchronizer made dogfighting more deadly and commonplace. Tactics were developed through trial and error, being the *Dicta Boelcke* by german Ace Oswald Boelcke one of the earliest compilations of air combat maneuvers and general rules for aerial warfare. From these early efforts many air combat tactical manuals have been derived, and have become a mainstay for NATO's air combat academies.

Over the following decades the advancements in technology (the widespread adoption of jet propulsion, guided munitions, onboard radar, fly-by-wire, stealth, etc.) have lead military historians to classify jet fighter aircraft in different categories following their technological sophistication, usually tied to specific conflicts in the XX & XXI century (RAAF, 2012):

- 1st Generation: WWII (1939-1945); transonic regimes, conventional armament.
- 2nd Generation: Korea War (1950-1953); limited supersonic, radar, air-to-air missiles.
- 3rd Generation: Vietnam War (1955-1975); multi-purpose, fighter-bombers.

- 4th Generation: Gulf War (1990-1991); supersonic multirole, high efficiency, high maneuverability.
- 5th Generation: War on Terror (2001-2021); advanced integrated avionics, stealth.

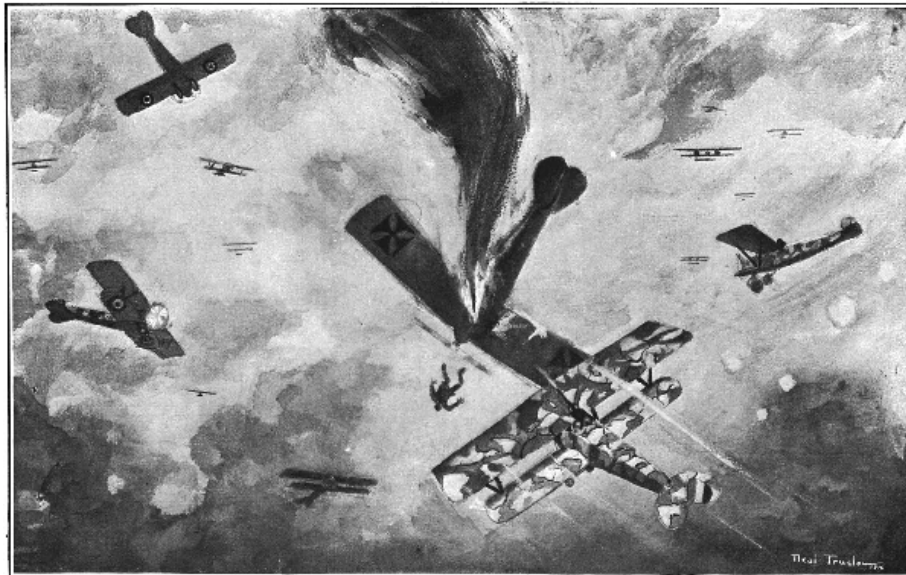


Fig. 1. Artistic representation of early aerial combat, courtesy of the Scientific American Magazine.

The advancements in aerial warfare over the past four decades (that is, since the development and implementation of stealth technology) have severely handicapped most fighters' operational capabilities; previously unmatched aircraft such as the F16 and F15 have been relegated to secondary roles once air dominance is achieved due to their lack of stealth technologies; and newer designs such as the Eurofighter lack the edge to outperform its new generation rivals. This now widespread adoption by various countries (the U.S., Russia and China primarily) has meant Europe no longer has the initiative and technological prowess it shared with the U.S. during the Cold War and has rendered the common airspace vulnerable.

Although numerous efforts are being undertaken to push European technology to the forefront, such as the FCAS program, these may arrive too little too late to ensure airspace security in the near future. This final degree project aims at providing a 6th Generation air superiority stealth fighter design proposition which will occupy the gap nowadays left unguarded in European defense strategy.

1.2. State of the Art

For inspiration, 5th Generation aircraft now in use around the world can be used as references: the Lockheed Martin F-22 “Raptor” & F-35 “Lightning”, the Sukhoi SU57 “Felon” and the Chengdu J-20. These aircraft represent the state of the art in aerial combat by combining low observability technologies, high connectivity and high maneuverability which makes them currently unmatched.



Fig. 2. Lockheed Martin F-22 Raptor.



Fig. 4. Sukhoi SU-57.



Fig. 3. Lockheed Martin F-35 Lightning.



Fig. 5. Chengdu J-20.

In the near future, these will be superseded by 6th Generation fighters. Although no 6th Generation aircraft currently in use as of June 2023, there exists several programs around the world, these include the FCAS in Europe, the Tempest in the UK, the Mikoyan PAK DP in Russia, the F/A-XX in the US and the Mitsubishi F-X in Japan.



Fig. 6. BAE Systems Tempest.



Fig. 8. Boeing F/A-XX.



Fig. 7. Mitsubishi F-X.



Fig. 9. FCAS system.

While still in early stages of development (no prototypes officially exist yet), several distinct characteristics common to many 6th Generation fighters have evolved. The main objective is to enhance current air-to-air, survivability and ground support capabilities of current 5th Generation fighters by developing a technology portfolio and applying it to a revised platform (CSR, 2022); these include:

1. High capacity networking, Artificial Intelligence, enhanced cyber warfare capabilities and battlefield command, control and communications capabilities.
2. Unmanned capabilities, meaning the aircraft could be flown using a pilot or a ground station.
3. Enhanced human-systems integrations; this capability is already being exploited in the F-35 with its helmet-mounted displays. 6th Generation fighters will drive this characteristic further by replacing conventional instrument panels.



Fig. 10. F-35 advanced helmet design.

4. Advanced variable-cycle engines, meaning power plants capable of performing at high efficiencies in all flight regimes. An emerging concept is the three-stream architecture, in which an adaptive fan can direct air into a third bypass stream which

can be used to increase bypass ratio when fuel efficiency is required, or have additional airflow directed to the core for greater power (USAF, 2010).

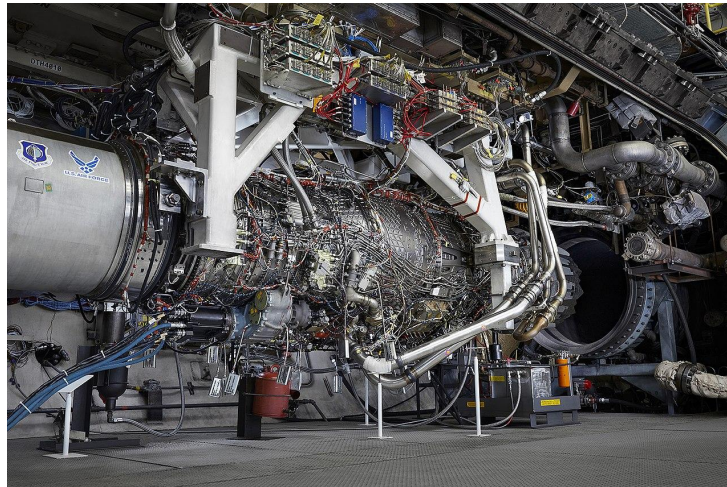


Fig. 11. General Electric XA-100, an adaptive cycle engine.

5. Potential use of direct energy weapons, such as lasers.



Fig. 12. Artistic representation of a direct energy weapon system in action, courtesy of Boeing.

1.3. Mission, Objectives & Top Level Requirements

Estadea’s main mission will be to act as the primary striker against all enemy aircraft present in a given airspace where air dominance, defined as the establishment and maintenance of control of the skies in a given conflict area (CRS, 2022), has not yet been achieved. For this purpose it will be equipped with the necessary technologies, tools and capabilities to ensure its survivability and success against SAMs (Surface-to-Air Missiles), modern anti-aircraft artillery, and best or at least match current 5th Generation aircraft. To achieve this mission, this Final Degree Project possesses the following objectives:

- General Objective: provide a preliminary design proposition of a stealth air superiority fighter which analytically demonstrates similar or superior performances to current 5th Generation fighters.
- Specific Objectives:
 1. Provide a General Arrangement where stealth design concepts are shown.
 2. Design of Wings, Fuselage, Landing Gear and Control Surfaces.
 3. Powerplant Selection.
 4. Provide a Structural Design Proposition & Weight Estimation.
 5. Provide a General Placement of aircraft systems (radar, electric, hydraulics, general cabin arrangement, etc.).
 6. Provide an Aerodynamic analysis (high AoA maneuvers, high G maneuvers, static and dynamic stabilities, performance at different flight regimes, etc.).
 7. Provide a Flight Envelope & Payload-Range Diagram for all mission configurations.
 8. Compare performances with current 5th Generation aircraft.

Finally, to match current 5th Generation fighters, as taken as an average from its general performance capabilities, Estadea should comply with the following top level requirements (D. P. Raymer, 1996):

1. A top speed of at least Mach 2.0.
2. A ferry range greater than $R_{ferry} = 3000.0km \approx 1620.0 nmi$ without refueling in-flight.
3. A payload of 8+ missiles and a gun for both BVR (Beyond Visual Range) and WVR (Within Visual Range) engagements, all in one mission.
4. Possesses the necessary maneuvering characteristics to match current 5th Generation aircraft in a dogfight, i.e. 20 deg/sec turn rate at 350 kt, 15,000ft.



(This page has been intentionally left blank)

G.M.L.

CHAPTER 2. GENERAL DESIGN CONSIDERATIONS

Before jumping into the design of any aircraft, a closer look must be taken to its top level requirements and mission set to discern noteworthy design considerations; for this matter the concerning military certification regulations and relevant theory shall be commented on this second chapter so as to demonstrate the logic behind the design choices.

2.1. Airworthiness & Certification Regulations

Estadea, as a combat aircraft, does not fall into CS/FAR-23 or CS/FAR-25 regulations as most civilian aircraft. In the context of NATO, the European Defense Agency provides general guidance for the certification of military aircraft by compiling the different documents (Def-Stan, STANAGs, etc.) from NATO's NMAA, as it appears in the EMAAC handbook (EDA, 2018). For this project and considering its objectives, the relevant rules contained in Section 1 "General Requirements" in Def-Stan 00-970 Part 1, relevant for fixed wing aircraft, will be taken into consideration:

1. NOISE AND VIBRATION (UK Ministry of Aviation, 2015):
 - a. “(1.1.6) In designing the airplane, consideration shall be given to problems that can be caused by noise and vibration which can unduly affect the airplane’s structure, its instruments and avionic equipment, as well as the operational efficiency of the crew.”
2. CONDITIONS OF OPERATION (UK Ministry of Aviation, 2015):
 - a. “(1.1.12) All installations and systems shall function correctly under all conditions, on the ground, in flight and at altitude, for which they are required to operate.”
3. POWER OPERATED SYSTEMS (UK Ministry of Aviation, 2015):
 - a. “(1.1.13) The aim shall be to ensure that a single failure of any power-operated service or system shall not prevent adequate functioning of any other power-operated service which is vital to any of the following: (a) safety of the airplane in flight or in landing, (b) escape of the crew from the

airplane, and (c) ability of the airplane to perform its operational mission or, if failure would mean canceling the mission, return safely.”

- b. “(1.1.14) Failure of any or all the engines in flight shall not result in the pilot being unable to operate those powered services which are essential to retaining control for sufficient time to enable the engine(s) to be re-started, an emergency landing to be made, or if this is not possible for safe evacuation of the airplane”.

4. CAMERA RECORDERS (UK Ministry of Aviation, 2015):

- a. “(1.1.17) On all airplanes having fixed guns a camera recorder shall be installed to operate both automatically when the fixed guns are fired and independently of them when so desired. When rockets are fitted in addition to fixed guns it shall be possible to operate the camera recorder in conjunction with either the rockets or the fixed guns.”

5. HEAD UP DISPLAY RECORDERS (UK Ministry of Aviation, 2015):

- a. “(1.1.20) On all aircraft fitted with a Head Up Display (HUD), a HUD recorder capable of being operated by the gun trigger and the camera button shall be provided.”

6. ICE DETECTION (UK Ministry of Aviation, 2015):

- a. “(1.1.38) Means shall be provided for the crew to be warned of the build-up of ice, either by visual observation of a representative section of the main-plane or tail-plane, or by use of an ice detector system.”

2.2. Supersonic Flight

2.2.1. The wing:

As the fighter accelerates and approaches the speed of sound the wing must contend against a sudden increase in parasite drag due to the emergence of wave drag. Wave drag is a component of pressure drag due to compressibility effects caused by the formation of shock waves around a body (R. T. Jones, 1956). Although shock waves are typically associated with supersonic flow, they can form at subsonic aircraft speeds on areas of the body where local airflow accelerates to supersonic speed ($M \geq 1.0$). Wave drag is not negligible at speeds over that of the Critical Mach (the lowest Mach number at which the airflow at some point of the aircraft reaches $M = 1.0$) of the aircraft.

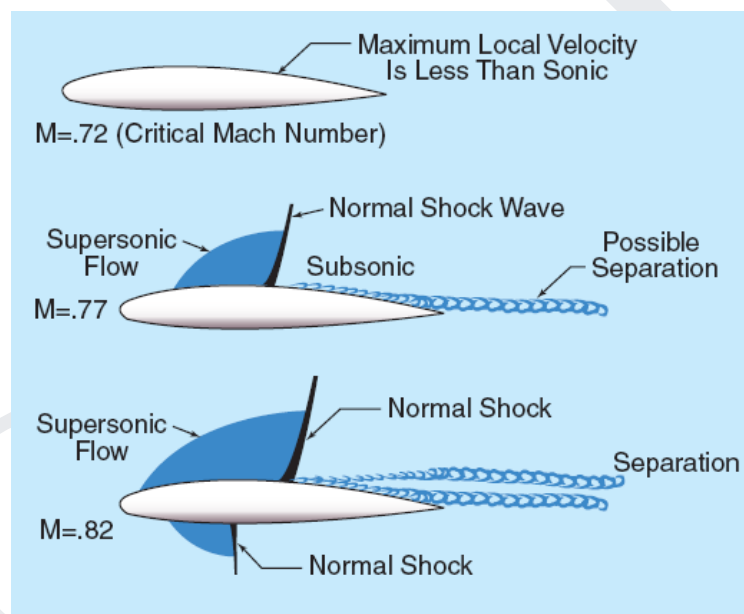


Fig. 13. Formation of shock waves over an airfoil at the critical Mach number.

The strength of the shock wave, for a given freestream Mach number, depends on the relative thickness of the airfoil (thicker airfoils require the air to reach higher local speeds) and on the velocity distribution around the airfoil (the same amount of lift can be generated by several local speed distributions) (R. Llamas, 2023). Therefore, airfoils which minimize the velocity peaks around the airfoil at transonic speeds produce weaker shock waves and reach the drag divergence (sudden increase in drag due to shock wave generation) later than conventional low speed airfoils; these airfoils are characterized by a very small relative thickness.

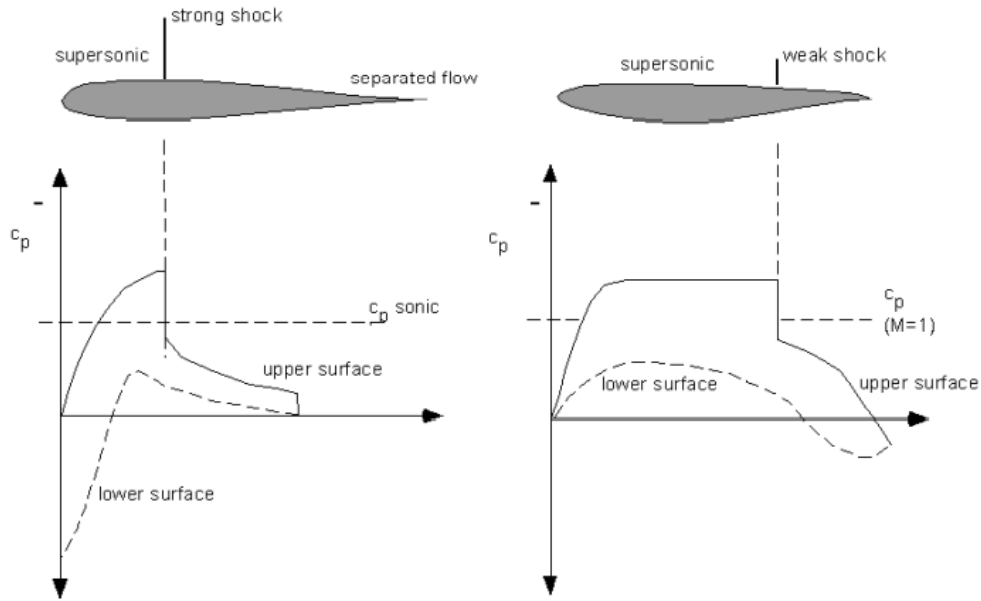


Fig. 14. Cp distribution on conventional low speed and supercritical airfoils.

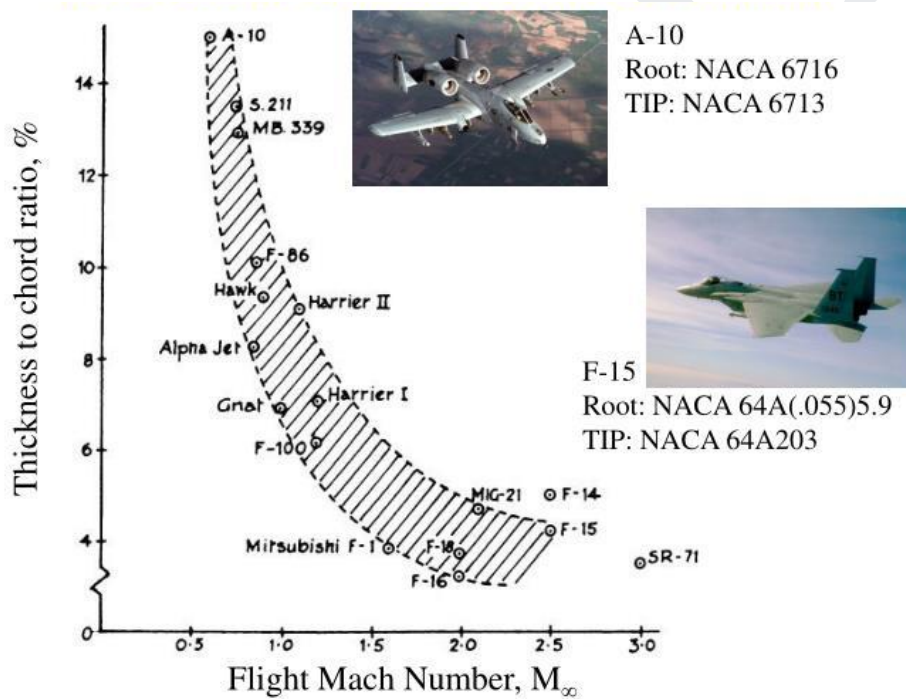


Fig. 15. Relative thickness vs. Mach number trend.

Once the fighter accelerates beyond Mach 1.0 (the speed of sound), the wing now generates lift by deflecting the oblique shock waves generated over its surface. Supersonic airfoils are variations of two basic shapes characterized by a sharp LE: the double wedge and biconvex shapes.

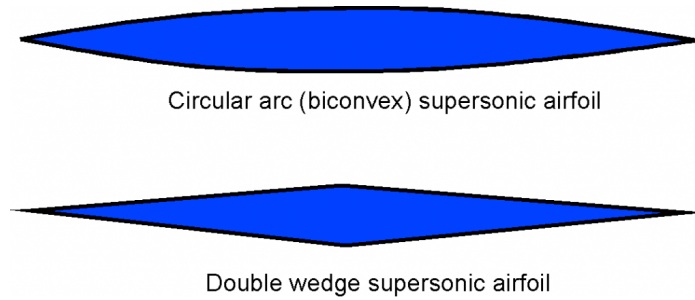


Fig. 16. Basic supersonic airfoil shapes.

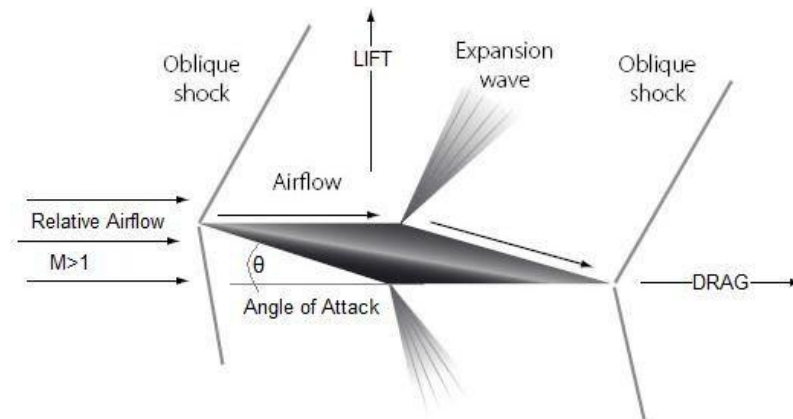


Fig. 17. Lift generation in a supersonic airfoil.

In this context, the design of Estadea is faced with a conundrum since at supersonic speeds a normal shock wave (also known as “Bow Wave”) is formed off the front of the typical blunt LE present on subsonic airfoils which generates drag whereas the sharp LE typical of supersonic airfoils comes as a disadvantage to produce lift at subsonic speeds.

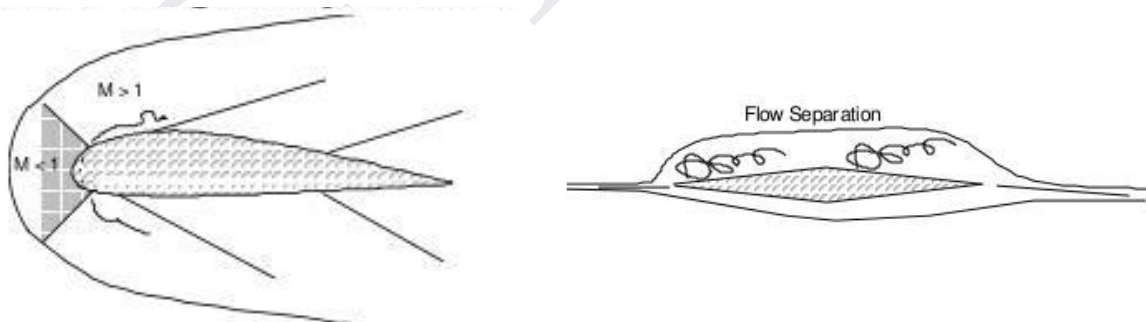


Fig. 18. Subsonic airfoil at supersonic speeds & supersonic airfoil at subsonic speeds at 0° AoA.

To solve this conundrum, two main solutions are applied simultaneously. The first solution is to increase the sweep angle of the wing; this increases the effective chord of the airfoil section while maintaining its thickness, the result is a lower relative thickness as the air “sees” more chord, thereby increasing the critical Mach number.

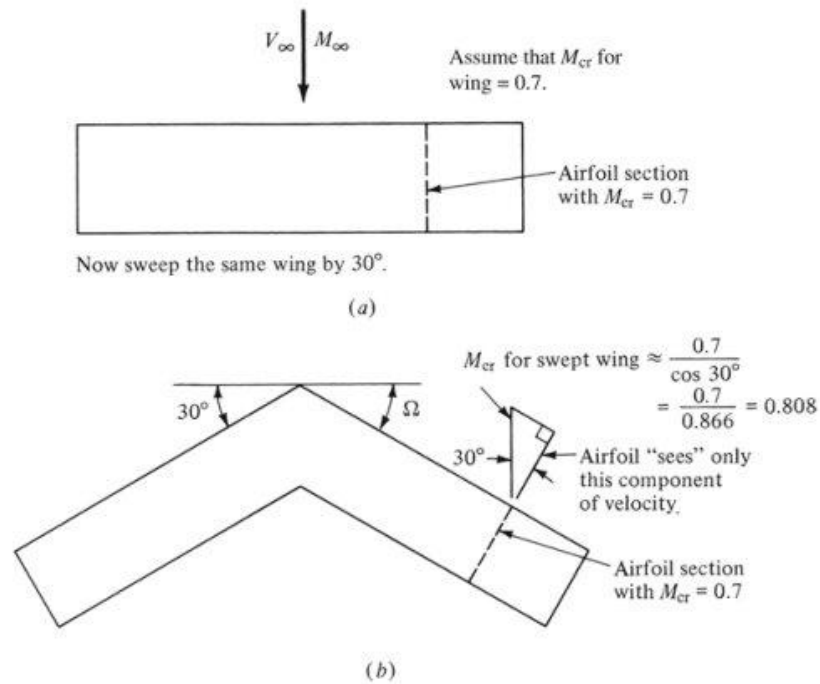


Fig. 19. Effect of wing sweep on the critical Mach number

The equivalent Mach number normal to the LE is given by

$$M_{equ.} = \sqrt{M_{\perp}^2 + M_{vert.}^2} = \sqrt{(M_{\infty} \sin \alpha)^2 + (M_{\infty} \cos \alpha \cdot \cos \Lambda)^2} \quad (2.1)$$

where M_{∞} is the freestream Mach number, α the wing AoA and Λ the sweep angle. Equivalent Mach number decreases with an increase of sweep; by taking this to the extreme (i.e. delta wings) the resultant equivalent mach number is subsonic even while flying at supersonic speeds, permitting the usage of blunt LEs suitable for subsonic speeds.

In the context of supersonic flight, the Mach Cone must also be considered. Pressure disturbances produced by the movement of the fighter through the air travel at the speed of sound; at supersonic speeds, since the aircraft is flying faster than the pressure disturbances, it remains outside the envelope of the sound waves; these wave fronts form a disturbance envelope given by the straight line BC, which is tangent to the family of circles. This line of disturbances is defined as a Mach wave (J. D. Anderson, 2017).

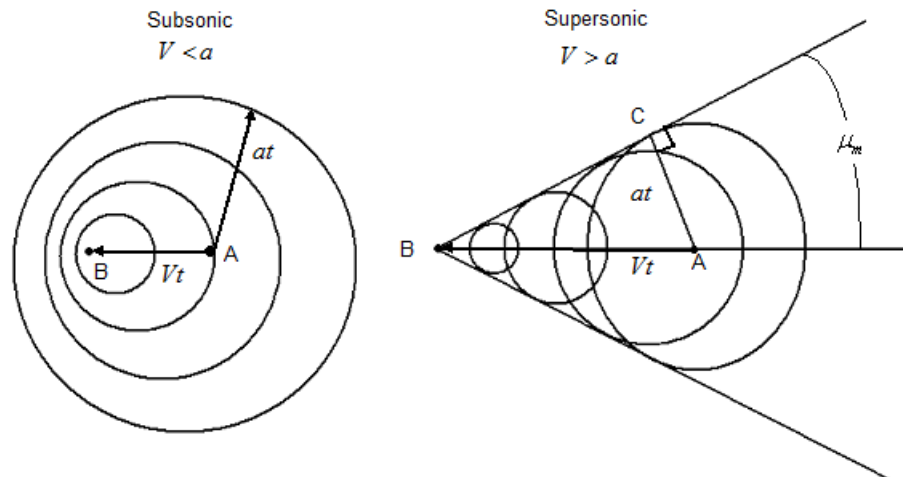


Fig. 20. Sound wave topography at subsonic and supersonic speeds, extracted from Chapter 9 “Compressible Flow” by J. D. Anderson.

The Mach cone angle, μ , is given by

$$\mu = \arcsin\left(\frac{1}{M}\right) \quad (2.2)$$

where M is the Mach number; at a maximum speed of $M = 2.0$ the resultant angle is $\mu = \arcsin\left(\frac{1}{2}\right) = 30^\circ$. The Mach wave, that is, the envelope of disturbances in the supersonic flow, is clearly oblique to the direction of motion. If the disturbances are stronger than a simple sound wave, then the wave front becomes stronger than a Mach wave, creating an oblique shock wave at an angle β to the freestream, where $\beta > \mu$. This comparison is shown in Figure 21. However, the physical mechanism creating the oblique shock is essentially the same as that described above for the Mach wave. Indeed, a Mach wave is a limiting case for oblique shock (i.e., it is an infinitely weak oblique shock) (J. D. Anderson, 2017).

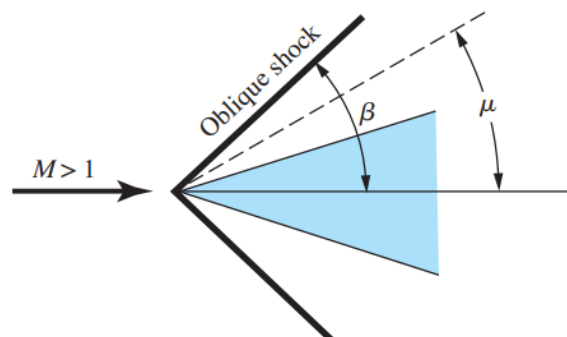


Fig. 21. Relation between the oblique shock-wave angle and the Mach angle, extracted from Chapter 9 “Compressible Flow” by J. D. Anderson.

By modifying deflection angle, θ , the Mach number after the shock, M_2 , can be controlled; this is the second solution to the conundrum.

$$M_2 = \frac{1}{\sin(\beta-\theta)} \sqrt{\frac{1 + \frac{\gamma-1}{2} M_1^2 \sin^2(\beta)}{\gamma M_1^2 \sin^2(\beta) - \frac{\gamma-1}{2}}} \quad (2.3)$$

where γ is the adiabatic constant (it is assumed to be $\gamma = 1.4$ for diatomic gasses) and $M_1 \equiv M_\infty$ is the Mach number before the shock or the freestream Mach number. From the equation it can be easily noticed that by increasing the deflection angle, M_2 in turn decreases.

A maximum corner angle, θ_{max} , exists for any upstream Mach number. When $\theta > \theta_{max}$, the oblique shock wave is no longer attached to the corner and is replaced by a detached bow shock, producing higher drag (J. D. Anderson, 2017).

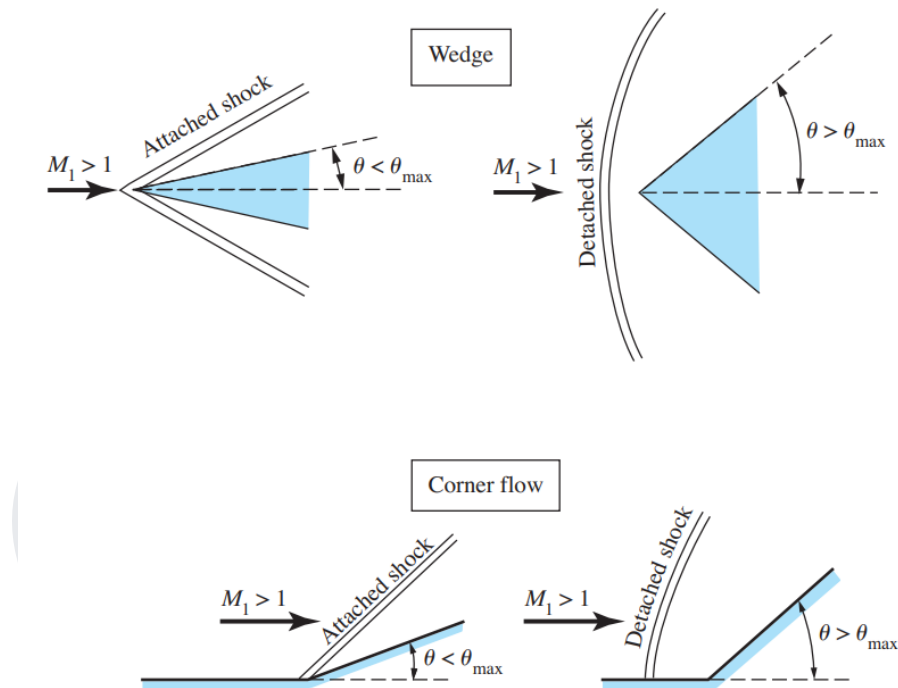


Fig. 22. Attached and detached shocks, extracted from Chapter 9 “Compressible Flow” by J. D. Anderson.

Therefore, every wedge and corner angle must be carefully selected. For this task, a second equation may be used:

$$\tan \theta = 2 \cot \beta \frac{M_1^2 \sin^2 \beta - 1}{M_1^2 (\gamma + \cos 2\beta) + 2} \quad (2.4)$$

This formula is called the θ - β -M relation, and it specifies θ as a unique function of M_1 and β (J. D. Anderson, 2017).

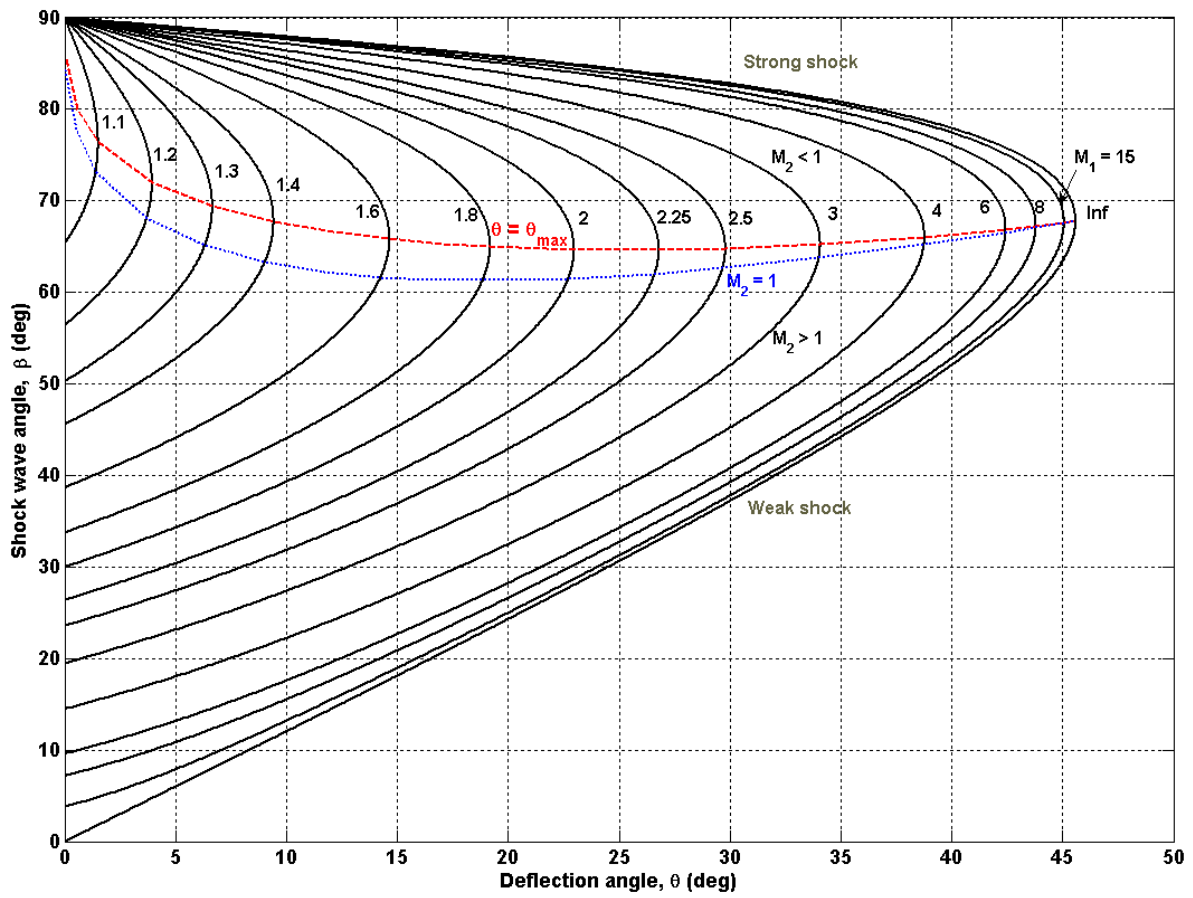


Fig. 23. θ - β -M relation courtesy of Wikipedia.

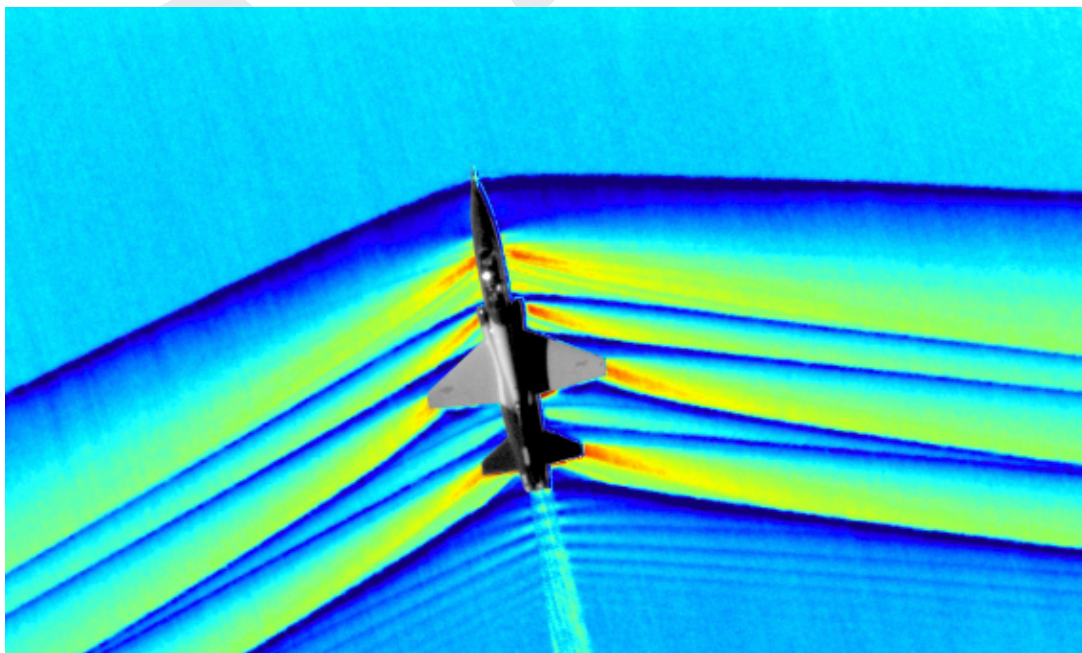


Fig. 24. Shock wave distribution over a fighter, courtesy of NASA.

Inferred from Figure 24, the primary areas of concern will be the nose cone, inlet, wing and tail angles.

It is of paramount importance that all the wing planform remains inside the Mach cone, otherwise the sections outside of it would produce high loads of drag due to the bow shock waves forming before the blunt LEs. This requirement may further force to increase the wing sweep angle in order to accommodate it inside the Mach wave angle.

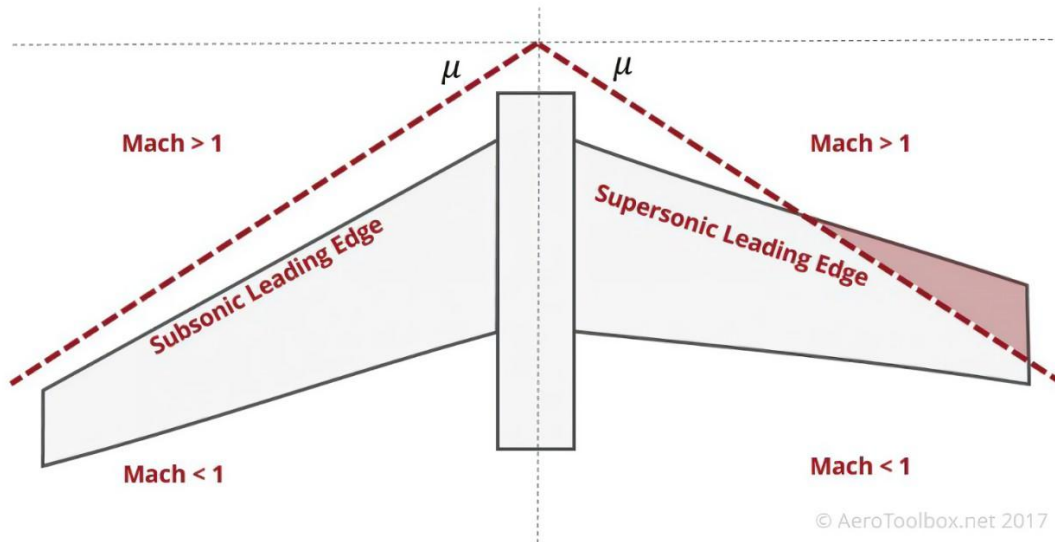


Fig. 25. Accommodation of wing planform through sweep angle inside the Mach cone, courtesy of AeroToolbox.net.

Another noteworthy consideration is the position of the A.C., the point in the airfoil chord where pitching moment,

$$M = \frac{1}{2} \rho v^2 c_m S \quad (2.5)$$

where c_m is the moment coefficient and S the wing planform surface, does not vary with

AoA; $\left. \frac{dc_m}{d\alpha} \right|_{A.C.} = 0$. For thin airfoils, A.C. position is considered to be independent from

AoA. The pressure distribution over the entire airfoil can be reduced to a single lift force and pitching moment around the A.C.; for the whole wing planform this point lies within the A.C. of the MAC.

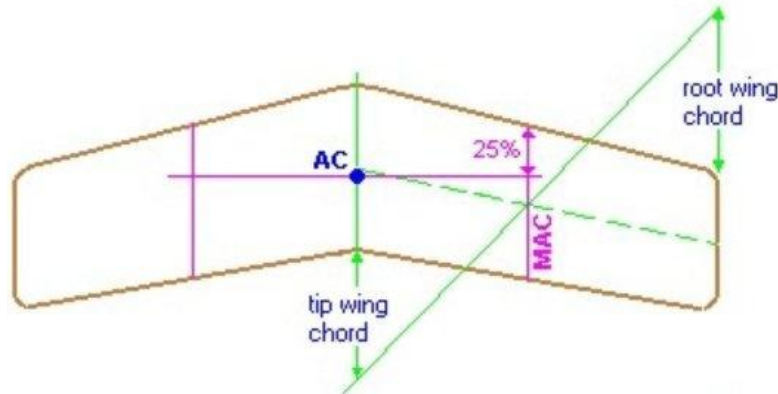


Fig. 26. Geometric calculation of the MAC and wing A.C.

When entering and existing supersonic flight regimes, the wing A.C. may move as a result of the variation of pressure distribution. This movement depends on the wing planform selection; for modern high performance fighters three wing type options are in use today: delta wings, trapezoidal wings and sweptback wings of low AR.

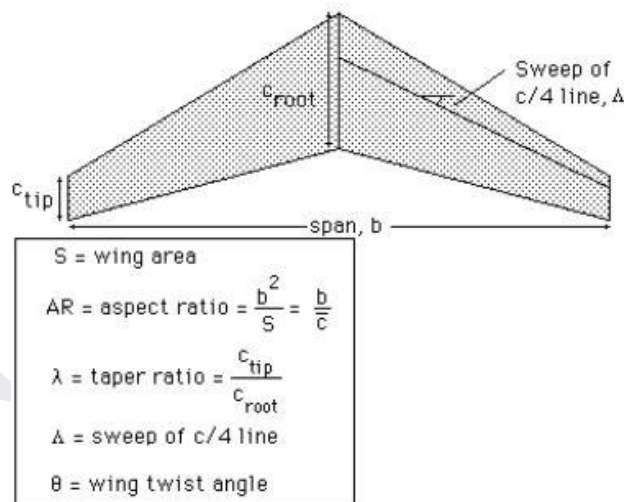


Fig. 27. Wing Magnitudes.

Taking as reference the wing LE, in subsonic conditions, the wing A.C. lies at 25% of the MAC for both trapezoidal and sweptback wings and at $\frac{2}{3}$ of the root chord for delta wings. At supersonic conditions the wing A.C. moves backwards to 40% of the MAC for both trapezoidal and sweptback wings whereas it remains unchanged in delta wings (D. P. Raymer, 1996). As it will be seen in the next section of this Chapter, the positioning and movement of the wing A.C. with respect to the Center of Mass of the whole aircraft affects the aircraft overall longitudinal stability, tail positioning and sizing. Each wing planform offers some tradeoffs with respect to the other two options, namely (G. Dimitriadis, 2017):

1. Delta Wing:

Advantages:

- They possess a long root chord and therefore can have a thick main spar while retaining a low thickness-to-chord ratio.
- Large wing area and therefore low wing loading even when maneuvering.
- Large internal volume for fuel and landing gear.
- It does not require a horizontal tail.

Disadvantages:

- Higher parasite drag due to its large surface area.
- High induced drag at subsonic speeds due to its low AR.
- Poor deep stall performance (the wake “blankets” the rudder and flaperons).
- Pitch control is achieved through the usage of flaperons, which reduce the total lift generated by the wing when deflected upwards.

2. Trapezoidal Wing:

Advantages:

- Better performance than Delta wings at transonic speeds and when transitioning between flight speed regimes.
- The wing A.C. lies further aft than in Delta wings therefore the tail must not lie too far back on the fuselage or possess as much surface area.
- More suitable for stealth applications.
- Flaps can be easily used for takeoff and landing.

Disadvantages:

- Higher wing loading than Delta wings.
- They stall at lower AoA than Delta wings although this problem can be easily solved through the addition of LE root extensions (LERX) or canards which serve as vortex generators.

3. Sweptback Wing:

Advantages:

- Higher wing area than trapezoidal wings.

Disadvantages:

- They require LERX such as trapezoidal wings.
- They generate higher parasite drag than trapezoidal wings.



Fig. 28. Examples of delta, trapezoidal and sweptback wings.

2.2.2. The Tails:

In transonic conditions, the movement of the wing A.C. and the loss of authority for the elevators or canards due to shock wave formation may induce a nose-down pitching moment which could put the safety of the aircraft and its crew in jeopardy. This effect, known as Mach Tuck, was especially prevalent during WW2 when fighters or dive bombers would perform a dive and accelerate to transonic speeds; the induced nose-down moment made pulling the nose up impossible and the aircraft would crash. In combination with the wing design, as seen previously, the solution entailed making the elevators or canards all-movable so as to possess greater authority and counteract the increase in pitching moment (J. A. Axelson, 1947). The absence of any hinge prevents the formation of shockwaves at supersonic speeds and the deflection of the whole surface generates greater pitching moment with very little effort, making turns tighter and needing less surface area. Fighter aircraft use three different types of designs:

1. Stabilator: the surfaces move as a single piece around its A.C.
2. Tailerons: the surfaces can move independently for the added benefit of increased roll rate at the expense of more weight and complexity.
3. Ruddervators: the tailerons are arranged in a V-tail and are used as both rudders and stabilators; the simplification reduced drag, weight and RCS at the expense of more complex control systems.



Fig. 29. Examples of stabilators, tailerons and ruddervators.

2.2.3. The Fuselage:

The fuselage itself is a major contributor to drag, and additional considerations must be taken into account in order to reduce wave drag at transonic and supersonic speeds. For that purpose Whitcomb’s and Jone’s transonic and supersonic regime area rules, respectively, will be used to shape the fuselage and determine the positioning of the wing and tail within the fuselage. In any case, these rules must be applied taking into account the internal space requirements for fuel, systems and armament (as it will be discussed more profoundly in Chapter 3, stealth aircraft are required to carry their combat load inside the fuselage).

Whitcomb’s Transonic Area Rule, in itself a design technique, indicates that two aircraft with the same longitudinal cross-sectional area distribution have the same wave drag, independent of how the area is distributed laterally (i.e. in the fuselage or in the wing). In order to avoid the formation of strong shock waves (normal shock waves) the external shape of the aircraft has to be carefully arranged so that the cross-sectional area changes as smoothly as possible going from nose to tail. To satisfy this rule, one of the more typical design choices is to narrow the fuselage wherever the wing meets it.

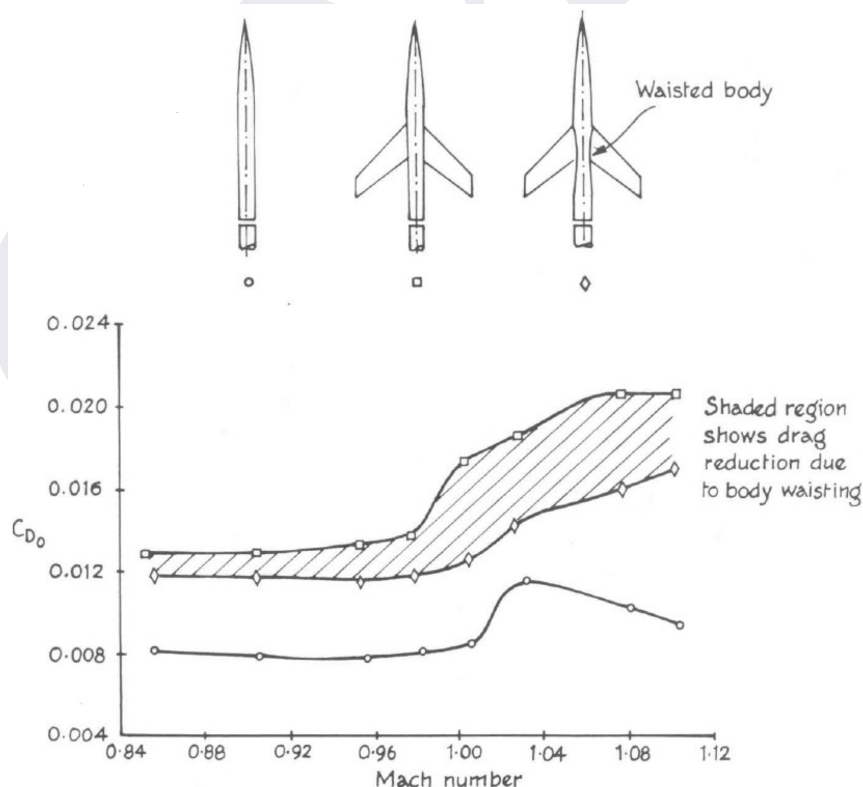


Fig. 30. Wave drag reduction due to fuselage waisting, extracted from “Theory of Wing-Body Drag at Supersonic Speeds” by R. T. Jones.

R. T. Jones’s Supersonic Area Rule is an evolution of Whitcomb’s for supersonic conditions; it indicates that at supersonic speeds, the reference plane used to determine the cross-sectional area distribution should not be that perpendicular to the flow but inclined at the same angle as the Mach Cone (R. T. Jones, 1956). This consideration results in an ideal cross-sectional distribution which is biased rearwards.

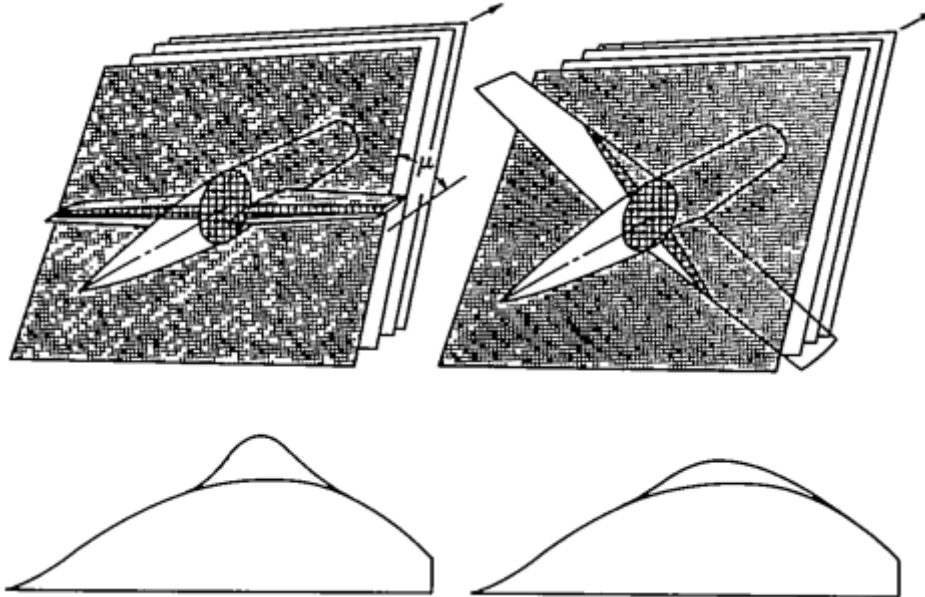


Fig. 31. Cross-sectional distribution through mach plane reference, extracted from “Theory of Wing-Body Drag at Supersonic Speeds” by R. T. Jones.

Taking into consideration both rules, Estadea’s wing should be positioned backwards and the fuselage at that section should be waisted in order to reduce wave drag as much as possible. These design choices can be seen on modern stealth fighters such as the Lockheed Martin F-35; notice the wing positioning and reduction in the fuselage cross-section:



Fig. 32. F-35 side view.

The nose cone, an essential part of the fuselage, deserves a closer look since, as discussed before, its selected shape will affect all other aerodynamic components due to its key interaction with the Mach Cone. Nose cone shapes available for choosing are many: conic, spherically blunted conic, bi-conic, tangent ogive, spherically blunted tangent ogive, secant ogive, elliptic, parabolic, power series and Haack series are the cone designs generally used for aerospace applications (A. Rajan Iyer & A. Pant, 2020). However, not all shapes are adequate for Estadea’s mission profile.

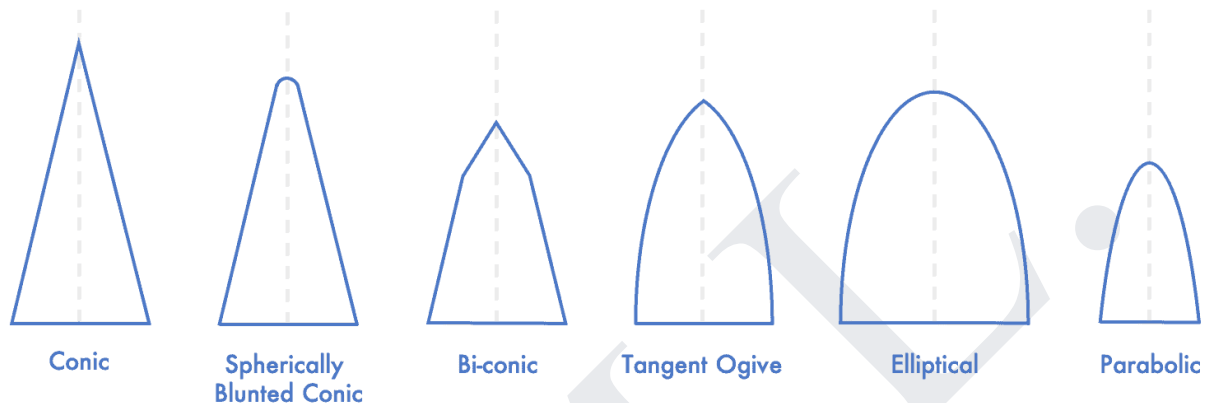


Fig. 33. Typical nose cone geometries for aerospace applications.

The factors affecting nose cone drag are basically the general shape, fineness ratio ($FR = \frac{Length}{Diameter}$) and bluntness ratio ($BR = \frac{Tip\ Diameter}{Base\ Diameter}$). At supersonic speeds, the fineness ratio has a significant effect on nose cone wave drag, particularly at low ratios, but there is very little additional gain for ratios increasing beyond 5:1 (A. Rajan Iyer & A. Pant, 2020). As the fineness ratio increases there is an increase in wetted area, and thus the parasite drag will also increase. Therefore, the minimum drag fineness ratio is ultimately going to be a trade-off between the decreasing wave drag and increasing friction drag (A. Rajan Iyer & A. Pant, 2020).

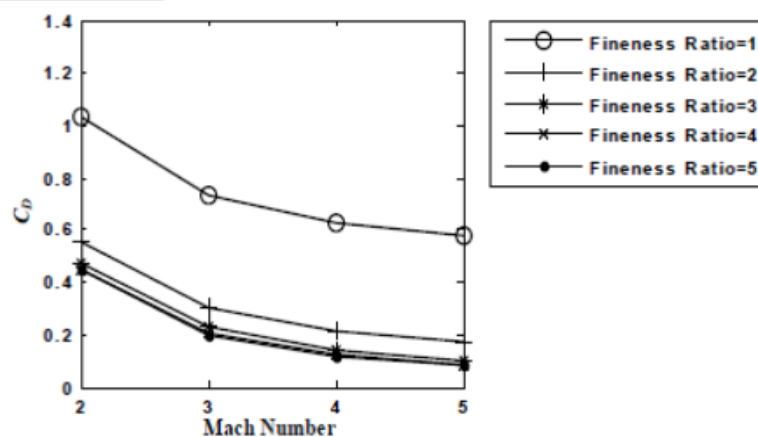


Fig. 34. Variation of drag coefficient with Mach number and fineness ratio for a conical nose design.

In order to prevent the formation of a bow shock wave, the nose cone must use a sharp tip ($BR \approx 0$). In terms of geometric shape, Von Karman shapes are shown to be better performers at transonic and supersonic regimes than their conical or ogive counterparts; they are often used in fighters, albeit slightly modified to accommodate instrumentation.

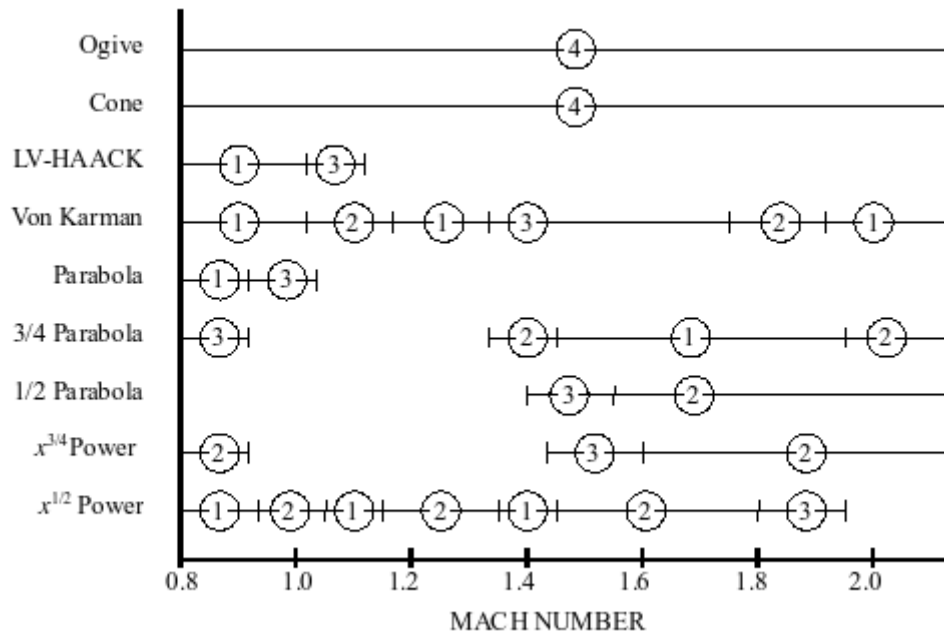


Fig. 35. Quantitative comparison between nose cone geometries at transonic and supersonic speeds, courtesy of USAF Missile Datcom (1:Best to 4:Worst).



Fig. 36. Von Karman nose cone shape.

2.2.4. Powerplant Installation & Components:

For legacy fighters such as the F-14, F-15, F-16, and F-18, inlet and exhaust integration were driven primarily by performance requirements, with weight an important but secondary consideration. These aircraft feature either two-dimensional (F-14 or F-15) or conformal (F-16 and F-18) inlets, and axisymmetric, non-vectoring engine mounted exhaust systems (J. W. Hamstra & B. N. McCallum, 2010).

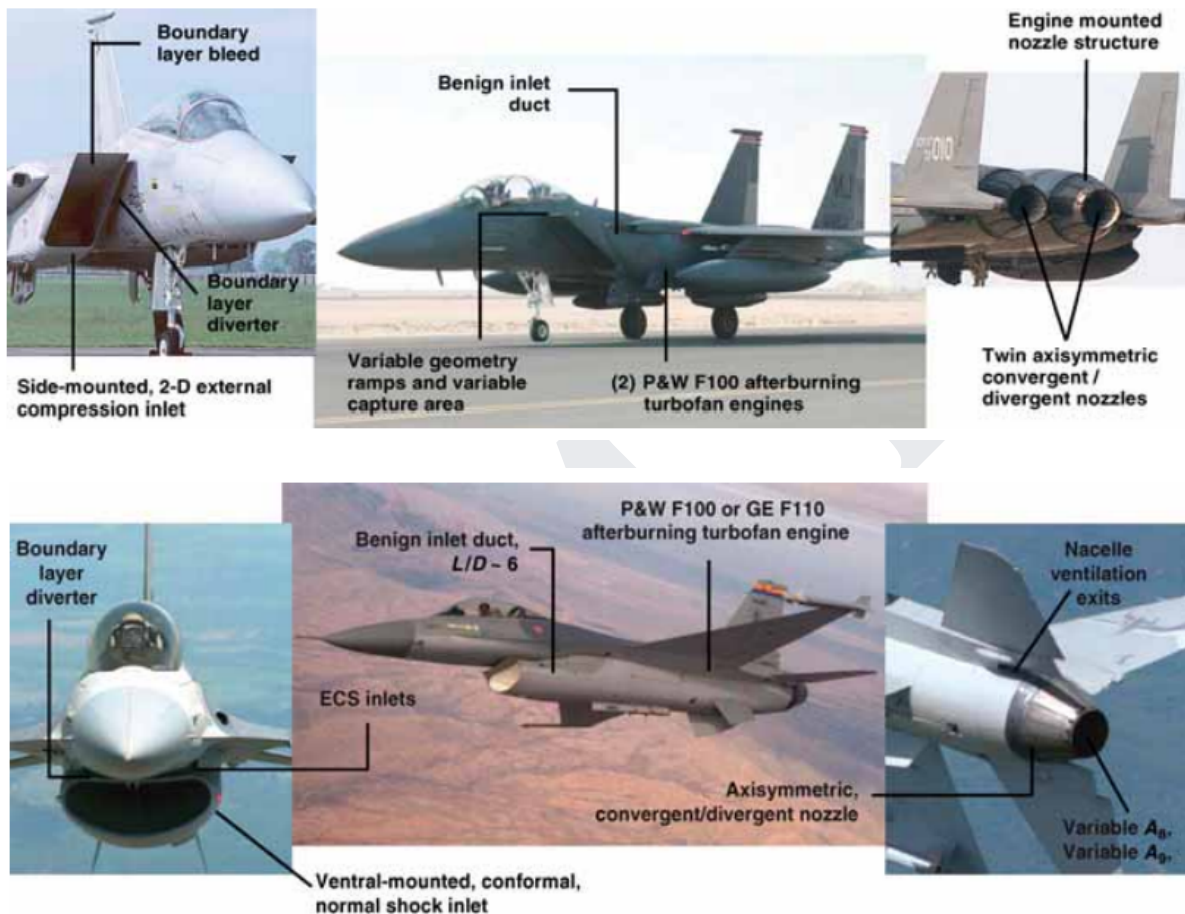


Fig. 37. Legacy fighter’s inlet and nozzle systems, courtesy of Lockheed Martin.

These fighters spent most of their service life flying in subsonic conditions. For example, based on historical data, the F-16 exceeds Mach 1 less than 1% of flight time (J. W. Hamstra & B. N. McCallum, 2010). Their inlet design was then focused on maximizing performance at those speeds, although fixed geometry inlets such as those of the F-16 and F-18 achieved limited supersonic capabilities. Fighters which were expected to possess extended supersonic capabilities, such as the F-15, were outfitted with variable geometry inlets, which reduce shock losses (J. W. Hamstra & B. N. McCallum, 2010). These, however, have the added liability of increased complexity, maintenance and radar signature (J. W. Hamstra & B. N. McCallum, 2010).

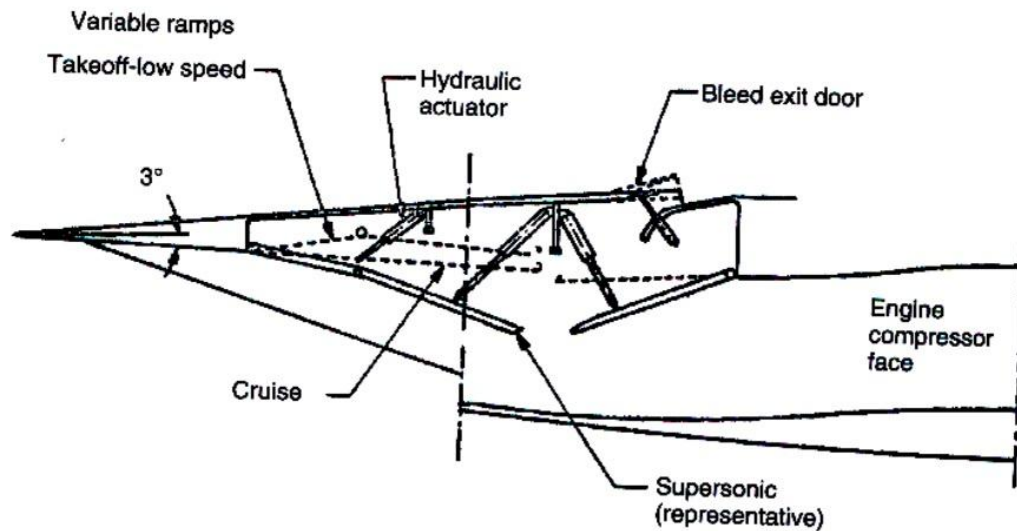


Fig. 38. Example of a variable geometry inlet design.

Additionally, legacy fighter inlets incorporate a boundary layer diverter as identified on the F-15 in Figure 35. The boundary layer diverter offsets the inlet from the fuselage and provides a passage for the forebody boundary layer to spill between the inlet and forebody. The diverter prevents the low energy boundary layer from entering the inlet and degrading performance, and, during supersonic flight, isolates the inlet shock from the boundary layer to improve aerodynamic stability. Tactical aircraft inlets may also contain variable bleed and bypass systems. The bleed system prevents significant boundary layer buildup on compression ramps to improve aerodynamic stability and performance. Bypass systems may be necessary to match inlet airflow to engine demanded airflow (J. W. Hamstra & B. N. McCallum, 2010).

Since Estadea, as an air superiority fighter, is expected to possess extended supersonic capabilities specially to transition to and from the battlefield rapidly, and stealth is a key aspect in its survivability, inlet design choice is key. One optimal option is the Caret inlet design, mounted in aircraft such as the F-22 and F/A-18E/F (J. W. Hamstra & B. N. McCallum, 2010). The primary trait of Caret inlets is a pair of oblique compression ramps that generate a 2-D flow field and coplanar shock waves at the supersonic design point. Primary advantages of the caret inlet are efficient supersonic flow compression (as with the F-14 or F-15) and swept inlet edges that can be aligned with the aircraft planform which, in combination with a warped duct (known as “S” ducts) to hide the engine components, reduces radar signature (J. W. Hamstra & B. N. McCallum, 2010).



Fig. 39. Caret Inlet design and example.

Caret inlets necessitate boundary layer diverters as in most fighter aircraft; this is not needed for the second option for inlet design: the diverterless inlet. This particular design integrated a highly three-dimensional bump compression surface with a forward-swept cowl. This combination produces a pressure gradient that diverts the majority of the boundary layer and provides a stable interaction between the inlet shocks and remaining boundary layer, eliminating the need for both boundary layer diverter and bleed systems (J. W. Hamstra & B. N. McCallum, 2010).

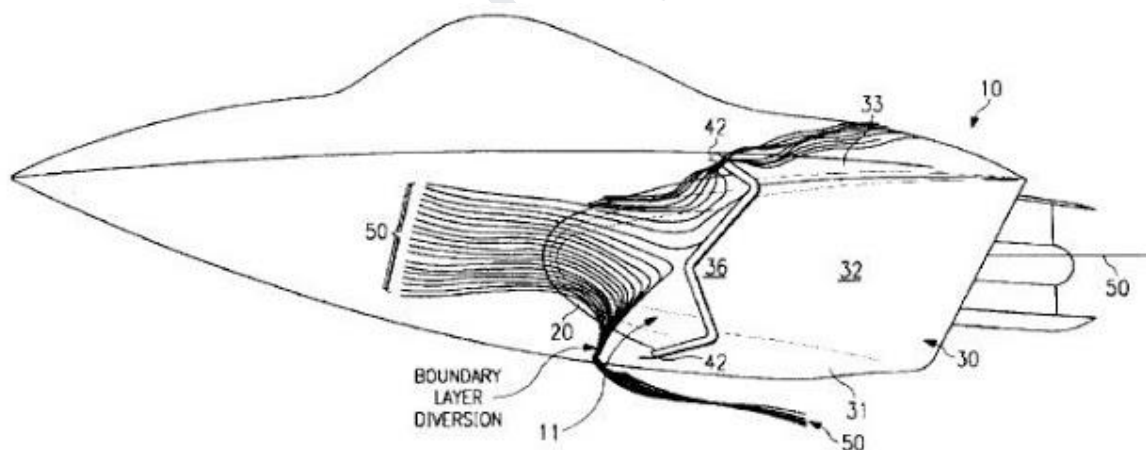


Fig. 40. Diverterless inlet or “bump” inlet design of the YF-23, patent US2007181743.

Both design options are fixed geometry inlets with mixed compression; this means the flow deceleration to subsonic conditions is achieved through a set of shocks situated between the forebody and intake lip (identified as external shocks), and a second set of the shocks found between the nose lip and the intake throat (called internal shocks). This design

has the added benefit of a very high pressure recovery factor, the ratio of the average total pressure at the exit of the inlet to the free-stream total pressure (A. F. El-Sayed, 2016):

$$r_d = \frac{P_{02}}{P_{\infty}} \quad (2.6)$$

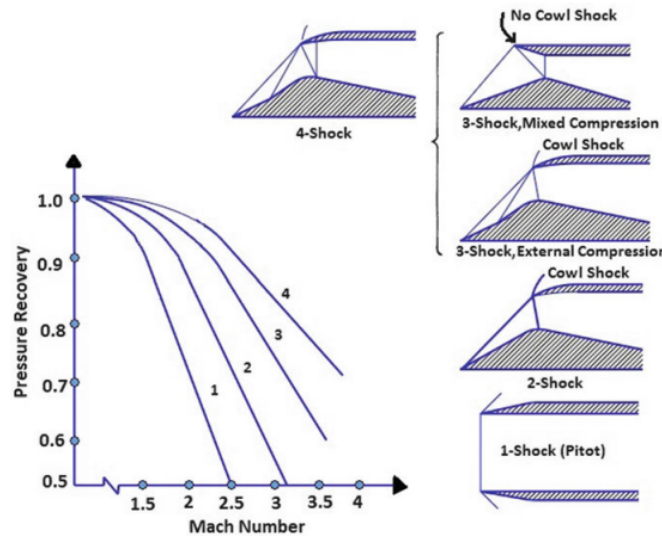


Fig. 41. Various types of intake geometry and their effect on pressure recovery, extracted from Chapter 8 “Stationary Modules Intakes, Combustors and Nozzles” by A. F. El-Sayed.

For flight at Mach numbers much beyond 1.6, variable-geometry features must be incorporated in the inlet to achieve high-inlet pressure recoveries together with low external drag (A. F. El-Sayed, 2016). The absence of external variable geometry components does not mean these inlet designs don’t incorporate active components. The F-22 for example, uses overpressure relief doors located just before the engine fan.

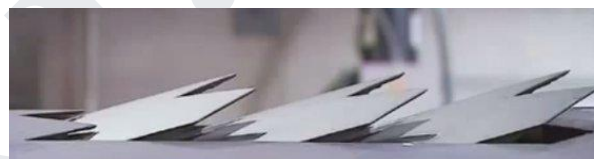


Fig. 42. F-22 overpressure relief doors.

The supersonic intake possesses two distinctive deceleration sections: the supersonic section, where a combination of three oblique shocks and a normal shock bring the flow velocity to subsonic conditions ($M < 1.0$), characterized by a convergent inlet; and subsonic section, where a divergent inlet further decelerates the flow to the engine operating conditions (we assume $M_{max,engine} \approx 0.4$) (H. Ran & D. Mavris, 2005).

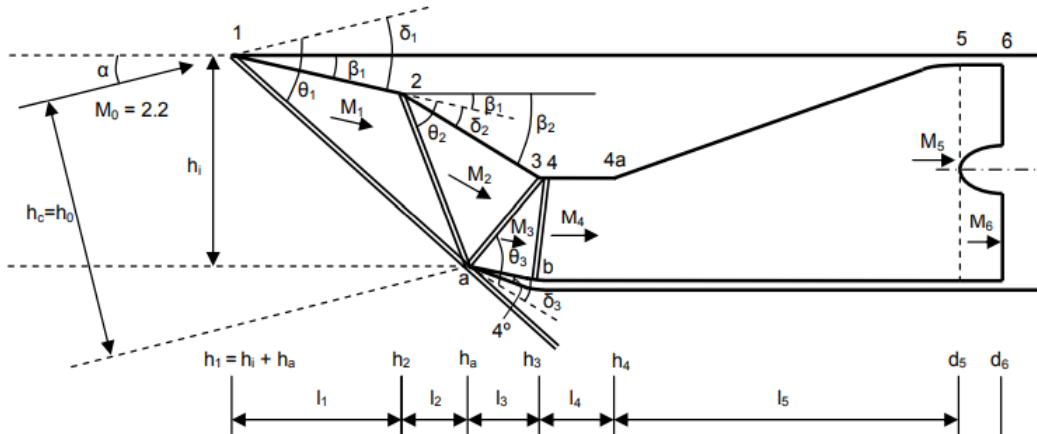


Fig. 43. Sketch of the whole inlet system with on-design shock positions, courtesy of the Georgia Institute of Technology.

- For the oblique shocks the following equations are used (H. Ran & D. Mavris, 2005):

$$M_n = \frac{1}{\sin(\beta-\theta)} \sqrt{\frac{1 + \frac{\gamma-1}{2} M_{n-1}^2 \sin^2(\beta)}{\gamma M_{n-1}^2 \sin^2(\beta) - \frac{\gamma-1}{2}}} \quad (2.7)$$

$$\tan \delta_n = \frac{2 \cot \theta_n (M_{n-1}^2 \sin^2 \theta_n)}{2 + M_{n-1}^2 (\gamma + 1 - 2 \sin^2 \theta_n)} \quad (2.8)$$

- For the normal shock, its corresponding relations are used (H. Ran & D. Mavris, 2005):

$$M_n^2 = \frac{(\gamma-1)M_{n-1}^2 + 2}{2\gamma M_{n-1}^2 - (\gamma-1)} \quad (2.9)$$

- In the subsonic section, the area-Mach number relation is used (H. Ran & D. Mavris, 2005):

$$\left(\frac{A_n}{A^*}\right)^2 = \frac{1}{M_n^2} \left[\frac{2}{\gamma+1} \left(1 + \frac{\gamma-1}{2} M_n^2 \right) \right]^{\frac{\gamma+1}{\gamma-1}} \quad (2.10)$$

From “Preliminary Design of a 2D Supersonic Inlet to Maximize Total Pressure Recovery” by H. Ran and D. Mavris, these equations were applied to determine the dimensions of an optimal 2D supersonic inlet in terms of pressure recovery at $M_\infty = 2.2$ at $h = 55,000ft$. This design, since it fits into Estadea’s top level requirements, will be used as the basic design for the fighter:

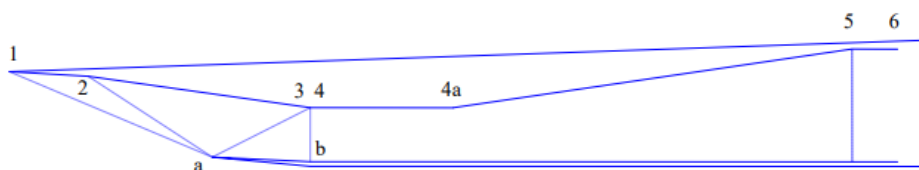


Fig. 44. Optimized inlet sketch, extracted from “Preliminary Design of a 2D Supersonic Inlet to Maximize Total Pressure Recovery” by H. Ran and D. Mavris.

The advantage of their approach is that all inlet dimensions are given in terms of engine fan diameter, meaning the design can be easily adapted to the selected engine in Chapter 6.

$l_1_d_6$	$l_2_d_6$	$l_3_d_6$	$l_4_d_6$	$l_5_d_6$
0.568	0.700	0.537	0.890	2.641
$h_1_d_6$	$h_2_d_6$	$h_3_d_6$	$h_4_d_6$	$h_a_d_6$
0.801	0.751	0.445	0.445	0.043

Total pressure recovery: TPR = 0.942 . Total length: 5.336 times engine face diameter.

Table 1. Normalized inlet dimensions.

From Table 1, l_n is the distance between two station points, measured along flight direction, and h_n the height of n^{th} station point, measured from the lower surface of the inlet and perpendicular to the flight direction.

In terms of engine nozzle architecture, for fighters it is mandatory to mount a variable geometry convergent-divergent nozzle mechanism. Although it adds in weight and complexity, the mechanism will ensure the nozzle exit pressure is equal to the ambient pressure (adapted nozzle, $P_e = P_\infty$) and avoid the formation of shockwaves at the nozzle's exit which would greatly reduce the thrust generated as the exhaust gasses' speed is greatly reduced (A. F. El-Sayed, 2016).

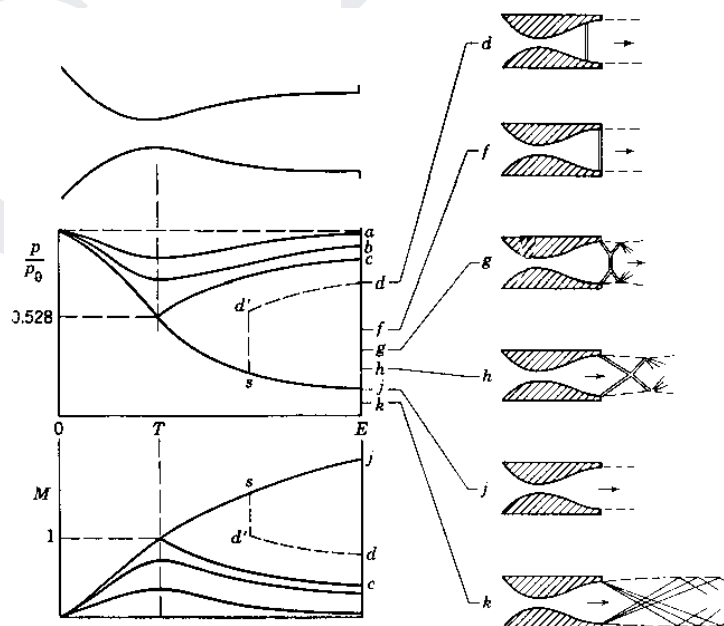


Fig. 45. Effects of ambient pressure in C-D nozzles at subsonic and supersonic conditions.

- At subsonic speeds the nozzle mechanism closes the divergent section so the whole nozzle is convergent; $\frac{P_{0, nozzle}}{P_{\infty}} < 1.89$ to avoid choking:

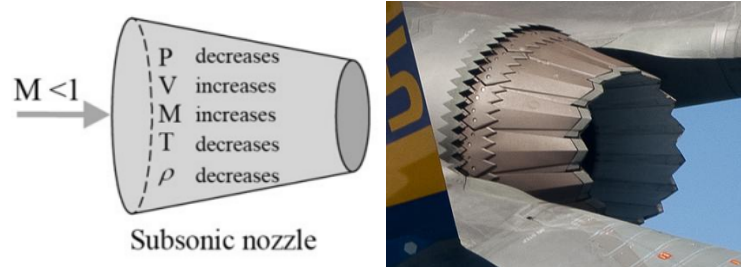


Fig. 46. C-D nozzle subsonic configuration.

- At supersonic speeds, the nozzle mechanism forms the divergent section:

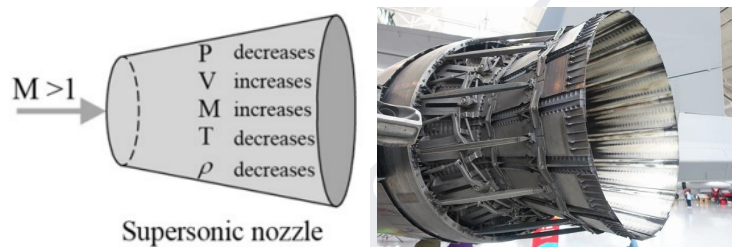


Fig. 47. C-D nozzle supersonic configuration

- Assuming the nozzle is always adapted, for pure turbojets the thrust equation reduces to

$$T_{NET} = (\dot{m}_a + \dot{m}_f)v_e - \dot{m}_a v_{\infty} \equiv \text{Momentum Thrust} - \text{Momentum Drag} \quad (2.11)$$

$v_e = \sqrt{\frac{2\gamma\eta RT_{06}}{(\gamma-1)} \left[1 - \left(\frac{P_{\infty}}{P_{06}}\right)^{\frac{\gamma-1}{\gamma}} \right]}$ (2.12) is the exhaust gas velocity; R is the ideal gas constant and T_{06} , P_{06} are the static temperature and pressure at the turbine exit, respectively.

- Modern fighters also mount low bypass turbofans; assuming the nozzle is always adapted, the thrust equation reduces to

$$T = (\dot{m}_{a, core} + \dot{m}_f)v_{e, core} + \dot{m}_{a, fan} v_{e, fan} - \dot{m}_a v_{\infty} \quad (2.13)$$

$$v_{e, core} = \sqrt{\frac{2\gamma\eta RT_{08}}{(\gamma-1)} \left[1 - \left(\frac{P_{\infty}}{P_{08}}\right)^{\frac{\gamma-1}{\gamma}} \right]} \quad (2.14)$$

$$v_{e, fan} = \sqrt{\frac{2\gamma\eta RT_{010}}{(\gamma-1)} \left[1 - \left(\frac{P_{\infty}}{P_{010}}\right)^{\frac{\gamma-1}{\gamma}} \right]} \quad (2.15)$$

Fighter aircraft engines mount additionally an afterburner in between the turbine and the nozzle for access to increased levels of thrust, specially when dogfighting. The afterburner is another combustion chamber added between the turbine and the nozzle that utilizes the unburnt oxygen in the exhaust gas to support combustion. When the afterburner is turned on, additional fuel is injected, which burns and produces additional thrust (A. F. El-Sayed, 2016). Whenever operational, the static pressure and temperature used in the exhaust velocity equations must be those of the afterburner exit.

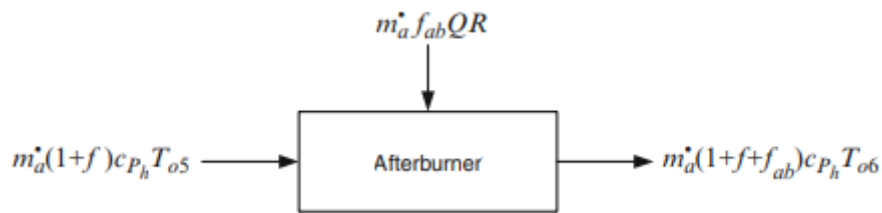


Fig. 48. Energy balance in the afterburner, extracted from Chapter 6 “ Turbine-Based Engines: Turbojet, Turbofan, and Turboramjet Engines” by A. F. El-Sayed.

Other noteworthy parameters for both turbojet and turbofan engines include the exhaust gas temperature, EGT, engine pressure ratio, EPR ($EPR = \frac{P_{07}}{P_{02}}$ (2.16)) and thrust specific fuel consumption, TSFC. Having discussed both inlet and nozzle considerations for supersonic flight, two installation options, depending on the chosen engine type, can be appreciated:

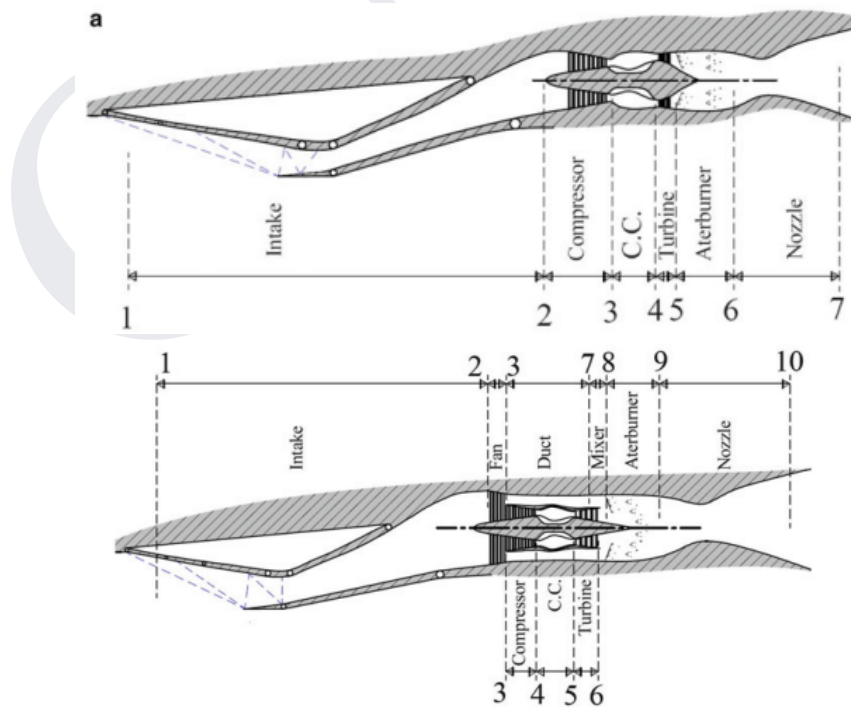


Fig. 49. Turbojet and low bypass turbofan simplified installation sketches.

2.2.5. External Fuel Tanks:

Fighter aircraft external fuel tanks, often mounted on the underside of the wing using pylon attachments, are tailored in shape to reduce wave drag. This shape corresponds to the Sears-Haack body (R. T. Jones, 1956), the shape with the lowest theoretical wave drag in supersonic conditions.



Fig. 50. Sears-Haack body drop tank design.

Drop tanks will extend the range of the fighter in all mission configurations although they must be dropped in combat to reduce both weight and radar signature. Following the Sears-Haack body geometry for the fuel tank design:

$$V = \frac{3\pi^2}{16} R_{max}^2 L \quad (2.17)$$

$$r(x) = R_{max} [4x(1-x)]^{\frac{3}{4}} \quad (2.18)$$

$$c_{D, wave} = \frac{9\pi^2 R_{max}^2}{2L^2} \quad (2.19)$$

2.2.6. Aerodynamic Heating:

The moving fluid over the aircraft surface has a certain amount of kinetic energy; in the process of flowing over a surface, the flow velocity is decreased by the influence of friction and hence the kinetic energy is decreased. This lost kinetic energy reappears in the form of internal energy of the fluid, hence causing the temperature to rise. This phenomenon is called viscous dissipation within the fluid (J. D. Anderson, 2017). In turn, when the fluid temperature increases, there is an overall temperature difference between the warmer fluid and the cooler body.

Since heat is transferred from a warmer body to a cooler body, heat will be transferred from the warmer fluid to the cooler surface. This is the mechanism of aerodynamic heating of a body (J. D. Anderson, 2017). Aerodynamic heating becomes more severe as the flow velocity increases, because more kinetic energy is dissipated by friction, and hence the overall temperature difference between the warm fluid and the cool surface increases (J. D. Anderson, 2017).

Airframe temperature due to friction can reach $-29.0\text{ }^{\circ}\text{C}$ at $M = 0.8$, $54,4\text{ }^{\circ}\text{C}$ at $M = 1.6$, 83.3°C at $M = 1.8$ and 116.8°C at $M = 2.0$ at the nose cone (J. D. Anderson, 2017), LEs and inlets which must be reinforced with materials which retain their strength even at high temperatures, such as titanium and Inconel alloys (from Special Metals Co.).

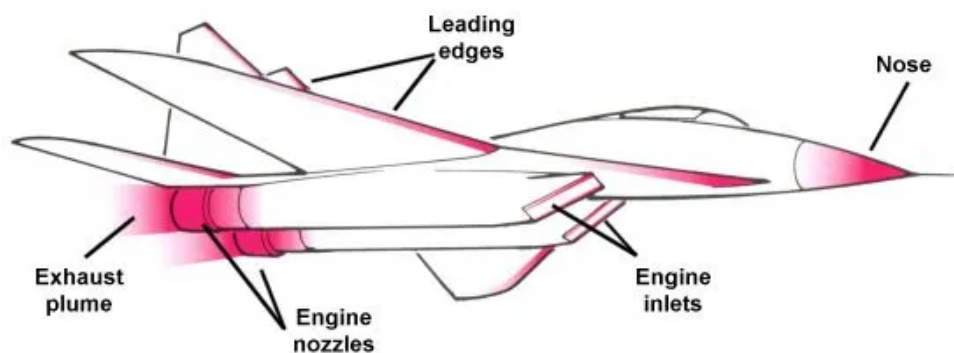


Fig. 51. A fighter's "hot points".

2.3. Stall Characteristics, Control Surfaces, High Lift Devices & Maneuverability

2.3.1. Stall Characteristics:

Since Estadea is expected to perform high AoA maneuvers, it is of paramount importance to examine the airfoil’s post-stall behavior; the latter is determined by analyzing the c_l versus AoA or “ c_l vs. alpha” curve. The AoA for stall (loss of lift generation) can be determined as the first point in which c_l decreases. The desired post-stall behavior is that of a gradual and smooth decrease in c_l . For thin airfoils:

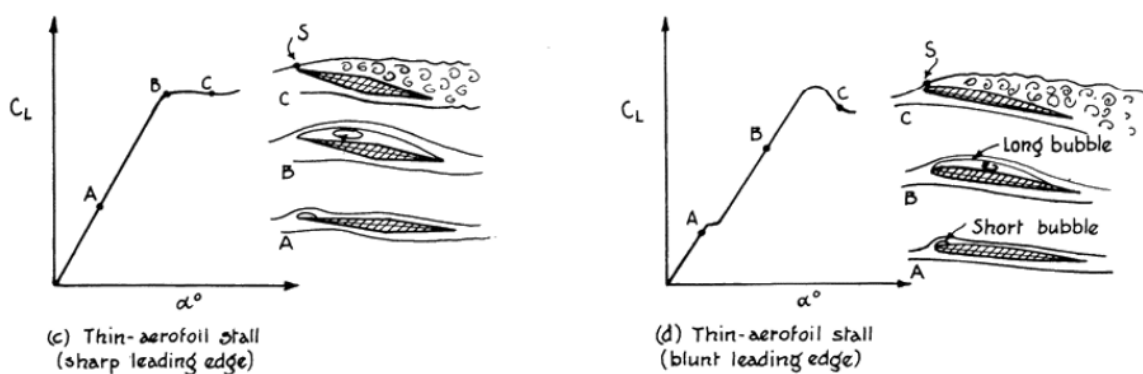


Fig. 52. Thin airfoil c_l vs. alpha curves, extracted from “Aerodynamic and Propulsive Forces” by R. Llamas.

The shape of the wing planform determines its stall progression, meaning which areas of the wing stall first and how this stall progresses as the AoA increases. In any case, it is preferable that the wing first stalls at the root; in that case the pilot will have enough reaction time to decrease the fighter’s AoA without fearing loss of control (wing tip stall).

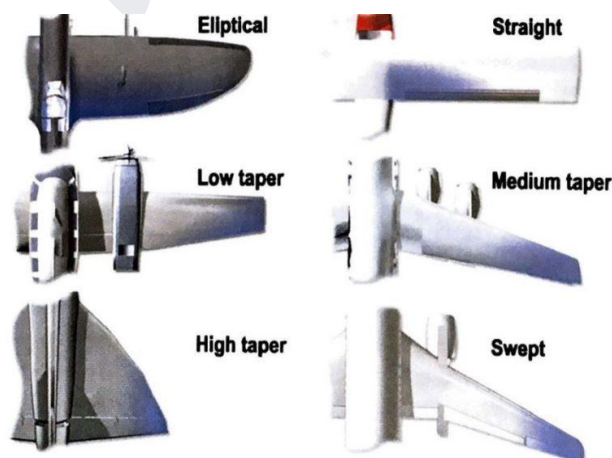


Fig. 53. Stall progression (blue) in various wing planforms.

The selected candidates for Estadea’s wing planform: delta, trapezoidal and sweptback planform, all possess objectively bad stall progression characteristics (as seen in Fig. 50). To solve this issue the tips of the wing will be physically displaced to lower AoA than the wing root through the addition of a negative twist angle to the wing planform, ensuring this section will be the last to stall. The addition of this negative twist has some added benefits; as a lower AoA decreases the c_l and therefore lift generation at the tips, the lift aerodynamic load is displaced inward, reducing the wing root bending moment. This is especially beneficial at high load maneuvers, such as tight sustained turns.

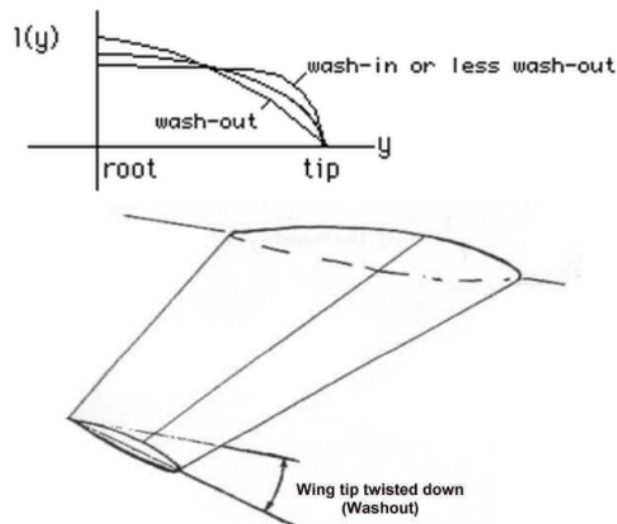


Fig. 54. Effects of negative tip twist in spanwise lift distribution, extracted from “Wing Design” by R. Llamas.

Another benefit is the reduction of lift induced drag as the spanwise lift distribution is approximated to the ideal elliptical distribution:

$$C_{D,i} = \frac{C_L^2}{\pi e AR} \quad (2.20)$$

Where e is the Oswald Factor, a correction factor that represents the change in drag with lift of a three-dimensional wing or airplane, as compared with an ideal wing having the same AR and an spanwise elliptical lift distribution (D. P. Raymer, 1996). It is noteworthy to know that the Oswald factor greatly decreases at supersonic speeds although c_l is also greatly reduced (speed complements the reduction of AoA for lift generation).

Additionally, stall angle itself can be very easily increased in detriment of $c_{L,max}$ by having a short wing (AR) which in itself is required to fit inside the Mach Cone at supersonic speeds as seen in the previous section.

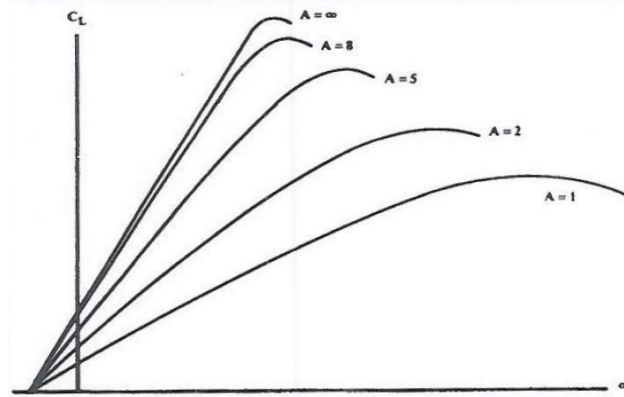


Fig. 55. Effects of AR in stall angle and $c_{L,max}$.

Finally, in combination with low AR wings, the inclusion of LERX (LE Root Extensions) can have an increased benefit for the fighter's stall characteristics. LERX brings forth to other planforms the main benefit of Delta wings. For a sharply-swept Delta wing, as air spills up round the LE due to the pressure difference between the upper and lower wing areas, it flows inwards to generate a characteristic vortex pattern over the upper surface. The lower extremity of this vortex remains attached to the surface and also accelerates the airflow, maintaining lift. A LERX is in itself a small Delta wing and behaves as such, energizing the flow over the main planform delaying its separation and subsequent stall; although this vortex, in interaction with other control surfaces, can have detrimental effects (vortex bursting). For example, it is well known that VTP fatigue problems in the F/A-18 Super Hornet are provoked by the interaction of the former with the vortex generated by the LERX. Careful consideration must be given to the tail positioning if LERX is included, keeping them away from the vortex path.

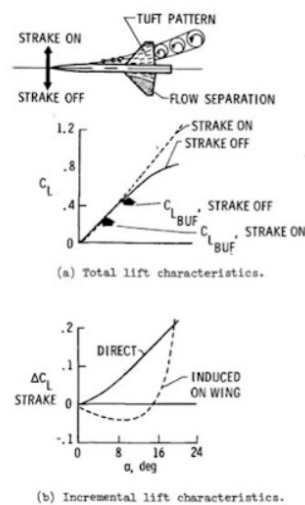


Figure 8.- Influence of maneuver strakes on wing-airflow characteristics.

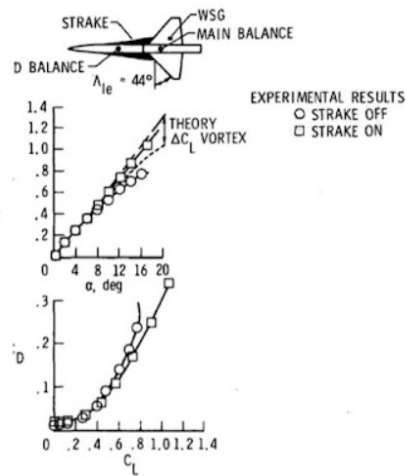


Figure 7.- Effect of maneuver strake on lift and drag characteristics. $M = 0.85$.

Fig. 56. Lift enhancement via LERX addition at intermediate and high AoA.

2.3.2. Control Surfaces & High Lift Devices:

In addition to all-movable tails, as seen in the previous section, Estadea needs to incorporate additional control surfaces and high lift devices within the wing to supplement both the former and latter in take-off, landing and general in-flight maneuvers.

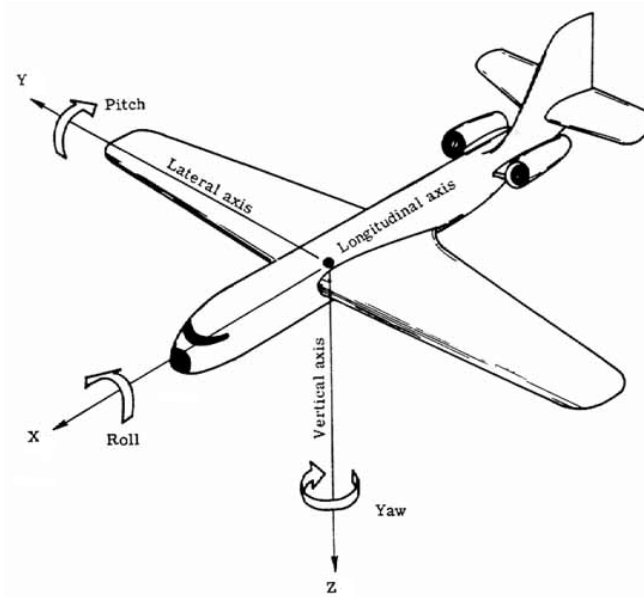


Fig. 57. The three aircraft DOFs.

- X-Axis: Roll.

Rolling moments will be primarily induced by two ailerons, each located in one wing end. To induce higher rolling moments, the two ailerons will be aided by two flaperons, all movable flaps which serve as both flaps in approach and take-off and supplemental ailerons when dogfighting.

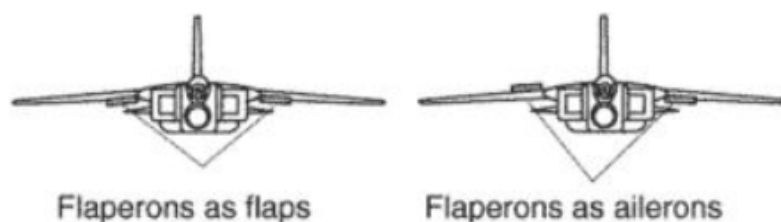


Fig. 58. Flaperon positioning and functioning.

- Y-Axis: Pitch.

Pitching moments will be induced primarily by the all-movable tails, although flaperons can and will complement the former to achieve higher pitch rates in engagements.

- Z-Axis: Yaw.

In this case, yawing moments will be induced by the movement of the tails.

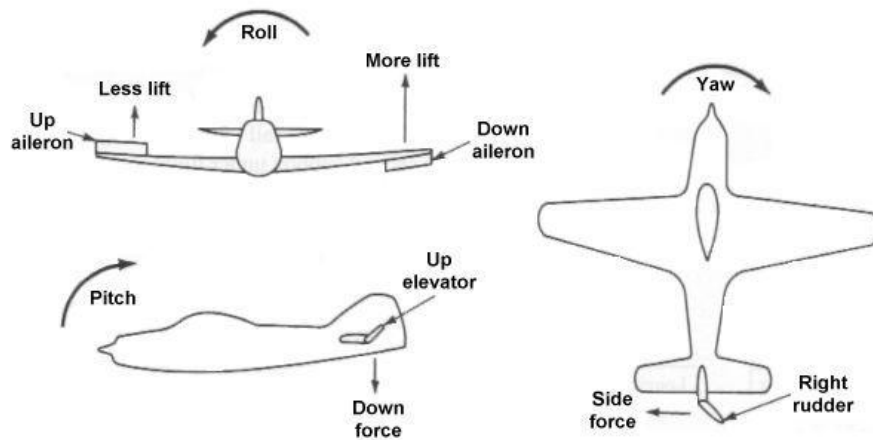


Fig. 59. Roll, pitch and yaw moments.

In addition to conventional fighter aircraft control surfaces, Estadea will include thrust vectoring, an additional nozzle mechanism which redirects the exhaust gas in multiple directions, inducing pitch, roll and yaw moments on the airframe. Thrust vectoring can be relegated to an extra aid in turning and pitching maneuvers and stall recovery (such is its usage in the F-22) to a source of control when conventional control surfaces are stalled in which each nozzle can be operated independently (being the best example the Su-57). In any case, thrust vectoring can compensate for the increase in weight and complexity by reducing the workload of the control surfaces, either reducing their needed surface to maintain similar pitch, roll and yaw rates or increasing the previous rates when maintaining their surface at the cost of increasing weight. Estadea will ideally sport a 3D thrust vectoring, capable of inducing additional moments in all directions

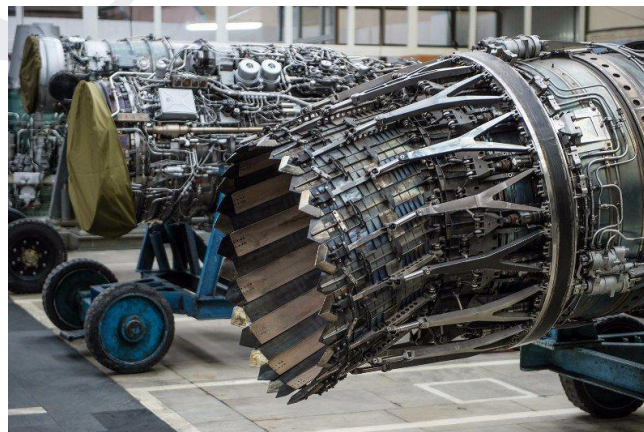


Fig. 60. SU57 thrust vectoring mechanism.

Finally, low speed maneuvers, including approach, take-off and landing, necessitate high lift devices for added safety and increased performance. The purpose of these devices can be summarized to decreasing the aircraft stall speed by increasing $c_{L,max}$:

$$L < W \Rightarrow v_{stall} = \sqrt{\frac{2W}{\rho c_{L,max} S_w}} \quad (2.21)$$

Estadea, due to its stealth design requirements, must possess an overall smooth profile (as it will be seen in Chapter 3); this relegates the available high lift devices to those which modify the wing camber and can conceal their internal mechanism: leading and TE flaps. Additionally, due to the wing's low thickness, the flap mechanisms are forced to be simpler than in traditional airliners. Finally, since flaps will be used as secondary ailerons in combat, these must pitch up and down. These three constraints narrow the options available to the plain flap and LE flaps.

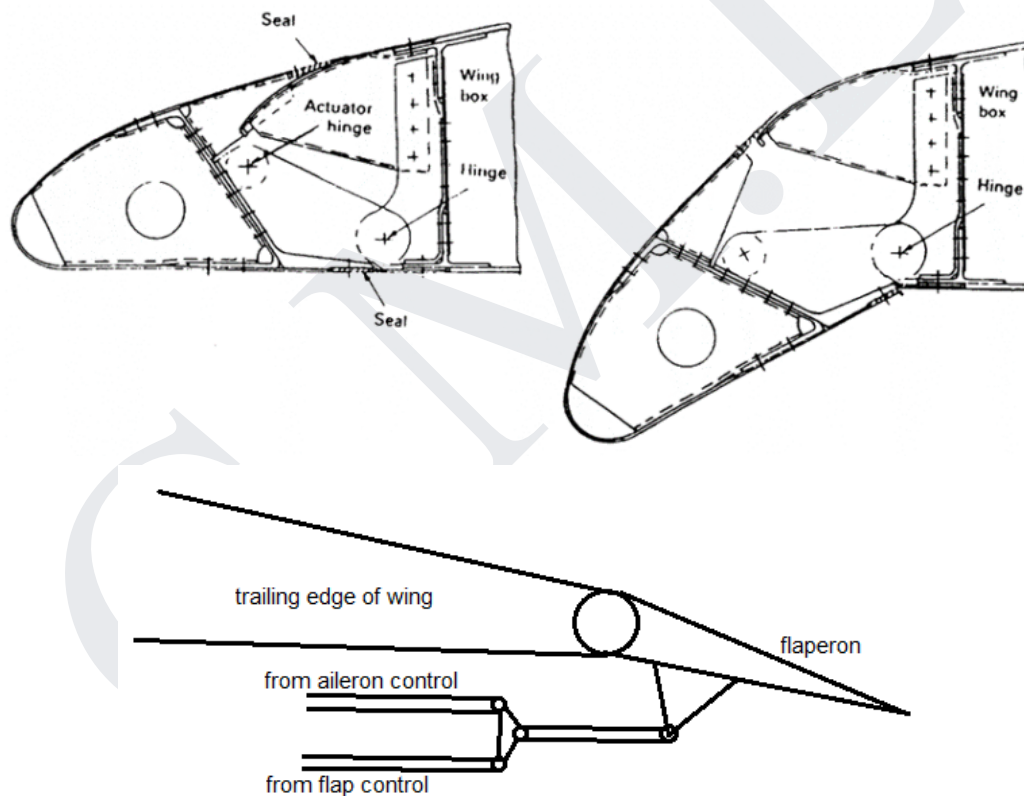


Fig. 61. LE Flap and Flaperon mechanism examples.

Although the plain flap is the weakest TE high lift device in terms of $c_{L,max}$ increase, the inclusion of a slat not only adds to this increase but also, when deployed alone, increases the stall angle as it reduces the pressure peaks over the downstream airfoil, delaying boundary layer separation and therefore increasing the stall angle (A. M. O. Smith, 1975).

Considering this, the flaperon will be deployed in its flap configuration in combination with the slat in approach, landing and take-off maneuvers; the wing will sport a clean configuration at high speed cruise conditions for reduced drag, and, when entering combat, the LE flap will be deployed for maximum maneuverability.

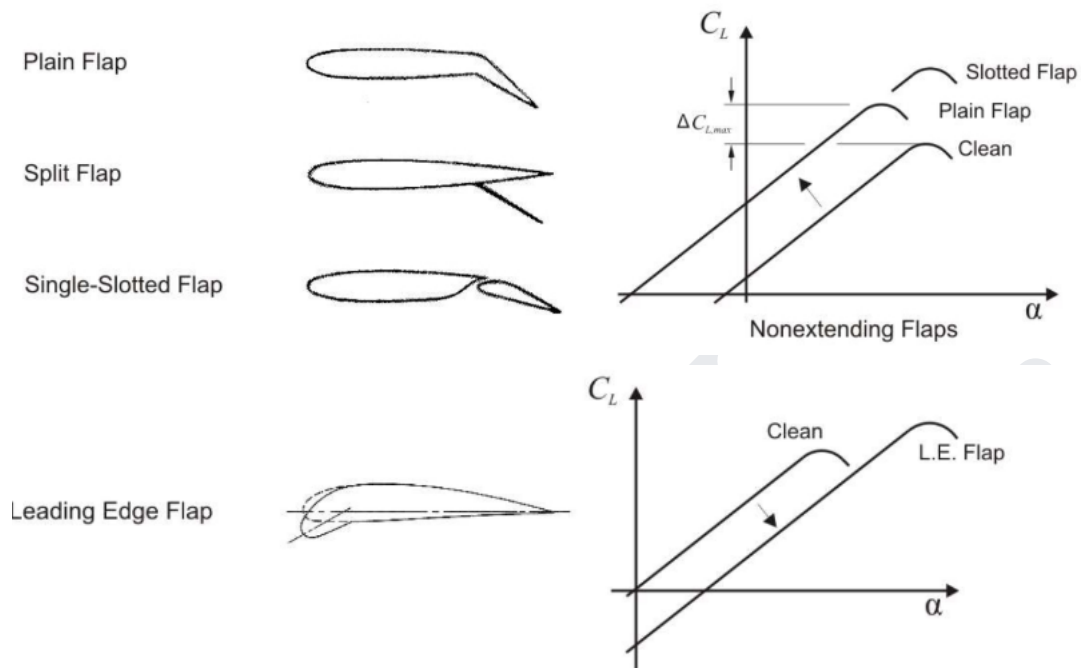


Fig. 62. Effects of non-extending flaps and LE flap on c_l curves.

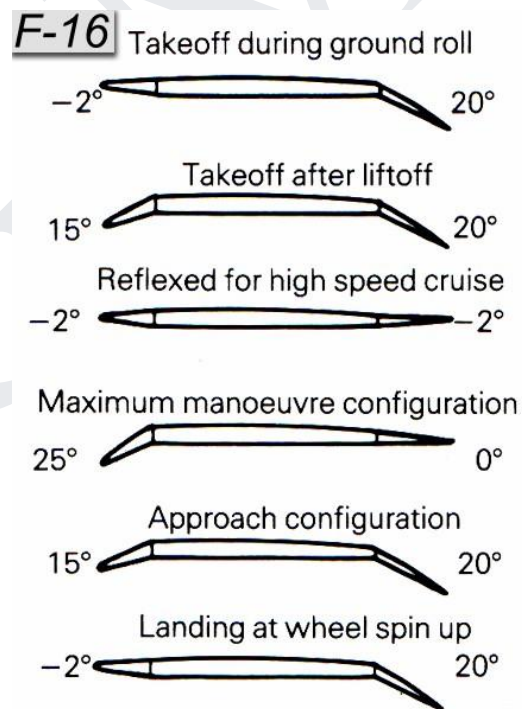


Fig. 63. F-16 LE and TE flap configuration for its different flight regimes.

2.3.3. Maneuverability

Maneuverability can be broadly defined as the ability for the aircraft to commence and sustain maneuvers, its responsiveness and its performance in roll or turn rate and pitch rate. Estadea, as an air superiority fighter, needs to be an excellent dogfighter to succeed in its role. Without increasing the size of the control surfaces in order to avoid the increased penalty of weight and drag, the fighter’s maneuverability can be greatly increased by upsetting the weight balance in the longitudinal axis (pitch) and selecting the correct wing placement with respect to the lateral axis (roll). These measures make the aircraft unstable in the previous axis, increasing its responsiveness. Within the concept instability, it is convenient to differentiate between static stability and dynamic stability:

- Static stability describes the tendency of an aircraft to retain its original position when subjected to unbalanced forces or moments.

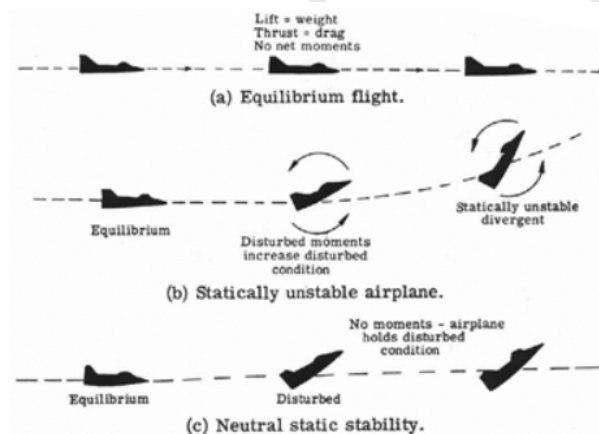


Fig. 64. The concept of static stability.

- Dynamic stability describes the form of motion an aircraft in static stability undergoes when it tries to return to its original position; usually, the motion is described as an oscillation, dynamic stability can be determined in terms of the damping ratio, ζ :

$$\zeta > 0 \Rightarrow \text{Dynamically Stable (2.22)}$$

$$\zeta = 0 \Rightarrow \text{Dynamically Neutral (2.23)}$$

$$\zeta < 0 \Rightarrow \text{Dynamically Unstable (2.24)}$$

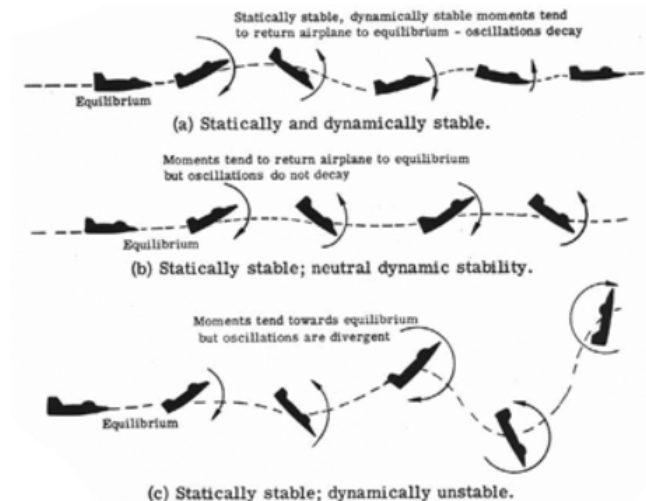


Fig. 65. The concept of dynamic stability.

It is important to remember that an aircraft cannot be statically unstable and dynamically stable at the same time.

- Longitudinal Axis (Pitch):

In this axis, in terms of static stability, the main concern is the position of the CoG with respect to the NP, the point in which, for a complete aircraft, the aerodynamic moment does not change with AoA; and the MP, the point beyond which the aircraft is no longer controllable with the available control surfaces, located aft the NP. In order to induce an instability in the pitch axis, the weight balance of the aircraft must be upset in this axis; meaning the aircraft's CoG must be pushed backwards towards the NP (static neutral longitudinal stability or “relaxed” stability) or even slightly aft of the former (static instability) but never beyond the MP.

$$\frac{dc_{My}}{d\alpha} > 0 \Rightarrow \text{Static Instability in Pitch} \quad (2.25)$$

In terms of the whole aircraft, the location of the NP and MP with respect to the position of the CoG (l_{NP} , l_{MP}) and $\bar{c}_w = MAC_w$ can be easily calculated:

$$\frac{l_{NP}}{c_w} = - \frac{\frac{dc_M}{d\alpha}}{\frac{dc_L}{d\alpha}} \quad (2.26)$$

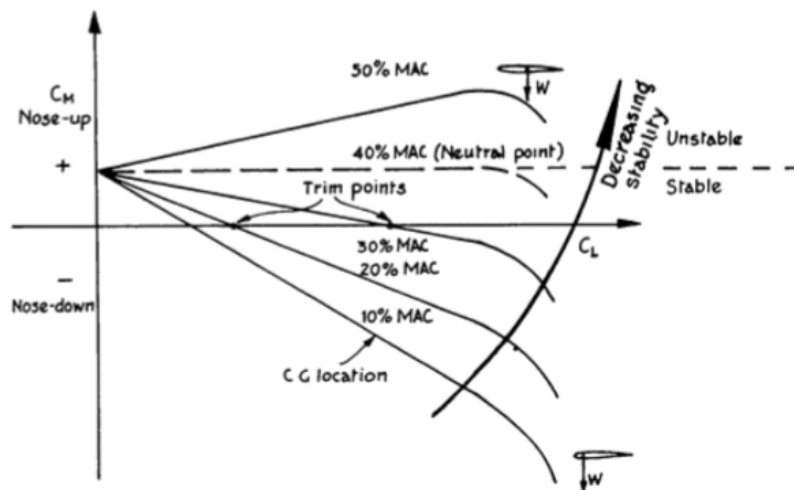


Fig. 66. Effects of pushing CoG aft on $\frac{dc_M}{d\alpha}$.

- Lateral Axis (Roll):

In this axis, in terms of static stability, the main concern is the placement of the wing with respect to the fuselage. For neutral stability, the wing must be placed in line with the CoG; the inclusion of a small negative dihedral angle can induce roll instability. Fighter’s usually possess either mid or low-mounted wings for neutral or unstable roll characteristics.



Fig. 67. Wing mounting options.

Estadea’s stealth design requirements, as it will be seen in Chapter 3, force the wing configuration to be mid-mounted. However, the mid-wing option possesses several advantages in comparison with the low-mounted and high-mounted wing options: greater ground clearance than the low-wing and better visibility than the high-wing.

- Tail Placement:

Most civil aircraft are longitudinally stable, meaning CoG is located before NP; to counteract the wing pitching moment without the usage of reflex airfoils (self-stabilized), some sort of tail installation is needed. Conventional HTP configuration generates some downforce to balance the aircraft, which results in a lower net lift when compared with stable canard (wing fwd HTP configuration) which adds to the net lift. In an unstable configuration (CoG aft AC), since CoG is aft the wing AC, this condition is reversed. Estadea will greatly benefit from a conventional tail placement in terms of cruise performance and load, since these generate extra lift, while using its inherent instability in combat.

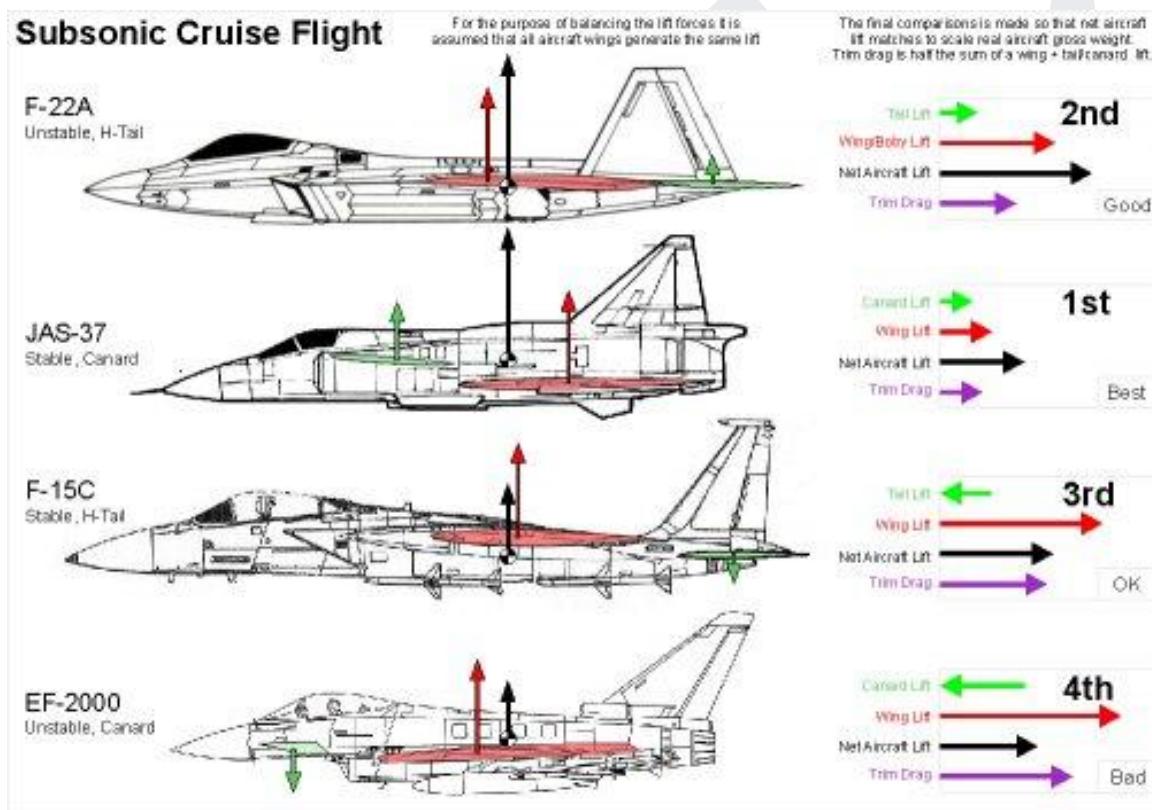


Fig. 68. Fighter tail and CoG placement comparison in terms of net lift and trim drag.

Another consideration in tail placement is its relative location with respect to the rudder. In terms of spin recovery, it is preferred to place the tails either well separated or aft the VTP in order for the rudder to have access to a free flow of air in flat spins and high AoA maneuvers; otherwise the aircraft will have a great tendency to spin which will endanger the safety of both aircraft and pilot.

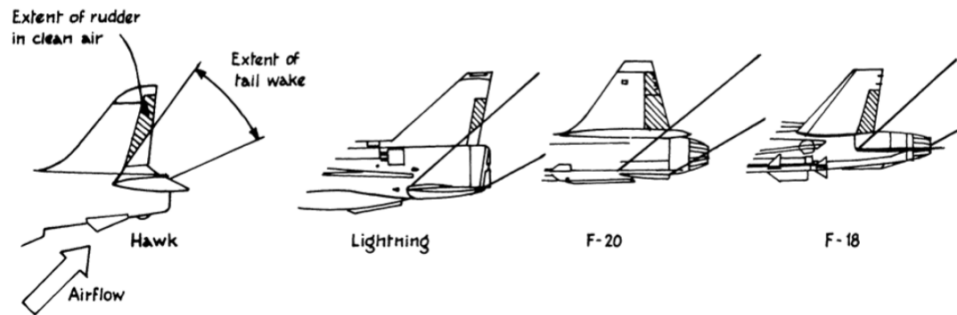


Fig. 69. Tail placement and extent of the tail wake at high AoA maneuvers for various fighters.

- Thrust vectoring:

Estadea's thrust vectoring will enable the aircraft to unlock a set of tactical maneuvers not possible with purely aerodynamic control surfaces. This is the concept of supermaneuverability. These types of maneuvers, such as Pugachev's Cobra and the Herbst maneuver, are extremely taxing on the fighter's kinetic energy, relegating them to one-on-one duels.



Fig. 70. Pugachev's Cobra maneuver performed by a SU-27.

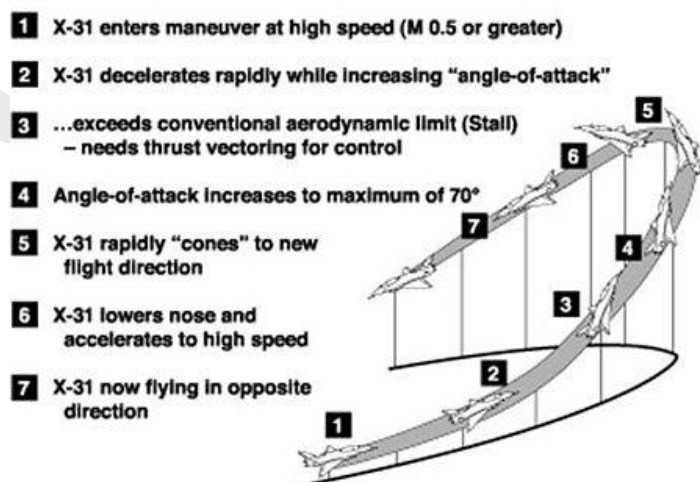


Fig. 71. Herbst maneuver performed by an X-31, courtesy of NASA.

- General Considerations for Combat Maneuvers:

Combat maneuvers involve a wide range of tactics; however, although various and of increasing complexity, Estadea's general combat performance can be predicted and improved by considering a set of variables which define and take part in all duels and their outcomes (R. L. Shaw, 1985):

1. Flight Envelope:

One of the most common and useful tools for the study of aircraft performance is known as a "Flight Envelope" a graphical plot of load factor capability versus airspeed (R. L. Shaw, 1985).

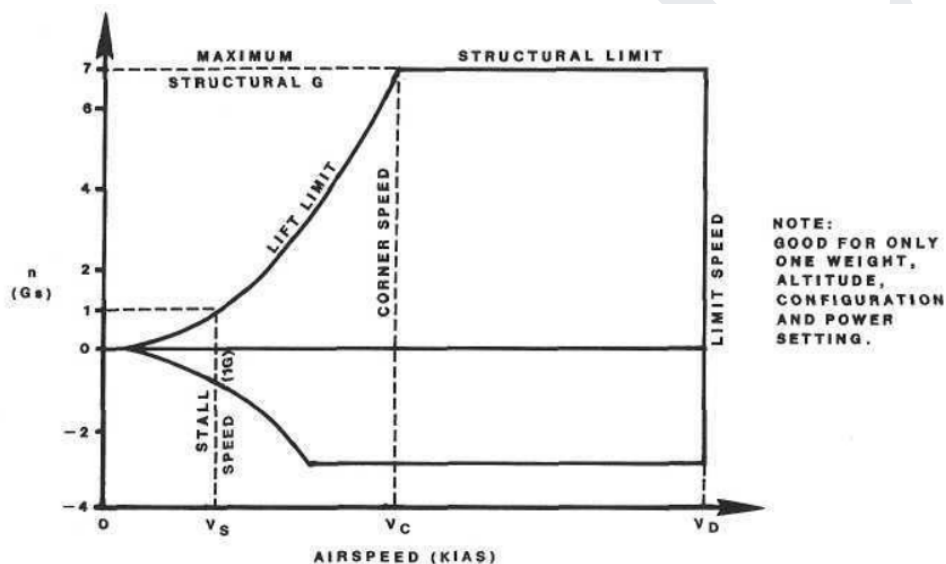


Fig. 72. Example of a flight envelope or "V-n Diagram", extracted from the Appendix of "Fighter Combat: Tactics and Maneuvering" by R. L. Shaw.

The left side of the diagram, labeled "lift limit," indicates the maximum load factor this fighter can generate at a specified airspeed. The curvature of this boundary primarily reflects the variation of lift capability with the square of the airspeed value. Along this line the aircraft is operating at maximum positive lift (pulling upward relative to the aircraft) in the upper half of the diagram and maximum negative lift (pushing downward relative to the aircraft) in the lower half. One important speed which may be identified along this boundary is the minimum 1G flight speed, known as the unaccelerated stall speed (V_S). The upper and lower boundaries of the diagram depict the structural-strength limits of the aircraft in the

positive and negative directions, respectively. The most important of these boundaries is the upper (positive) one, which indicates maximum structural-G capability. Greater load factor requires the wings to support more weight (R. L. Shaw, 1985). The maximum and minimum structural limits of Estadea, as for most advanced fighters, is 9G and -3G respectively. Naturally, a safety factor of 1.50 (or 50%) will be applied for both limits.

The intersection of the positive aerodynamic boundary (lift limit) and structural limit defines a speed that is crucial in fighter performance. This is known appropriately as the corner speed (V_c) or maneuvering speed. At this airspeed a fighter attains maximum instantaneous turn performance (R. L. Shaw, 1985).

$$V_c = \sqrt{\frac{2n_{pll}}{c_{L,max}}} \sqrt{\frac{W_{max}/S_w}{\rho}} \quad (2.27)$$

The fourth boundary of the diagram is the right side, which indicates the aircraft's maximum speed limit, or dive speed (VD). This limit may be the result of structural, aircraft-control, engine-operation, or some other considerations (R. L. Shaw, 1985). The aircraft may be able to exceed this speed in level flight, or VD may not be attainable even in a power dive, depending on the particular design (R. L. Shaw, 1985).

2. Instantaneous Turn Performance:

It refers to the aircraft's maximum turn capabilities at any given moment under the existing flight conditions (i.e. speed and altitude) (R. L. Shaw, 1985). These are comprised of the turn rate (Ω), turn radius (R) and bank angle (ϕ). These are determined by the speed, altitude and load factor of the fighter at a given time.

$$(R_{min})_{stall} = \frac{\cos^2 \gamma}{g \sqrt{\left(\frac{\rho C_{L,max}}{2W/S_w}\right)^2 - \frac{\cos^2 \gamma}{V^4}}} \quad (R_{min})_{load} = \frac{V^2 \cos^2 \gamma}{g \sqrt{\left(n_{pll} \frac{W_{max}}{W}\right)^2 - \cos^2 \gamma}} \quad (2.28) \quad (2.29)$$

$$(\Omega_{max})_{stall} = g \sqrt{\left(\frac{\rho C_{L,max}}{2W/S_w}\right)^2 V^2 - \frac{1}{V^2}} \quad (\Omega_{max})_{load} = \frac{g}{V} \sqrt{\left(n_{pll} \frac{W_{max}}{W}\right)^2 - 1} \quad (2.30) \quad (2.31)$$

$$\cos \phi = \frac{1}{n} \quad (2.32)$$

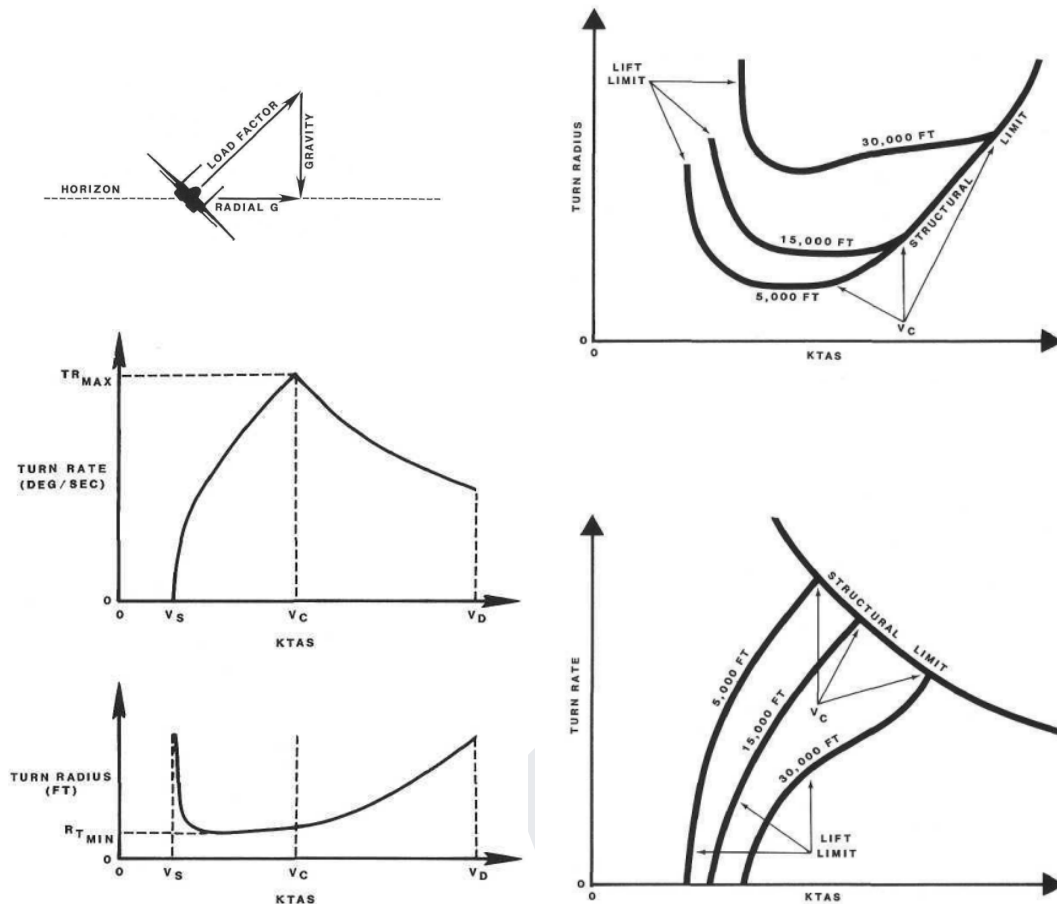


Fig. 73. Variation of turn rate and turn radius with altitude and speed, extracted from the Appendix of “Fighter Combat: Tactics and Maneuvering” by R. L. Shaw.

3. Climb Performance:

The ability to climb fast towards the cruise altitude in a scramble or position itself in a dominant position with respect to an adversary in a dogfight is crucial for any fighter. Climb performance is comprised by the climb gradient (γ) or the angle of climb and climb rate (V_c) or the climbing speed. Climb gradient is determined by thrust available, thrust pitch angle (α_T) and thrust required (drag) whereas climb rate is determined by excess power, the difference between available and required power.

$$\sin \gamma = \frac{T_A \cos \alpha_T - D}{W} \quad (2.33)$$

$$V_c = \frac{P_A - P_R}{W} \quad (2.34)$$

As excess power decreases with altitude, so does climb rate; the altitude where climb rate is 0 is referred to as the absolute ceiling or the maximum altitude the aircraft can reach. The variation of engine thrust with speed also affects the thrust available and therefore the previous variables.

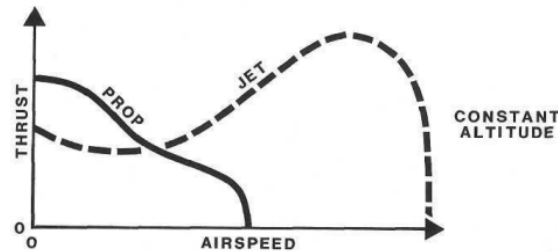


Fig. 74. Engine thrust variation with airspeed, extracted from the Appendix of "Fighter Combat: Tactics and Maneuvering" by R. L. Shaw.

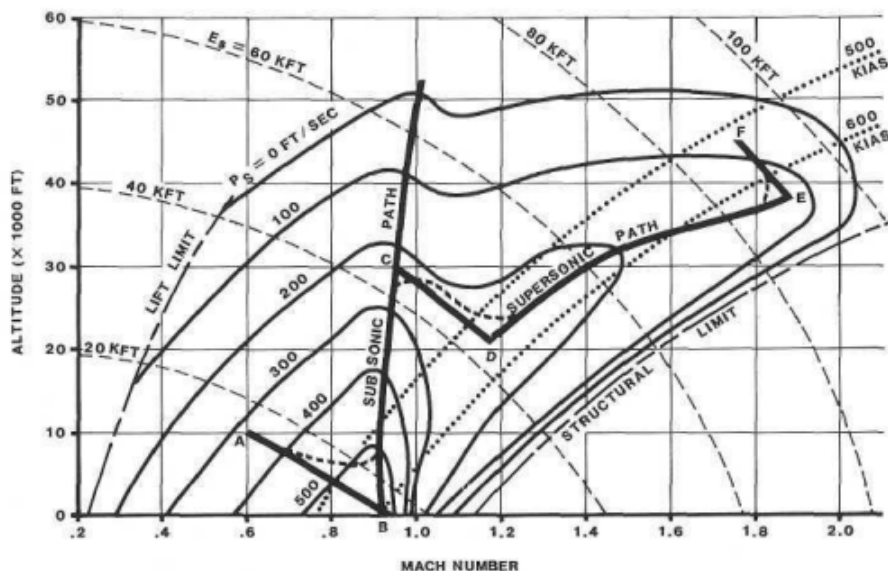


Fig. 75. Example of a jet fighter climb profile, extracted from the Appendix of "Fighter Combat: Tactics and Maneuvering" by R. L. Shaw.

4. Roll and Pitch Performance:

Roll performance is the ability of an aircraft to change the lateral direction of its lift vector. It indicates the ability of a fighter to change its plane of maneuver. Therefore, although roll performance is not, in a strict sense, maneuverability, it does have a direct relationship with maneuverability. Roll performance may be defined as a measure of the aircraft's "agility." (R. L. Shaw, 1985).

As speed increases, the force required to maintain full control deflection increases. To maintain roll performance at high speeds, power-assisted or fully powered controls are often

employed to enable the pilot to attain full control deflection. With powered controls the pilot's control inputs usually position valves that allow hydraulic fluid pressure to move the control surfaces (R. L. Shaw, 1985).

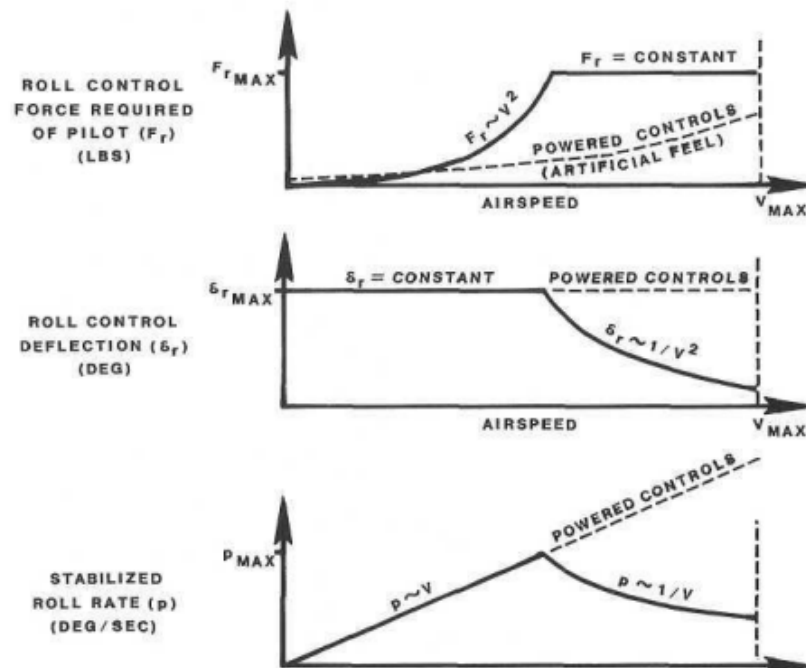


Fig. 76. Variation of roll rate with speed, extracted from the Appendix of "Fighter Combat: Tactics and Maneuvering" by R. L. Shaw.

Pitch performance is the ability of a fighter to rotate about an axis that is parallel to its wings (i.e. the lateral axis). In level flight this would mean rotating the nose of the aircraft upwards or downwards. Like roll performance, pitch rate is a measure of the fighter's agility (R. L. Shaw, 1985). The pitch performance of a fighter (pitch rate and acceleration), is a function of the effectiveness of the pitch controls and the resistance the aircraft presents to a pitching motion (R. L. Shaw, 1985). Greatest pitch performance is often found near corner speed (R. L. Shaw, 1985)

5. Specific Energy:

Energy is a primary factor in controlling and maneuvering an aircraft. If an attacker has too much energy, it may be easy to get in range but difficult to prevent an overshoot. Too little energy and the attacker may not be able to get in range at all. If the defender has more energy than the attacker, an escape may be possible, but too little energy and the defender will lose its capability to maneuver (R. L. Shaw, 1985). Energy comes in two forms:

- Kinetic energy is a function of the fighter's mass and speed.

$$KE = \frac{1}{2}mv^2 \quad (2.35)$$

- Potential energy is a function of its mass, gravity and altitude.

$$PE = mgh \quad (2.36)$$

The combined potential and kinetic energy is called the total energy. Because the energy package is the combination of mass, speed and altitude, a fighter flying at low altitude but a high speed may have the same total energy as a fighter of equal mass, but flying at a low speed and high altitude (R. L. Shaw, 1985). To compare two aircraft of different total masses, specific energy is used:

$$e = \frac{KE+PE}{W} \quad (2.37)$$

When two aircraft meet in combat, they may have different energy states and energy retention. Typically, the fighter with higher energy and better retention will make an "energy move", usually involving a climb, while the fighter at an energy disadvantage (angles fighter) will make an "angles move" such as a break turn, trying to use the opponent's energy to their own advantage (R. L. Shaw, 1985).

6. Energy Management:

A faster, heavier aircraft may not be able to evade a more maneuverable aircraft in a turning battle, but can often choose to break off the fight and escape by diving or using its thrust to provide a speed advantage. A lighter, more maneuverable aircraft can not usually choose to escape, but must use its smaller turning radius at higher speeds to evade the attacker's guns, and to try to circle around behind the attacker (R. L. Shaw, 1985). In terms of instability, although more unstable aircraft will commit to the maneuver faster, regaining equilibrium requires more energy than less unstable aircraft; to understand this, the classic analogy of the ball on the hill can be used: the more unstable the aircraft is, the steeper the hill is, requiring more energy to return it to its original position.

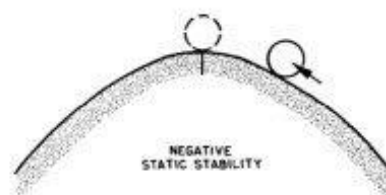


Fig. 77. Static stability analogy.

7. Thrust-to-Weight Ratio:

Thrust-to-weight ratio is an efficiency factor for total aircraft propulsion. An aircraft with a high thrust to weight ratio has high acceleration. For most flight conditions, an aircraft with a high thrust to weight ratio will also have a high value of excess thrust (which results, as seen before, in improved climbing performance). To achieve high values, powerful engines must be mounted and both structural weight and payload must be as reduced as possible; this is the reason, in combination with drag and RCS reduction, why fighters ditch their external fuel tanks and do not usually carry more than 50% of their internal fuel volume capacity before engaging in combat.

$$TW_{ratio} = \frac{T}{W} = \frac{1}{\frac{L}{D}}; \text{ if } \frac{T}{W+D} \geq 1.0 \Rightarrow \text{sustained vertical climb (2.38)}$$

2.4. Armament Compatibility

Due to Estadea's stealth design requirements, as it will be seen in Chapter 3, all weapons must be carried internally. This section includes both the weapons selection and internal volume requirements which will determine the center fuselage cross-section. From the top level requirements listed in Chapter 1, Estadea must carry an array of at least 8 missiles for both BVR and WVR engagements and a gun exclusively for WVR engagements. Since this aircraft is aimed to be used primarily by NATO's members, the internal weapon bays will be tailored to the dimensions of the alliance's shared equipment.

2.4.1. Gun:

The selected gun for Estadea is the Rheinmetall/Mauser BK-27 27mm revolver cannon. Compared with typical gatling gun designs, it does not require an electrically cycling system since its gas-operated (although the firing pin is operated electrically) making the overall gun system lighter and more reliable; firing is performed instantaneously without the need to bring the barrel system up to certain revolutions, meaning more shots on target even with a lower fire rate due to possessing a single canon. Expel cases will be gathered and stored internally in compliance with regulations for minimum CoG shifts. The gun will be placed as close as possible to the fighter's center line as to minimize the moment produced by its recoil when firing.



Fig. 78. Mauser BK-27 revolver cannon and feeding system.

Empty Weight (Gun+Feeding System)	217kg
Round Weight	516.0g
Length	2.31 m
Typical Loadout	150 rds
Total Weight	294.4kg
Firing Rate	1000-1700 rds/min
Total Firing Time	9.00-5.29"
Range	2,500 m
Recoil	28.0 kN

Table 2. BK-27 Specifications, courtesy of Rheinmetall.

2.4.2. BVR Missiles (Fox-3):

The selected BVR missiles for Estadea are the European MBDA Meteor and American AIM-120 AMRAAM. Similar in operation, just before launch the fighter communicates the target's bearing, altitude and speed to the missile through the information provided by its own radar; the missile is launched and guided to the target's general area through its inertial navigation system. Both platforms are capable of receiving updated information on the target while in-flight either through the fighter or a third party (usually AWACS). In the final phase, the missile operates independently maneuvering towards an interception course using its inboard radar. Estadea will carry up to six AMRAAMs or Meteors.

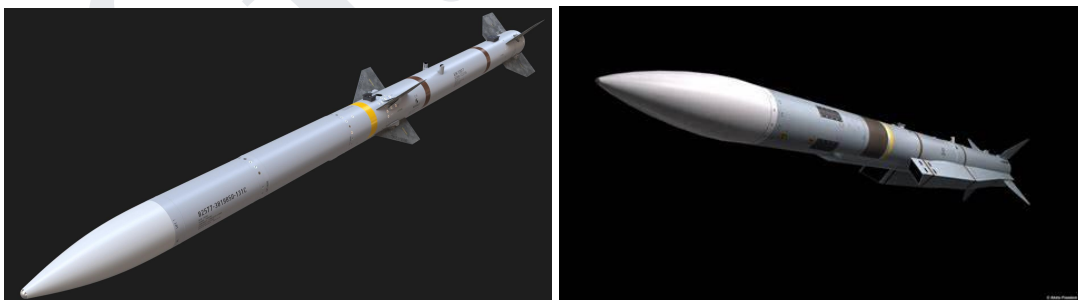


Fig. 79. AIM-120 AMRAAM and MBDA Meteor missiles.

Weight	190 kg
Length	3.65 m
Span	0.534 m
Range	200 km (60 km NEZ)
Loadout Weight	1140 kg
Loadout Volume	4.905 m ³

Table 3. MBDA Meteor Specifications, courtesy of MBDA.

Weight	152 kg
Length	3.70 m
Span	0.530 m
Range	160 km (50 km NEZ)
Loadout Weight	912 kg
Loadout Volume	4.90 m ³

Table 4. AIM-120 AMRAAM Specifications, courtesy of Raytheon.

2.4.3. WVR Missiles (Fox-2):

The selected WVR missiles for Estadea are the European IRIS-T and american AIM-9X Sidewinder. Similar in operation, these short-range missiles incorporate an infrared camera to detect and adjust their course to follow the heat emanated from the exhaust plume. Estadea will carry internally two WVR missiles on top of the aforementioned 8 BVR missiles. Both models have the added benefit of being suitable for ground targets.



Fig. 80. AIM-9X Sidewinder and IRIS-T missiles.

Weight	85.3 kg
Length	3.02 m
Span	0.279 m
Range	1-35.4 km
Loadout Weight	170.6 kg
Loadout Volume	0.935 m ³

Table 5. AIM-9X Sidewinder Specifications, courtesy of Raytheon.

Weight	87.4 kg
Length	2.94 m
Span	0.447 m
Range	1-25 km
Loadout Weight	174.8 kg
Loadout Volume	0.92 m ³

Table 6. IRIS-T Specifications, courtesy of Diehl.

2.4.4. General Purpose Ordinance:

For harder targets, such as fortified SAM or radar sites, Estadea needs to pack more powerful ordinance. For this purpose, JDAM is an excellent option, since this system converts unguided bombs into PGM. The aircraft first provides position and velocity vectors to the bomb before release; once in free-fall, GPS and an inertial navigation system guides the ordinance to the desired target location with increased accuracy. Since this aspect of Estadea’s mission is secondary, the fighter will only carry two Mk83 JDAMs combined with a reduced air-to-air loadout.



Fig. 81. JDAM kit installed in a free-fall Mk83 bomb.

Weight	460.2 kg
Length	3.035 m
Span	0.498 m
Range	24 km
Loadout Weight	920.4 kg
Loadout Volume	1.18 m ³

Table 7. Mk83 bomb Specifications, courtesy of the USAF.

G.M.L.

2.5. Ground Interface Considerations

Estadea needs to be ready for takeoff anytime and anywhere. As mighty a stealth fighter is in the air, their most vulnerable point is while on the ground waiting for refueling/rearmament and maintenance operations. For this project, several surface-level measures, based on the swedish Bas 90 system and the publicly available F-22’s internal design features have been taken to minimize the overturn and maintenance periods:

1. Reinforced Landing Gear: this will enable Estadea to land on rough terrain (ideally, public roads) and not depend on centralized bases. Estadea’s landing gear will be inspired by the designs used in seaborne operations, with higher sink rate, for example, than normal.
2. Small Clearance Radius: as Estadea will be able to use public roads, ideally, it must possess a small clearance radius, this is achieved through a high nose tire deflection and short distance between nose and main landing gear.
3. Easy Access: the F-22, for example, sits only 36 inches (0.914 m) off the ground, allowing maintainers to have shoulder-height access (or lower) to nearly every component or system (such as avionics racks, engines and weapons) without the use of ladders or workstands (Global Security, 2023).
4. Modular Design: modular avionics could allow the operator to pull out a non-functioning module and plug in another in rapidly.
5. Self-sufficiency: this includes the inclusion of an APU to turn on the engines and provide electric power to all the aircraft’s systems
6. Fast turn-around: The F-22 allows for simultaneous gun ammunition and missile reloading, a process that normally goes in sequence only. It also has pneudraulic extend and retract missile launchers, which means that there are no pyrotechnics to be concerned with while the aircraft is being turned (Global Security, 2023).



(This page has been intentionally left blank)

G.M.L.

CHAPTER 3. STEALTH DESIGN CONSIDERATIONS

To survive in the modern battlefield, Estadea needs to be designed and outfitted with the necessary technologies to avoid detection and/or tracking. This chapter, divided into passive (shape, paint scheme, inclusion of RAM materials, etc.) and active (electronic countermeasures and flares) camouflage, includes the necessary considerations to reduce Estadea’s detection in each of the light spectrums: visual, radar and IR.

3.1. Passive Camouflage

3.1.1. Visual Camouflage:

When two fighters engage each other at close ranges (WVR engagements), the main detection method used by the pilot to track the whereabouts of the other is through the usage of his own eyes; therefore, introducing a paint scheme on the fighter surface skin which would make its visual tracking more difficult actually gives it an edge over the opponent; this paint scheme is known as a camouflage pattern. Camouflage patterns can be divided into static camouflage, which aims to conceal the object within its background and dynamic camouflage, which aims to increase the difficulty of tracking the object as it moves (A. Newman & H. Blenchman, 2004). For a moving object such as a fighter a disruptive approach is more effective (A. Newman & H. Blenchman, 2004); this approach aims at “breaking” the outline of the object, making tracking more difficult: a light color is applied unevenly on the edges to blur them with the background, a darker color is applied as spots mimicking shades and shadows, finally a cold shade (gray, black, dark blue, dark green, brown, etc.) is used as the base color. Tiger fur is a great example of disruptive camouflage.

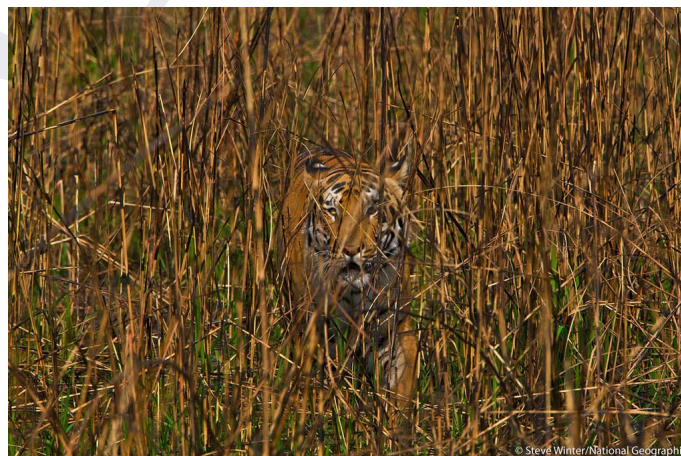


Fig. 82. Example of disruptive camouflage, courtesy of National Geographic.

3.1.2. Radar Detection:

Radar detection is the main method used to detect aircraft in BVR engagements. This subdiscipline of stealth is primarily focused on reducing the aircraft’s RCS or radar signature (in m^2), a measure of how detectable an object is through radar:

$$RCS = \lim_{r \rightarrow \infty} 4\pi r^2 \frac{S_s}{S_i} \quad (3.1)$$

Where r is the distance between the aircraft and the radar antenna, S_s is the scattered power density at the receiving location and S_i the incident power density of the transmitter at the radar target. Therefore, to reduce the RCS of Estadea, it must either absorb or redirect the radar waves away from the receiving antenna. RCS can be divided into four factors:

1. Specular Return: radar waves reflected by high incidence angles (near perpendicular) directly back to the receiver.
2. Traveling Waves: when striking a surface, radar waves generate a secondary wave which travels along the surface of the aircraft, if it encounters bumps or gaps, it is scattered in all directions. Traveling wave echoes are traveling waves that hit the wing edges and have some of its energy reflected back to the source.
3. Creeping Waves: traveling waves graping around a circular or tubular object and returning to the receiving antenna.
4. Diffraction: occurs when the radar waves hit a corner or wedged edge, scattering in all directions.

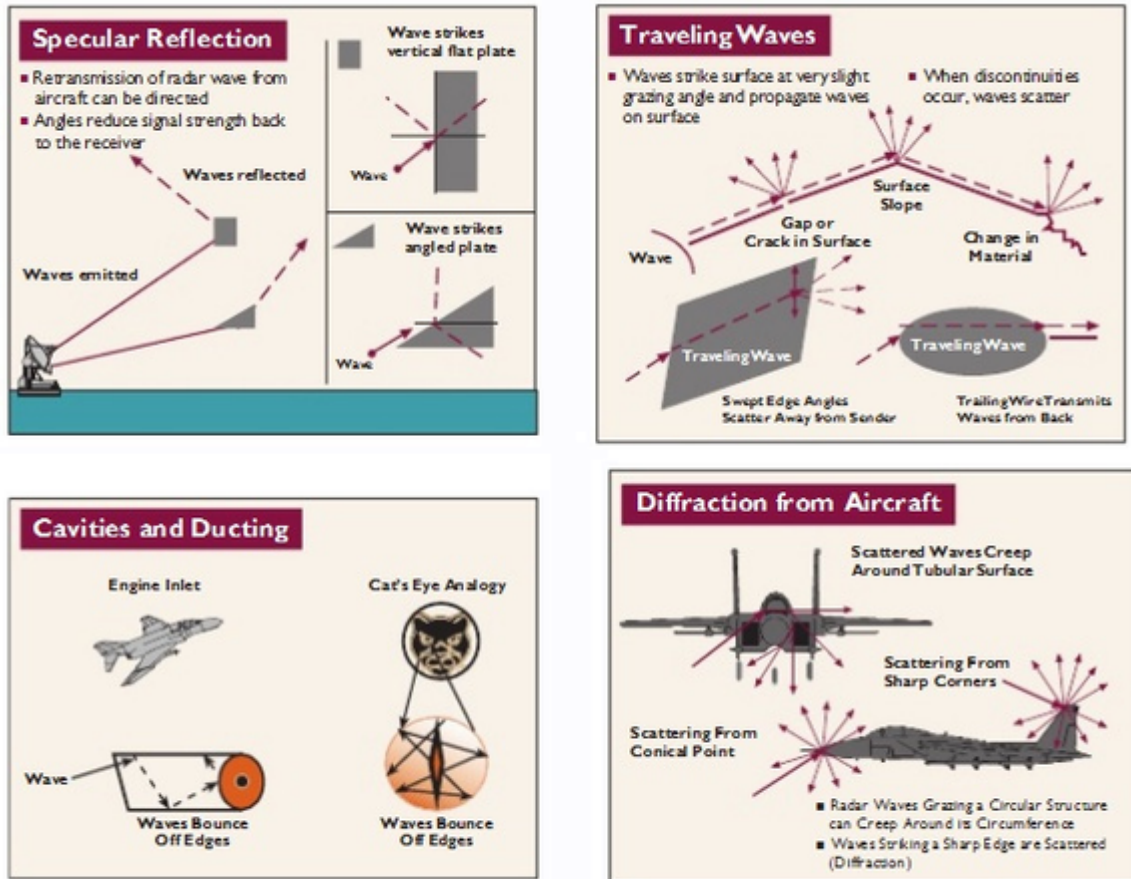


Fig. 83. Types of radar reflection, courtesy of Quora.

To minimize each of the RCS factors, several design choices must be taken into account.

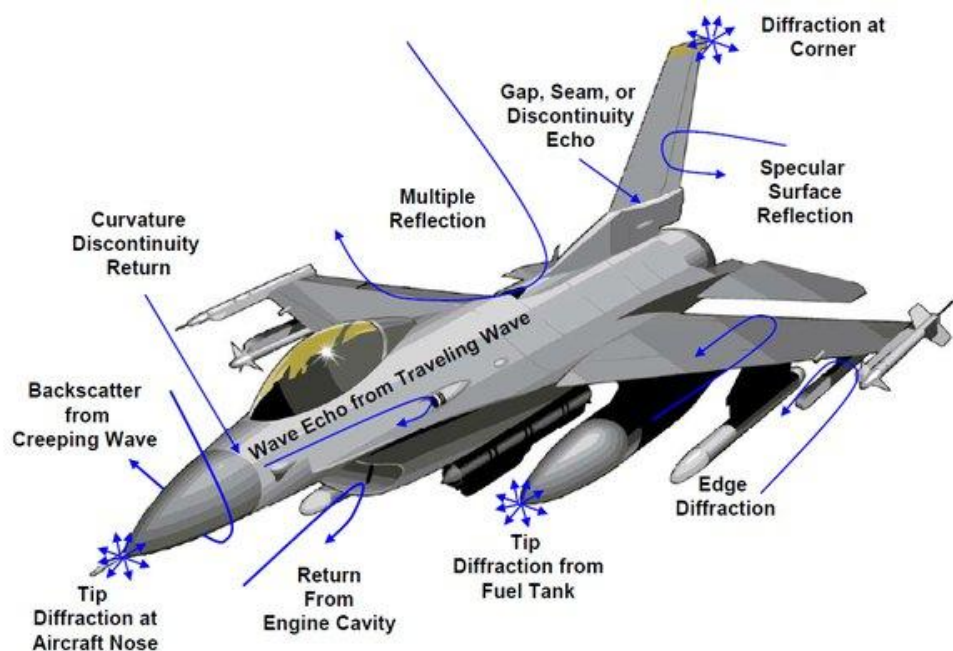


Fig. 84. RCS factors and main sources of radar detection in fighters, courtesy of Quora.

1. Specular Return:

To avoid specular return, 90° degree angles between surfaces and corners must be avoided in all the surfaces of the aircraft, this includes the angle between the tails and fuselage, wing edges and fuselage, etc. (Global Security, 2023). Additionally, serrations must be used in the engine nozzles and BVR missile bay doors to avoid both detection from the back and when firing, respectively. WVR missile bay doors and gun trapdoor can be flat shaped since they will only be opened in WVR engagements, where radar detection is unavoidable due to the close range.

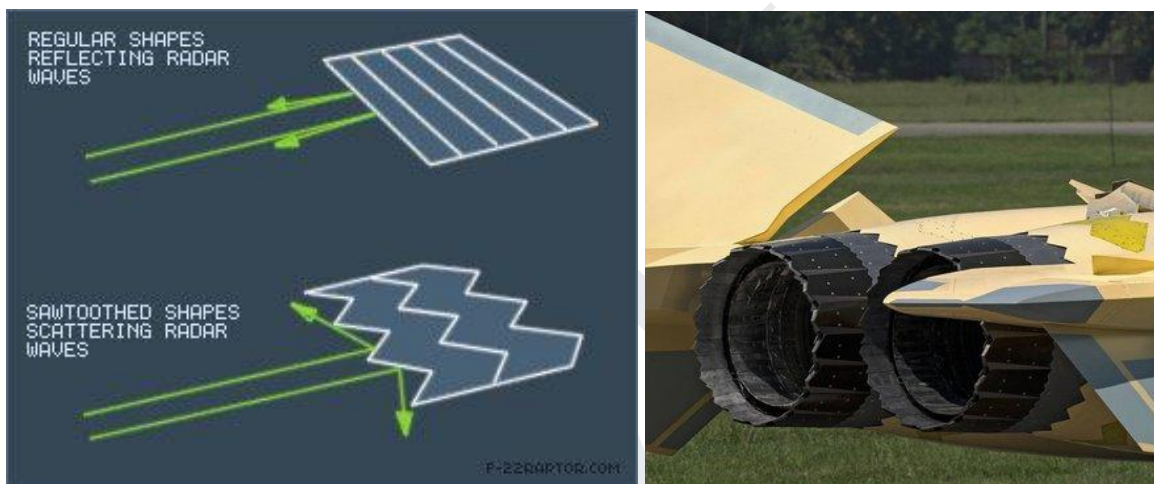


Fig. 85. Effect of edge serrations, courtesy of Quora.

2. Traveling Waves:

To avoid the scattering of traveling waves, the aircraft surface must be as smooth as possible. On the other hand, the issue of traveling wave echoes is resolved through the usage of edge serrations on the wing and tails LE and TE so as to scatter the traveling waves away from the source either when being detected from the front or back (Global Security, 2023).

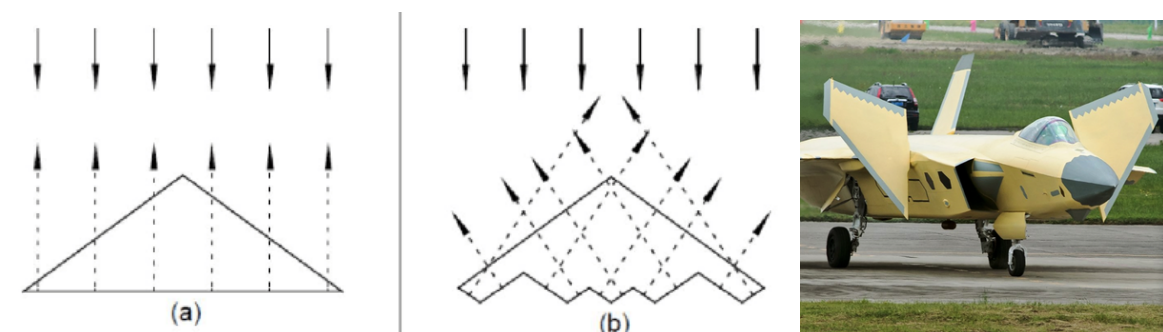


Fig. 86. Edge diffraction from the TE of a straight and serrated wing, courtesy of Quora.

3. Creeping Waves:

To avoid creeping waves from wrapping around the fighter, it is convenient to dispose of a sharp crease through the usage of flat faces and sharp edges in the fuselage geometry. Once it encounters these discontinuities, the creeping wave will scatter (Global Security, 2023).

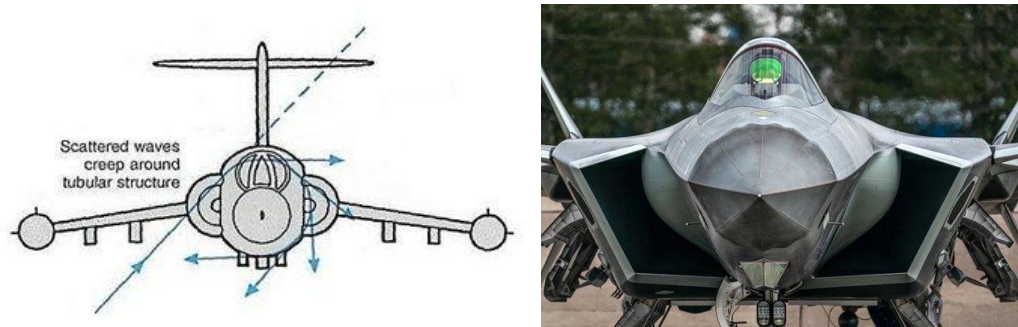


Fig. 87. Creeping wave return and geometric countermeasure, courtesy of Quora.

4. Diffraction:

All edges scatter radar waves; however, several measures to reduce the energy scattered and redirect energy away from the source are available. To reduce the amount of energy scattered, stealth fighters use non-conductive materials on the wing and tails edges. On the other hand, edge alignment is used to both reduce the number of directions the energy will scatter and redirect it away from the source (Global Security, 2023).

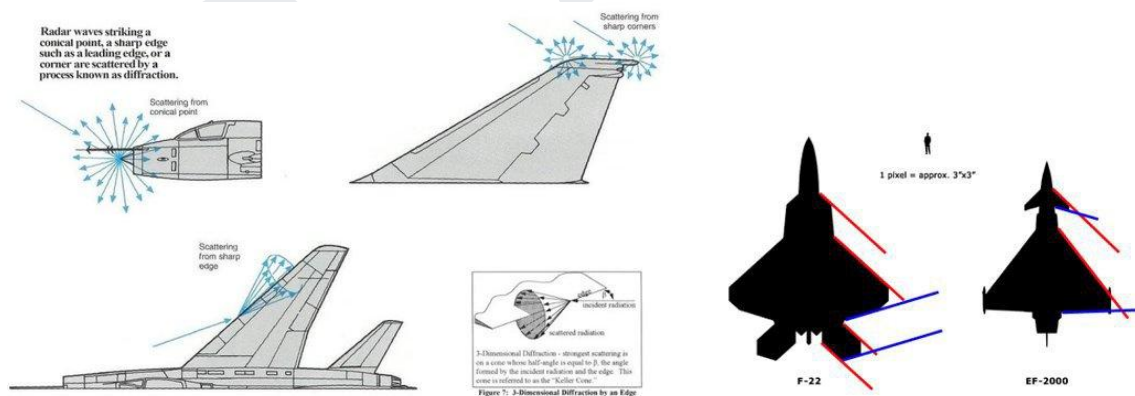


Fig. 88. Edge scattering and effects of edge alignment, courtesy of Quora.

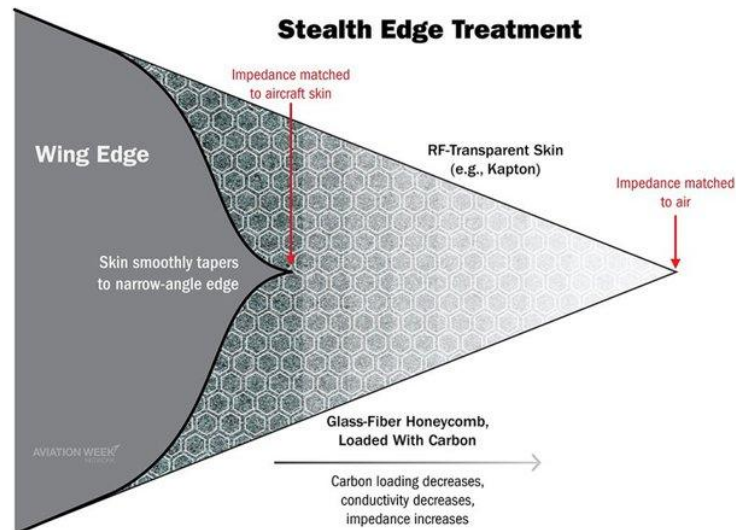


Fig. 89. Stealth edge treatment, courtesy of Quora.

Asides from the aforementioned measures, a closer look must be given to the canopy, air inlets, and the fighter’s own radar assembly:

5. Canopy:

If untreated, the canopy allows radar waves into the cockpit and be reflected off the instrument panels, seat, pilot helmet, etc. To avoid this reflection, the inside of the canopy is coated with a special gold based or ITO (indium tin oxide) chemical (Global Security, 2023). This additional measure has two main benefits: applying such transparent conducting film enables, while maintaining transparency to visible radiation, both a radio wave stealth property which scatters radio waves in various directions so as not to be detected by radar, and an electromagnetic wave shield which prevents harmful electromagnetic waves, except for visible radiation, to enter inside the cockpit, much like an additional sunscreen (Global Security, 2023).



Fig. 90. F-22 canopy glass showing stealth coating.

6. Radar Assembly:

The nose cone itself must be transparent to radar waves in order for the fighter’s own radar to emit and receive. This means that the radar energy can reflect directly off of the flat areas around the sides of the radar, as well as the radar itself (Global Security, 2023) as seen in the case of specular return. The biggest return would come from directly bouncing off the radar. This is fixed by angling the radar either up or down in a similar manner as the tails so as to redirect the energy away from the source. On second note, there could still be some return if the radar had any gaps in its assembly; this is fixed with strict manufacturing tolerances (Global Security, 2023). Finally, radar waves can hit the exposed metal around the sides of the radar, as well as the sides of the radar itself; this issue is fixed through the addition of RAM to these sections (Global Security, 2023).

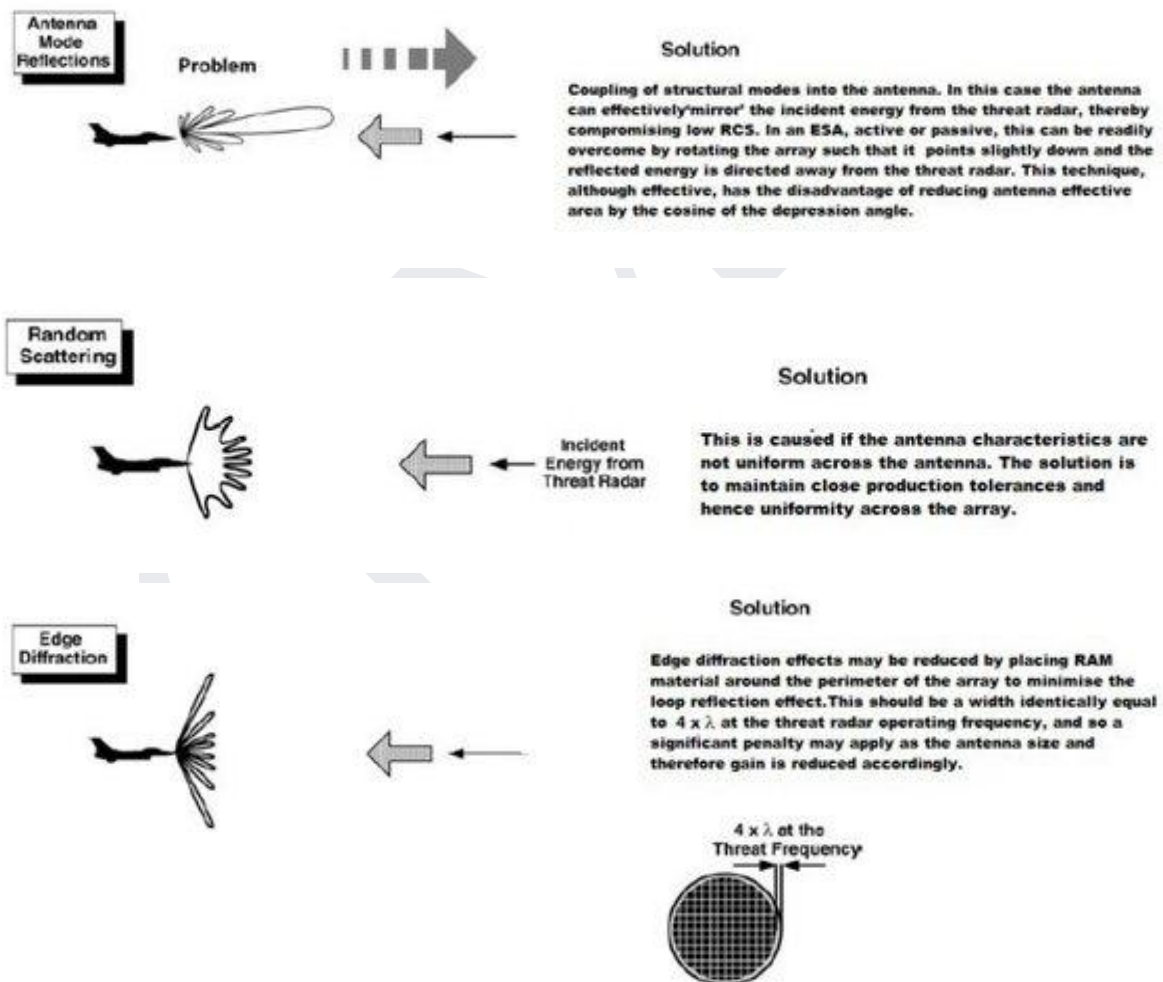


Fig. 91. Types of radar assembly radar return and solutions, courtesy of Quora.

7. Air Inlets:

In order to prevent radar waves from reflecting off the engine compressor/fan blades, several measures must be taken. The first and already discussed is partially or entirely masking the blades from the outside through the usage of an “S” duct geometry. Other measures include the usage of RAM around the inlet lips and inside walls to absorb the radar waves which manage to enter and a blocker just before the engine fan/compressor which guides and dissipates the remaining radar energy (Global Security, 2023).

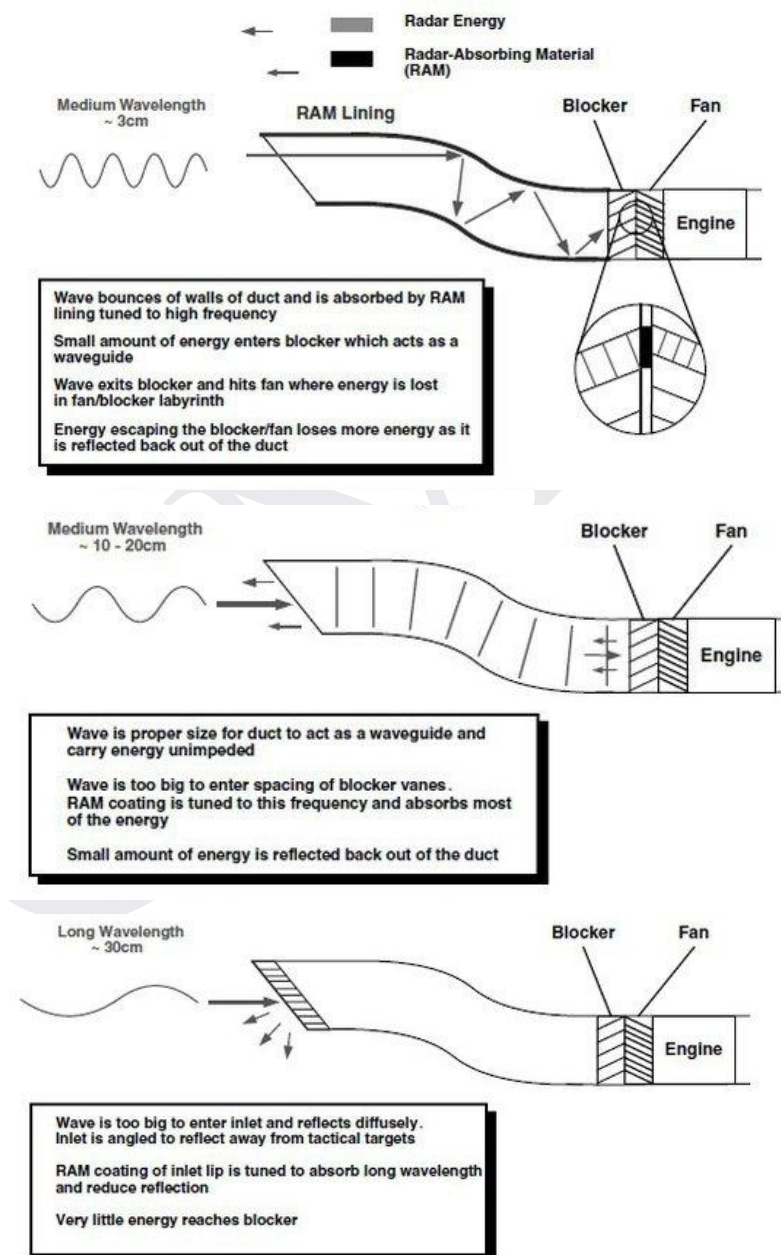


Fig. 92. F-35 inlet countermeasures for short, medium and long radar wavelengths.

3.1.3. IR Detection:

Recalling Figure 50 from Section 2.2. the different “hot points” present in the fighter can be visualized. By far, the biggest contribution to IR signature is the fighter’s exhaust plume (Global Security, 2023) and the main concern in this project in this aspect. To mask the exhaust plume several measures will be applied. In terms of geometry, the exhaust nozzles will be positioned in between the tails so as to hide the exhaust gasses from certain angles. On the other hand, mixing the exhaust gasses with the air of the engine cooling channel helps to both reduce the average plume temperature and accelerate the dissipation with the surrounding air as seen in the F-35 (Global Security, 2023).



Fig. 93. F-35 method of IR signature reduction.

Other solutions involve the usage of non-circular tail pipe to minimize the exhaust cross-sectional volume and maximize the mixing of hot exhaust with cool ambient air at the expense of some thrust generation (Air Power Australia, 2014). This solution is seen in the F-22, although the integration of a 3D thrust vectoring assembly using this option may prove difficult.



Fig. 94. F-22 rectangular nozzle design.

3.1.4. Stealth Paint:

In combination with the aforementioned design cues, Estadea’s skin will be coated in a RAM-based paint to further absorb radar energy and decrease its RCS. Perhaps the most advanced stealth paint currently under development (allegedly) is the carbon nanotube-based stealth coating (MIT Tech Review, 2011). The long straws of pure carbon, each just a few nanometers in diameter, absorb a broad spectrum of light, from radio waves through visible light through the ultraviolet, almost perfectly (MIT Tech Review, 2011). This property has three main benefits: absorbing radar waves and visible light, complementing the camouflage pattern, at a lower density than traditional iron ball based stealth coatings.



Fig. 95. Maintenance operations in the F-22’s stealth coating, courtesy of Lockheed Martin.

3.2. Active Camouflage

3.2.1. Flares and Chaff:

In combat, two main countermeasures are used to confuse both the enemy’s own detection systems (mainly radar) and the systems contained within the weapons fired against Estadea: flares and chaff.

Flares are used in WVR engagements to confuse short-range, IR-guided missiles. Basically, when the missile is launched or about to be launched (the pilot’s own training and experience determines this last aspect), flares will be launched on the pilot’s order from their dispensers outwards towards the sides of the aircraft; the intense heat released by the devices aims at mimicking the exhaust plume’s heat signature and divert the missile away from the aircraft.

Chaff, on the other hand, is used to confuse both enemy radar and inboard radar of the incoming BVR missiles. Dispensed in a similar manner as flares, chaff is a recollection of small pieces of aluminum, metallized glass fiber or plastic which reflects radar waves, appearing as a second radar signature or masking the aircraft’s own while it hides behind elevated terrain. The objective of chaff is similar to that of flares, directing the missile away from the aircraft, with the added benefit of confusing the enemy fighter’s radar. Both chaff and flare dispenser need to be hidden behind a serrated trapdoor to maintain Estadea’s stealth characteristics.

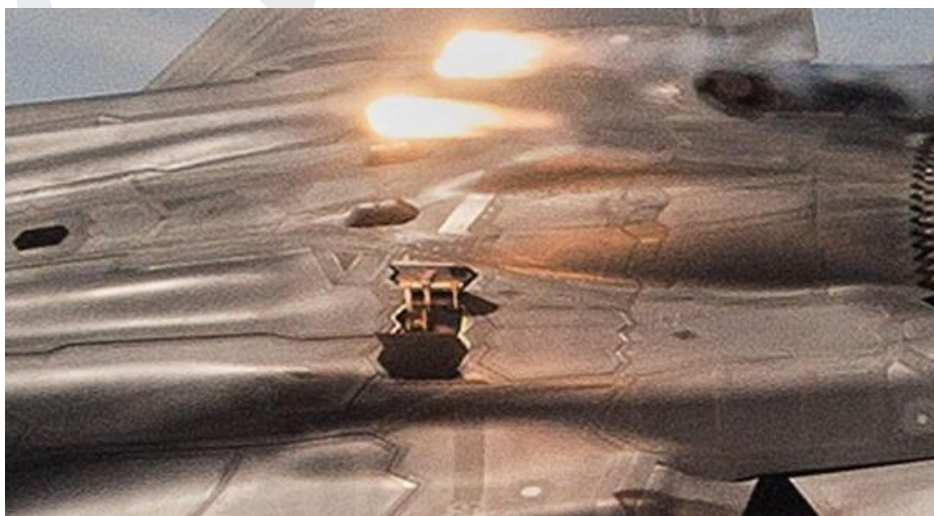


Fig. 96. F-35 flare dispenser trap door detail.

3.2.2. Electronic Countermeasures:

In combination with flares and chaff, it is convenient that Estadea carries integrated within its airframe an offensive/defensive electronic warfare system in order to enhance the fighter’s offensive capabilities and the survivability of both aircraft and pilot while maintaining its stealth characteristics. The benefits of said system is the integration of radar warning, targeting support and countermeasures in one system, reduced weight, multispectral capabilities, reduced long-term life cycle costs and, by correctly locating the different antennas within the airframe, 360° view of the battlefield as seen in the F-35 (Aircraft 101, 2017). This system, coupled with the HUD and pilot’s helmet, can drastically reduce the pilot’s workload and complexity of the cabin instruments allowing for increased awareness and overall, lethality.



Fig. 97. Electronic warfare modules and their position within the F-35 airframe, courtesy of www.Aircraft101.com.

The most important offensive modules include the AESA radar andIRST system. This type of radar is composed of numerous small solid-state transmission/reception modules. By possessing various independent modules, the radar can generate several sub-beams at different frequencies (Aircraft 101, 2017). Due to this characteristic, on some fighters (F-35, F-22 and F-18E/F), their fire-control radars are used not only to locate and track enemy forces but also to jam enemy’s radar, attack enemy’s network and stream data at high speed (Aircraft 101, 2017).

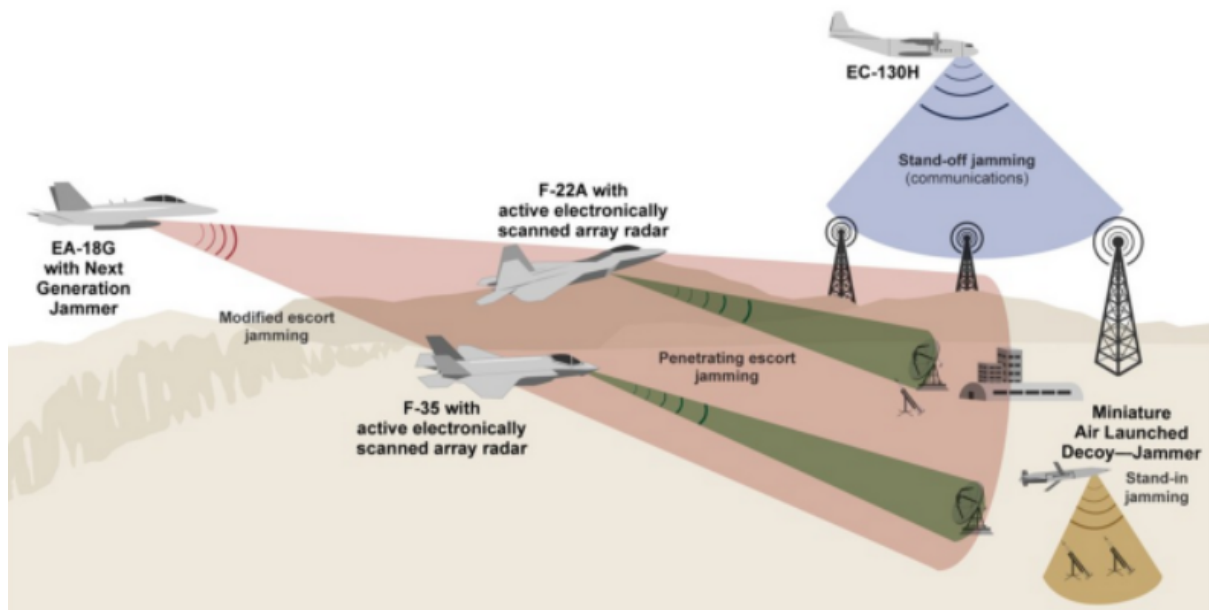


Fig. 98. General USAF jamming procedure to close-in radar and SAM sites, courtesy of www.Aircraft101.com.

The most important defensive modules include the RWR, which detects the radio emissions of enemy fire control radars and issues a visual and auditory warning to the pilot, and the MAW, which detects attacking missiles and warns the pilot to make a defensive maneuver and deploy the available countermeasures. Modern IR-based MAW systems can also serve as tracking devices of enemy aircraft and therefore function asIRST systems, such as Northrop Grumman’s AN/AAQ-37 360° view system seen in the F-35 (Aircraft 101, 2017).



Fig. 99. F-35 front view. Top: IRST module part of Northrop Grumman’s AN/AAQ-37 360° view system. Bottom: Lockheed Martin’s EOTS, intended for ground targets.

(This page has been intentionally left blank)

G.M.L.

CHAPTER 4. AIRCRAFT GENERAL ARRANGEMENT

Estadea's design is based on the strengths of several 5th generation fighters, both in service and prototype aircraft, and the theory mentioned in the previous chapters:

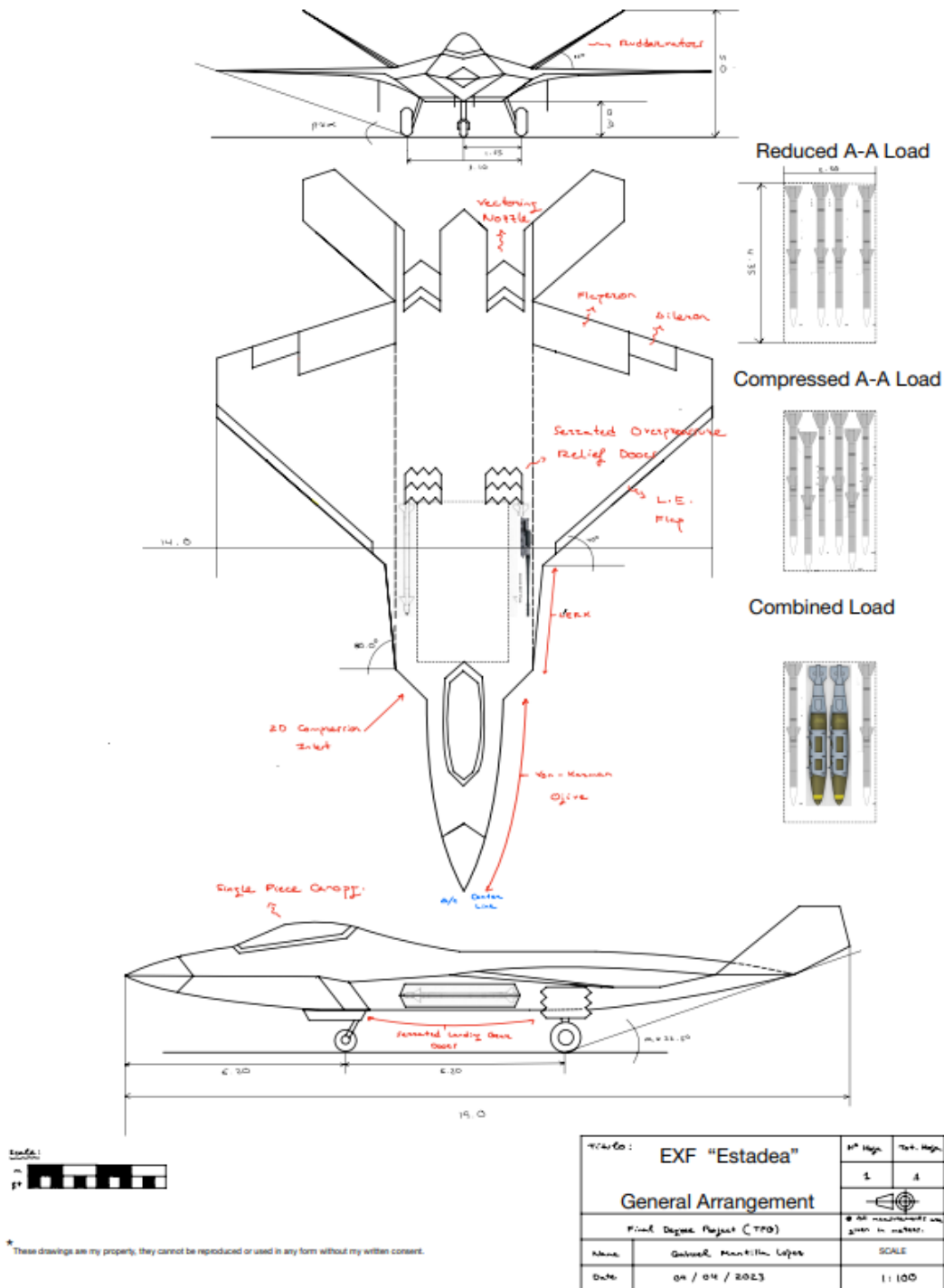


Fig. 100. Estadea's General Arrangement.

From Figure 97, several design cues may be noticed. The nose follows the shape of a Von Karman ogive, modified to include a sharp crease to break creeping waves; the canopy is made from a single glass piece and provides the pilot with a 360° view horizontally.

The fuselage uses a trapezoidal cross-section to break creeping waves and minimize specular return; all doors and apertures are saw-toothed to minimize specular return when opened and scatter traveling waves when closed. All weapons are carried internally with three basic configurations (reduced air-to-air, compressed air-to-air and combined air-to-air and air-to-ground); missiles and bombs are loaded using hydraulic arms, with fox-2 missiles positioned forward the wing LE and launched from the sides of the fuselage so as to not obscure its IR camera when fired; the main gun is buried just under the upper fuselage surface, a small trap door opens up to reveal the barrel end when firing. Similarly, the engines are buried in the fuselage and positioned on the back end in order to push the CoG aft and closer to the wing's AC. Notice the fuselage waisting at the engine area following Whitcomb's Area Rule. The necessary air flow is provided by two “S” duct, Caret inlets positioned on the fuselage sides for better ground clearance and ingestion at a wide range of AoA. Notice how the engines have been pushed apart laterally similar to the Su-57 to provide both split throttle capabilities and additional roll moments when coupled with the rectangular vectoring nozzles, besides from pitching moments and reduced IR signature. Notice the serrations at the back end in the top view for traveling wave echo scattering, edge alignment and reduced specular reflection, which provide Estadea with all-around stealth.

The wing planform follows a clipped and cropped delta shape for edge alignment and fitting inside the Mach Cone, similar to that of the F-22, coupled with LERX to provide high AoA capabilities. The LE flaps, flaperons and ailerons are shown. The wing positioning is biased rearwards following Jone's Supersonic Area Rule. Notice the wing is positioned vertically in the mid section of the fuselage and possesses no dihedral angle for neutrally stable roll characteristics. Pitch and yaw control are provided by two powerful, all-movable flaperons, similar to the YF-23 prototypes in order to reduce the overall aircraft's RCS and increase significantly the tailstrike angle. Notice the edge alignment in both top and front view between the outer edges and the absence of right angles.

(This page has been intentionally left blank)

G.M.L.

CHAPTER 5. ENGINE SELECTION

5.1. Candidate Selection

As seen in Chapter 4, Estadea will mount two jet engines. This decision has been made in line with the geometry and main mission of the aircraft: air superiority. Mounting two powerful engines will provide the aircraft with great climbing, acceleration and maximum speed performance characteristics, as well as providing a redundancy in thrust generation in the event of engine damage in compliance with regulations. It is in the aircraft’s best interest to provide a modern, efficient but powerful engine. At this point, the most modern and effective NATO and European aircraft (the F-35, F-22, Eurofighter, Rafale and Grippen, respectively) possess the following engines:

	P&W F135-100	P&W F119-100	Eurojet EJ-200	Snecma M88	GE F404
Length (m)	5,59	5,16	4	3,5	3,9
Fan Diameter (m)	1,09	1,16	0,737	0,9	0,899
Max, Diameter (m)	1,17	1,16	0,737	0,9	0,899
Dry Weight (kg)	1700	1769	1000	1000	1036
Tmax Static, S.L., (kN)	125	116	60	50	48,9
Tmax Static Augmented, S.L., (kN)	191	156	90	75	78,7
TSFC (kg/kp*h)	0,700	0,886	0,828	0,78	0,826
TSFC Augmented (kg/kp*h)	1,95	1,95	1,764	1,72	1,775

Table 8. Modern NATO and European fighter’s engine public data.

Notwithstanding purchase costs, the best engine for the fighter’s mission will be the most efficient and powerful one. The selected candidate from Table 9 for Estadea is therefore the Pratt & Whitney F135-100 turbofan engine, currently in use by the Lockheed Martin F-35. The F135-100 is an upgrade over the F-119-100, currently in use by the Lockheed

Martin F-22, offering significant thrust, efficiency and weight benefits over the previous model, and an ideal candidate for Estadea. However, it must be analyzed at different altitudes and speed regimes in order to determine the available thrust.

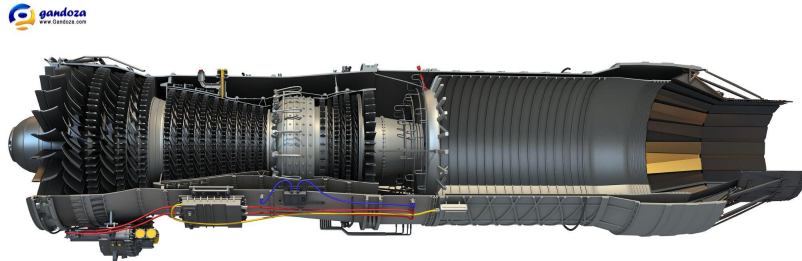


Fig. 101. Cutout of the F135-100 turbofan engine, courtesy of Gandoza.com.

Each engine will be paired by an independent inlet. The inlet design was based on the one described in Figure 42 and adapted to the F-135-100 fan diameter:

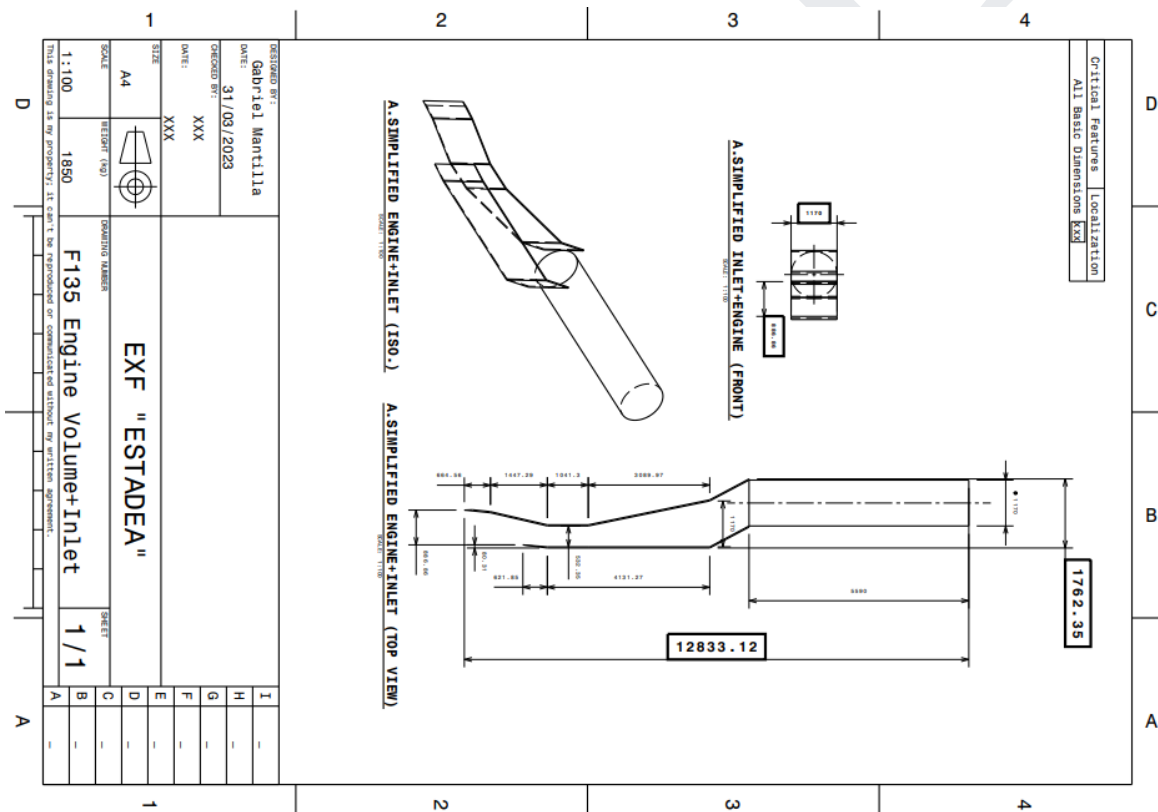


Fig. 102. Estadea’s simplified inlet design (dimensions given in meters).

This original inlet shape, however, may need to be further modified in order to fit the weapons systems. Another issue is determining the inlet frontal area. Due to the F-135-100’s usage as a military engine, its details are classified. To determine the approximate inlet frontal area, the engine will be simplified to a turbojet and analyzed in static, S.L. conditions:

It is assumed the efficiency of all components is $\eta = 1.0$, $v_\infty = 0 \text{ m/s}$,
 $T_\infty = 288.15 \text{ K}$, $P_\infty = 101325 \text{ Pa}$, $\gamma = 1.4$, $L = 44 \text{ MJ}$ and $cp = 1004 \text{ J/kg}$.

- INLET:

$$T_{02} = T_\infty = 288.15 \text{ K} \quad (41)$$

$$\frac{P_{02}}{P_\infty} = \left(\frac{T_{02}}{T_\infty}\right)^{\frac{\gamma}{\gamma-1}} \quad (5.1) \Rightarrow P_{02} = 101325 \text{ Pa} \Rightarrow \text{constant } \rho \text{ throughout the inlet}$$

- COMPRESSOR:

$$P_{03} = OPR \cdot P_{02} \quad (5.2) = 28 \cdot P_{02} = 2837100 \text{ Pa}$$

$$T_{03} = T_{02} \left(\frac{P_{03}}{P_{02}}\right)^{\frac{\gamma-1}{\gamma}} \quad (5.3) = 746.61 \text{ K}$$

- COMBUSTION CHAMBER:

$$\frac{L}{cp\Gamma} = T_{04} - T_{03} \quad (5.4) = 1513.39 \text{ K} \Rightarrow \Gamma = 28.958 \Rightarrow f = 0.0345$$

$$P_{04} = P_{03} \quad (5.5) = 2837100 \text{ Pa}$$

- TURBINE:

$$\text{Coupling Equation: } \frac{1}{f}(T_{03} - T_{02}) = \left(\frac{1}{f} + 1\right)(T_{04} - T_{05}) \quad (5.6)$$

$$T_{05} = 1815.284 \text{ K}$$

$$P_{05} = P_{04} \left(\frac{T_{05}}{T_{04}}\right)^{\frac{\gamma}{\gamma-1}} \quad (5.7) = 1317653.25 \text{ Pa}$$

- NOZZLE:

$$P_{05} = P_{06} = 1317653.25 \quad (5.8); \quad \frac{P_{06}}{P_\infty} > 1.89 \Rightarrow M_6 = 1.0 \quad (5.9)$$

$$P_6 = P_{06} \left[1 - \left(\frac{\gamma-1}{\gamma+1}\right)\right]^{\frac{\gamma}{\gamma-1}} \quad (5.10) = 696092.21 \text{ Pa} = P_{exit}$$

$$\left(\frac{T_{05}}{T_6}\right) = \frac{\gamma+1}{2} \quad (5.11) \Rightarrow T_6 = EGT = 1512.74 \text{ K}$$

$$v_{exit} = \sqrt{R\gamma EGT} \quad (5.12) = 779.63 \frac{\text{m}}{\text{s}}$$

$$T_{net, S.L.} = 125,000 \text{ N} = \dot{m} \cdot v_{exit} \quad (5.13) \Rightarrow \dot{m} = 160.33 \frac{\text{kg}}{\text{s}}$$

$$\dot{m} = \dot{m}_a + \dot{m}_f; \quad f = \frac{\dot{m}_f}{\dot{m}_a} \quad (5.14) \Rightarrow \dot{m}_a = 28.958 \cdot \dot{m}_f \Rightarrow \dot{m}_f = 5.352 \frac{\text{kg}}{\text{s}}, \quad \dot{m}_a = 154.98 \frac{\text{kg}}{\text{s}}$$

$$\dot{m}_a = \rho v A_{frontal, inlet} = \rho v_{suction} A_{fan} \quad (5.14) \Rightarrow v_{suction} = 135.58 \frac{\text{m}}{\text{s}} \Rightarrow A_{frontal, inlet} \simeq 0.93 \text{ m}^2$$

5.2. Engine Performance Assessment

The F135-100 will be analyzed at maximum normal and augmented thrust from 0 to 25km of altitude and from Mach 0 to Mach 2.2 (inlet design Mach) in a standard day (ISA+0), hot day (ISA+30) and cold day (ISA-30), using the following simplified formulas for jet engines (assuming the F135-100, due to its low bypass ratio, behaves closely to a turbojet engine):

$$T_{A,h} = T_{max.,S.L.} \cdot \frac{\rho_h}{\rho_{S.L.}} \quad (5.15)$$

$$\text{Subsonic Conditions: } T_{A,h} \approx cte. \quad (5.16)$$

$$\text{Supersonic Conditions: } T_{A,h} \approx T_{A,h; Mach 1} (1 + 1.18(M_\infty - 1)) \quad (5.17)$$

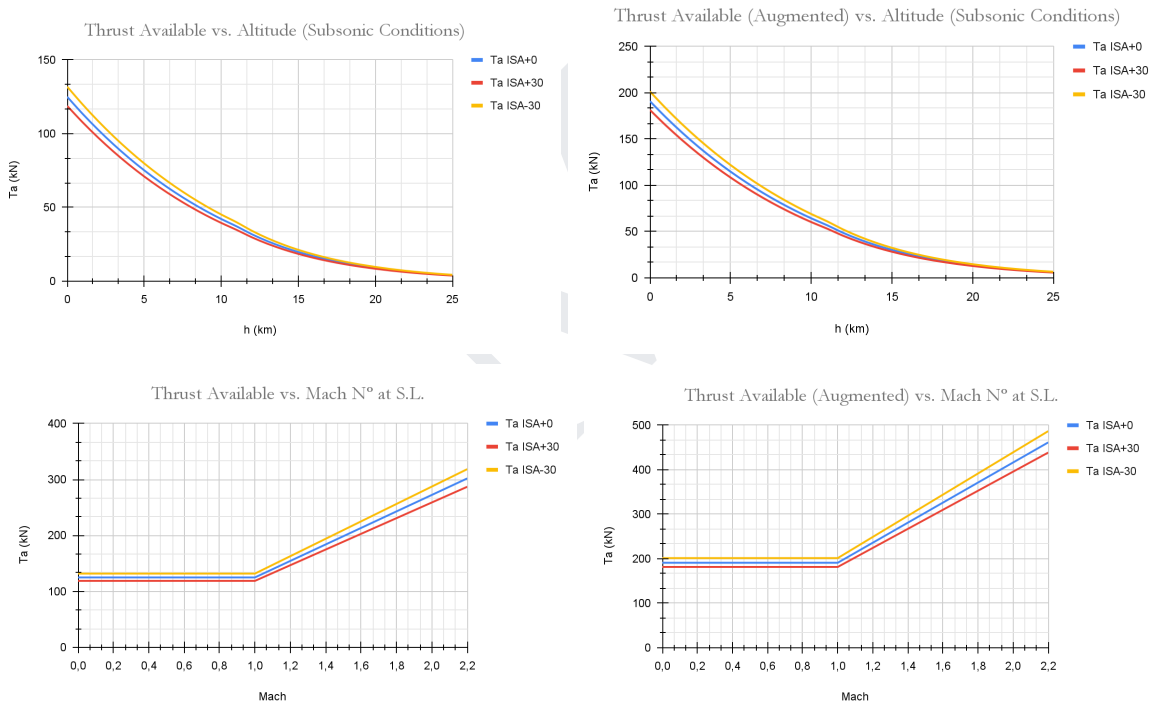


Fig. 103. Pratt & Whitney F135-100 engine performance assessment.

(This page has been intentionally left blank)

CHAPTER 6. 3D Design & Weight Estimation

All 3D components were designed using the open source OpenVSP software according to the general arrangement drawings and adapted to ensure proper spacing and fitting of all necessary equipment and armament.

6.1. Wing and Ruddervators:

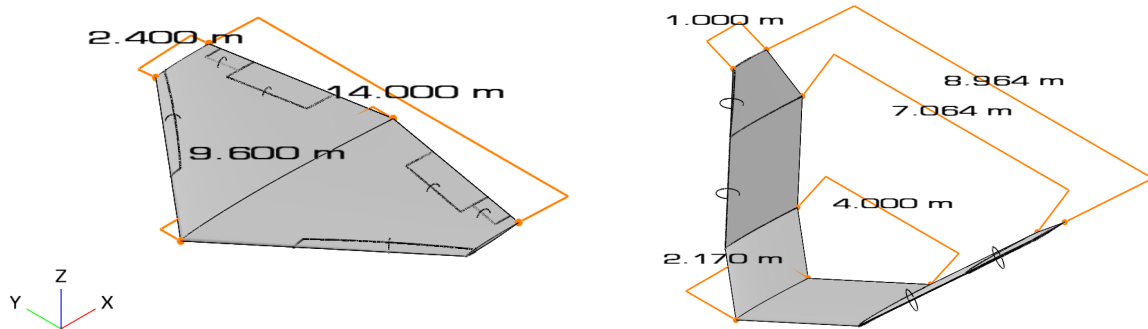


Fig. 104. 3D wing and ruddervator planforms.

	Wing	Ruddervator
Span (m)	14	10.48
Area (m^2)	84	21.29
AR	2.33	3.77
Sweep Angle (°)	40	40
Dihedral (°)	0	40
Twist Angle (°)	-3	0
MAC	4.46	1.93

Table 9: Wing and Ruddervator planforms' general characteristics.

6.2. Fuselage

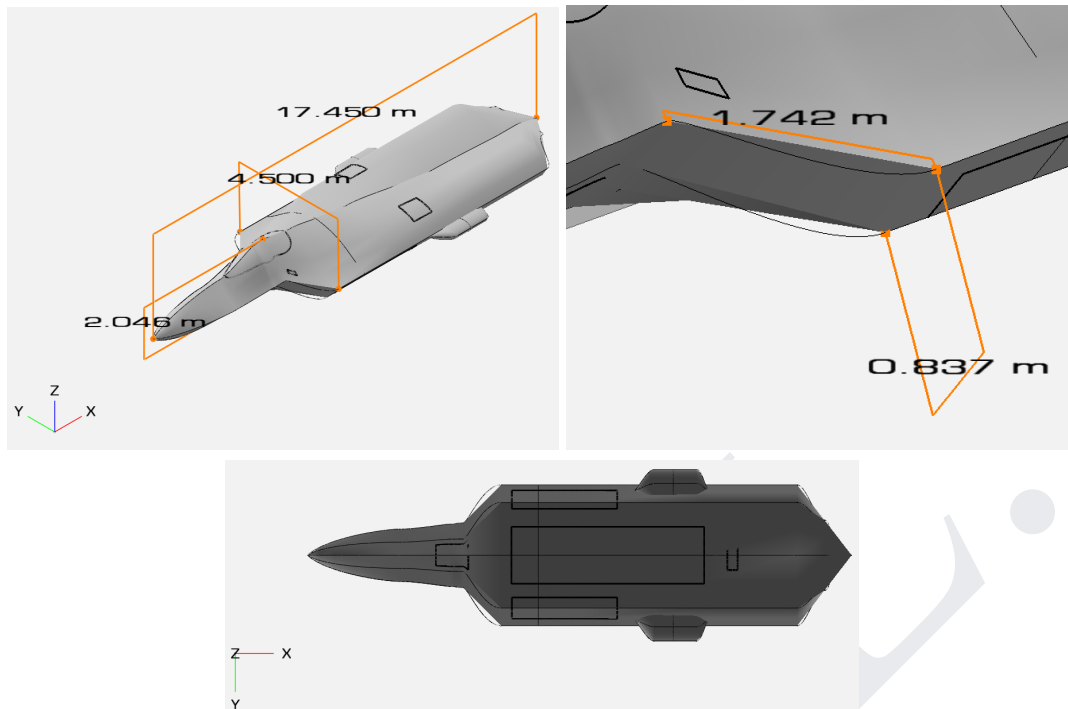


Fig. 105. 3D Fuselage Design.

- The available inlet frontal area per engine is:

$$A_{a, inlet} = 1.742 \cdot 0.837 \cdot \cos 40^\circ = 1.11 \text{ m}^2$$

Notice the addition of the canopy, gun trapdoor (top, left), overpressure relief doors (top), fox 2 bay doors (sides), fox 3 bay doors (bottom), flare and chaff dispenser door (bottom, aft), nose landing gear doors (bottom, front) and main landing gear housing (sides). Both gun positioning and missile rack arrangement were modified from the general arrangement drawings to fit the engine and inlet assembly. The fuselage geometry was divided in 8 distinctive sections, from front to back:

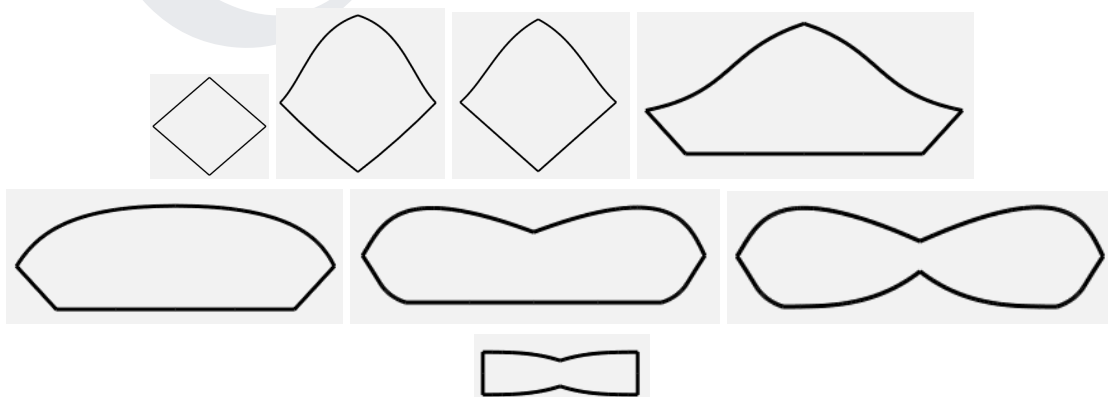


Fig. 106. Fuselage sections (scaled).

As shown by the fuselage sections, wasting was applied to the back sections (engine area) to reduce wave drag in accordance to Whitcomb’s and Jone’s Area Rules, while maintaining a healthy volume upfront to easily fit all necessary components and equipment. Joining the wing, LERX and ruddervators with the fuselage results in the simplified 3D model which will be used in all aerodynamic computations:

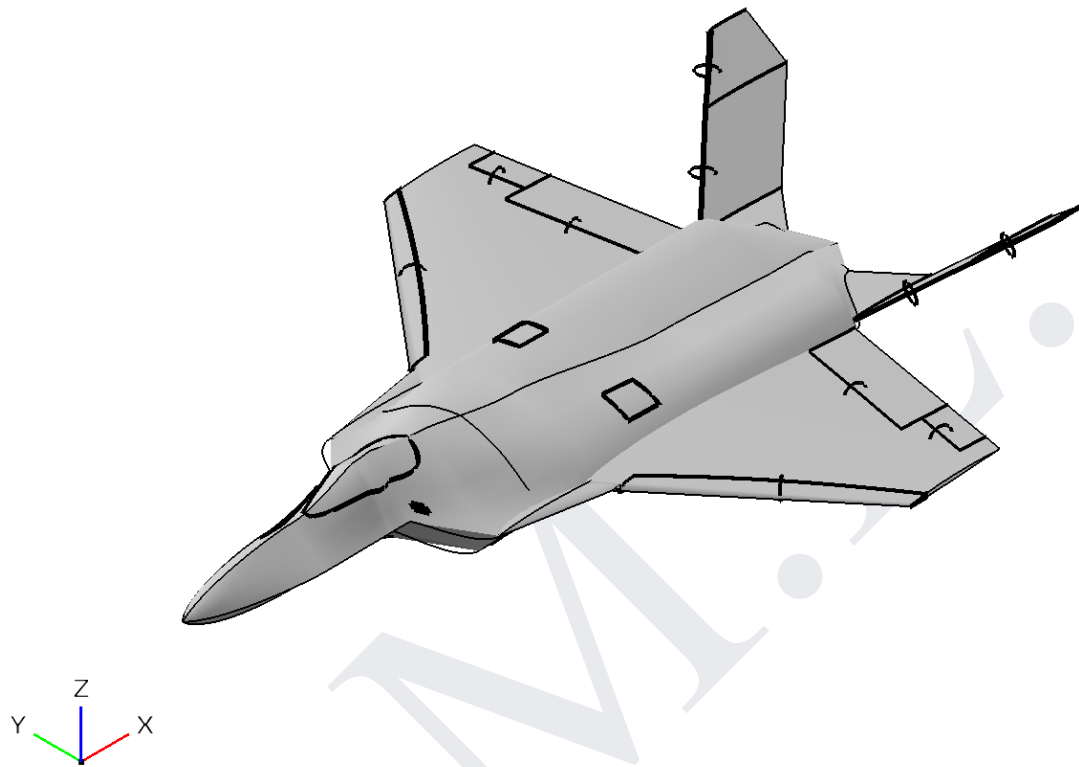


Fig. 107. Simplified 3D model.

6.3. Major Internal Components & Systems

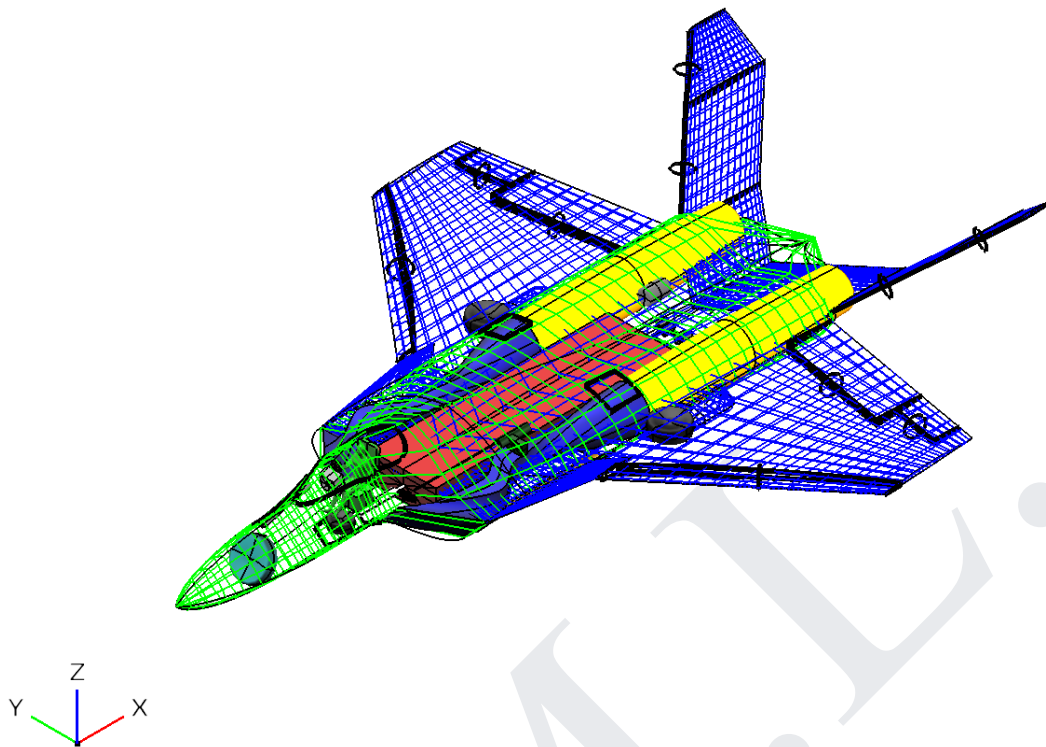


Fig. 108. General internal components arrangement.

6.3.1. Weapon Systems:

As mentioned previously, the main weapons bay dimensions had to be modified in order to fit it in between the engines from a single row to two-row rack disposition. The side bays are represented by two AIM-9X missiles. Finally, a feeding system with the necessary dimensions to hold 150, 27mm rounds was added to the gun system.

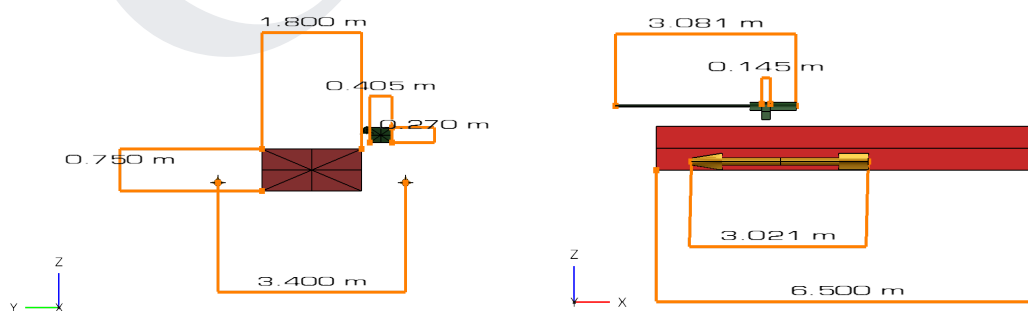


Fig. 109. Weapon systems arrangement.

6.3.2. Propulsion & Auxiliary Power Systems:

The propulsion systems are composed by two Pratt and Whitney F-135-100 engines, an APU module based on the Panavia Tornado auxiliary power systems (it is supposed to represent the Honeywell G350 currently embedded with the F135-100 engines, although no public information regarding size and weight of such APU was found), and two inlets, one for each engine. The inlets were modified from the initial design by displacing each characteristic cross-section in the yz plane to both allow the fitting of the side weapon bays and obtain the characteristic S-duct shape which obscures the engine front face from an outside viewer.

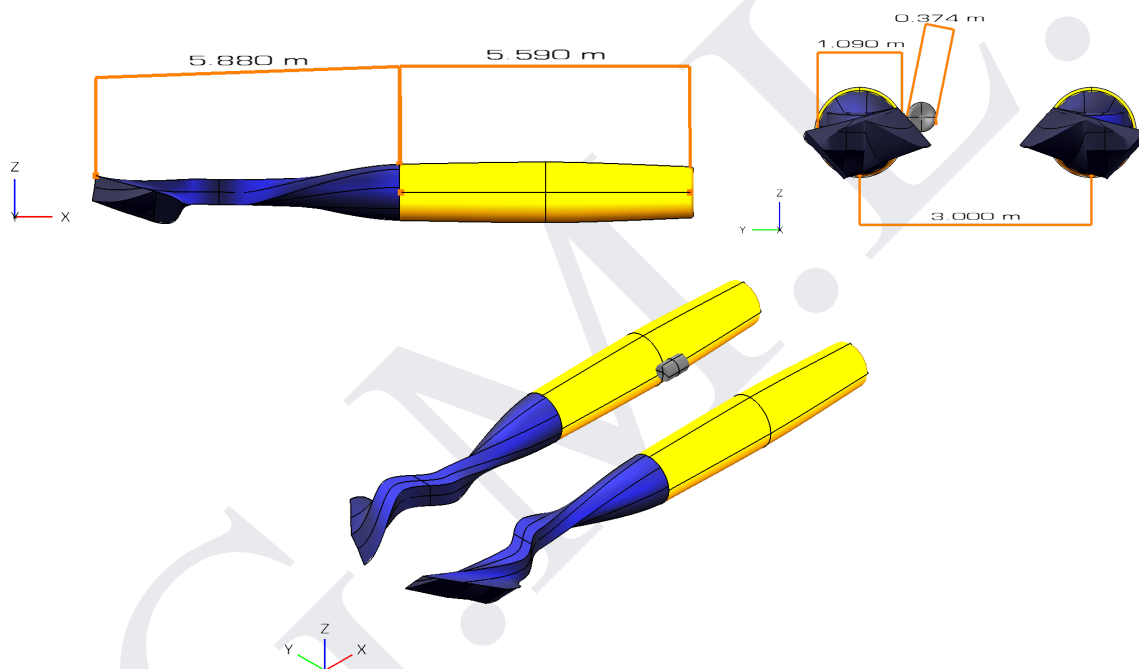


Fig. 110. Propulsion & auxiliary power systems arrangement.

6.3.3. Landing Gear:

Estadea’s landing gear follows a similar storage and deployment design similar to the F-35; the main landing gear when retracted is stored in between the fuselage and the wing root and deployed backwards in a swing-arm fashion. Goodyear tyres of dimensions 22 x 7.75-9 and 36 x 11.0-18 for nose and main landing gear, respectively, taken from the F-15 Eagle, of similar dimensions as Estadea, were incorporated (Goodyear, 2022). Notice its broad footprint and greater ground clearance for added stability and safety when landing and operating on rough terrain.

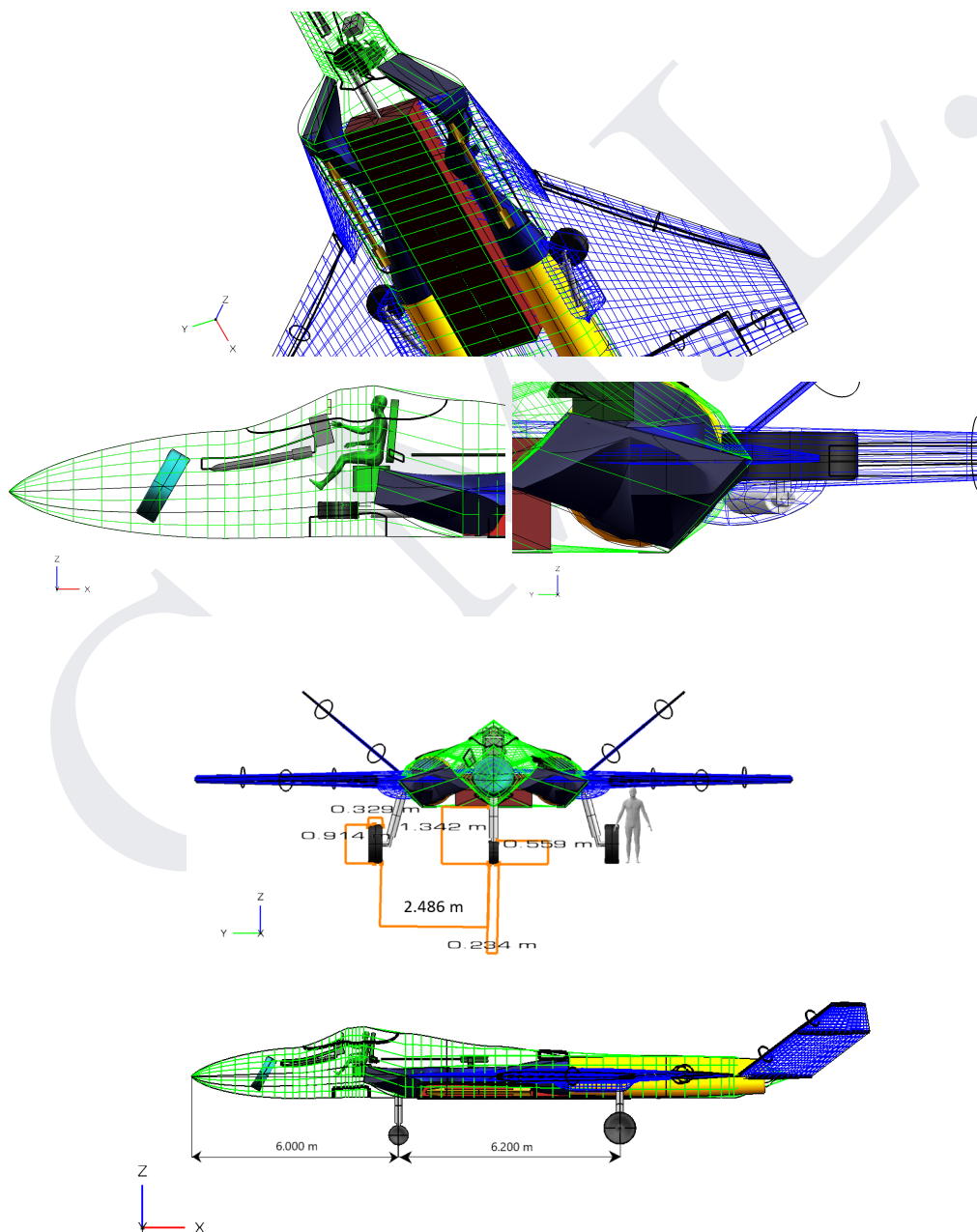


Fig. 111. Landing gear arrangement.

6.3.4. Countermeasures:

The flare and chaff dispensers are based on the AN/ALE-47 system currently in use in most U.S. aircraft. Each D-56/D-63 dispenser can be configured independently of to hold up to 60 flares or chaff tubes for a total of 120 slots in the basic configuration (additional dispensers can be added if needed). The dispensers are angled so the released flares and chaff are launched to stand clear from the sides of the aircraft, ensuring the countermeasures are visible to radar or missiles from any external point of view.

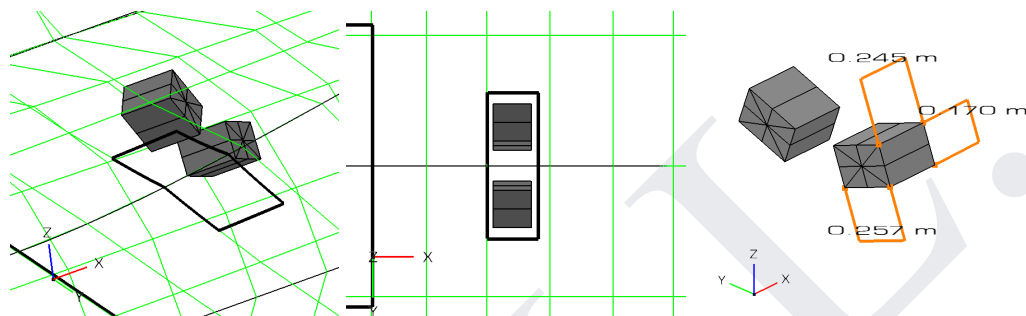


Fig. 112. Countermeasures arrangement.

6.3.5. Aerial Refuelling System:

For prolonged missions, it is of paramount importance that Estadea counts with some sort of aerial refueling system. For this purpose, a hidden fuel probe was added next to the cockpit which deploys in line with the pilot’s fieldview to catch the drogue released by the tanker aircraft in a typical probe-and-drogue fashion.

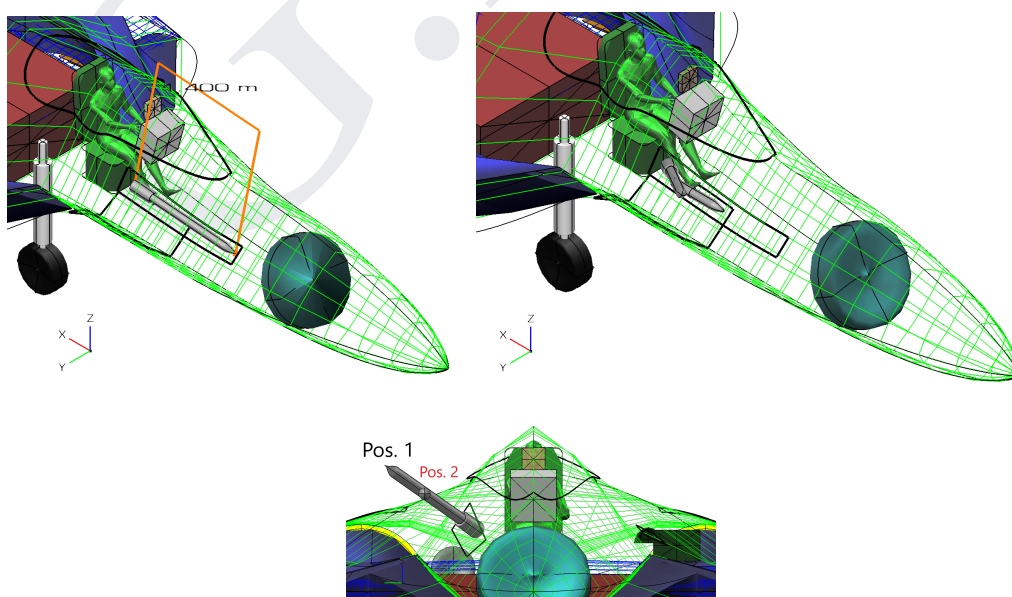


Fig. 113. Fuel probe arrangement.

6.3.6. AESA Radar Assembly:

For its air superiority role, Estadea must mount the latest AN/APG-81 AESA radar. However, due to its classified nature, little information was found concerning exact dimensions and weight. It was assumed a general diameter of 1.0 m and 0.25m of thickness for the antenna and 150.0 kg of weight for the whole system. The antenna is angled to reflect incoming radar waves away from the receiver in line with the stealth design principles discussed in Chapter 3.

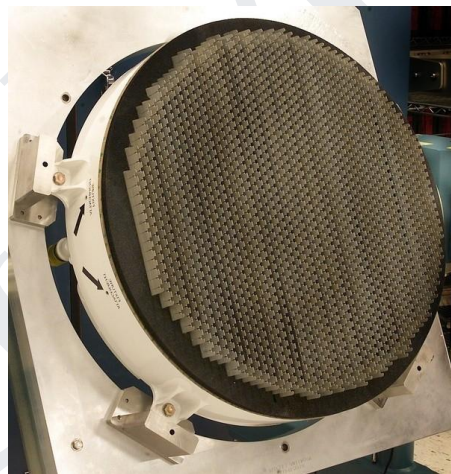
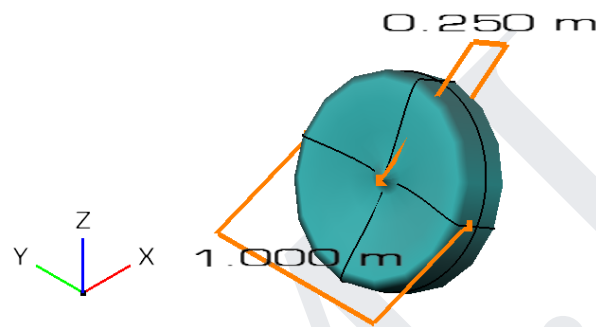


Fig. 114. AESA radar antenna arrangement.

6.3.7. Cockpit Arrangement:

It is of paramount importance to provide the pilot with a spacious, comfortable and tidy cockpit in order to decrease the workload in combat missions and patrols. To achieve this objective, three main considerations were taken:

1. Good Visibility.

Visibility can be quantified by analyzing the visibility pattern, composed of two variables: the fieldview or how far up and down the pilot can see while seated and the pilot axis or the head movement of the pilot. Estadea, in its current iteration, presents the following visibility pattern:



A319/A320/A321 flight deck – pilot’s field of view

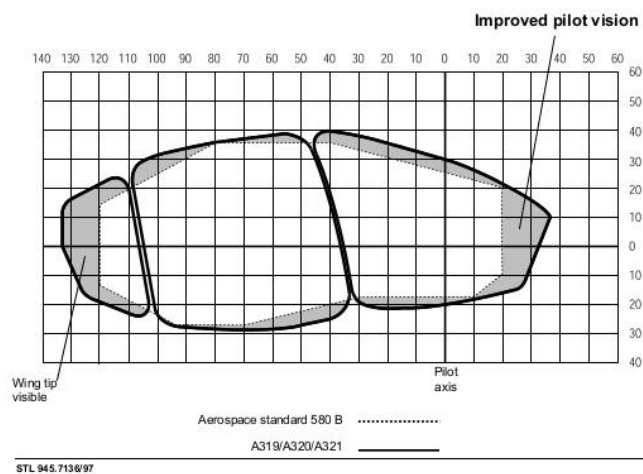


Fig. 115. Estadea vs. Airbus A319/A320/A321 and Aerospace standard 580B visibility patterns.

From Figure 109, it can be seen that Estadea, due to its single piece canopy, offers similar downward vision angles as current airliners, increased upwards visibility and total horizontal visibility in terms of the pilot axis. This increased capability offers the greater situational awareness necessary for combat and the ability to easily detect ice buildups.

2. Simplified Controls.

Instead of overloading the dashboard and instrument panels with buttons, switches, etc., extensive LCD usage has been applied to reduce as much as possible the presence of physical controls, although the thrust lever and flight stick are present in a mechanical form. The thrust lever is positioned on the left side of the pilot and has been divided in two separate levers, each for one engine. The flight stick is positioned on the right side of the pilot for improved ergonomics allowing the ejection handle to be positioned in between his legs. The physical HUD can be completely removed when an advanced helmet (for example, the helmet design currently in use by F-35 pilots, in which the HUD is completely integrated) is available.

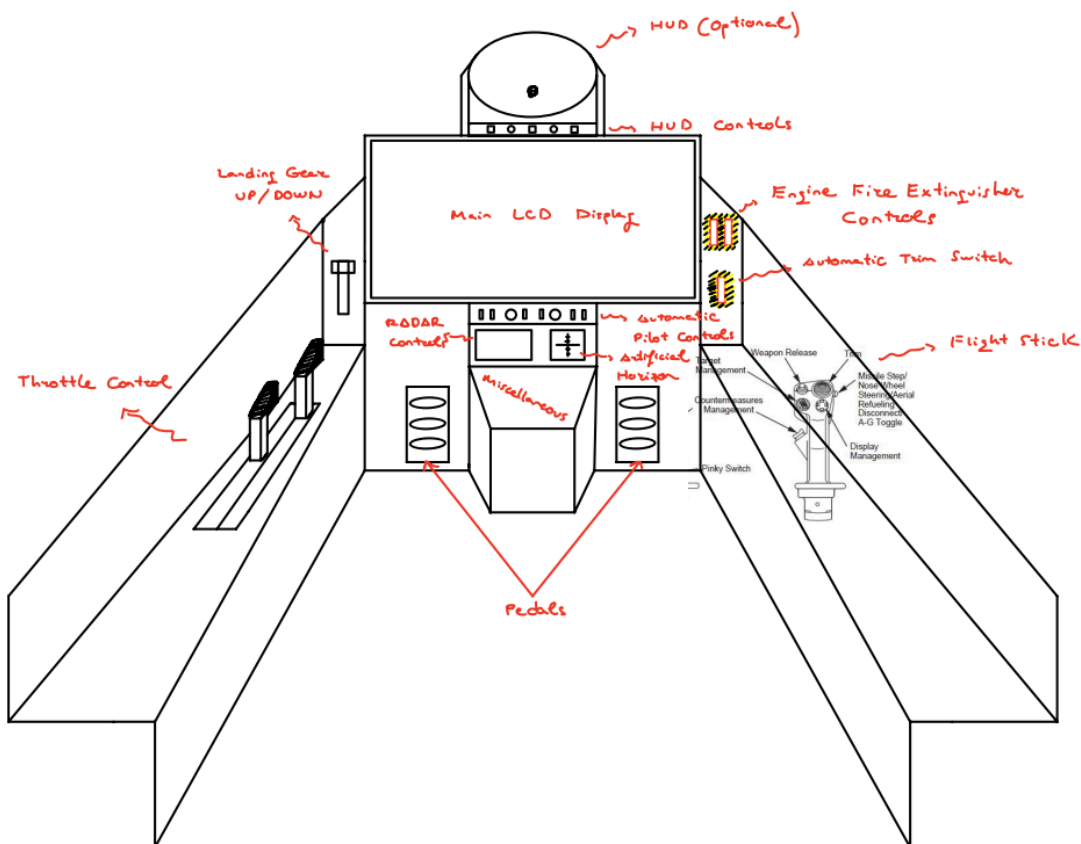


Fig. 116. Estadea cockpit design.

3. General Cockpit Ergonomics.

A generously dimensioned seat and good head and shoulder clearance adds tremendously to the pilot’s comfort. Additionally, the pedal column and seat should be fully adjustable in order to accommodate any pilot. In any case, a reference human model of 1.80m of height and 80.0kg of weight was used as the basic model.

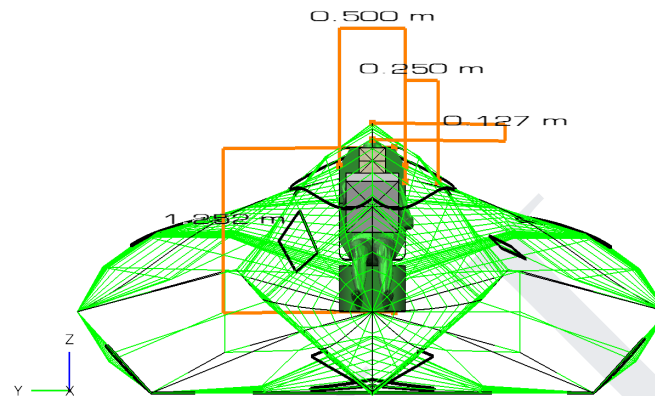


Fig. 117. Estadea’s cockpit ergonomics.

6.3.8. Electrical, Hydraulic & Backup Systems Arrangement:

No aircraft can fly without a minimum set of systems, however simple they may be, powering and controlling its different components (comms, control surfaces, sensors, landing gear, etc.); in this section the focus lands on two major systems: electrical and hydraulic systems. Several aspects have to be taken into account before designing the different systems of the aircraft:

- **Redundancy:** in case of failure of one primary system via bird strike, lightning, fire, structural damage, etc. there should be a backup ready to take over the duties of the former.
- **Correct Placement:** the systems should be placed preferably in the most secluded sections of the aircraft (i.e. away from the wing and tails leading edges, internal mechanical systems and buried deep inside the fuselage) without making them inaccessible for maintenance or repair operations.

- Adequacy: each system should be tailored to the components' needs and not the other way around (for example, the electrical system should have the sufficient power to feed the needs of all electrical components).

On that note we can show a simplified design of Estadea's electrical and hydraulic systems:

- Hydraulic System:

The hydraulic system has been greatly reduced in preference for a Power-by-Wire architecture for reduced complexity and increased reliability and survivability, similar to that of the F-35, opting for electro-hydraulic actuators (EHA) for the flaperons and ruddervators and electrical drive units (EDU) for LE flaps and ailerons.

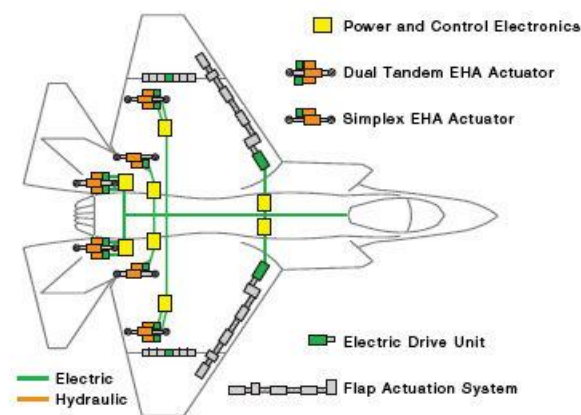


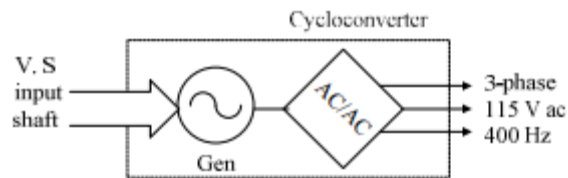
Fig. 118. Lockheed Martin F-35 Power-by-Wire architecture, courtesy of Lockheed Martin.

Additional EDU's were outfitted to the missile bay doors, gun trapdoor and countermeasure dispenser doors. In the case of the landing gear, it possesses a dedicated hydraulic system, being Blue the primary and Red its backup; additionally, the landing gear possesses an electrical pump.

- Electrical System:

Variable Speed Constant Frequency (VSCF): In this drive, the output speed (as given by the APU and engines) is variable and consequently the output generator frequency is variable. To provide an AC voltage with a constant frequency of 400Hz, a DC-link is formed between the generator side and the AC loads, using AC/DC and DC/AC power converters, or

by using a cycloconverter (AC/AC converter). The DC-link provides additional benefits for feeding high voltage loads (270V) and charging batteries (R. Abdel-Fadil, A. Eid & M. Abdel-Salam, 2013). This system is much simpler and reliable than other options and has proven itself in the many years of service of rugged aircraft such as the F-18 Super Hornet.



(c) VSCF

Fig. 119. VSCF electrical system diagram, extracted from “Electrical Distribution Power Systems of Modern Civil Aircrafts” by R. Abdel-Fadil, A. Eid & M. Abdel-Salam.

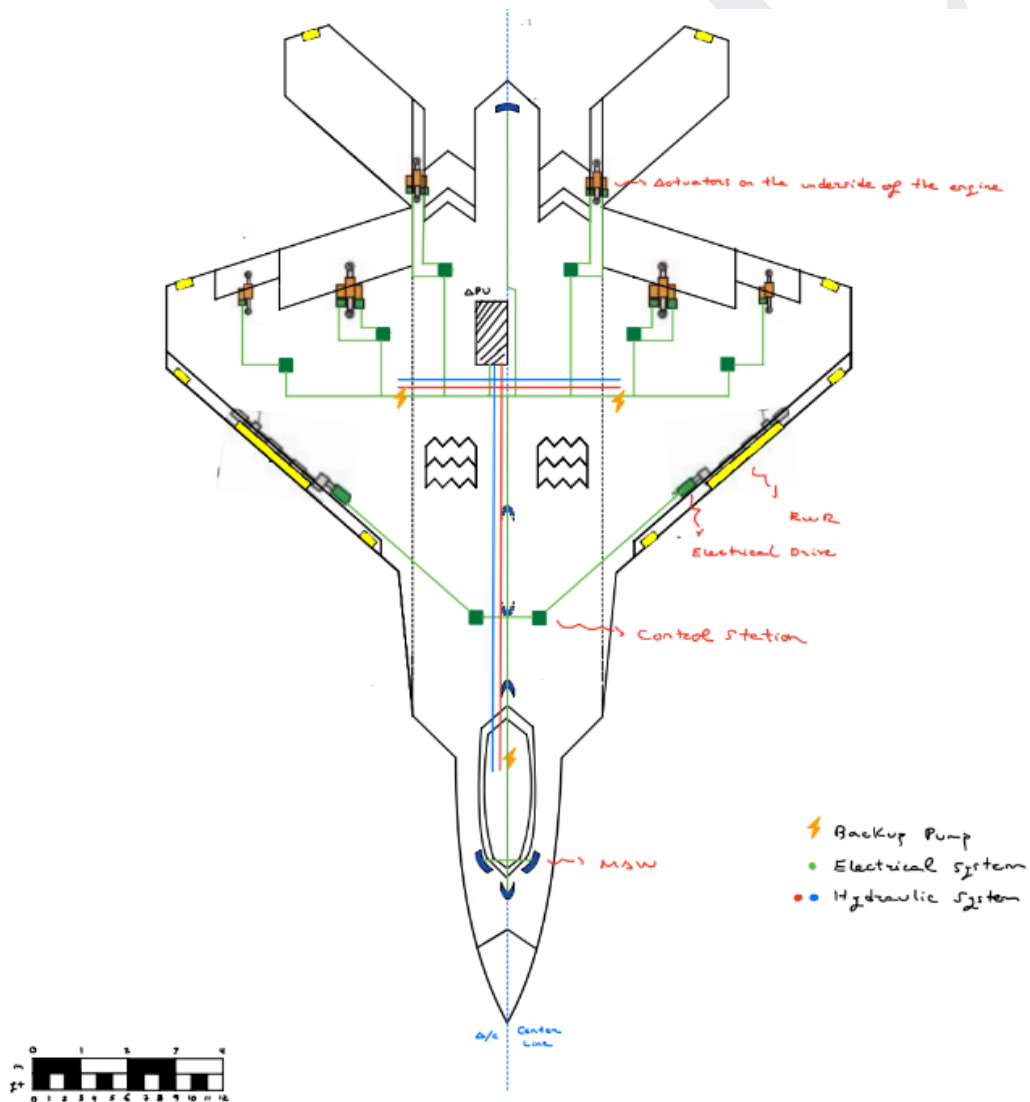


Fig. 120. Estadea’s primary systems arrangement.

6.4. Weight Estimation

The MTOW and EW estimation has been done by applying statistical techniques. It is important to note that Estadea’s real weight cannot be certainly determined until the Detailed Design phase, which lies outside the scope of this thesis. For Estadea’s weight determination three statistical correlations were used: MTOW and EW in terms of length, span and wing surface. The samples include current western and eastern 5th generation and modern 4th generation of different sizes and weights.

	Span (m)	Length (m)	Empty Weight (kg)	MTOW (kg)	Sw (m2)
F22	13,56	18,9	19700	38000	78,04
F35A	10,7	15,67	13300	31800	42,7
J-20	13,5	20,4	19391	37013	78
Su-35s	15,3	21,9	18400	34500	62
EF	11	16	11000	25300	50
YF-23	13,3	20,6	14970	29000	88

Table 10: Weight estimation statistical samples.

From the data samples the three statistical correlations could be easily obtained:

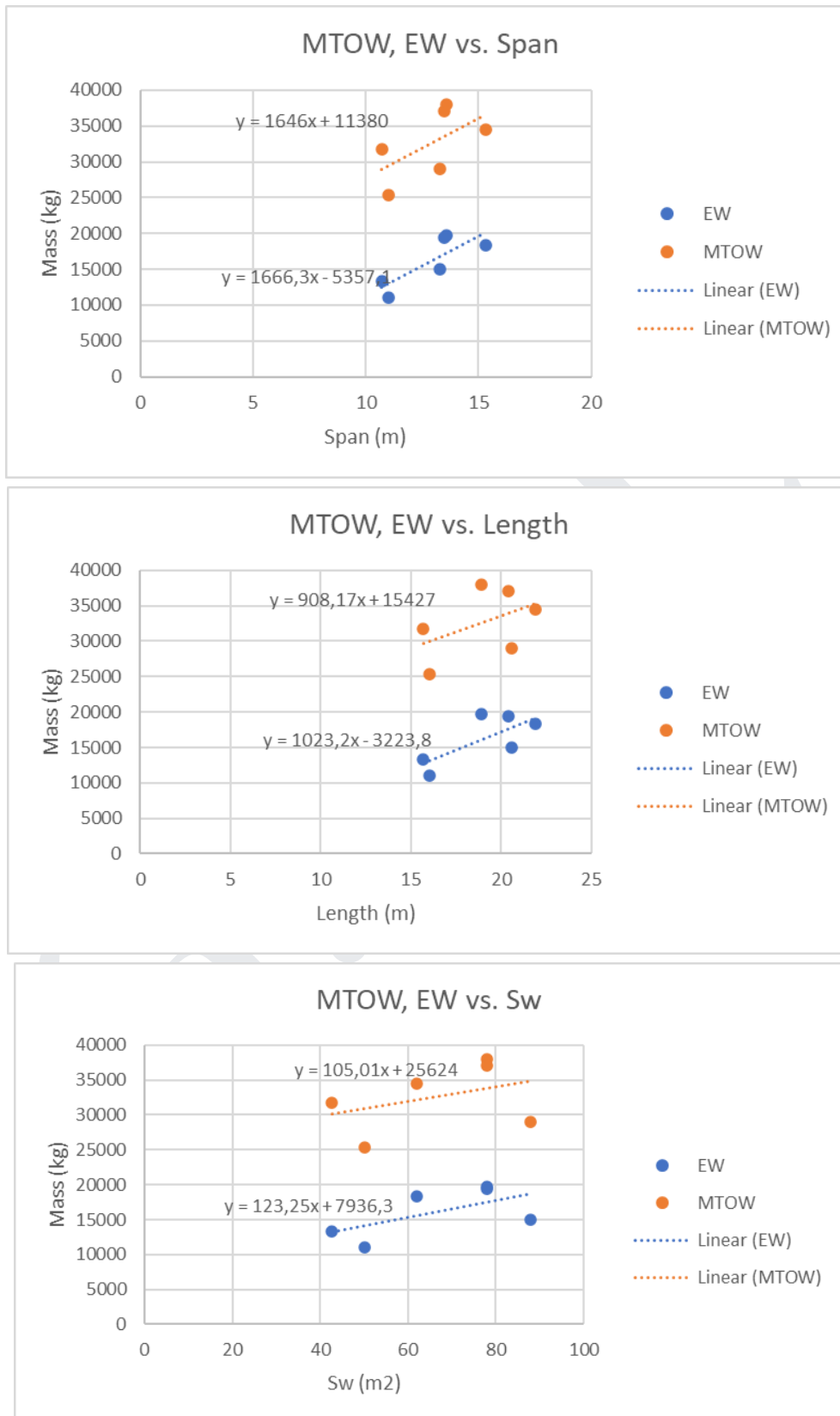


Fig. 121. Weight estimation statistical correlations.

	Span (m)	Length (m)	Empty Weight (kg)	MTOW (kg)	Sw (m2)
Estadea 1	14	19	17971,1	34424	84
Estadea 2	14	19	16217	32682,23	84
Estadea 3	14	19	18289,3	34452,4	84
Average	14	19	17492,47	33852,88	84

Table 11: Weight estimation results.

At first view the weight estimation results are plausible considering the smaller frontal cross-section of Estadea with its closest sample in terms of size, the Lockheed Martin F-22:

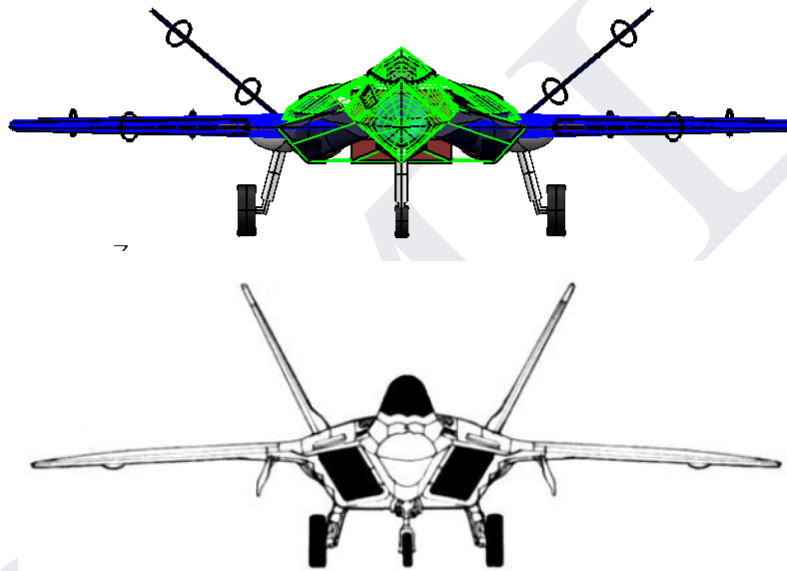


Fig. 122. Estadea and F-22's front view (scaled).

Nonetheless, the pilot weight and payload (stealth configuration) can be easily computed:

Crew Weight		Payload (A-A)		Payload (A-G)	
ITEM	Mass (kg)	ITEM	Mass (kg)	ITEM	Mass (kg)
Pilot	80	27mm Rounds	39	27mm Rounds	39
Flight Suit	0,18	Fox-2 Missiles	170,6	Fox-2 Missiles	170,6
G-suit	6,5	Fox-3 Missiles	974,4	Fox-3 Missiles	649,6
O2 Mask	0,214	TOTAL	1184	Bombs	894
Helmet	2,13			TOTAL	1753,2
Boots	1,134				
Gloves	0,454				
Safety Gear	10				
TOTAL	100,612				

Table 12: Crew and Payload weight calculations.

In the case of the fuel weight estimation, a different approach will be used; the empty volume in the 3D model will be filled by several compartments, each representing a single fuel tank. The internal fuel capacity will be approximated by adding the individual compartments' volumes.

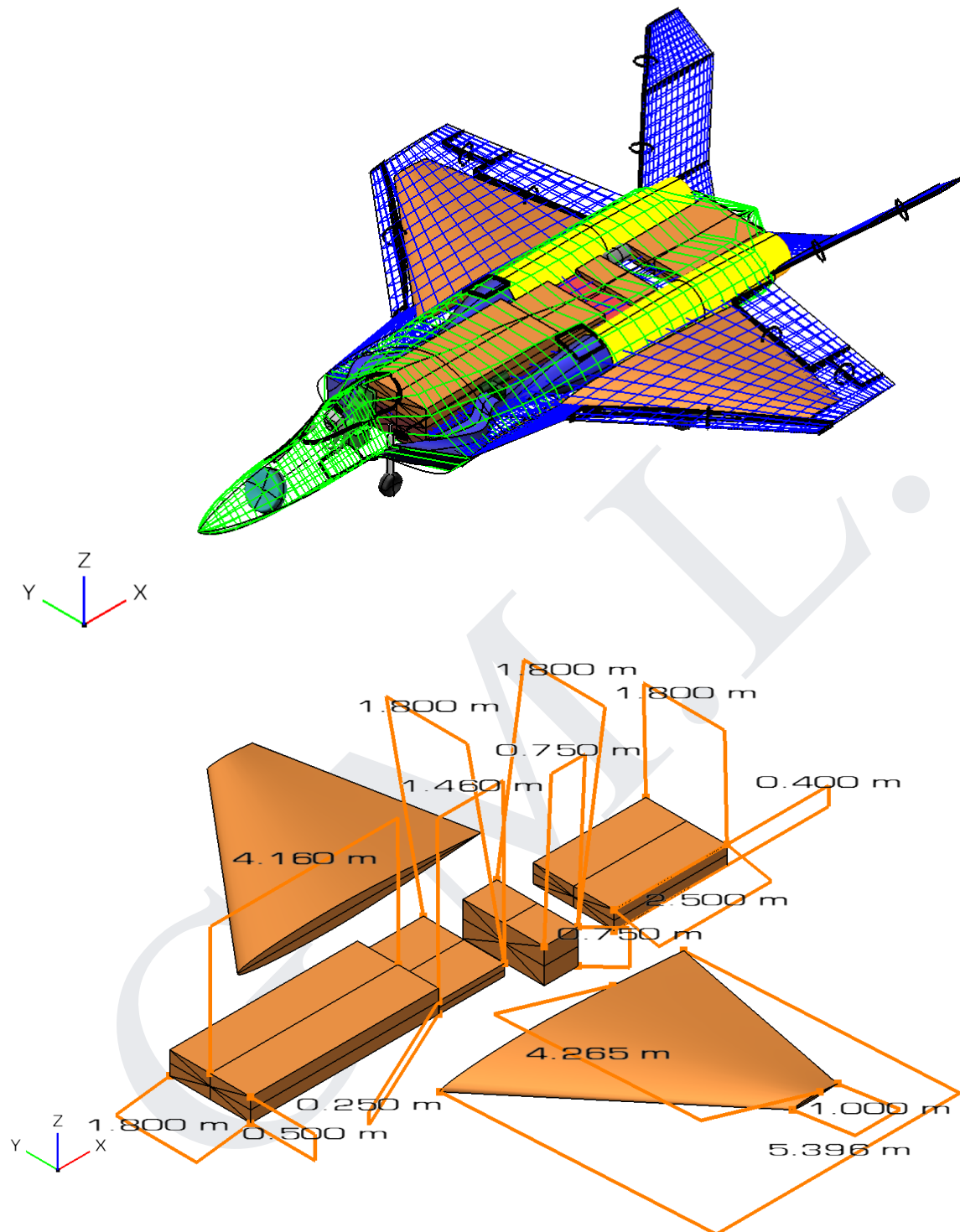


Fig. 123. Estadea’s fuel tank distribution.

Military jets use dedicated fuels; for example, the USAF uses the JP-8 fuel, similar in composition to the civilian Jet A-1 fuel. In any case it is assumed the fuel density to be similar to that of the Jet A-1; $\rho = 0.840 \text{ kg/l}$.

- $V_{internal\ fuel} = V_{aft\ tank} + V_{central\ tank\ 1} + V_{central\ tank\ 2} + V_{trim\ tank} + 2V_{wing\ tank}$ (6.1)

- From the wing fuel tanks a volume equivalent to the tyre well must be extracted,

$$V_{wing\ tank} \simeq A_{wing\ tank} \cdot t_{av} - V_{tyre\ well} \quad (6.2) = 13.59 \cdot 0.137 - 0.914^2 \cdot 0.329;$$

$$V_{wing\ tank} = 1.586\ m^3$$

- The total fuel capacity is:

$$V_{internal\ fuel} = 3.744 + 0.657 + 1.0125 + 1.8 + 2(1.586) = 10.3855\ m^3$$

- In terms of weight, the fuel load is:

$$W_{fuel} = 10.3855 \cdot 840 = 8723.82\ kg = 85580.6742\ N$$

The fuel capacity can be increased by adding external fuel tanks as mentioned in Chapter 2. The F-22 external fuel tanks are an excellent choice. Each tank contains 600 gallons of fuel (allegedly) which amounts to 1907.85 kg of extra fuel per tank (Global Security, 2023).

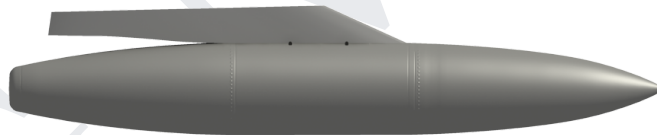


Fig. 124. F-22 external fuel tanks.

Assuming 100.0kg of empty weight for each tank, the drag penalty and extra weight imposed on Estadea can be calculated:

- $R_{max} = 0.415\ m; L = 6.604\ m$
- From OpenVSP $c_{D,wave} = 0.0028$.
- Estadea will carry two of these tanks in the long-range patrol and ferry configuration.

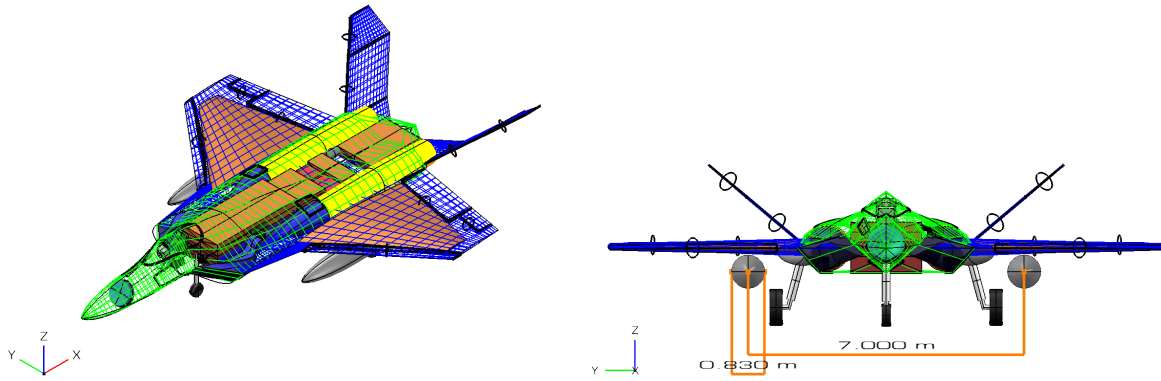


Fig. 125. Drop tanks arrangement.

- The drag penalty of the drop tanks is $D_{drop\ tanks} = \rho v^2 c_{D, drop\ tank} \pi R_{max}^2$ (6.3)

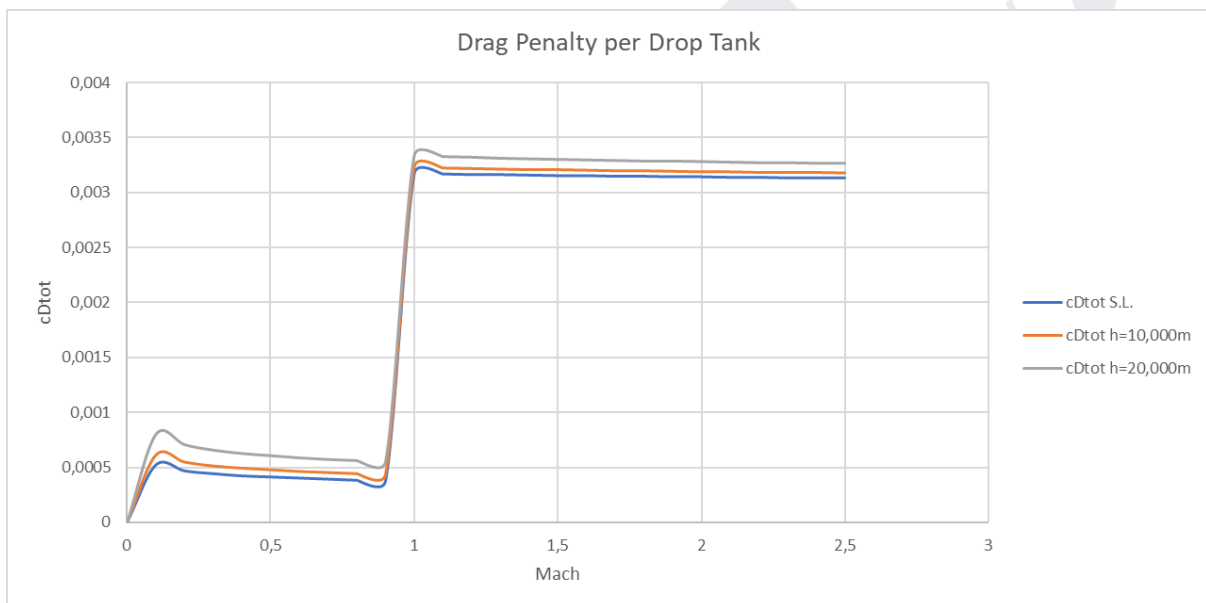


Fig. 126. Drag penalty per drop tank.

From the previous graph it can be seen how the drop tanks’ total drag greatly increases beyond sonic speeds due to the wave drag and how flying higher, and therefore at lower density altitudes, alleviates this exponential increase in drag. Finally, assuming constant density across components, the reference CoG for all aerodynamic analysis can be easily calculated from the “Mass Properties” tab in OpenVSP.

Mass Properties	
Num Slice:	25
Slice Direction:	X
Set:	All
Compute	
Draw Cg	
Results	
Total Mass	69.510
X Cg	10.274
Y Cg	0.005
Z Cg	0.041
I xx	230.751
I yy	929.920
I zz	1140.728
I xy	0.463
I xz	-13.249
I yz	0.141

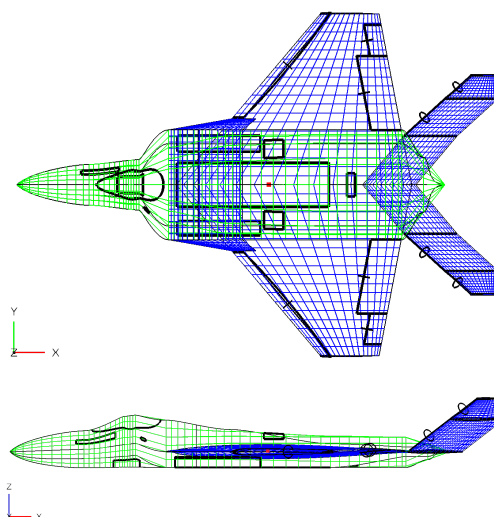


Fig. 127. CoG computation.

From the previous calculated weights, three distinctive weight configurations tailored for air superiority arise:

1. Ferry Configuration:

$$W_{ferry} = W_{internal\ fuel} + W_{external\ fuel} + W_{pilot} + W_{drop\ tanks} + W_{empty} \quad (6.4)$$

2. Air Patrol Configuration:

$$W_{CAP} = W_{internal\ fuel} + W_{external\ fuel} + W_{pilot} + W_{drop\ tanks} + W_{empty} + W_{A-A} \quad (6.5)$$

3. Combat Configuration (Stealth):

$$W_{combat} = 0.5 \cdot W_{internal\ fuel} + W_{pilot} + W_{empty} + W_{A-G} \quad (6.6)$$

Configuration	Ferry	Air Patrol	Combat (50% fuel, Stealth)
Fuel (kg)	12539,52	12539,52	4361,91
Payload+Pilot (kg)	300,61	1484,61	1853,81
Empty Weight (kg)	17492,47	17492,47	17492,47
Total (kg)	30332,60	31516,60	23708,19
T/W (S.L.)	0,84	0,81	1,07
T/W Augmented (S.L.)	1,28	1,24	1,64

Table 13: Estadea Weight Configurations.

(This page has been intentionally left blank)

G.M.L.

CHAPTER 7. AERODYNAMIC ANALYSIS

7.1. Airfoil Selection

As seen in Section 2.2 of Chapter 2, Estadea must incorporate airfoils of low relative thickness for both wings and ruddervators in order to delay the formation of shockwaves along their surface. In Section 2.3 of Chapter 2 it was noted the necessity of an airfoil with good post-stall characteristics. Besides from these requirements, the selected airfoils must yield high efficiencies and high c_l . It is preferable that the root airfoil possesses a higher relative thickness due to structural requirements as well as increasing the wing’s fuel tank volume. All airfoils will be evaluated in the open source software XFLR5. The analysis conditions are the following:

- Reynolds number (measure for flow turbulence): 300,000.
- Mach number: 0,00 (subsonic flow).
- Analysis type: Type 1.
- NCrit: 9.00.
- Forced transition position: 1.00 (for both upper and lower airfoil surfaces).
- AoA transition: -20° to 90° in 0.5° steps.

From www.airfoiltools.com, several NACA 6-series airfoils were extracted:

1. NACA 63-206.
2. NACA 63-209.
3. NACA 63-210.
4. NACA 63A210.
5. NACA 64-206.
6. NACA 64-208.
7. NACA 64-209.
8. NACA 64-210.
9. NACA 64-010.
10. NACA 65-206.
11. NACA 65-209.

12. NACA 66-206.

13. NACA 66-209

These airfoils are optimized to maximize laminar flow at high speeds and are most commonly found in most U.S. fighter aircraft. The results were as shown:

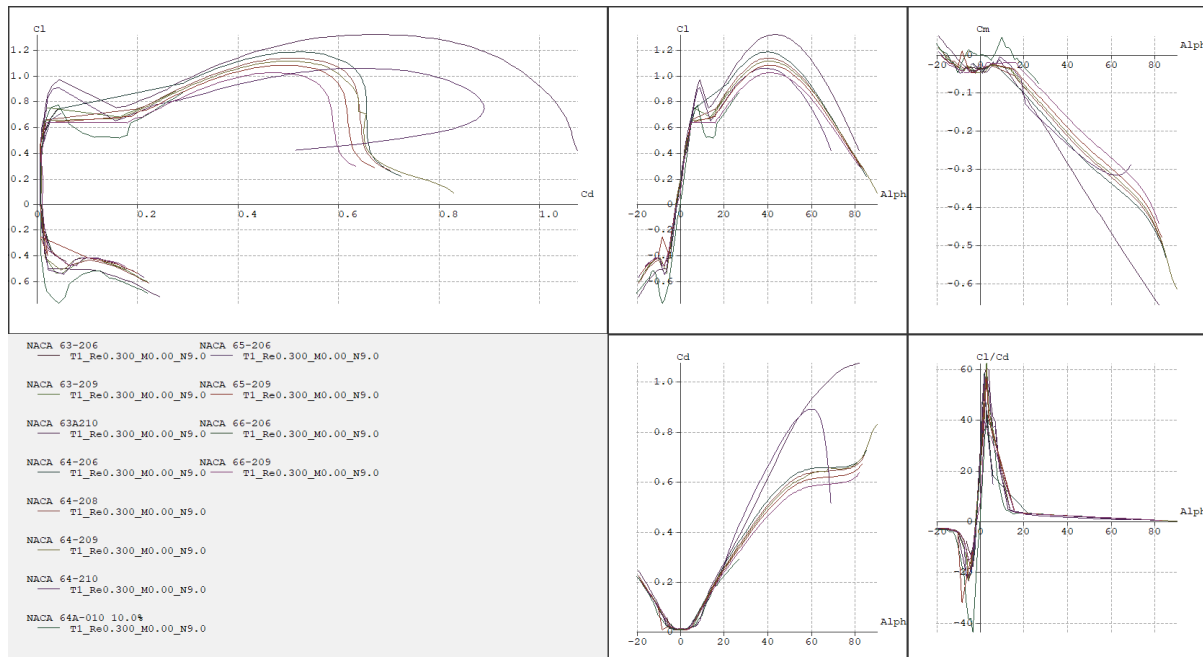


Fig. 128. NACA 6-series airfoils aerodynamic results.

The XFLR5 analysis results show all airfoils possess low c_d at low AoA ranges, decent efficiencies (most lie around a maximum of 60 at 5° AoA) and excellent post-stall characteristics, being the outlier the NACA 64-210 with a significantly higher maximum c_l . However, due to the speed range Estadea is expected to cover, airfoils with big relative thicknesses must be discriminated against in order to ensure low wave drag and sufficient lift generation at higher speeds. Being the NACA 64-210 the outlier in the 2D XFLR5 analysis, two airfoils adapted from the previous proponent were chosen: the symmetrical NACA 64A-006 for both wing root, LERX and ruddervators, and the cambered NACA 64A-204 for the wing tip.



Fig. 129. NACA 64A-006 and NACA 64A-204 airfoils.

By possessing a thicker symmetrical airfoil as wing root, Estadea has the added capability of inverted flight, higher fuel capacity and increased structural strength.

7.2. Wave Drag Coefficient Calculation

OpenVSP does not take into account the wave drag in its aerodynamic computations at supersonic conditions; however, it allows the wave drag to be independently calculated from Mach 1.0 to Mach 5.0. Using the simplified 3D model (clean configuration), wave drag will be calculated from Mach 1.0 to Mach 2.5 in steps of 0.25 (7 points). It is expected that the wave drag coefficient is at its highest in Mach 1.0 and gradually decreases as Estadea accelerates.

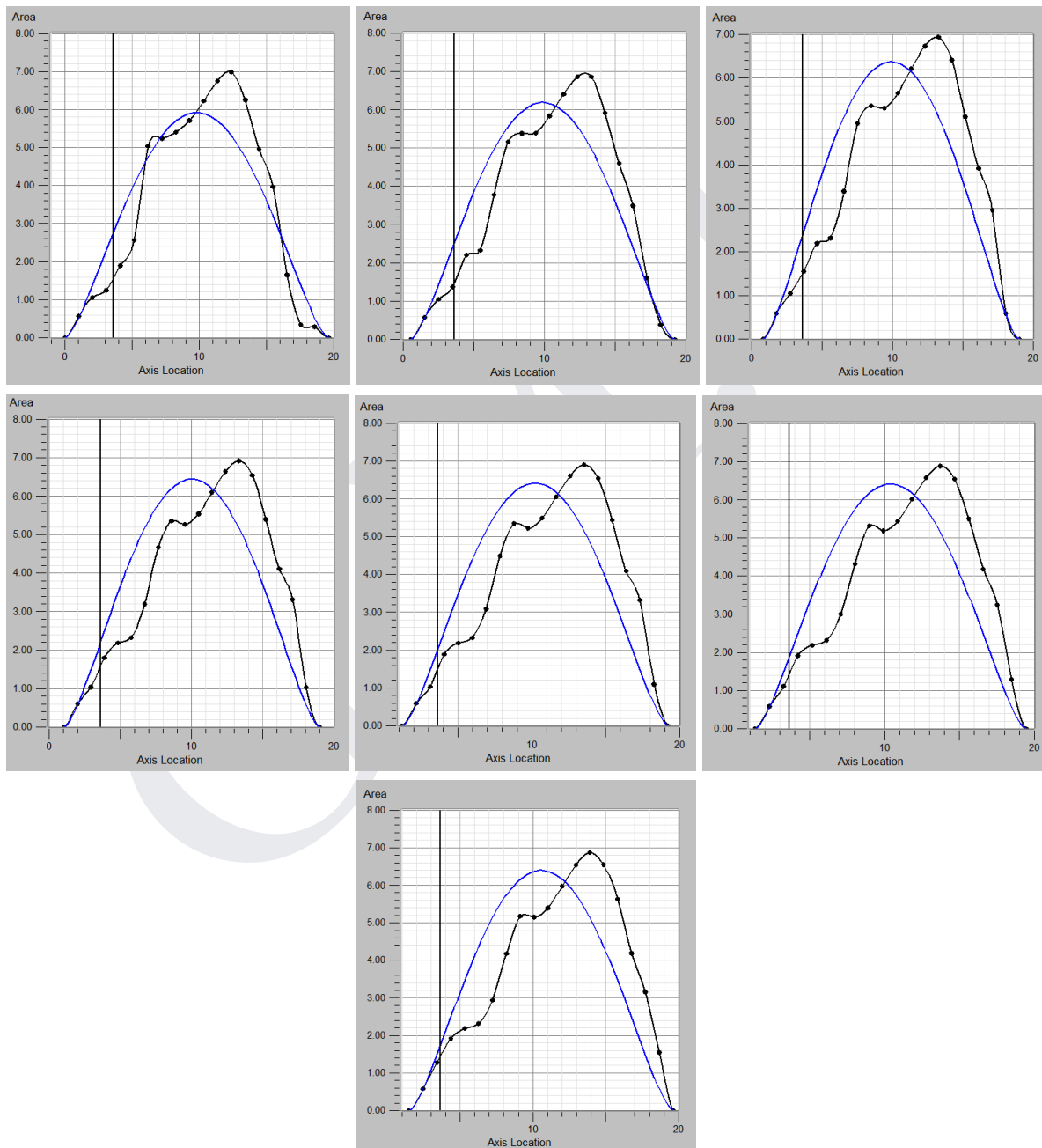


Fig. 130. Area plots (from left to right: Mach 1.0, 1.25, 1.50, 1.75, 2.0, 2.25 and 2.50).

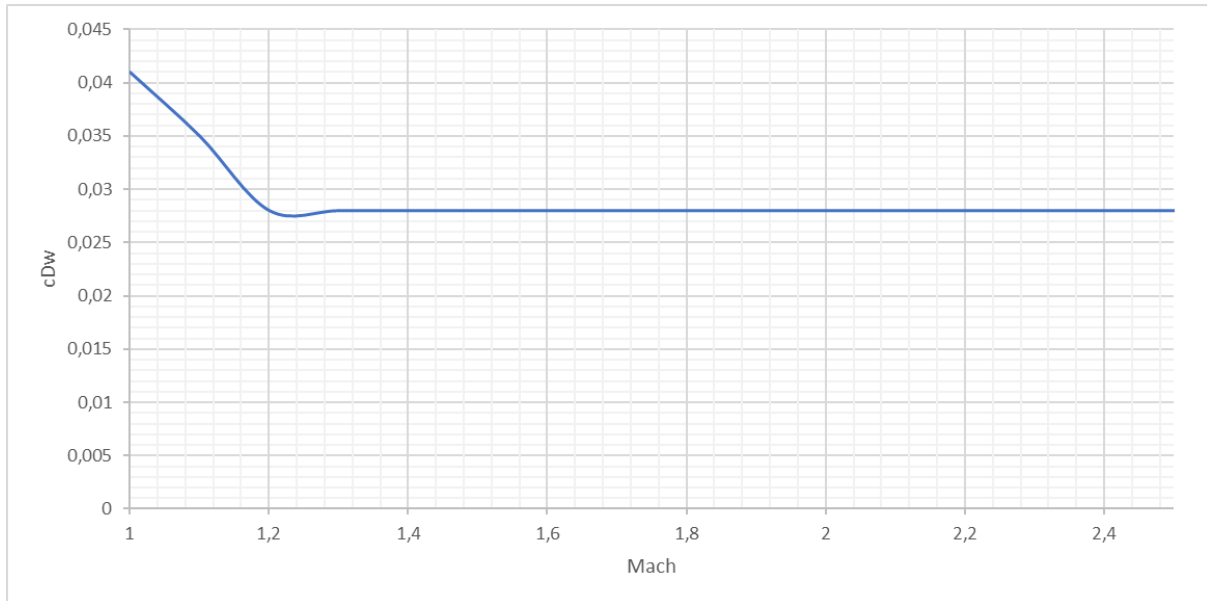


Fig. 131. Evolution of wave drag coefficient vs. Mach nº.

Figure 104 reveals Estadea to be on par in terms of wave drag coefficient with the F-4 Phantom and F-105 Thunderchief at low supersonic speeds, albeit showing a sharper decrease in wave drag at higher supersonic speeds. Further reduction could be achieved in the detailed design phase with more careful dimensioning.

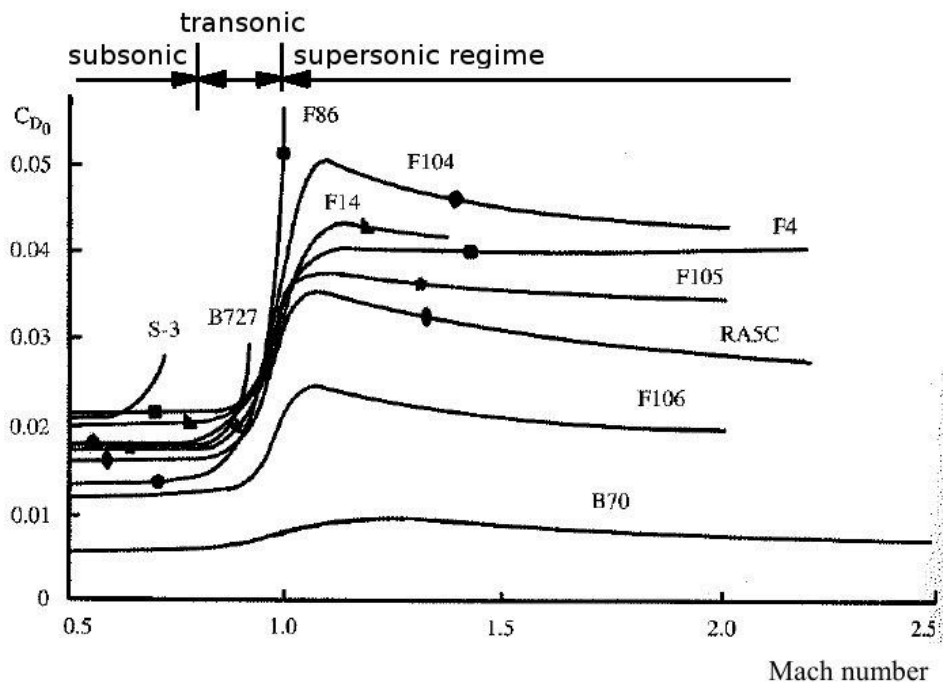


Fig. 132. Wave drag coefficient vs. Mach nº of several legacy fighters, courtesy of researchgate.net.

7.2. Subsonic Characteristics

In this section, using the same software and simplified 3D model, the general aerodynamic characteristics of Estadea will be analyzed (c_L vs. AoA, c_D vs. AoA, L/D vs. AoA, c_M vs AoA, etc.) in several cases, mainly: takeoff-landing, high-speed cruise and maximum maneuverability configuration. In all cases it is assumed the maximum deflection of the control surfaces is similar to the ones of the F-16 shown in Figure 60. In all cases Estadea will be analyzed in a broad range of AoA to determine post-stall behavior.

Control Surface	Deflection Angles
Ruddervators	-40/+40°
Flaperons	-20/+20°
Ailerons	-20/+20°
LE Flap	0/+25°
Nozzles	-20/+20°

Table 14: Control surfaces’ deflection angles.

OpenVSP’s results are not reliable at transonic speeds, therefore the subsonic analysis will be limited to low Mach numbers. All subsonic simulations were undertaken under the same basic settings:

- ISA+0, Sea Level Conditions: $\rho = 1.225 \frac{kg}{m^3}$; $T = 288.15 K$.

- Airspeed:

$$Mach\ 0.200 \Rightarrow v = 0.200 \cdot a = 0.200 \sqrt{287 \cdot 1.4 \cdot 288.15} = 68.05 \frac{m}{s}$$

- Reynolds Number: $Re = \frac{\rho v L}{\mu} (7.1) = \frac{1.225 \cdot 68.05 \cdot 9.6}{0.0000181206} = 4.42 \cdot 10^7$

7.3.1. c_L vs. AoA:

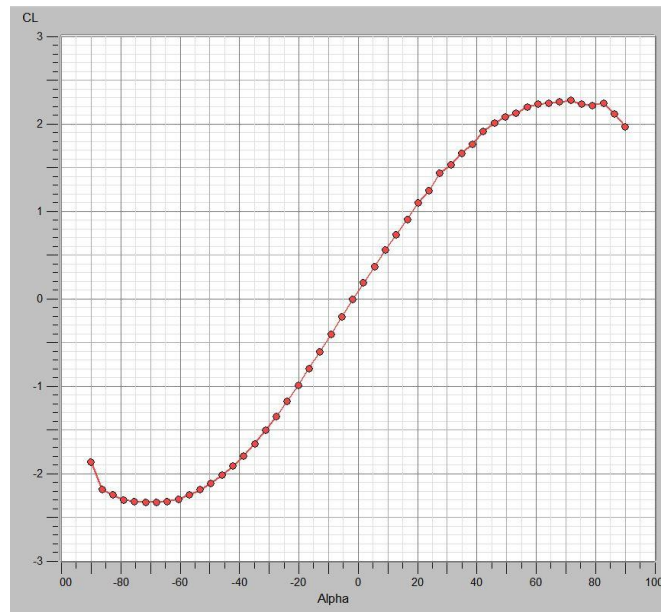


Fig. 133. c_L vs AoA, clean configuration, subsonic conditions.

By observing the curve the stall can easily be determined at around 70° of AoA for $c_{L_{max}} = 2.2$. Notice c_L is not 0 at 0° AoA due to the incorporation of the symmetrical NACA 64A204 as wing tip section and Estadea’s ability to fly inverted (as shown in the negative portion of the curve) thanks to the former. The incorporation of thin airfoils, a low aspect ratio wing and a LERX is reflected in the extremely large stall angle; this, however, is expected from aircraft of these characteristics, as shown in the following figure:

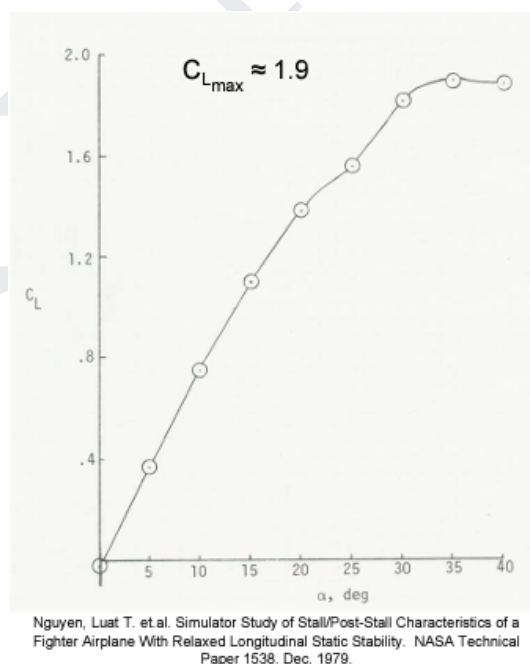


Fig. 134. F-16 clean configuration c_L vs. AoA curve, courtesy of NASA.

Notice the large stall angle in the F-16 and similar value for cL_{max} as Estadea. Although extremely useful in dogfights, these stall characteristics come as a disadvantage in the ground roll, where cL_{max} at takeoff and landing will be limited by the tailstrike angle. For a tailstrike angle of 22.5° , $cL_{max,ground} \simeq 1.1$. When deploying the LE flaps (15°) and flaperons (20°), although cL_{max} is shown to be unchanged, the slope in the pre-stall linear section of the curve increases, and $cL_{max,ground}$ is increased to around $cL_{max,ground} \simeq 1.5$, a 36% growth:

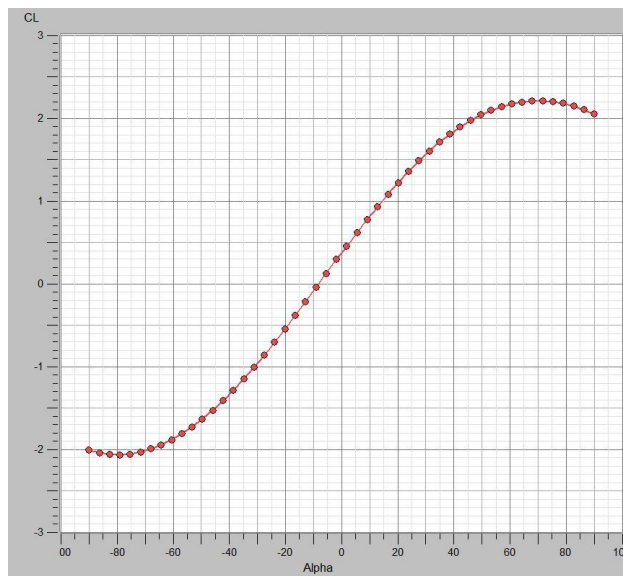


Fig. 135. cL vs. AoA, takeoff configuration.

Finally, in the maneuver configuration, in which only the LE flaps will be deployed (25°), a delay in stall is expected; as observed in the following curve, the stall angle is increased approximately 10° to a staggering 80° AoA:

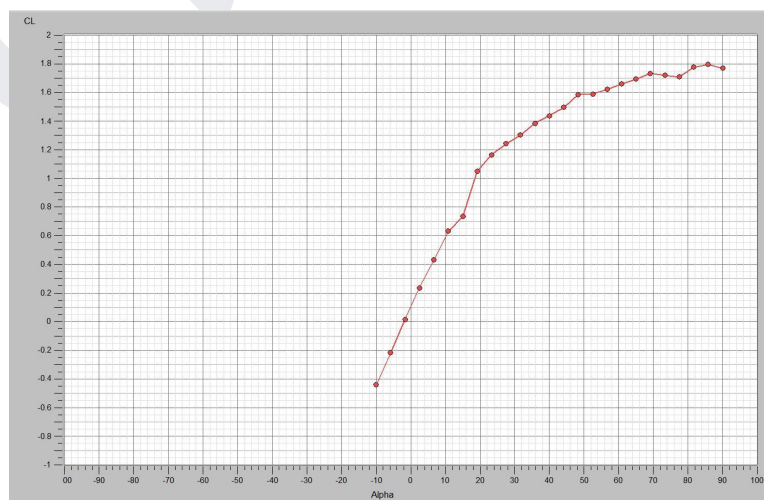


Fig. 136. cL vs. AoA, maneuver configuration.

7.3.2. c_L vs. c_{Dtot} :

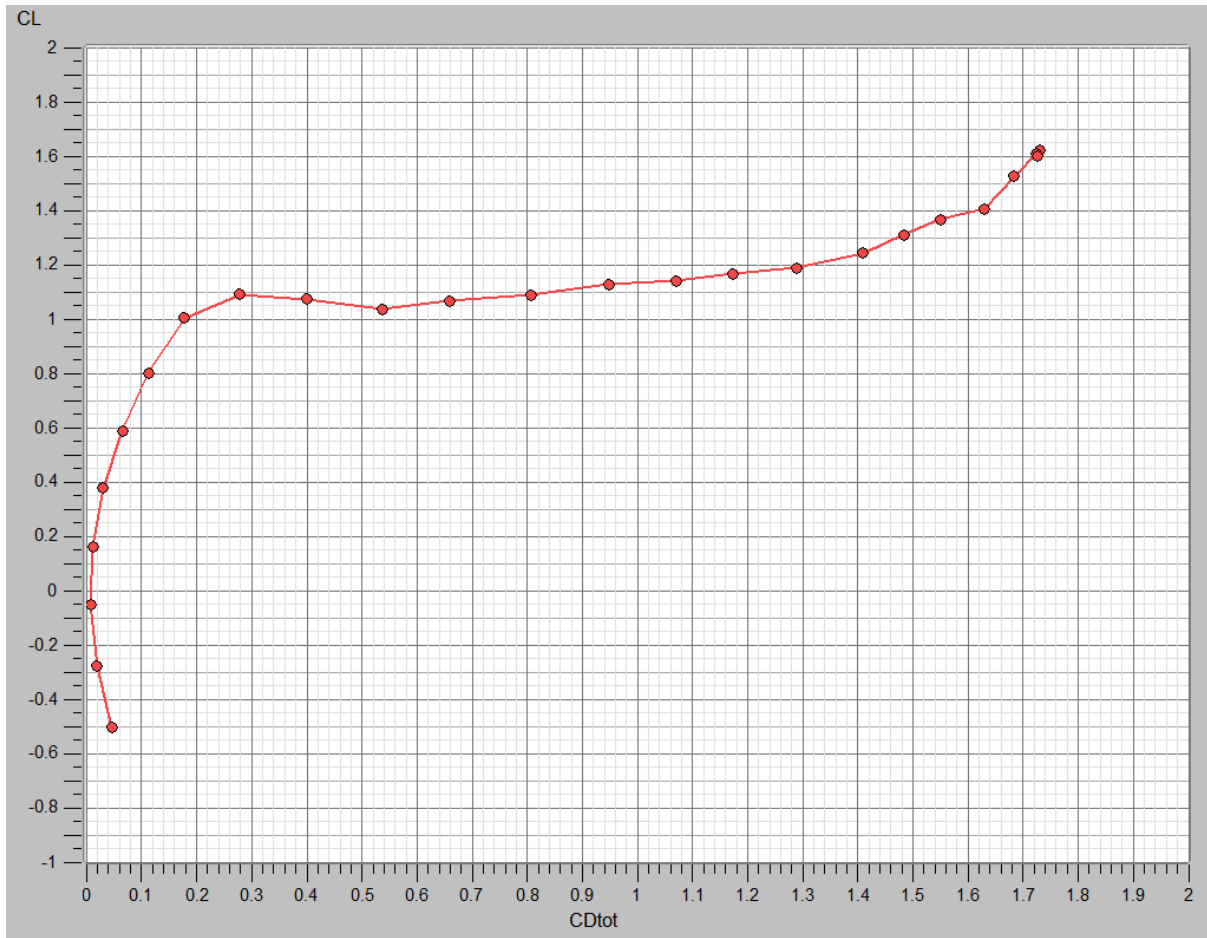


Fig. 137. Polar graph, clean configuration, subsonic conditions.

The smooth and sleek design of Estadea, necessary to ensure its stealth characteristics, has a major impact in its zero lift drag coefficient; as shown in the polar graph for the analysis settings $c_{D0} \approx 0.002$.

7.3.3. e vs. AoA:

Determining the Oswald Factor is crucial for the calculation of induced drag as part of the performance calculations in Chapter 9. The subsonic analysis reveals $e \approx 0.800$ for low angles of attack, quite impressive for a fighter.

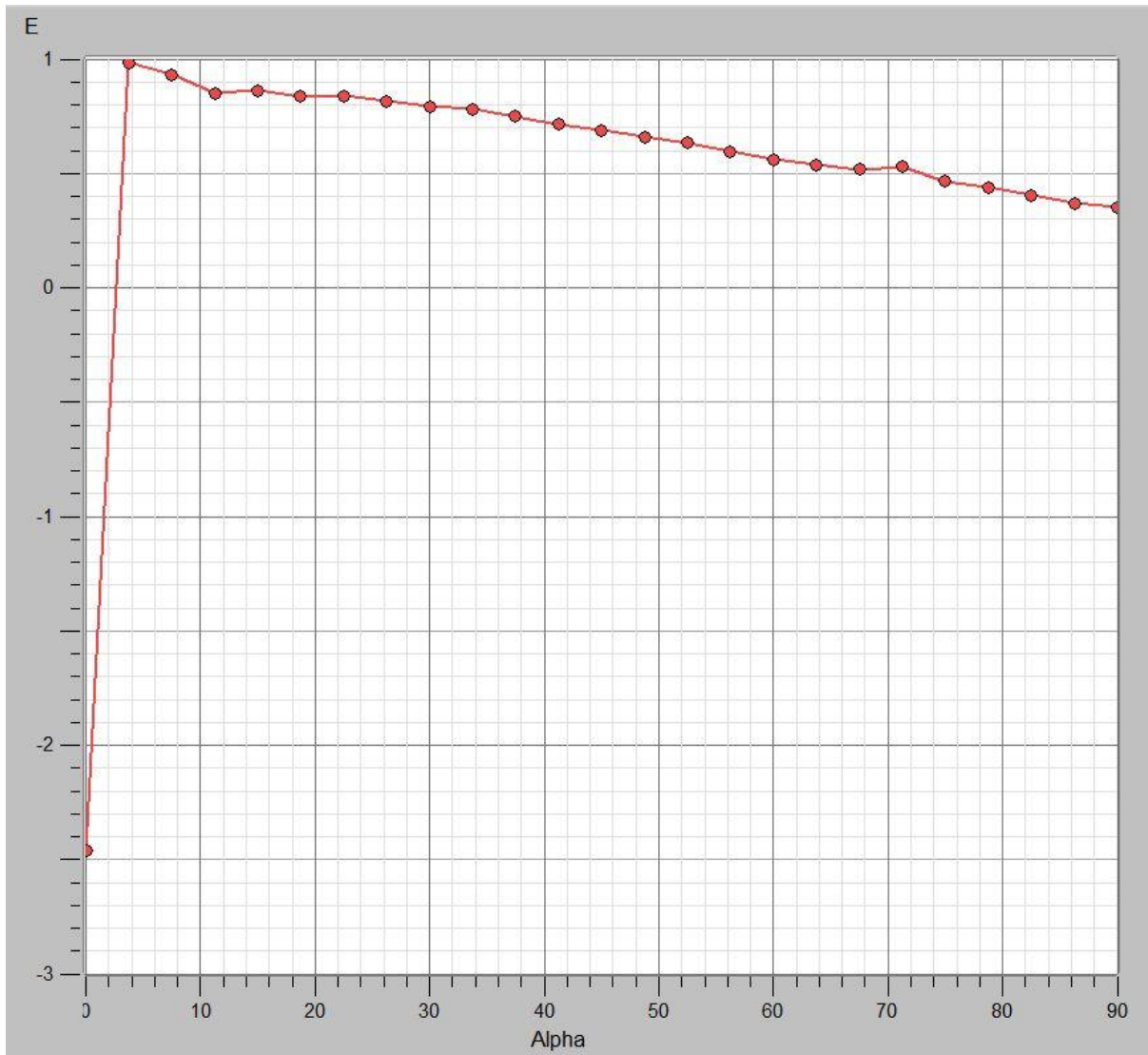


Fig. 138. Oswald Factor, subsonic conditions.

7.3.4. Load Distribution:

By analyzing the lift distribution over the wing the load distribution can be easily extrapolated. Notice in the following graph the effects of the negative twist angle on the lift distribution: the reduction of lift coefficient on the wing tips reduces the overall bending moment suffered by the wing and allows for optimal lift distribution over the span for maximum efficiency (elliptical distribution).

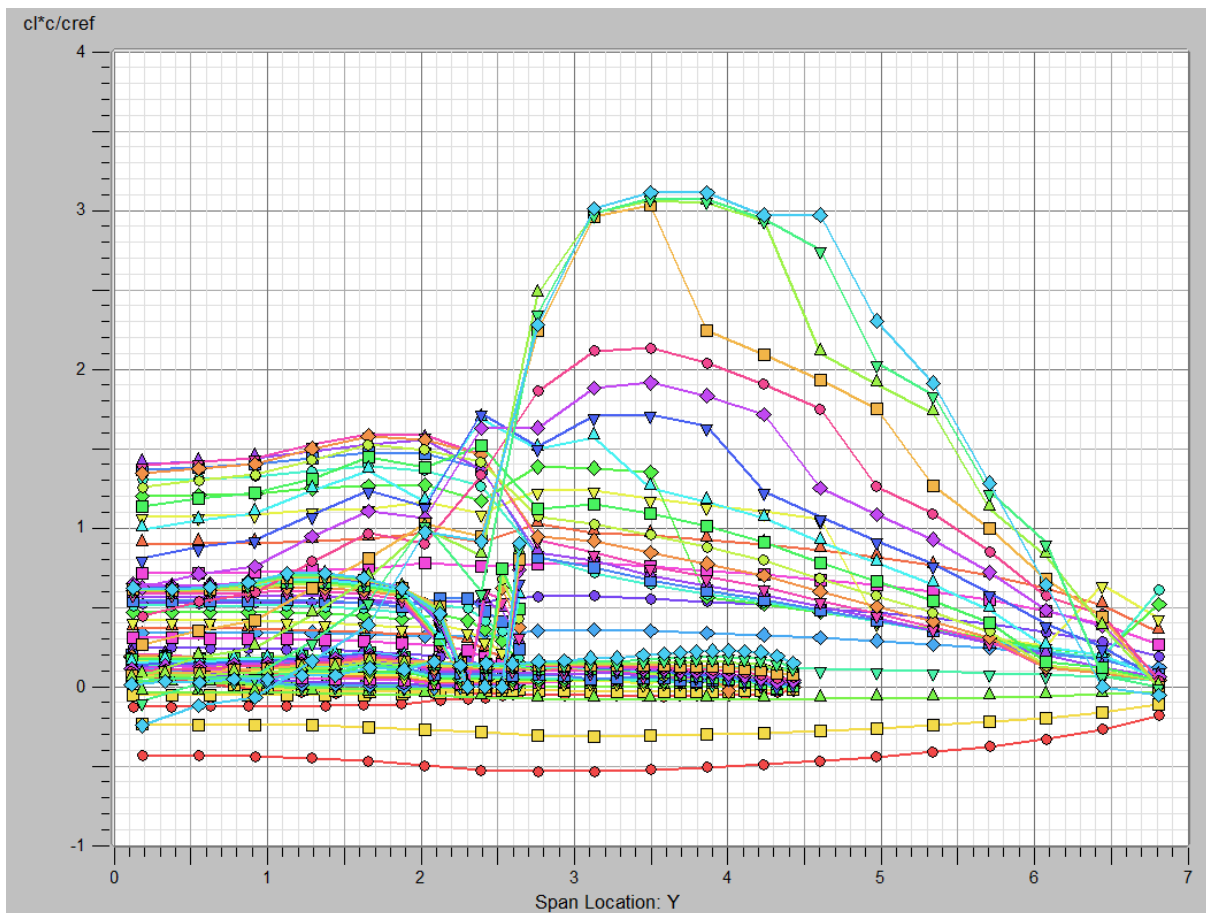


Fig. 139. Evolution of c_L distribution over the span with AoA, clean configuration.

7.3.5. L/D vs. AoA:

The primary information given by the evolution of aerodynamic efficiency (L/D) with AoA is the preferred flight angle of attack and maximum efficiency at subsonic conditions. As expected for a fighter and demonstrated in the graph, Estadea favors flight at low angles of attack (high-speed flight). At subsonic conditions $L/D_{max} = 14.0$, extremely impressive for a fighter.

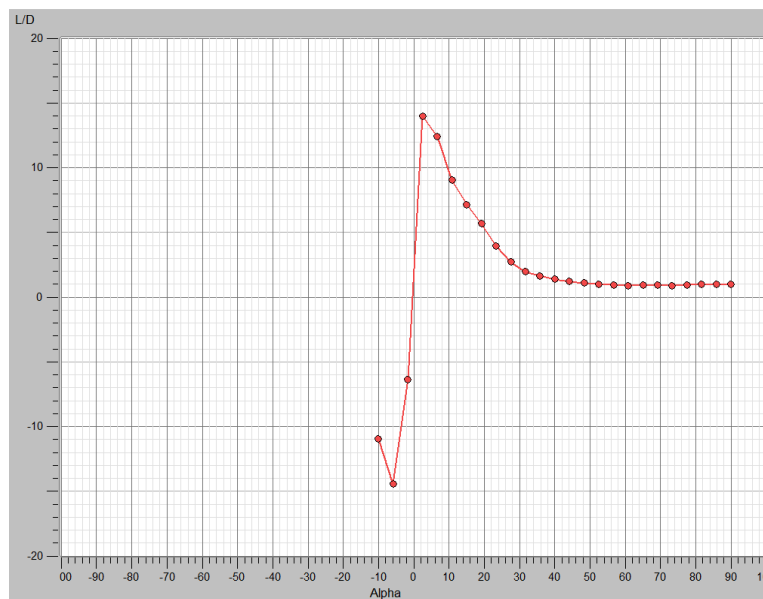


Fig. 140. L/D vs. AoA, clean configuration, subsonic conditions.

In the landing configuration, the higher lift generation produces an increase in lift induced drag, resulting in a 30% decrease in efficiency to $L/D_{max} = 9.9$; this is clearly reflected in the following figure:

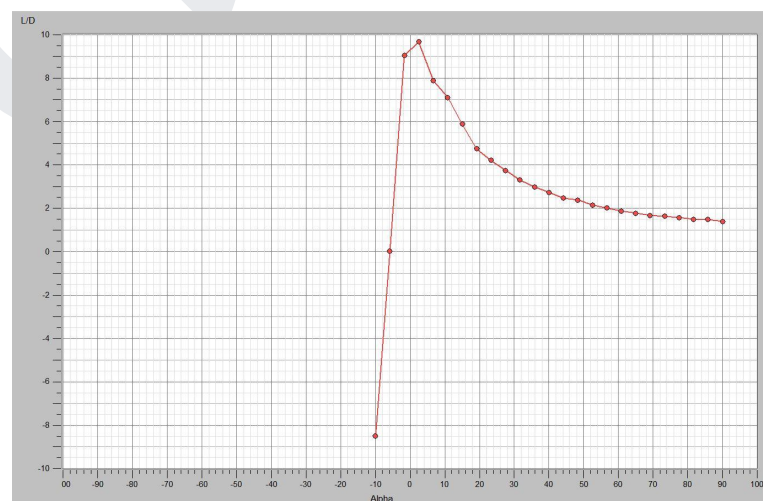


Fig. 141. L/D vs. AoA, takeoff configuration.

As the LE flaps only displace the lift curve to a higher stall angle, the effects on efficiency are negligible as demonstrated in the following graph:

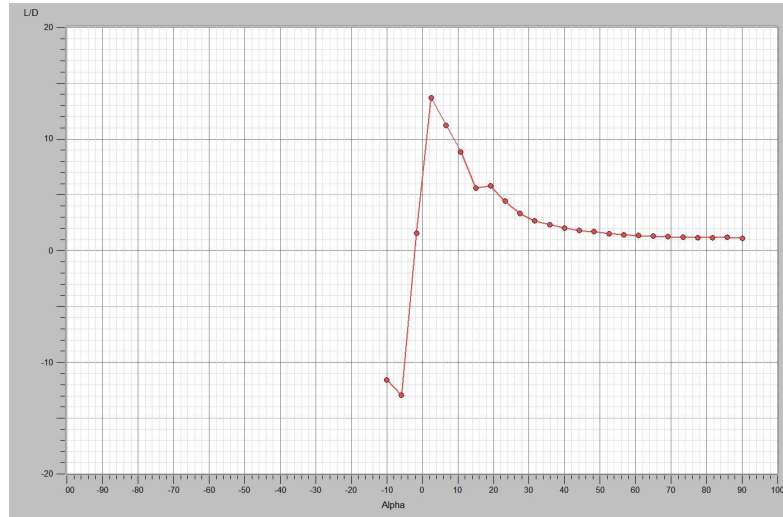


Fig. 142. L/D vs. AoA, maneuver configuration.

7.3.6. c_{M_y} vs. AoA:

The evolution of pitch moment coefficient with AoA describes the longitudinal static stability characteristics of Estadea for the reference CoG (in this case, $CoG = 10.274\text{ m}$ from the nose); these initial results will be used for the determination of the NP, MP and Fwd Limit. At the reference CoG, Estadea shows overall stable characteristics in the pitch axis:

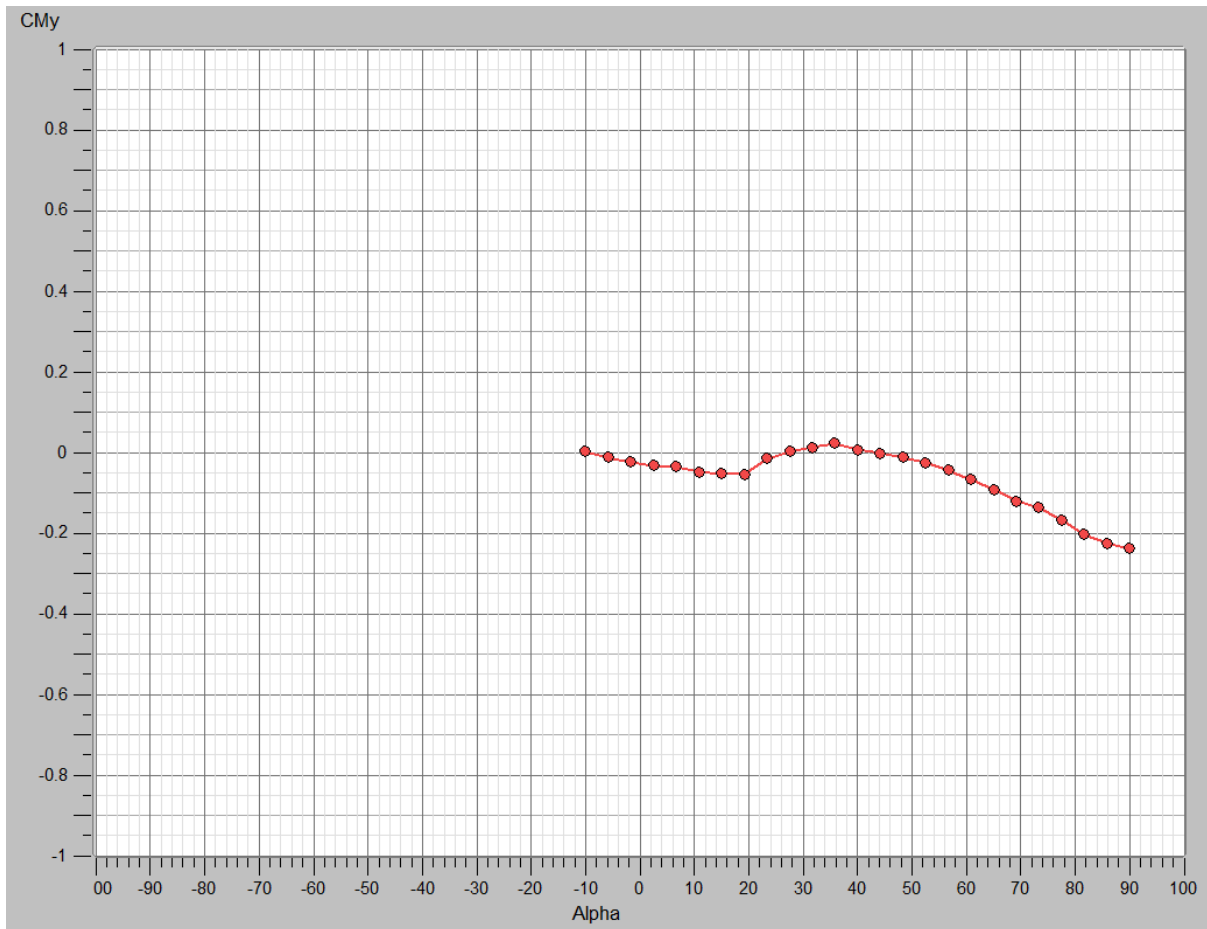


Fig. 143. c_{M_y} vs. AoA at $CoG=10.274\text{m}$, clean configuration, subsonic conditions.

By applying Equation 2.26, the NP can be easily calculated:

- $$\frac{l_{NP}}{c_w} = - \frac{\frac{dc_M}{d\alpha}}{\frac{dc_L}{d\alpha}} \Rightarrow X_{NP} = - 4.46 \frac{-0,0046}{0,056} + 10.274 = 10.64\text{ m}$$

from the nose. This is the ideal position for the CoG to ensure neutral static characteristics in pitch (“relaxed stability”) in order to greatly increase maneuverability.

7.3. Stability

7.4.1. Longitudinal Static & Dynamic Stability:

The MP and Fwd Limit will be interpolated through the evaluation of the evolution of wing and ruddervators pitch moments. For any position of the CoG, the ruddervators should counter the wing pitching moment to ensure controllability, specially at takeoff; a broad range for possible CoG locations will demonstrate, in principle, a correct sizing of the ruddervators for the selected wing planform.

- $M_{y, rudd.} = 2\left(\frac{1}{2}\rho v^2 c_{L, max, rudd.} S_{rudd.} \cos 40^\circ\right)(X_{AC, rudd.} - X_{CoG})(7.2)$; for a maximum deflection angle of $-40/+40^\circ$, $c_{L, max, rudd.} = 1.80$

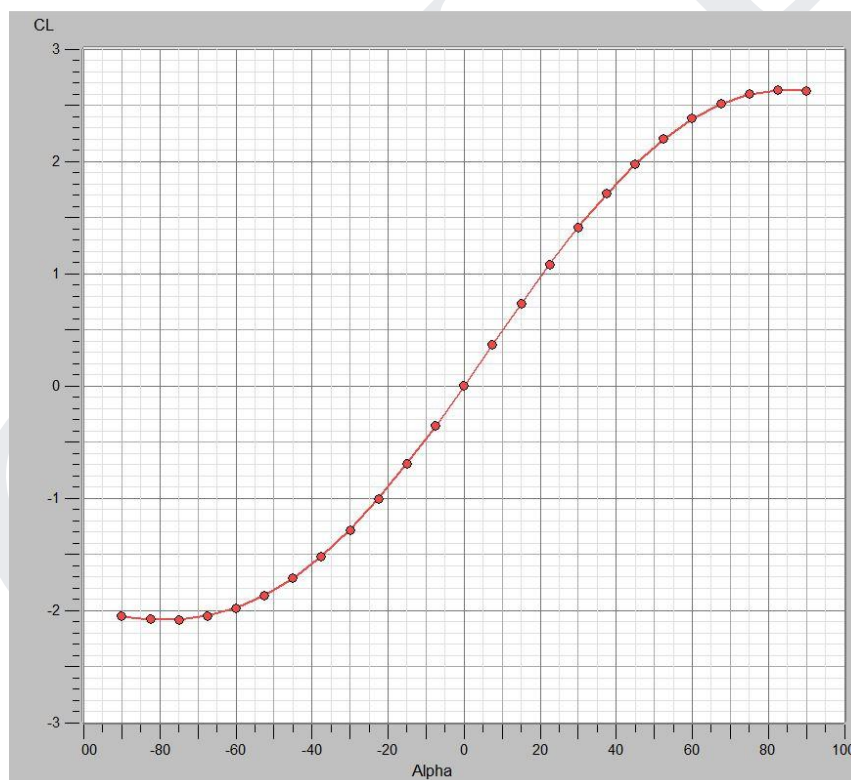


Fig. 144. Ruddervators cL vs. AoA, subsonic conditions.

- $M_{y, w} = \left(\frac{1}{2}\rho v^2 c_{L, max, w} S_w\right)(X_{AC, w.} - X_{CoG})(7.3)$. The wing pitching moment due to camber is assumed to be negligible.
- $M_{y, thrust} = T_{av.} \sin 20^\circ (X_{nozzle} - X_{CoG})(7.4)$

- Assuming the AC of both ruddervators and wing to be located at approximately 25.0% of their respective MAC, the absolute pitching moments can be easily calculated. For $v = 68.05 \frac{m}{s}$ at S.L., ISA+0 conditions.

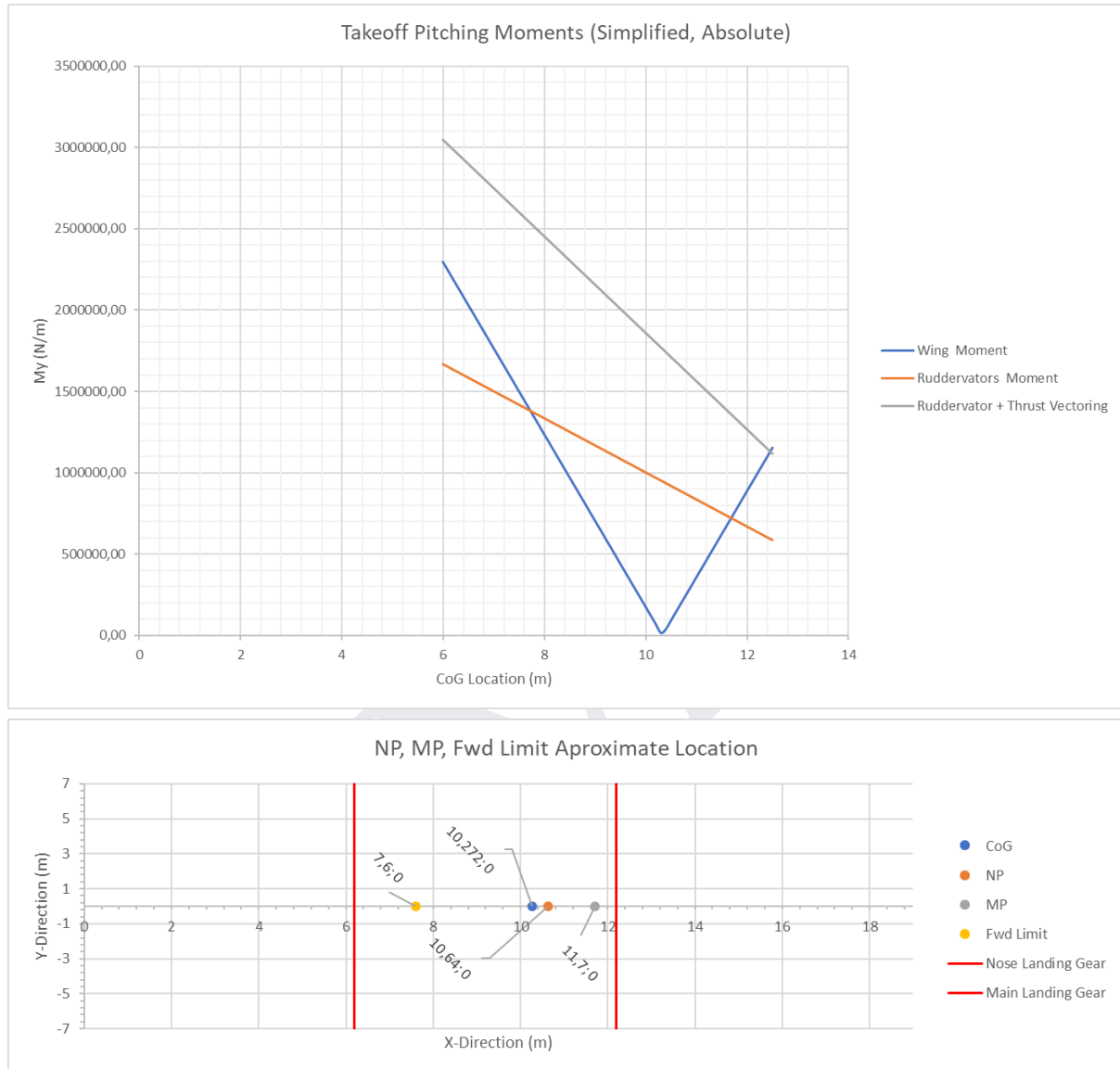


Fig. 145. NP, MP and Fwd Limit Determination, subsonic conditions.

From the previous results it is demonstrated that Estadea offers a wide CoG-envelope (5.8 m range for CoG location!) and that even in the most extreme of cases, when the CoG is located at the Fwd Limit or MP, the CoG never lies outside the landing gear support. Thrust vectoring offers an additional layer of safety by ensuring control even in the most extreme of cases. By correlation, if the CoG is positioned on the preferred locations, that is, between 10.640 and 12.0 m, Estadea will be dynamically neutral or unstable in pitch, respectively.

7.4.2. Normal Static Stability:

The condition for normal static stability is:

$$\frac{dc_{M,z}}{d\beta} > 0 \quad (7.5)$$

Where β is the sideslip angle. In the case of Estadea, the main source of normal static stability are the ruddervators. By inducing a sideslip angle at 0° AoA, this condition can be easily analyzed in Estadea. Due to the positioning of the ruddervators with respect to the CoG; even at the MP, it is expected that the aircraft is statically stable in the normal axis.

When $X_{CoG} = 11.7 \text{ m}$ (MP) at 0° AoA:

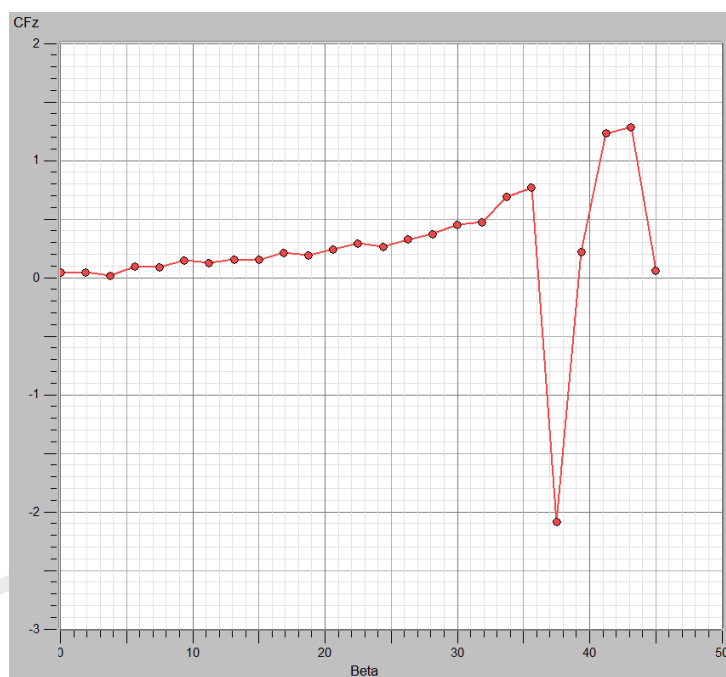


Fig. 146. cF_z vs. Beta at 0° AoA, clean configuration, subsonic conditions.

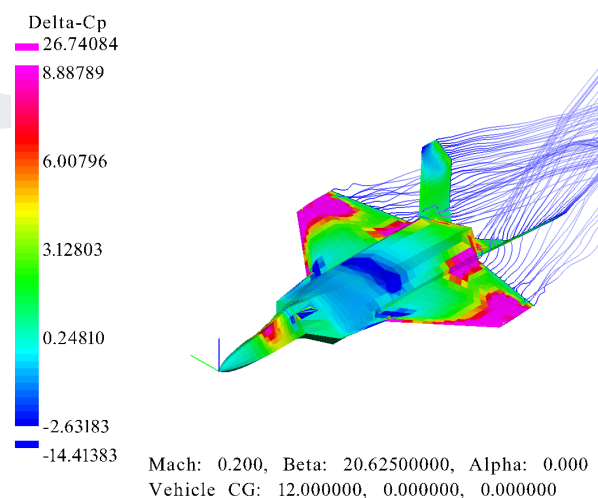


Fig. 147. Pressure contour at $\beta = 20.625^\circ$, 0° AoA, clean configuration, subsonic conditions.

Notice how the overall force exerted by the ruddervators in the normal axis (cF_z) increases as the sideslip angle increases (except for a couple outliers which can be condoned as calculation errors), meaning the condition for normal static stability is satisfied.

7.4.3. Lateral Static Stability:

The condition for lateral static stability is:

$$\frac{dc_{M,x}}{d\beta} < 0 \quad (7.6)$$

Since the CoG is aligned vertically with the wing, which does not have dihedral, and the ruddervators do not need produce lift when $X_{CoG} = 10.640 \equiv NP$ (no trim moment needed), it is expected that the aircraft is statically neutral in the lateral axis. When $X_{CoG} = 10.640 \equiv NP$ at 0° AoA:

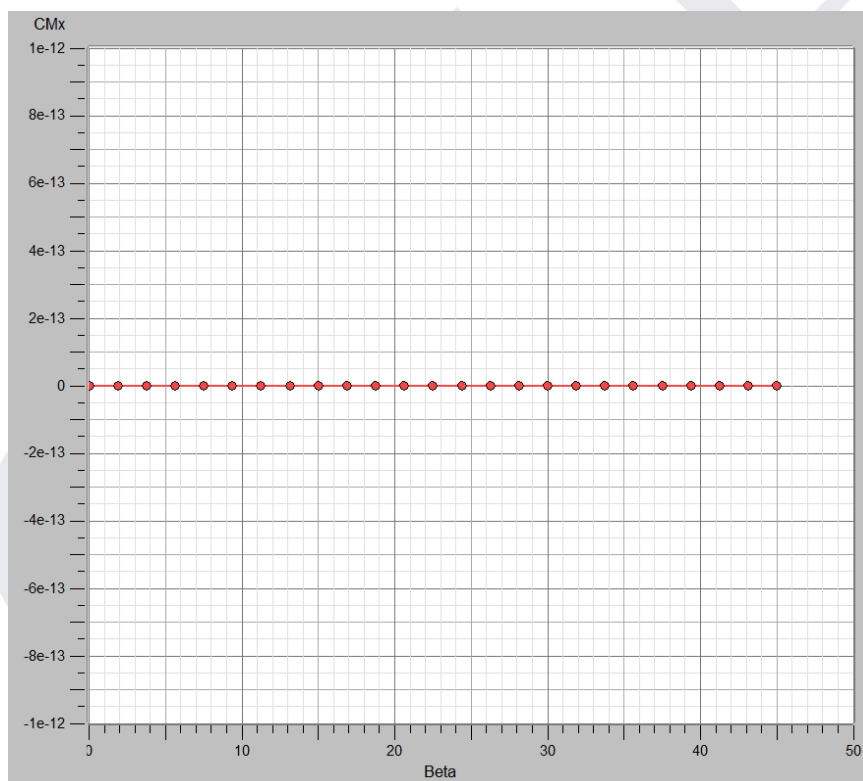


Fig. 148. cM_x vs. Beta at 0° AoA, clean configuration, subsonic conditions.

Notice how the moment exerted by the aircraft in the lateral axis (cM_x) remains constant at 0 as the sideslip angle increases, meaning the condition for lateral neutral stability is satisfied. By correlation, Estadea will be dynamically neutral in roll.

7.4. Supersonic Characteristics

The primary interest of this section is to determine how supersonic flow conditions affect Estadea’s performance. OpenVSP’s results are not reliable at transonic speeds, therefore the supersonic analysis will be limited to high Mach numbers. All supersonic simulations were undertaken under the same basic settings:

- ISA+0, $h = 10,000 \text{ m}$: $\rho = 0.413 \frac{\text{kg}}{\text{m}^3}$; $T = 223.15 \text{ K}$.
- Airspeed: $Mach\ 2.0 \Rightarrow v = 2a = 2\sqrt{287 \cdot 1.4 \cdot 223.15} = 598.87 \frac{\text{m}}{\text{s}}$
- Reynolds Number: $Re = \frac{\rho v L}{\mu} = \frac{0.413 \cdot 598.97 \cdot 9.6}{0.0000146884} = 1.62 \cdot 10^8$
- Clean Configuration.

7.4.1. c_L vs. AoA:

At supersonic conditions, $c_{L,max} = 1.1$, a 50% decrease with respect to the subsonic regime; the stall angle also drops to 35° AoA, a 50% decrease with respect to the subsonic regime. It is of paramount importance if this drop in lift coefficient will result in Estadea stalling at high speeds; this will be determined in the next sections. It is important to note that both wing and ruddervators experience a loss in lift generation which may impose further limitations in the CoG location; therefore, both wing and ruddervator will be analyzed separately and individually with the fuselage at different Mach and increasing Reynolds numbers.

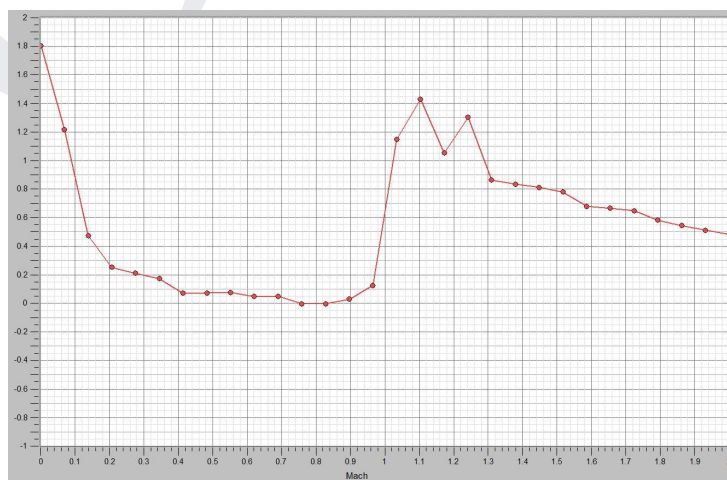


Fig. 149. Ruddervators $c_{L,max}$ evolution at different Mach (ignore transonic speeds).

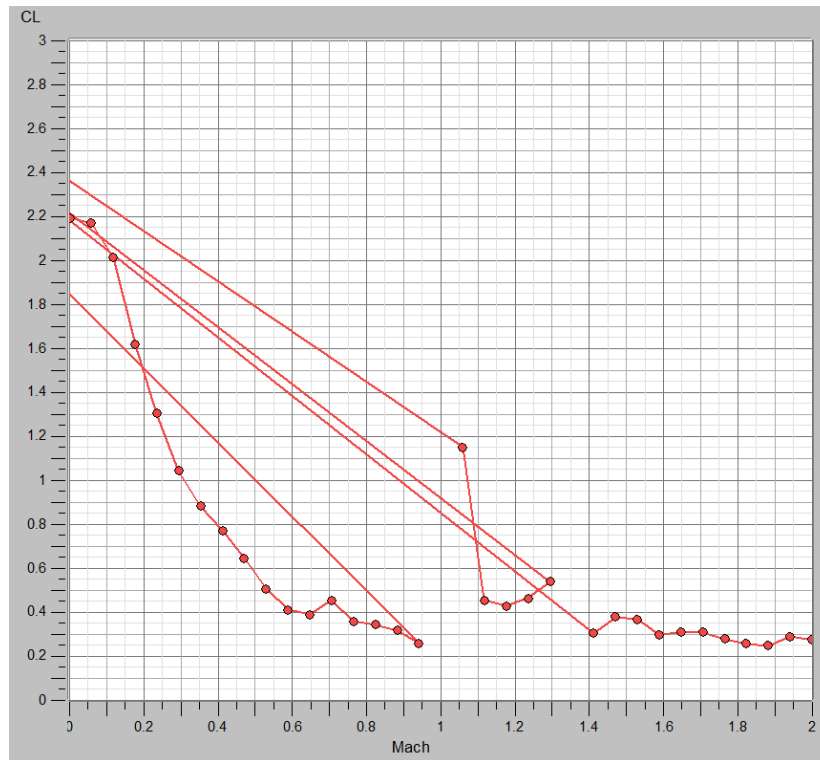


Fig. 150. Wing $c_{L,max}$ evolution at different Mach (ignore transonic speeds).

Notice in the previous a drop of 72% for the ruddervators and 86% for the wings; since the wings experience a higher loss in $c_{L,max}$ controllability can be assumed to be assured for supersonic speeds with the current CoG limits.

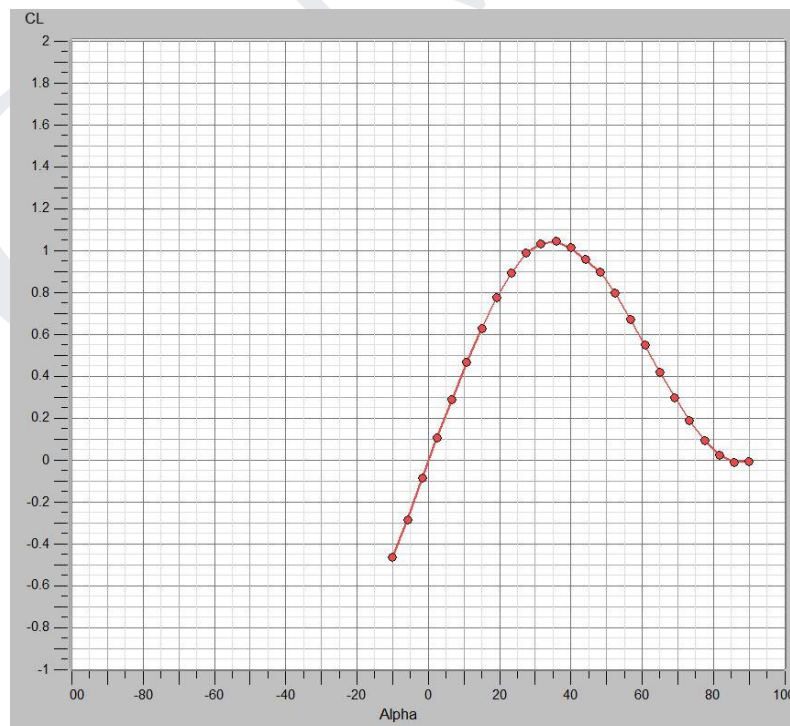


Fig. 151. c_L vs. AoA, clean configuration, supersonic conditions.

7.4.2. e vs. AoA:

A decrease in the Oswald factor is expected at supersonic speeds which in turn will increase induced drag and decrease the overall efficiency of the aircraft. This decrease must be accounted for in all aerodynamic computations.

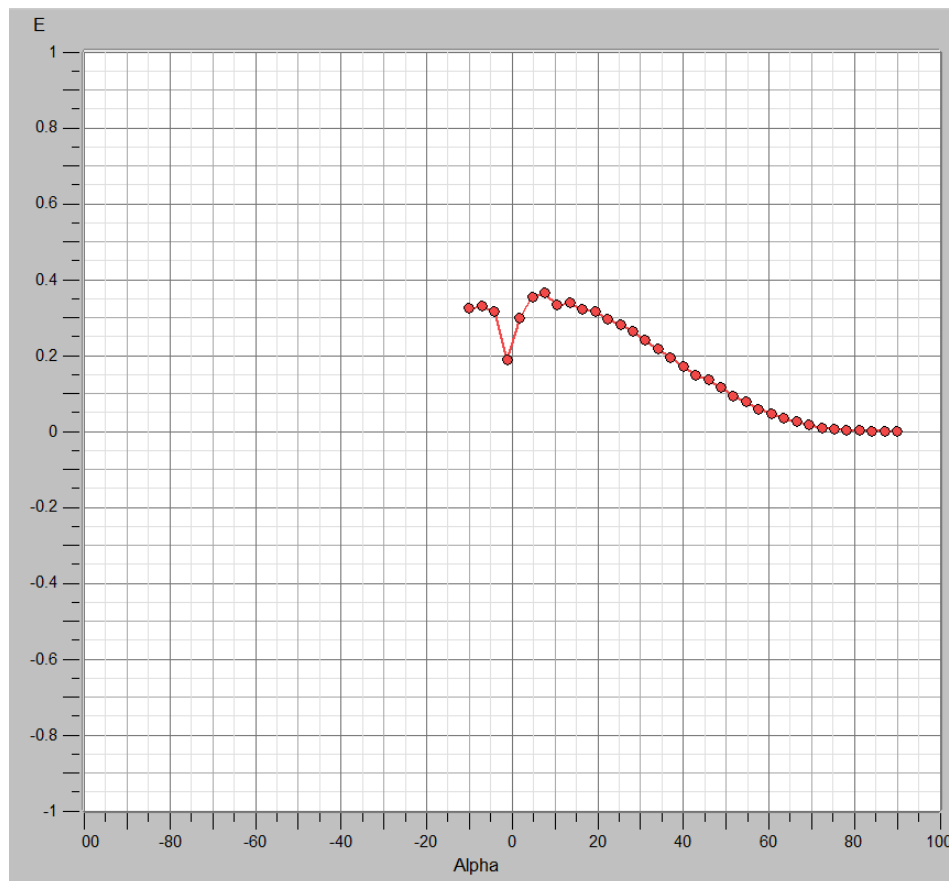


Fig. 152. e vs. AoA, clean configuration, supersonic conditions.

From the previous figure, it can be observed that the Oswald factor drops to $e = 0.350$ at low AoA, a 56% drop.

7.4.3. L/D vs. AoA:

The decrease in the Oswald factor decreases the overall efficiency of the aircraft to $L/D_{max} = 8.9$ as noted in the following figure:

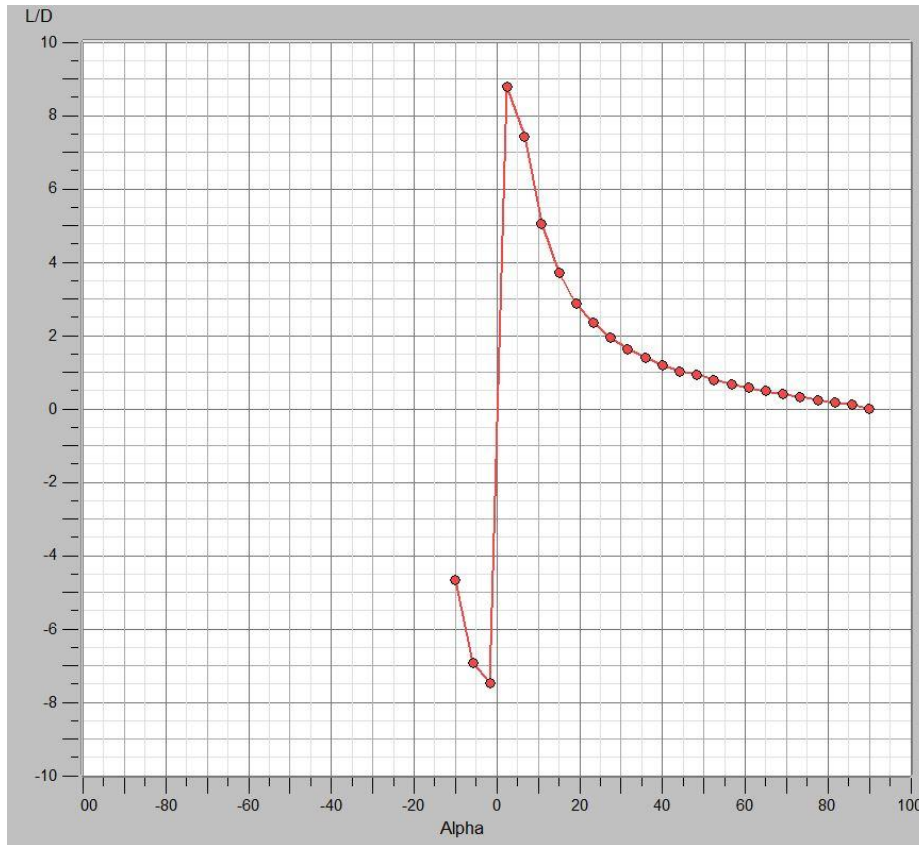


Fig. 153. L/D vs. AoA, clean configuration, supersonic conditions.

However, as OpenVSP does not include wave drag in its aerodynamic computations, the real L/D of the aircraft at supersonic conditions is bound to be much lower, as it will be seen in the following sections.

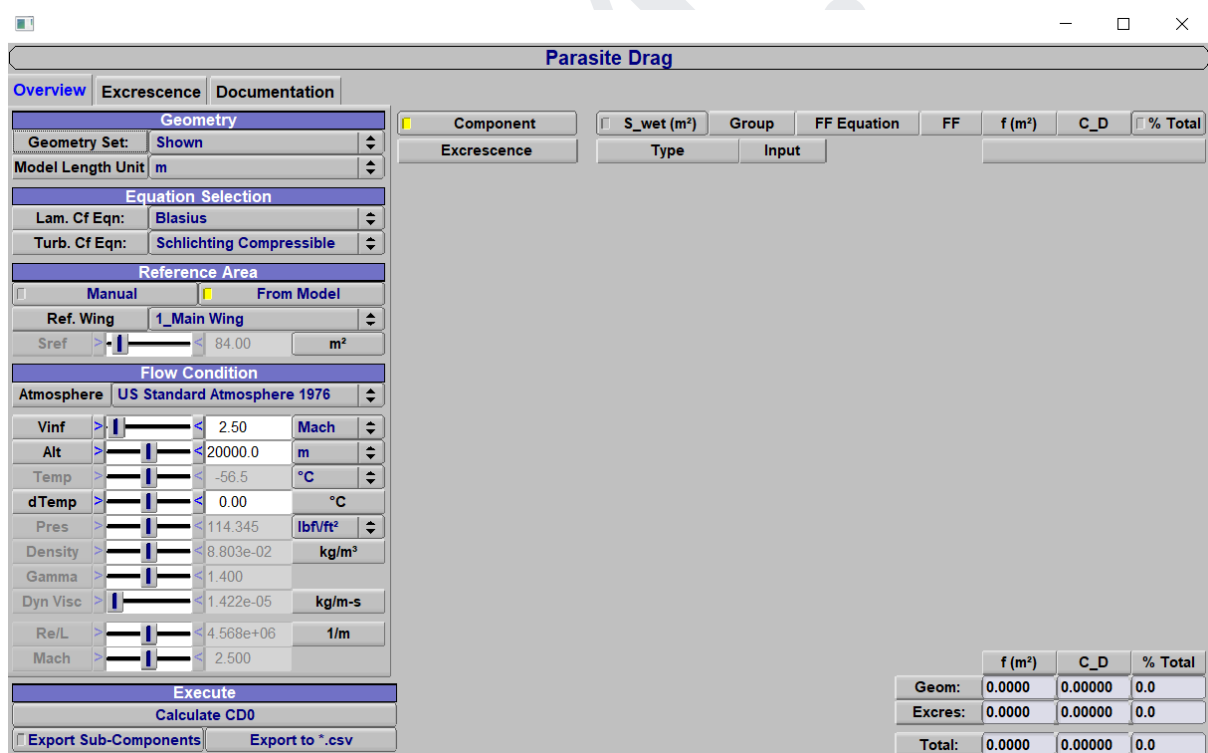
7.5. Total Drag Coefficient vs. Airspeed (Steady and Level Flight)

All performance computations, unless otherwise indicated, will be performed on and for a steady and level flight, at ISA+0 conditions, combat weight and clean configuration assuming the CoG to be located at the NP, therefore the ruddervators do not generate lift; the conditions for a steady and level flight are the following:

$$L = W \quad (7.7)$$

$$T = D \quad (7.8)$$

Three reference altitudes have been chosen for the analysis: 0, 10,000 and 20,000 m. In the total drag coefficient calculation the reduction in Oswald factor and the wave drag coefficient must be accounted for. The total drag includes the parasite drag, lift induced drag (refer to equation 2.20) and wave drag when applicable. Starting with the parasite drag coefficient, which is a function of temperature and speed, it can be easily calculated through OpenVSP in the “Parasite Drag” tab.



	f (m²)	C_D	% Total
Geom:	0.0000	0.00000	0.0
Excres:	0.0000	0.00000	0.0
Total:	0.0000	0.00000	0.0

Fig. 154. OpenVSP parasite drag tab.

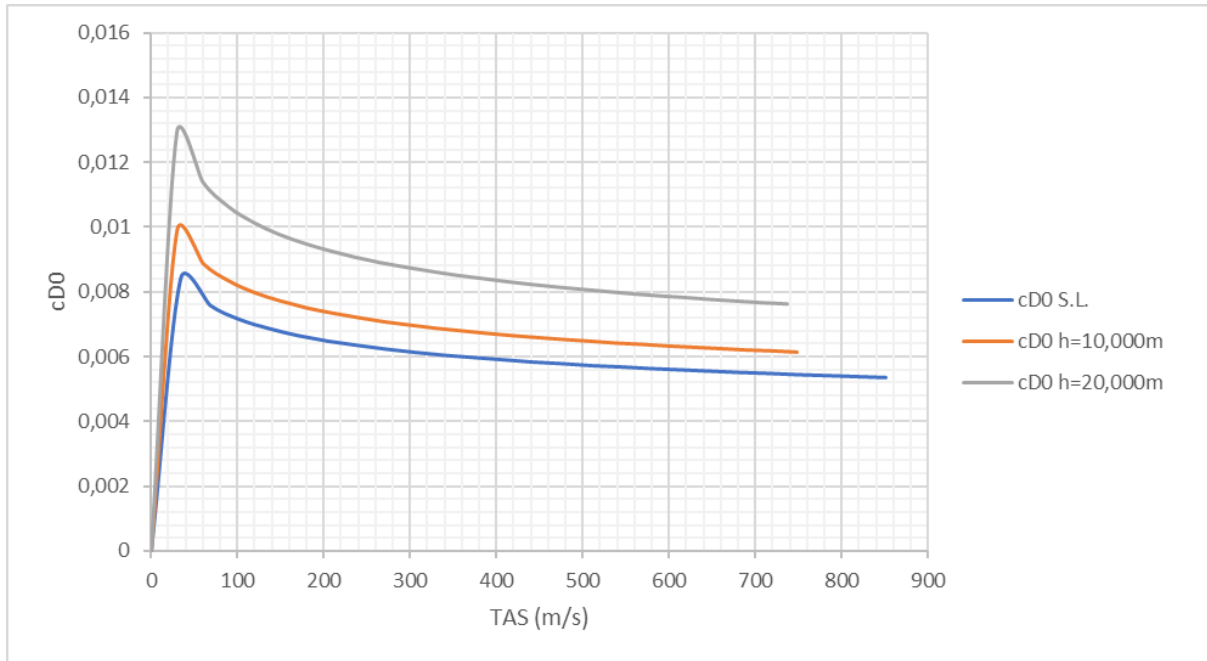


Fig. 155. Parasite drag evolution with airspeed and altitude, clean configuration.

Notice that as altitude increases, the drop in density and temperature (lower Reynolds numbers) increases the parasite drag coefficient.

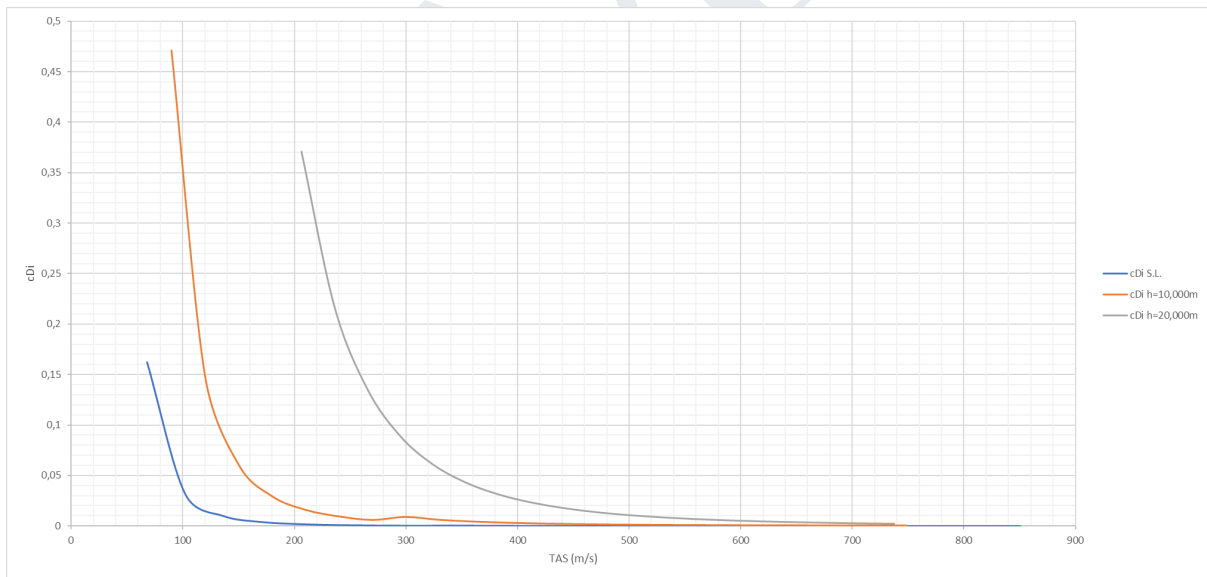


Fig. 156. Lift induced drag evolution with airspeed and altitude at combat weight.

Notice how lift induced drag, even when accounting for the reduction in the Oswald factor, is barely affected at any altitude as is greatly reduced at high speeds due to the lower c_L required for steady and level flight. Adding the previous results to the wave drag renders the total wave drag coefficient at different altitudes and airspeeds.

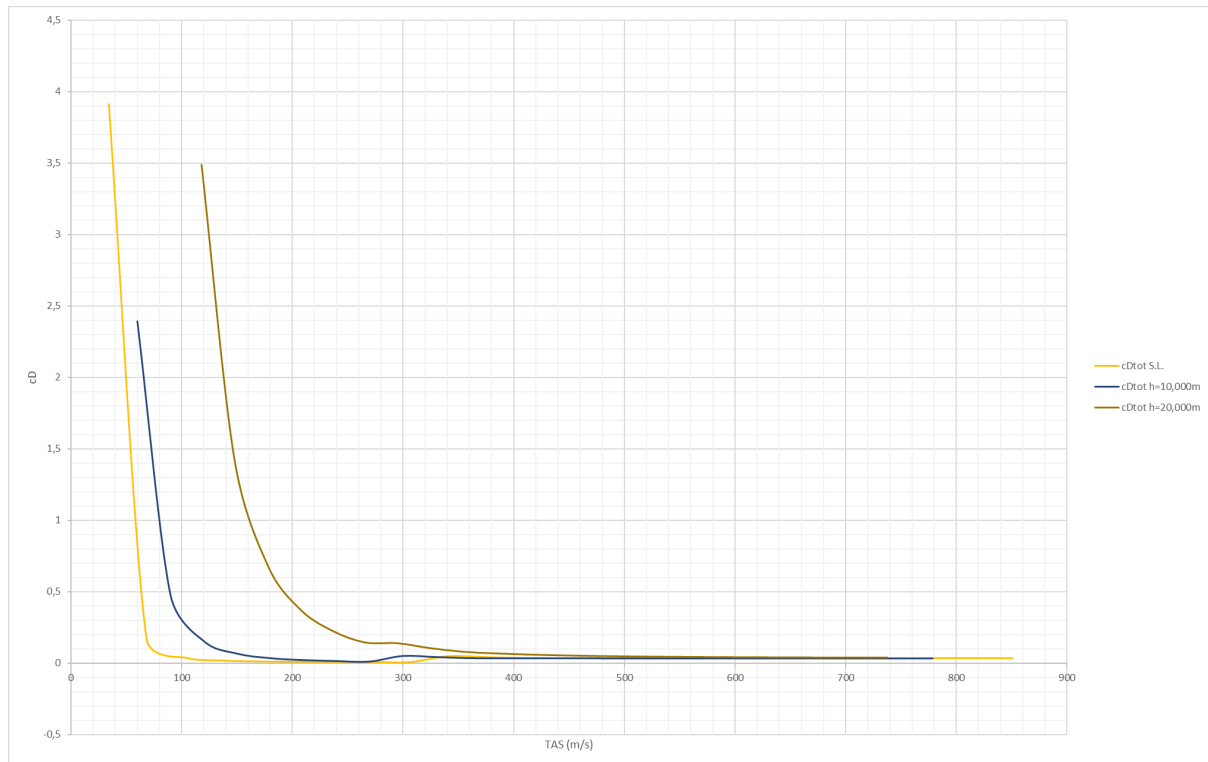


Fig. 157. Total drag evolution with airspeed and altitude at combat weight, clean configuration.

As expected, the highest drag coefficients are given at low airspeeds (high induced drag), and it increases slightly at sonic speeds, where the wave drag is not negligible.

7.6. c_L Requirements and Stall Speed (Steady and Level Flight)

From the equation of lift, the lift coefficient for steady and level flight can be easily calculated:

$$L = W = \frac{1}{2} \rho v^2 c_L S_w \Rightarrow c_L = \frac{2W}{\rho v^2 S_w} \quad (7.9)$$

Refer to equation 2.21 for the stall speed. Again, three reference altitudes will be analyzed (0, 10,000 and 20,000 m) for the c_L requirements whereas stall speed will be shown as a function of altitude. For the c_L requirements the most restrictive case will be used (MTOW) whereas stall will be calculated at ISA+0, ISA+30 and ISA-30 for the most and least restrictive weight configurations (MTOW and combat weight, respectively).

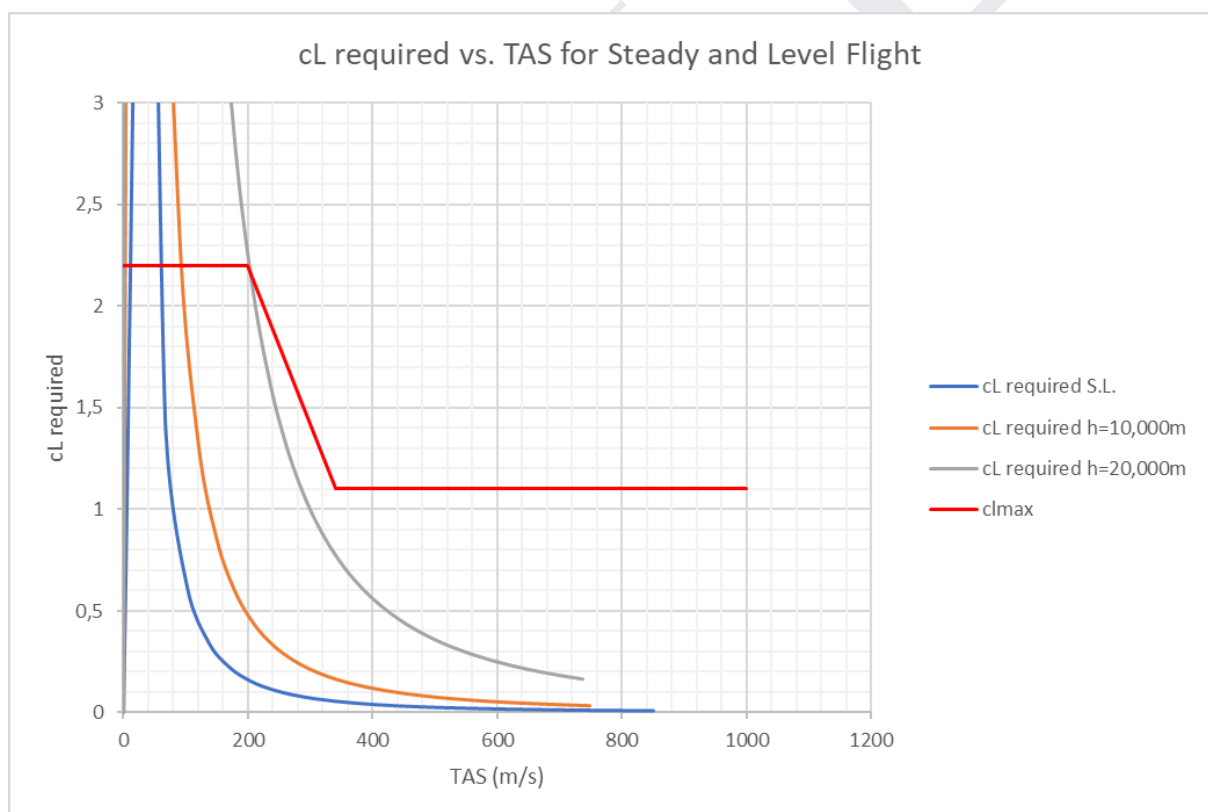


Fig. 158. c_L required evolution. airspeed at MTOW.

Notice from the previous figure how even in the most restrictive case Estadea will not stall unexpectedly at high speeds. The intersection between the $c_{L,max}$ and the c_L required corresponds to the stall speeds at this weight configuration for the respective altitude, notice how stall speed increases with altitude due to the decrease in air density.

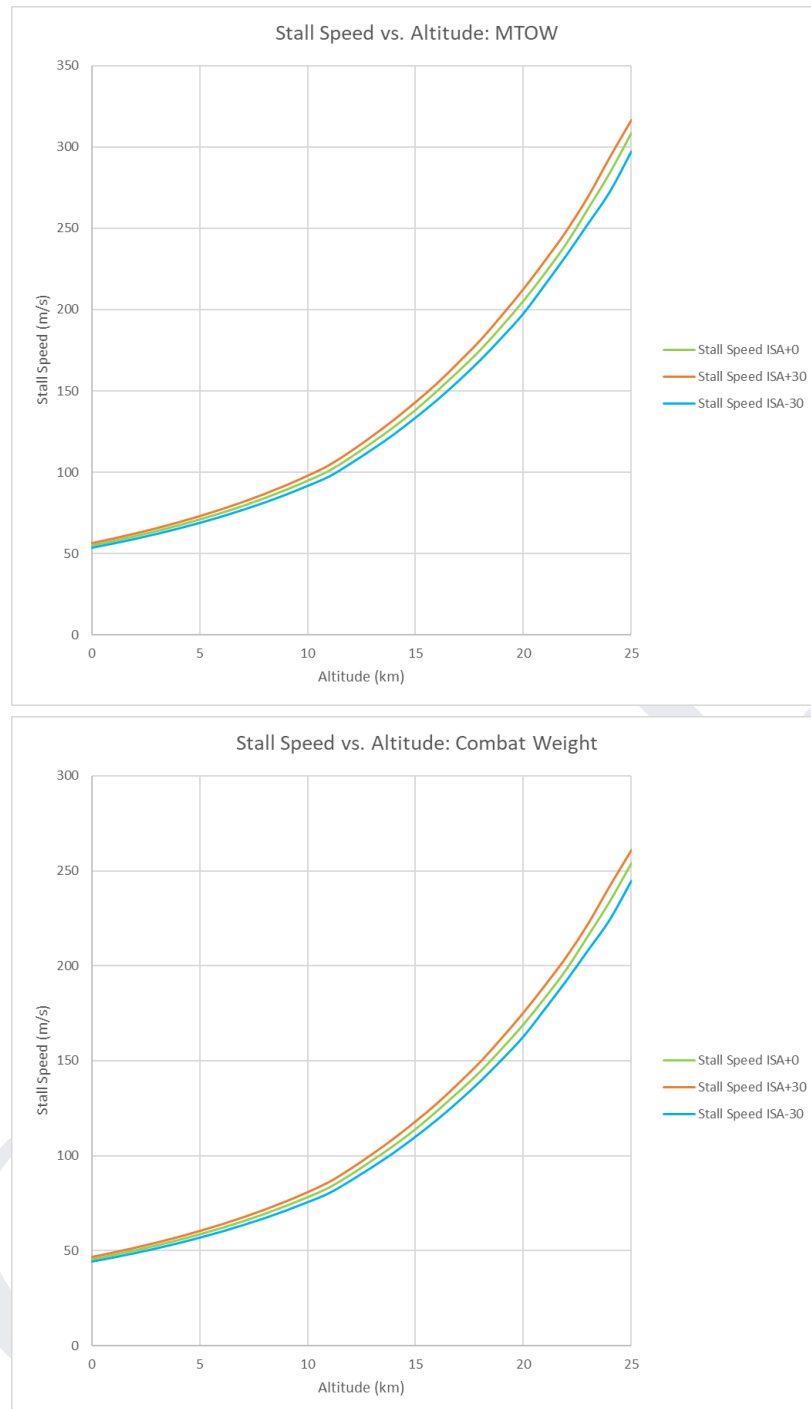


Fig. 159. Stall speed evolution with weight, altitude and temperature.

Notice the effects on temperature in stall speed (the lower the temperature, the higher the air density and consequently stall speed will be lower) and altitude (the higher Estadea flies, the lower the density of the surrounding air and therefore stall speed will be higher). Other intermediate weight configurations' stall speed (air patrol and ferry) falls in between the aforementioned.

7.7. Thrust Required vs. Airspeed (Steady and Level Flight)

In a steady and level flight, the thrust required for any given velocity and flight level is given by the total drag at those conditions. By comparing the available thrust and the required thrust, three main variables can be inferred: the minimum drag velocity, given when total drag force is at its minimum; the maximum velocity, given when thrust available and thrust required are similar; and finally the supercruise capabilities, meaning when the thrust required is lower than the available military thrust (no afterburner) at supersonic speeds.

In this case, it is convenient to choose the least restrictive case possible to determine the best capabilities of Estadea; therefore, the combat weight and a clean configuration will be used. The evaluation will take place at the three previous reference altitudes (0, 10,000 and 20,000 m) at ISA+0 conditions. To calculate the required thrust at steady and level flight, it is as simple as dividing the weight by the aerodynamic efficiency:

$$T_R = \frac{W}{\frac{L}{D}} = \frac{W}{\frac{c_l}{c_d}} \quad (7.10)$$

Notice that the thrust available does not take into account the loss of thrust when exceeding the inlet design mach number; therefore, the maximum velocities will be lower than shown in the following figure; it is assumed that the engines cannot exceed more than an extra 0.3 Mach from its design inlet Mach number to a maximum of Mach 2.5. On another note, surface heating limitations must be taken into account, specially at low altitudes; therefore, Estadea will be limited to Mach 1.2 at lower altitudes (5.0 km or lower), similarly to the Lockheed Martin F-22 (an aircraft of comparable size and configuration) even though it is capable of much higher speeds at these altitudes as it will be seen shortly.

The results for the reference altitudes where the following:

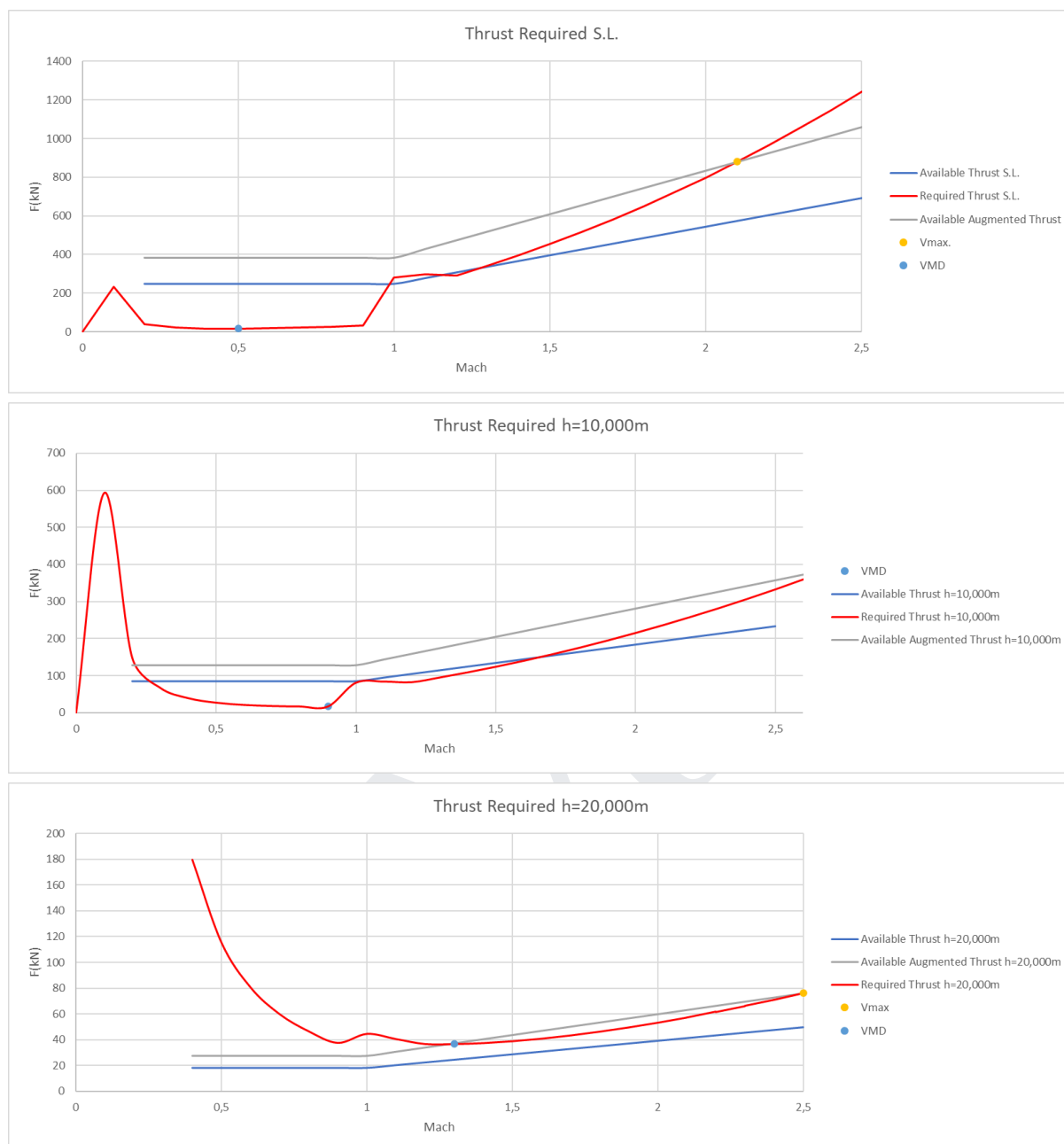


Fig. 160. Thrust required and thrust available vs. airspeed.

Notice how the reduction in available thrust and the increase in stall speed at higher altitudes requires flying faster to maintain steady and level flight. At combat weight Estadea can reach up to Mach 2.1 at S.L. and Mach 2.5 at altitude, while being able to supercruise up to Mach 1.6 at altitude. The minimum drag velocity increases as well from Mach 0.5 at S.L. to Mach 0.9 at 10,000 m and 1.2 at 20,000 m. The calculations show that even at 20,000 m Estadea can reach higher altitudes thanks to its incredibly powerful F-135 engines and sleek design.



(This page has been intentionally left blank)

G.M.L.

Chapter 8. STRUCTURAL DESIGN PROPOSITION

8.1. Wing

In order to ensure the structural integrity of the wing at high G maneuvers, a converging, multi-spar structure was chosen as the basis for the wing. This type of structure is quite typical in modern fighters as seen in the following figure:



Fig. 161. F-35 wing structure, courtesy of Lockheed Martin.

Asides from the multiple spars used to provide the sufficient bending stiffness for a wing of relatively small thickness, ribs are included to support the skin against buckling. Ribs also form a convenient structure onto which to introduce concentrated loads in the form of external weapon stores or drop tanks; therefore, these will mark the location to which the external missile pylons and fuel drop tanks will be attached. The skin itself provides the necessary torsional stiffness. These types of structures, due to the multiple spars contained within, do not require stringers to further support the skin against buckling as shown in the following figure:

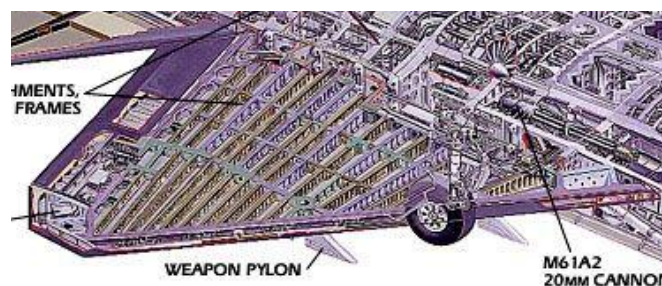


Fig. 162. F-22 wing structural design overview.

Estadea features a lightweight construction throughout the airframe as a whole. In the case of the wing, carbon epoxy AS4 3501-6 [+45°] (available in OpenVSP) will be used on the skin, ribs, flaperons and ailerons, whereas the wing spars and the skin of the LE Flap will be made in the titanium alloy Ti-6Al-4V (available in OpenVSP) to endure the higher temperatures resultant of aerodynamic heating at supersonic speeds with a small reinforcement in the tip for the latter.

Parameter	Value
Material	Titanium alloy (Ti-Al4-V6)
Tensile strength (MPa)	950
Elastic modulus (GPa)	114
Density (g/cm ³)	4.42
Specific heat (J/kg °C)	560
Vickers hardness (kgf mm ⁻²)	330
Longitudinal modulus E₁	21.3 (Msi)
Transverse modulus E₂	1.5 (Msi)
In-plane shear modulus G₁₂	1 (Msi)
Poisson's ratio ν₁₂	0.27 (Msi)
Longitudinal tensile strength F_{1t}	330 (Msi)
Transverse tensile strength F_{2t}	8.3 (Msi)
In plane shear strength F₆	11 (Msi)
Longitudinal compressive strength F_{1c}	250 (Msi)
Transverse compressive strength F_{2c}	33 (Msi)

Fig. 163. Ti-6Al-4V and carbon epoxy AS4 3501-6 properties, courtesy of researchgate.net.

Within the wing, both spars and ribs will have an “I” type section:

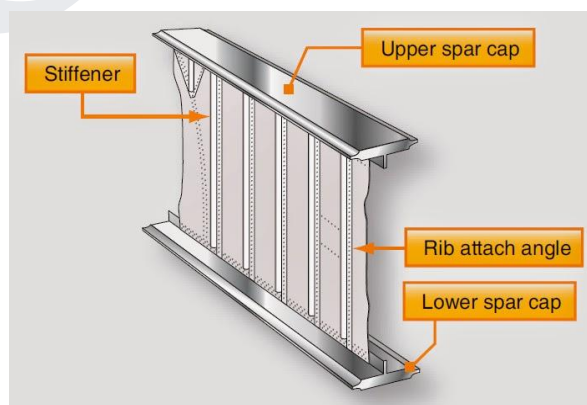


Fig. 164. I spar section description.

In OpenVSP, the structure can be easily built; notice the absence of a wing box typical of commercial aircraft, this is due to the small space available within the fuselage, instead the wing will be fixed to a series of heavy frames, one per spar, in typical fashion of fighter aircraft structures as shown in the previous figure:

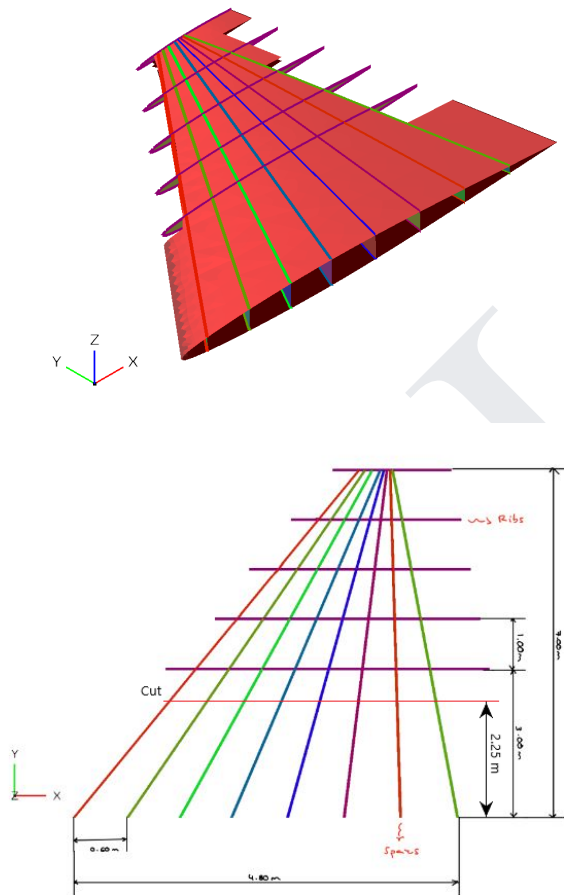


Fig. 165. Estadea’s wing structure (notice the applied cut at the 2.25 m mark).

With the following beam initial dimensions (parametrized by the wing chord) and skin thickness:

- Dim. 1: 567 mm.
- Dim. 2, 3: 250 mm.
- Dim. 4, 5, 6: 75 mm.
- Skin Thickness: 3.0 mm.

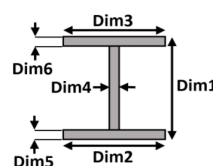


Fig. 166. “I” section beam dimensions.

8.2. Ruddervators

The all-movable ruddervators follow a similar structure to those typical of other fighter's tailerons: the pivot to which the EHA is connected is fixed inside the ruddervator thanks to an intercostal structure (made in Ti-6Al-4V for Estadea) usually formed by a main spar and a couple ribs; the gaps in the structure are filled with a honeycomb-type composite core and a carbon epoxy AS4 3501-6 [+45°] skin. Additionally, the ruddervator LE will be reinforced with titanium to avoid permanent deformations resulting from aerodynamic heating at supersonic speeds.

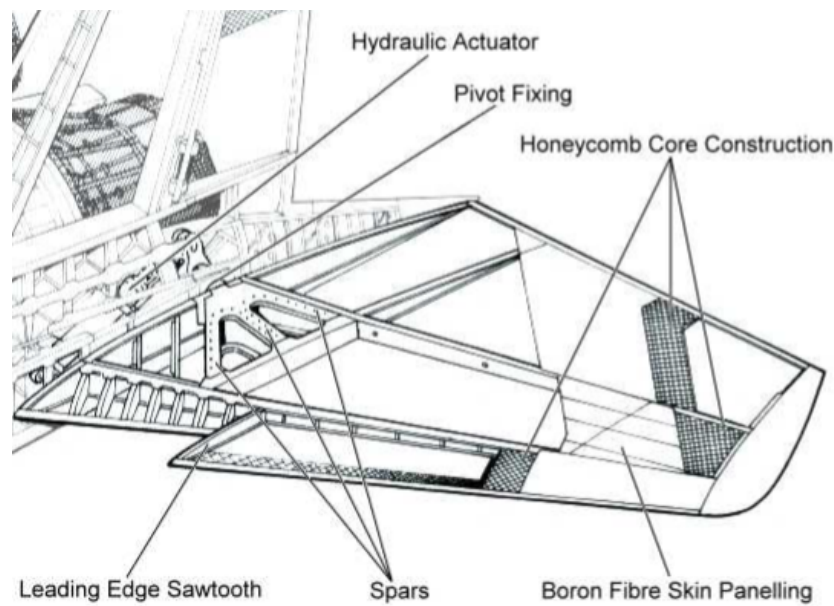


Fig. 167. F-15 taileron structure.

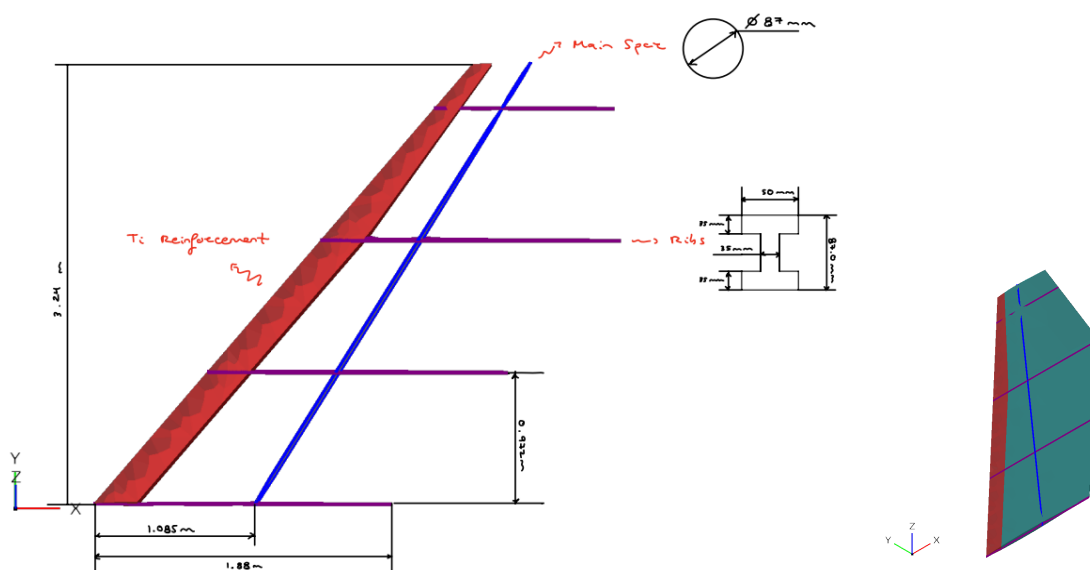


Fig. 168. Estadea's ruddervator structure.

The deflection mechanism for the ruddervators is quite simple: the main spar is extended at the root so a portion lies inside the fuselage. To this portion the electro-hydraulic actuator is connected through a lever arm which induces the rotation of the ruddervator when the actuator’s main arm is extended or retracted. The actuator’s connection to the fuselage must also be hinged to permit its movement up and down as it pulls or pushes the lever arm so its main arm does not strike the main spar and avoids buckling.

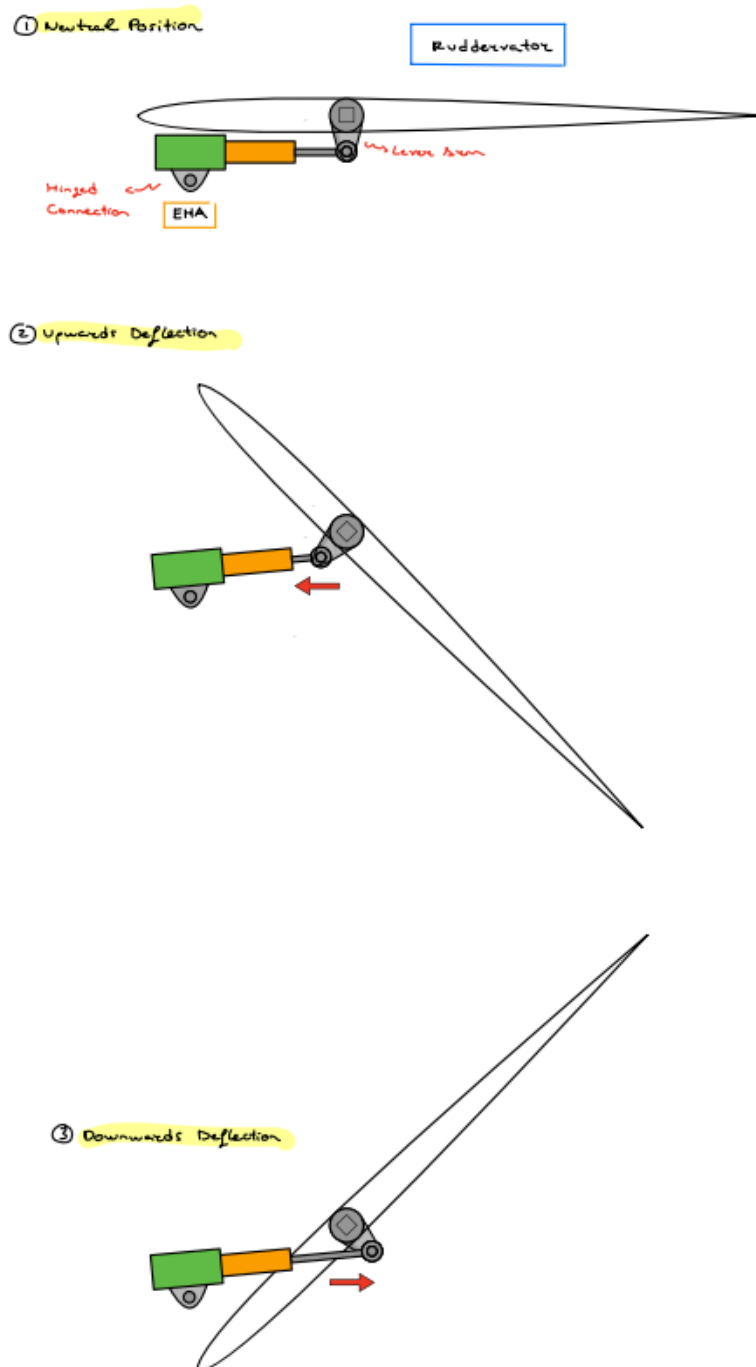


Fig. 169. Ruddervator actuation mechanism.

8.3. Control Surfaces

Asides from the ruddervators, the aircraft achieves controlled flight through the usage of two other control surface types, the flaperons and ailerons. As described in the systems arrangement, these surfaces are operated by electro-hydraulic actuators. As they possess similar deflection angles and shapes, the general assembly and deflection mechanism can be assumed to be similar for both control surface types.

Overall, the mechanism is quite simple: the EHA is connected to the control surface through a hinged strut which is moved up or down when the actuator's main arm is extended or retracted, respectively. The fairing for this mechanism has been fragmented in two sections, one connected to the wing and the other to the control surface to permit its movement with the surface deflection; it ensures the whole mechanism remains hidden from radar waves and external elements at any deflection angle within the range of motion of the control surface.

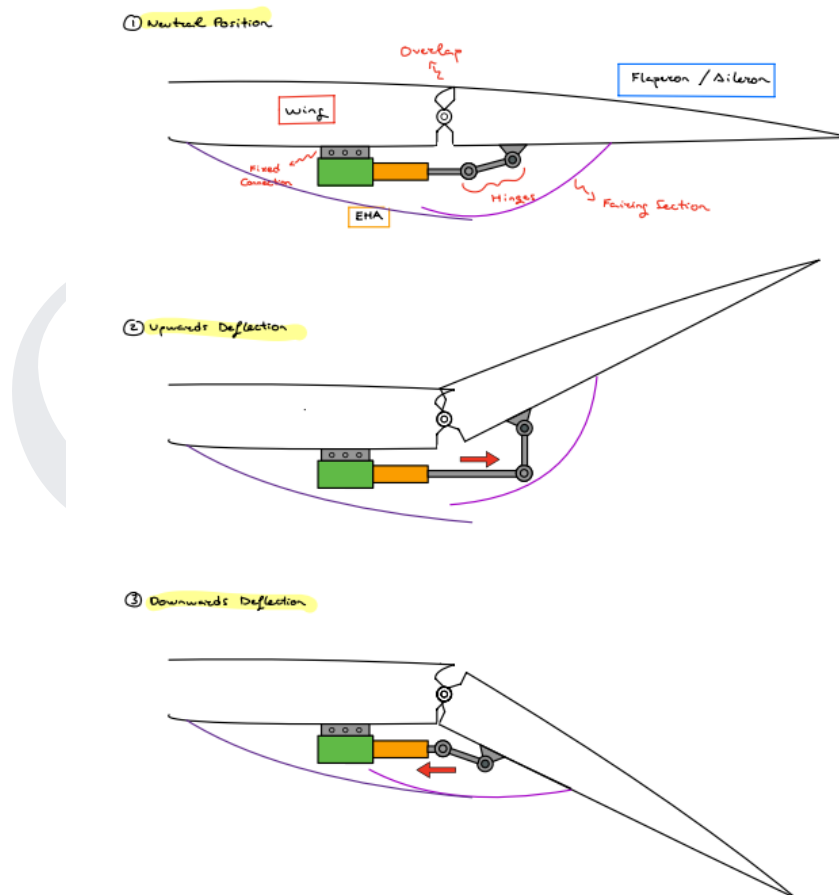
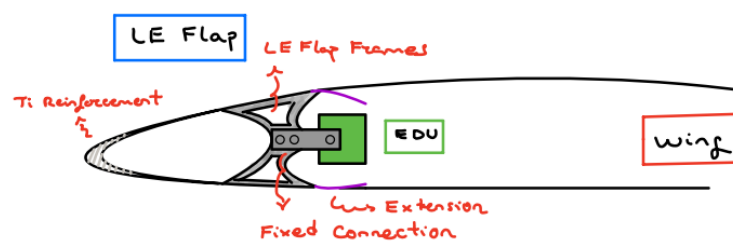


Fig. 170. Flaperon and aileron actuation mechanism.

On another note there is the LE flap deflection mechanism, which is somewhat different than the previous ones due to the smaller thickness available for its assembly. In this case the whole mechanism is buried inside the wing structure and, therefore, there is no fairing to be worried about. The LE flap relies on an electric drive unit for its deflection connected to a fixed connection within the frames of the former. Finally, the LE flap counts with a titanium tip reinforcement to avoid permanent deformations resulting from aerodynamic heating at supersonic speeds.

① Neutral Position :



② Downwards Deflection :

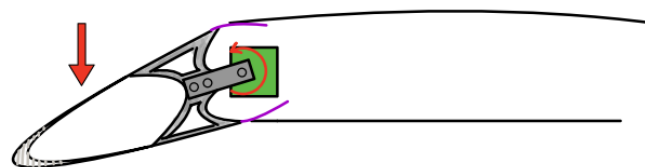


Fig. 171. LE flap actuation mechanism

8.4. Fuselage

The fuselage structure can be classified as semi-monocoque. It is formed by a series of frames following the shape of the fuselage cross-sections shown in section 6.2., joined through a series of stringers. In the fuselage mid-section lies the heavy frames, made in Ti-6Al-4V whereas the rest of the structure, including the skin, is made in carbon epoxy AS4 3501-6 [+45°]. Naturally, the canopy, missile bay doors and other openings must be taken into account within the structure.

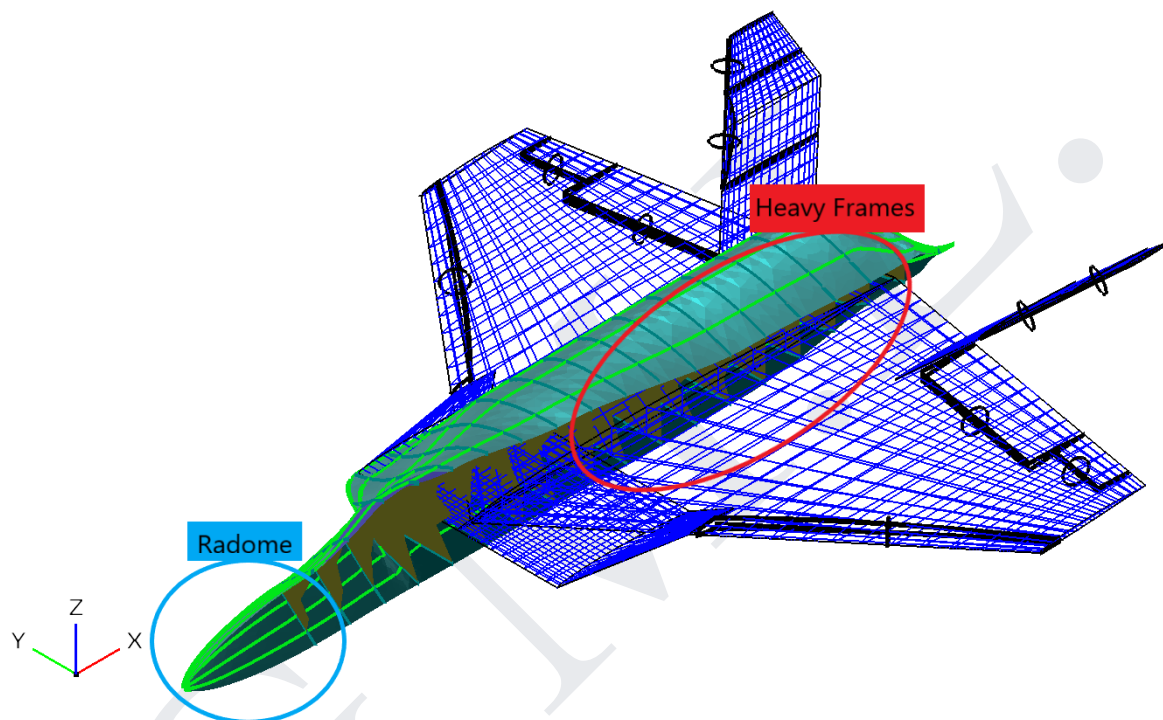


Fig. 172. Estadea’s fuselage structure.

Within the fuselage structure, it is convenient to describe the canopy and general door actuation mechanisms. The canopy, being a single piece, bubble-type design requires it to be displaced as a whole when opening and closing. The mechanism follows a clamshell, rotate-translate design in which a hydraulic actuator both rotates the canopy upwards to permit pilot entry or exit and slides it backwards to lock it into place through the usage of several pins. In an ejection, the actuator would disengage the lock by sliding the canopy forward.

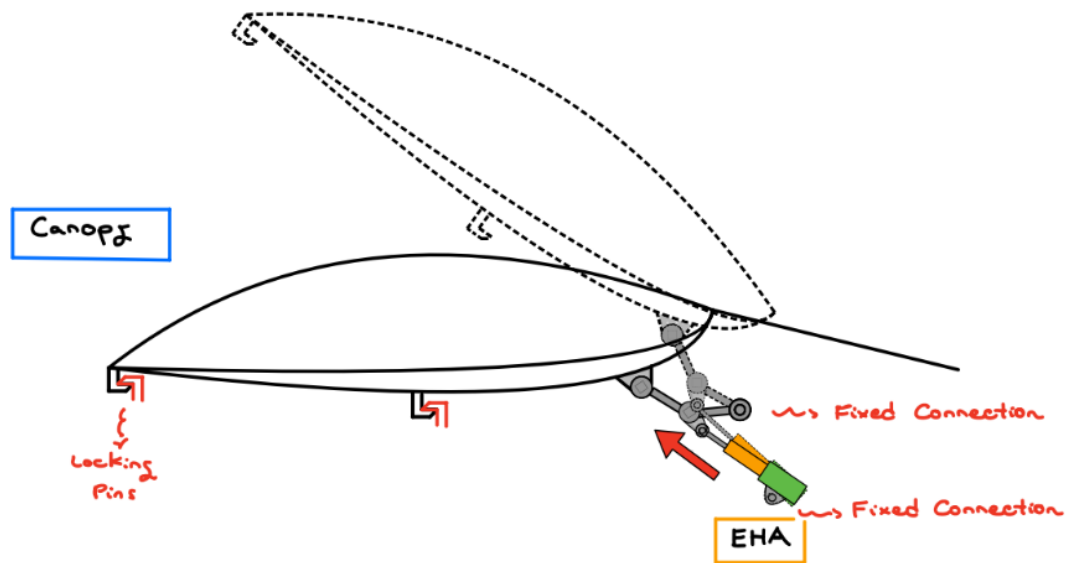


Fig. 173. Canopy actuation mechanism.

In the case of the multiple doors distributed throughout the fuselage structure (missile bay doors, side doors, flare and chaff dispenser doors, etc.) will be opened and closed using small electrical drive units for added simplicity and reliability in the benefit of combat performance and maintenance.

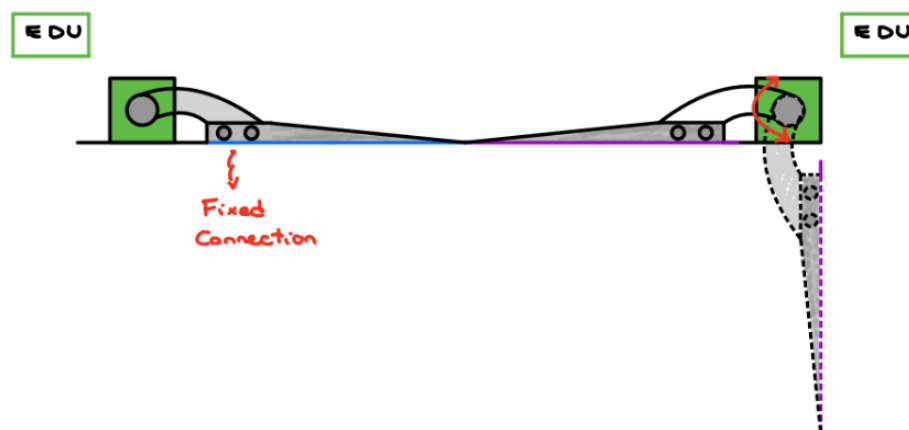


Fig. 174. Door actuation mechanism.

8.5. Landing Gear

The main landing gear, similar to the F-14 and F-35 designs, is retracted and deployed in a swing-arm fashion so it is stored parallel to the fuselage line. It is composed of a main boom with an angled pivot pushed by a hydraulic piston and a support boom fragmented in two folding arms. The 3D model has been modified from a free copy intended for 3D printing available in grabcad.com:

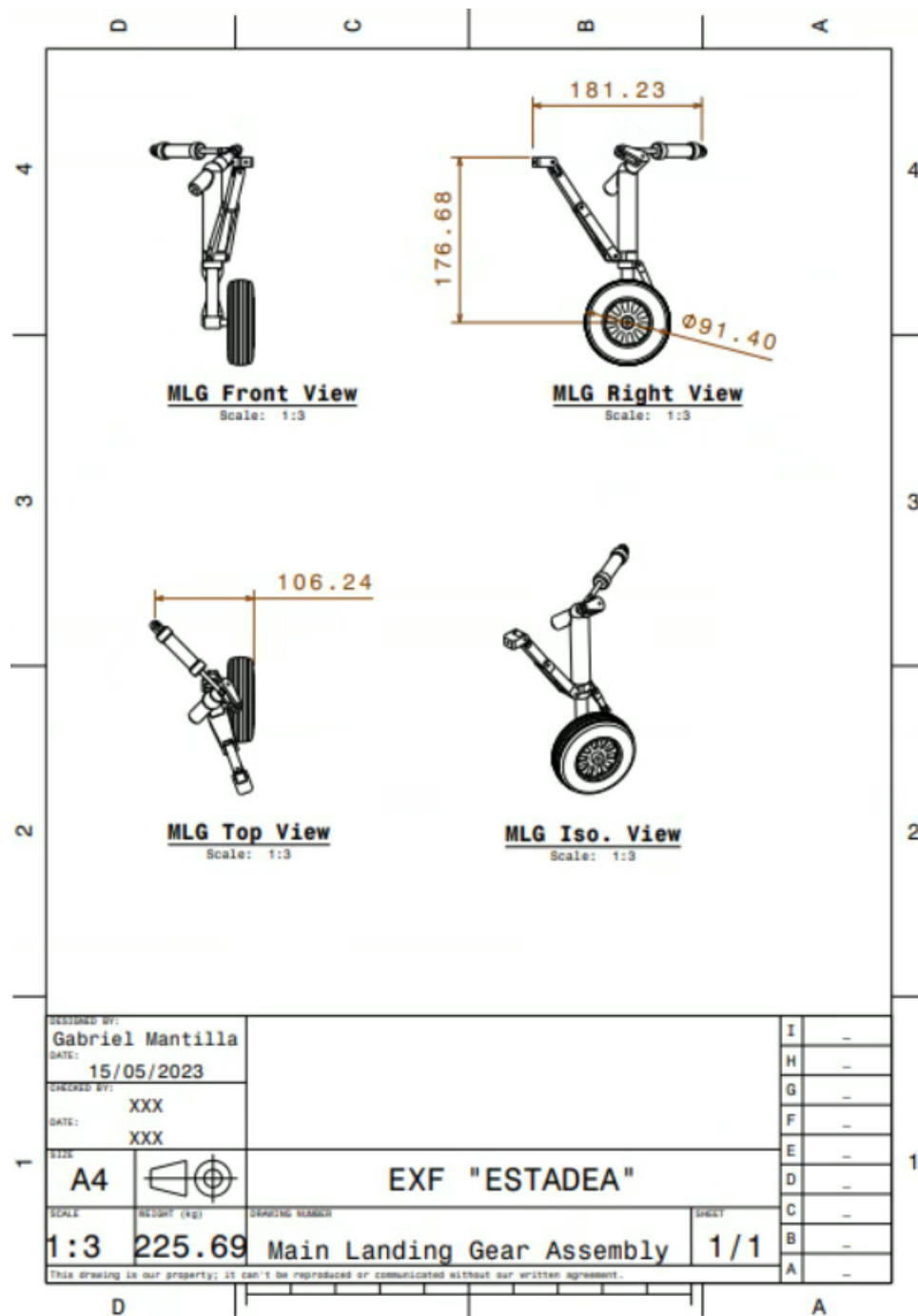


Fig. 175. Estadea's main landing gear design (dimensions given in centimeters).

The nose landing gear follows a similar design, it possesses a main boom and a segmented support boom. The main boom pivot is not angled such as in the main landing gear and it is the support boom connected to a hydraulic actuator which retracts and extends the nose landing gear. The 3D model has been modified from a free copy intended for 3D printing available in grabcad.com:

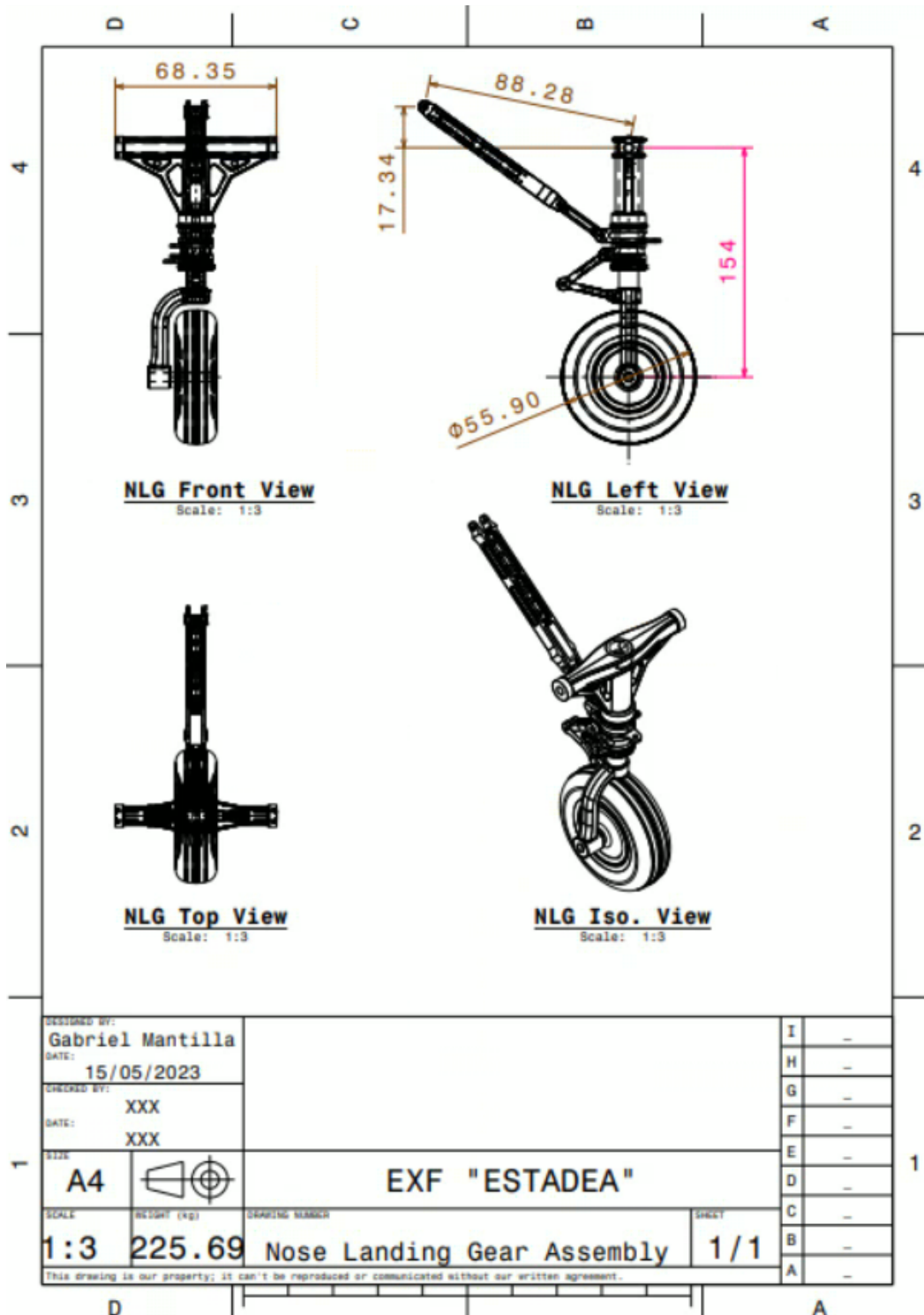


Fig. 176. Estadea's nose landing gear design (dimensions given in centimeters).

8.6. Thrust Vectoring Mechanism

Estadea incorporates a rectangular divergent section within its nozzles, each formed by two walls and covers. The covers can move independently up or down through electro-hydraulic actuators for both vectoring and to avoid nozzle choking. Each part has been beveled and serrated to reduce its specular reflection and break creeping waves, providing the aircraft with full-aspect stealth. This design is completely original:

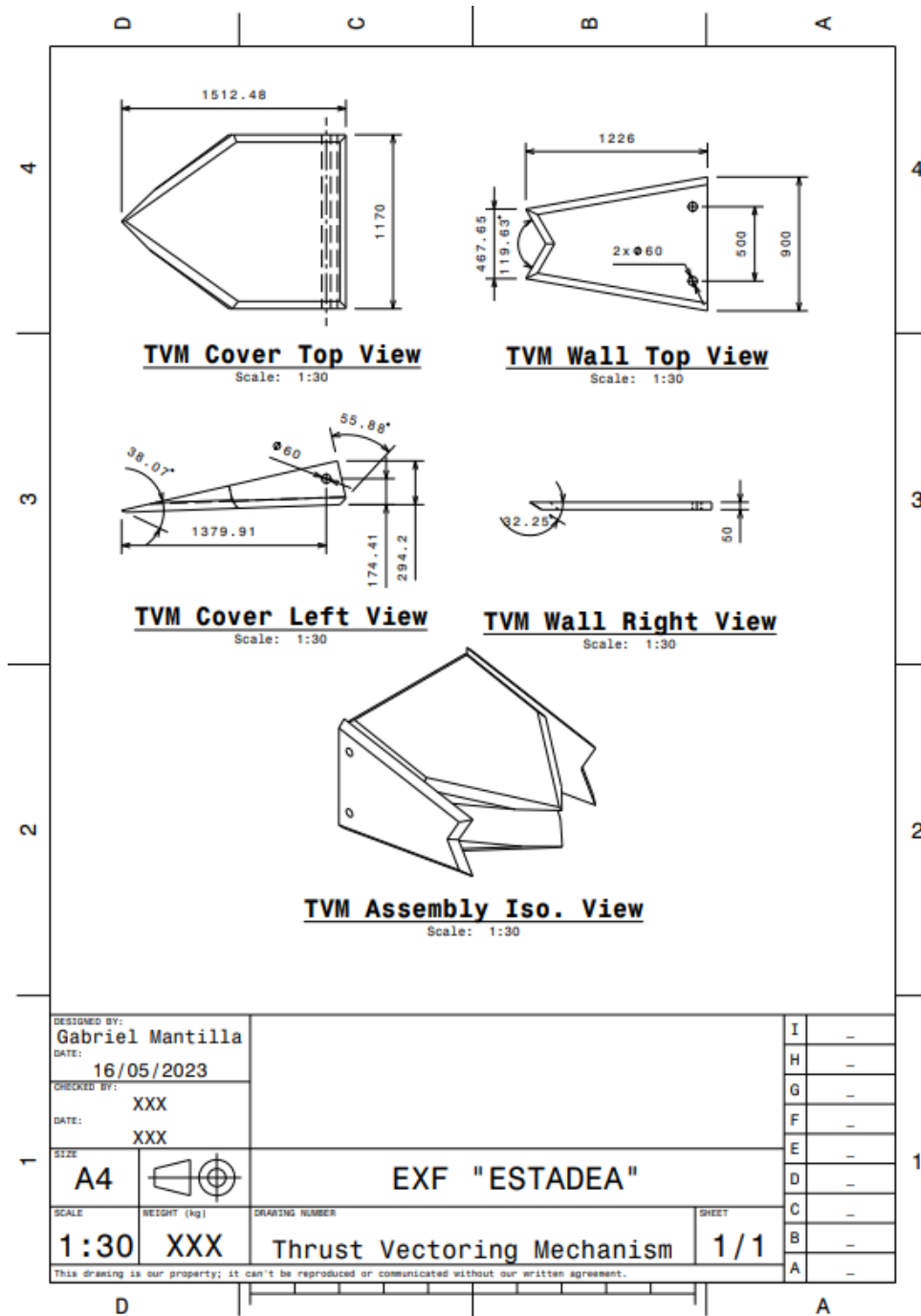


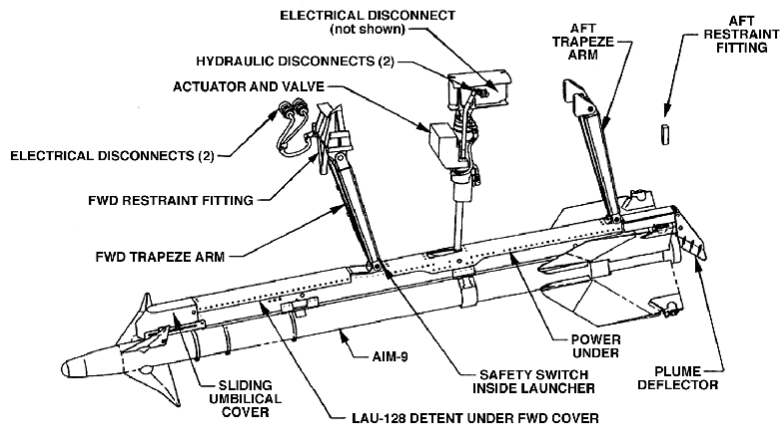
Fig. 177. Estadea's thrust vectoring mechanism (dimensions given in millimeters).

8.7. Missile Pylons

Estadea will use a set of standardized missile pylons for its internally and externally carried weapons currently in use by the USAF; these include the LAU-128/A rail launcher, the LAU-141/A hydraulic launcher and the LAU-142/A pneudraulic launcher for its fox-2 and fox-3 missiles:

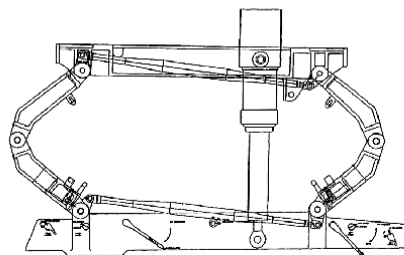


LAU-141/A Trapeze Launcher with Missile



LAU-142/A AMRAAM Vertical Eject Launcher

Extended for Ground Operations Such as Missile Loading or Servicing



Retracted with Missile Attached

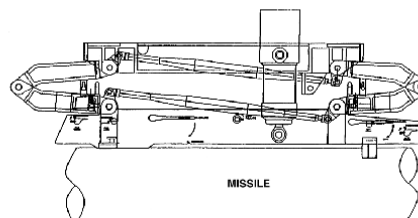


Fig . 178. From top to bottom: LAU-128/A, LAU-141/A and LAU-142/A missile launchers.

(This page has been intentionally left blank)

G.M.L.

Chapter 9. GENERAL PERFORMANCE & COMPARISON

In this closing Chapter the general performance calculations and results concerning maximum velocity, climb performance, general maneuvering performance, range, endurance, takeoff and landing ground run, etc. are shown. This calculations and comparison with current fighters will determine how competent Estadea is in the present military landscape. All figures and results are shown in customary aviation units (U.S. imperial units, FL, IAS). In order to determine the best performance figures Estada is capable of achieving, it has been analyzed primarily in its combat configuration (combat weight) at ISA+0 conditions.

9.1. Maximum Velocity and Supercruise Capabilities

From the figures contained in Section 7.7. “Thrust Required vs. Airspeed (Steady & Level Flight)”, which show the required and available thrust at three reference altitudes, and taking into account the safety measures discussed in the former (limiting speed for surface heating at lower altitudes and assuming engine performance limitations at higher altitudes), the maximum velocities and supercruise abilities of Estadea can be summarized:

- Maximum Speed S.L.: Mach 1.2 (1057 knots EAS).
- Maximum Speed in Supercruise: Mach 1.6 (540 knots EAS) at FL330.
- Maximum Speed: Mach 2.5 (845 knots EAS) at FL330.

In terms of top speed, Estadea is similar to the F-15 Eagle, with an alleged top speed of Mach 2.5 at altitude; this would make it the current fastest stealth aircraft unless the stealth paint requires further speed limitations at altitude due to surface heating. In terms of supercruise speeds, Estadea is similar to the EF-2000 Typhoon, with alleged top supercruise speed of Mach 1.5-1.6; it falls short of the alleged F-22’s supercruise top speed of Mach 1.80.

9.2. Climb Performance

As discussed in Chapter 2, climb performance is comprised by the climb rate and climb gradient. It is convenient to determine the evolution of both variables with altitude for a more accurate picture of Estadea’s overall climb performance; for this purpose a method of iteration of both rate and gradient (refer to formulas 2.33 and 2.34) over a speed range has been used at each flight level; from this iteration the best values for sustained climb (that is, maintaining constant airspeed and using all excess power to increase altitude) have been extracted taking into account the maximum speed and stall limits.

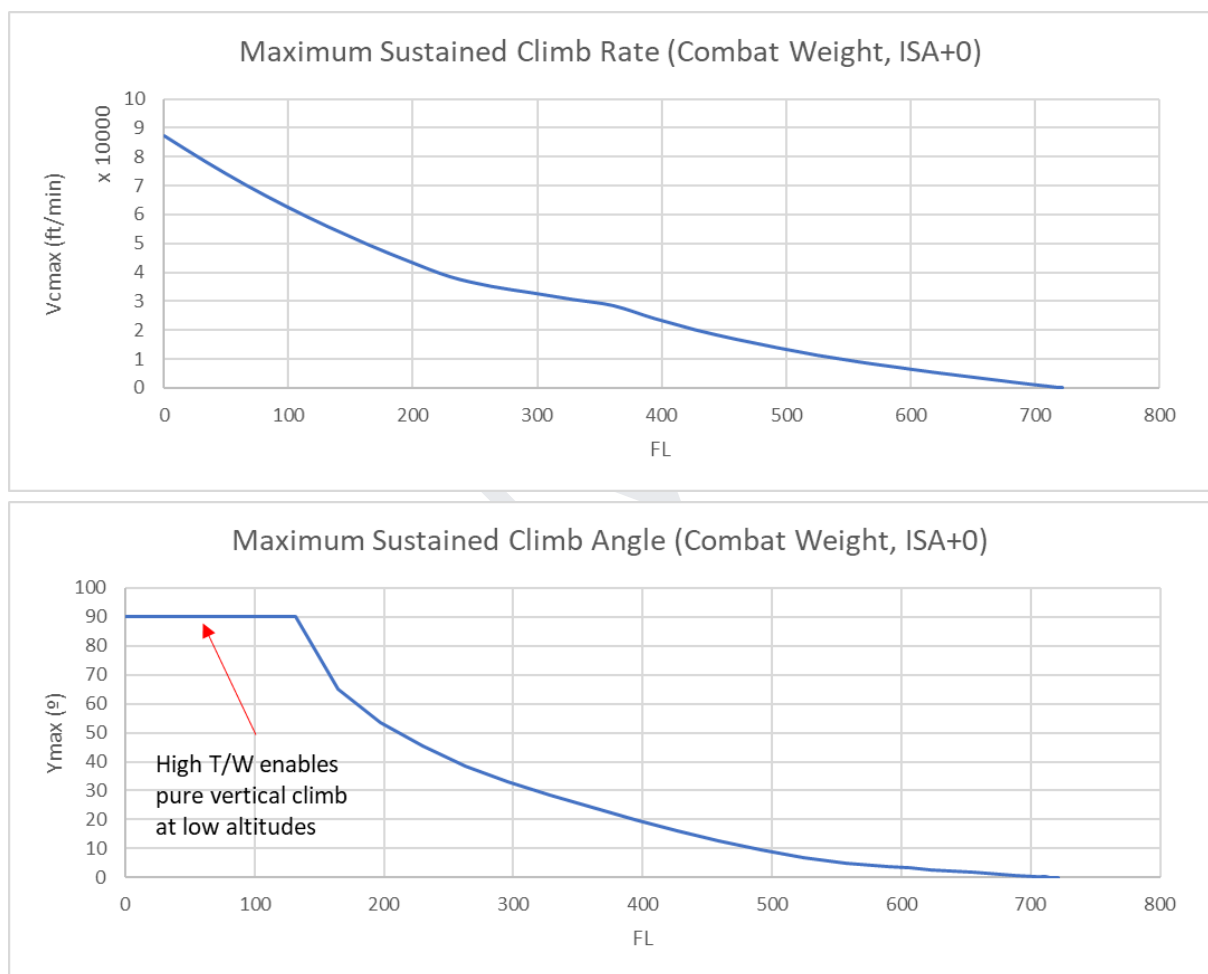


Fig. 179. Estadea’s climb performance.

Estadea shows incredible initial climbing speeds (over 85,000 feet per minute at S.L.) and the capability of pure vertical climbs (even when taking into account the drag force) up to 14,000 feet thanks to its incredibly powerful F-135 twin engines; which provide the aircraft with the highest thrust to weight ratio in the world at S.L. Notice how the maximum sustained

climb rate and gradient values are reduced as altitude increases due to the reduction of thrust to weight ratio; as shown in the following figure:

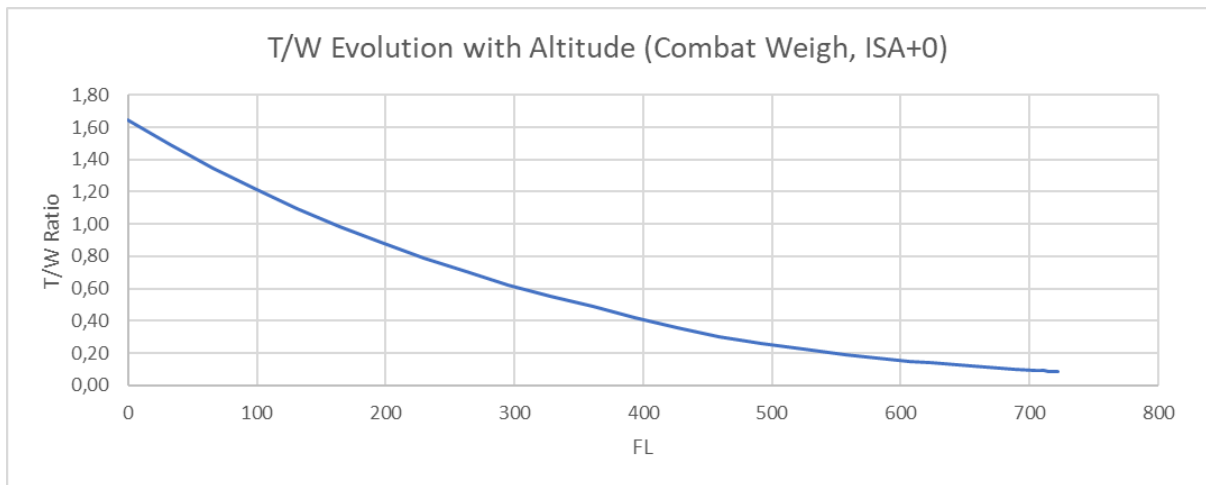


Fig. 180. Estadea’s thrust to weight ratio vs. altitude.

Estadea benefits from a maximum thrust to weight ratio of 1,64 at S.L. in its combat configuration to reach world record breaking initial climb rates; beating its closest competitor, the Mig-29 (with an alleged initial maximum climb rate of 65,000 ft/min) by more than 20,000 ft/min.

9.3. Absolute Ceiling, Service Ceiling, Cruise Ceiling

By analyzing the evolution of the climb rate with altitude, four variables can be determined (R. Llamas, 2022):

1. Absolute Ceiling: the maximum altitude reached by the aircraft where it can sustain steady and level flight (therefore, zoom climb is excluded from this calculation), where the climb rate is zero.
2. Cruise Ceiling: defined as the altitude where the aircraft reaches a maximum climb rate of 300 ft/min.
3. Service Ceiling: defined as the altitude where the aircraft reaches a maximum climb rate of 500 ft/min.
4. Combat Ceiling: defined as the altitude where the aircraft reaches a maximum climb rate of 500 ft/s or 30,000 ft/min.

Combining the stall limits and thrust limits for steady and level flight the altitude envelope (H-M diagram) can be easily plotted. To determine the thrust limits for steady and level flight (the maximum available thrust at a given airspeed and altitude equals or surpasses the thrust required for the same airspeed and altitude), an iteration method has been applied for the speed range at several altitudes up to the absolute ceiling. The results for the altitude envelope and the different ceilings are shown in the following figure.

- Absolute Ceiling: 72,178 ft.
- Cruise Ceiling: 71,250 ft.
- Service Ceiling: 70,900 ft.
- Combat Ceiling: 35,000 ft.

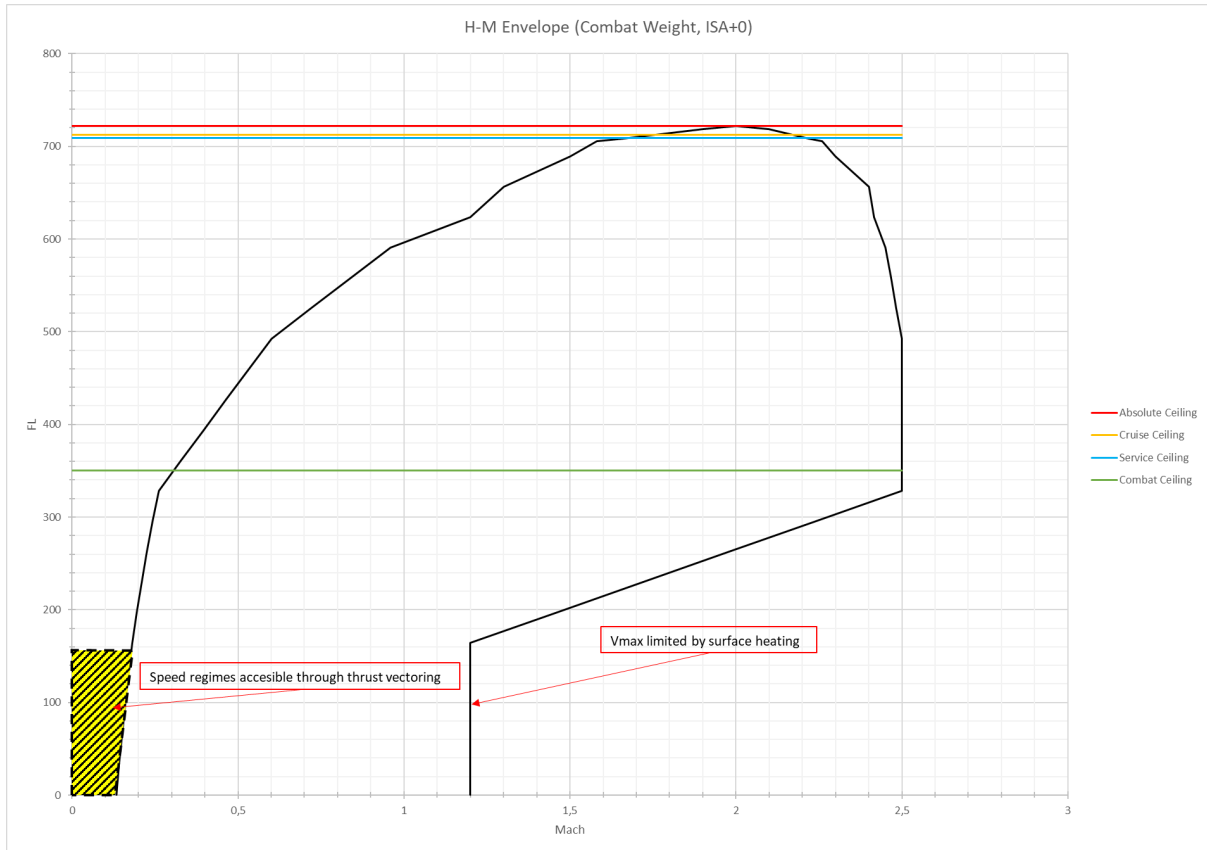


Fig. 181. Estadea’s H-M envelope (altitude envelope).

With a service ceiling of 70,900 ft, Estadea lies in between the service ceiling of dedicated air superiority fighters such as the F-22 and pure interceptors such as the Mig-25 and Mig-31.

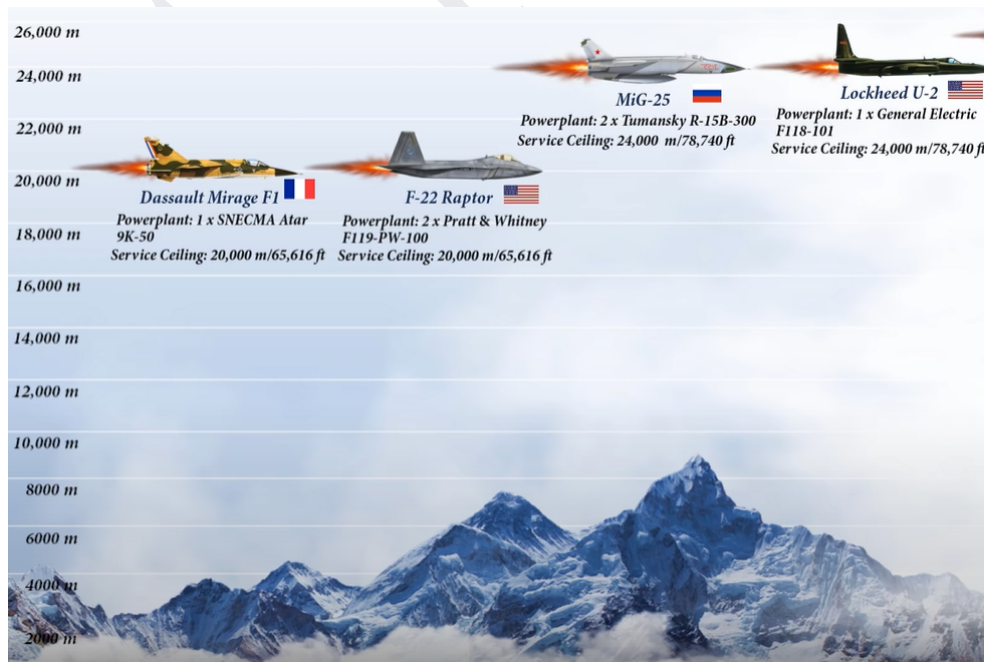


Fig. 182. Jet fighters service ceiling comparison, courtesy of The Buzz Youtube channel.

9.4. General Maneuvering Performance

As discussed in Chapter 2, good turn performance is a crucial ability any fighter must possess to excel in combat. In addition to the three main variables (banking angle, rate and radius), the pull-up and pull-down maneuvers have also been considered. It is convenient to determine the instantaneous turn performance (limited by the load limits and stall limits given by the formulas 2.28, 2.29, 2.30 and 2.31) but also the sustained turn performance, limited by the available thrust. In order to simplify the calculations, level and coordinated turns (no change in altitude and no skid or slip of the aircraft) are considered except for the pull-up and pull-down maneuvers (in which a change in altitude is unavoidable).

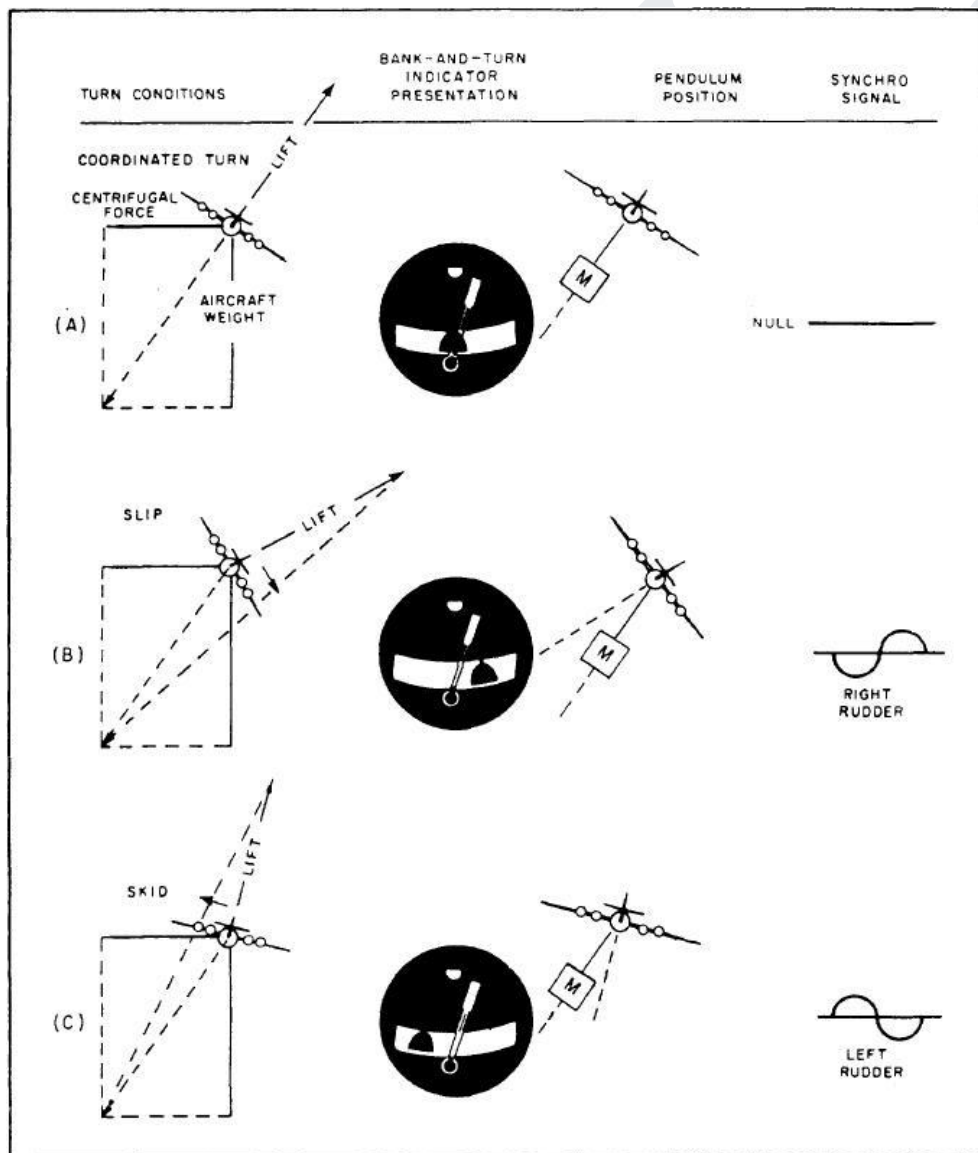


Fig. 183. Conditions for a coordinated turn.

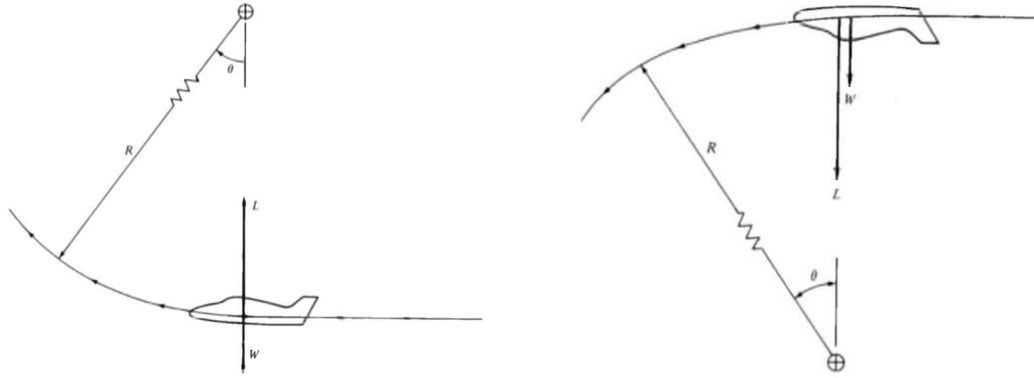


Fig. 184. Pull-up and pull-down maneuver, respectively.

In order to obtain the best turn performance Estadea is capable of achieving, it is assumed all maneuvers are performed at combat weight at full thrust with afterburner enabled:

- $W_{max} = MTOW = 74632.83 \text{ lbs.}$
- $W = W_{combat} = 52267.61 \text{ lbs.}$
- $\gamma = 0$ as only level turns are considered (except in pull-up and pull-down maneuvers).
- $n_{max, combat} = n_{pull} \cdot \frac{W_{max}}{W_{combat}} = 9.0 G \Rightarrow n_{pull} = 6.30$ (9.1) is the positive structural limit in the combat configuration, limited by the OWS for pilot well-being (U. I. Balldin, 2002). The negative limit is not considered in this analysis since pilot resistance to negative g-forces is much lower and these are avoided as much as possible since injuries are much more severe for these forces (U. I. Balldin, 2002).
- Speed measurements are given in terms of IAS:

$$IAS = \sqrt{\frac{2(P_{total} - P_{static})}{\rho_0}} = v \cdot \sqrt{\frac{\rho}{\rho_0}} \equiv TAS \cdot \sqrt{\frac{\rho}{\rho_0}} \quad (9.2)$$

9.4.1. Maximum Bank Angle:

The maximum bank angle is given by the enveloped formed by the stall and load limits of the aircraft:

- $\phi_{max.load} = \cos^{-1}\left(\frac{W_{combat}}{n_{pull} \cdot W_{max}}\right)$ (9.3) is the load limit.
- $\phi_{max.stall} = \cos^{-1}\left(\frac{W_{combat}}{n(v) \cdot W_{max}}\right)$ (9.4) is the stall limit, $n(v) = \frac{\frac{1}{2}\rho v^2 c_{L,max} S_w}{W_{max}}$ (9.5)

Combining both, the allowable envelope for maximum bank angle is obtained:

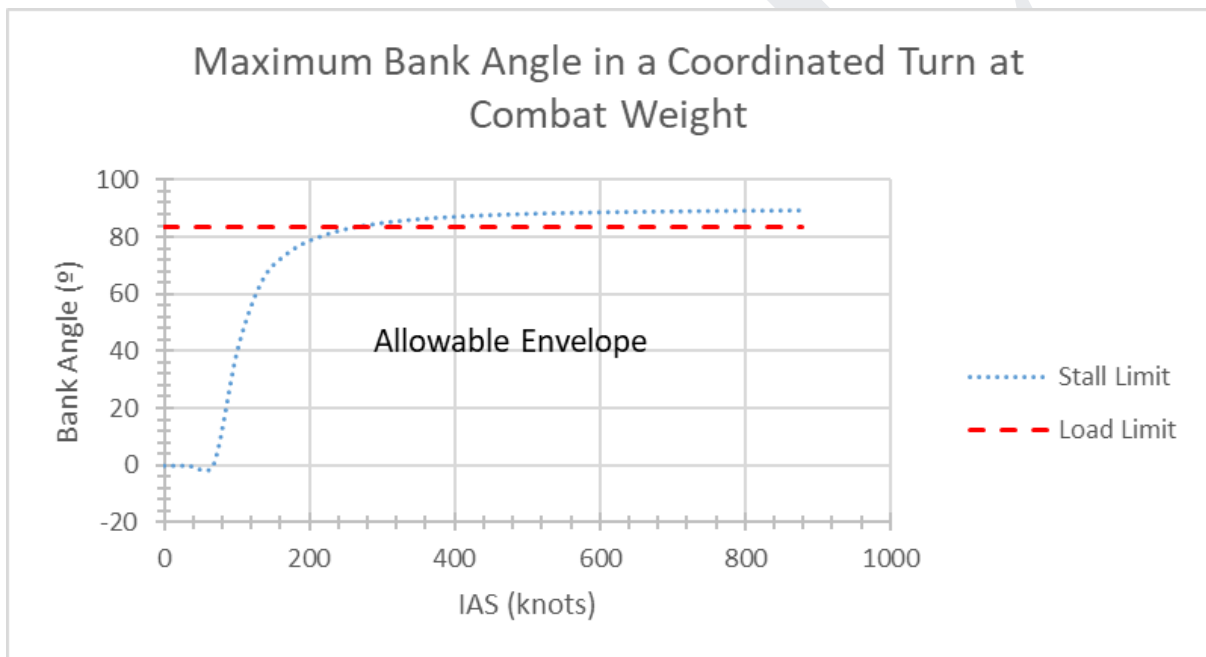


Fig. 185. Maximum bank angle in a coordinated turn at combat weight.

9.4.2. Turn Performance:

The stall and load limits for both radius and rate are given by the equations 2.28, 2.29, 2.30 and 2.31. For sustained turn rate and radius the formulas change significantly:

- $n_{max, sustained}(v, c_{L, max}) = \frac{\frac{1}{2}\rho v^2 c_{L, max} S_w}{W_{max}}$ (9.6) is the maximum sustained load factor in a level turn.
- $c_{L, max} = \sqrt{\pi e AR (\frac{2T_{av}}{\rho S_w v^2} - c_{D0} - c_{Dw})}$ (9.7) with a maximum limit of $c_{L, max} = 2.2$
- $\Omega_{sustained} = \frac{g}{v} \sqrt{n_{sus.}^2 - 1}$ (9.8) and $R_{sustained} = \frac{v^2}{g \sqrt{n_{sus.}^2 - 1}}$ (9.9)

Estadea’s turn performance will be evaluated at S.L. and at 15,000ft; a typical reference altitude for fighter turn performance:

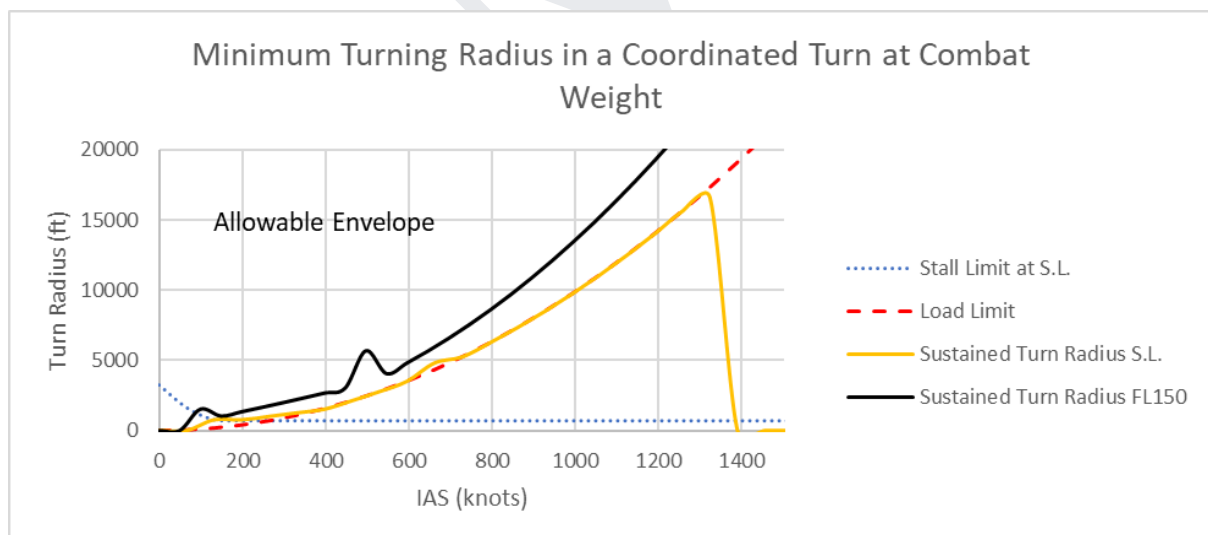


Fig. 186. Minimum turn radius in a coordinated turn at combat weight.



Fig. 187. Maximum turn rate in a coordinated turn at combat weight.

Estadea reaches a maximum instantaneous turn rate of almost 40°/s at 280 knots and a maximum sustained turn rate of 28.85°/s at its maneuver speed, 264.28 knots; it beats the estimated maximum sustained turn rates (from F16.net, extracted from DCS world at 50% of internal fuel, although the real values are classified) of the F-22, EF-2000 and others, making Estadea an extremely dangerous opponent in dogfights. Notice how both sustained turn rate and turn radius values are degraded with increasing altitude due to the lower thrust available. At 15,000ft Estadea can reach a maximum sustained turn rate of 17°/s at 300 knots and a maximum instantaneous turn rate of 35°/s at 350 knots.

9.4.3. Pull-up and Pull-down Maneuvers:

As discussed in Chapter 2, generally whoever points its nose first to the other will win the dogfight. Until now the main scope of analysis has been level turns, however it is important to remember that dogfights consist of horizontal and vertical maneuvers; it is therefore convenient to also determine Estadea’s ability to point its nose upwards and downwards.

- The pull-up turn rate is given by $\Omega_{up} = \frac{g(n-1)}{v}$ (9. 10).
- The pull-up turn radius is given by $R_{up} = \frac{v^2}{g(n-1)}$ (9. 11).
- The pull-down turn rate is given by $\Omega_{down} = \frac{g(n+1)}{v}$ (9. 12).
- The pull-down turn radius is given by $R_{down} = \frac{v^2}{g(n+1)}$ (9. 13).
- $n \equiv n_{sus.}$; load limits must also be applied, therefore $n \pm 1 \leq 9.0 G$.

The results were the following:

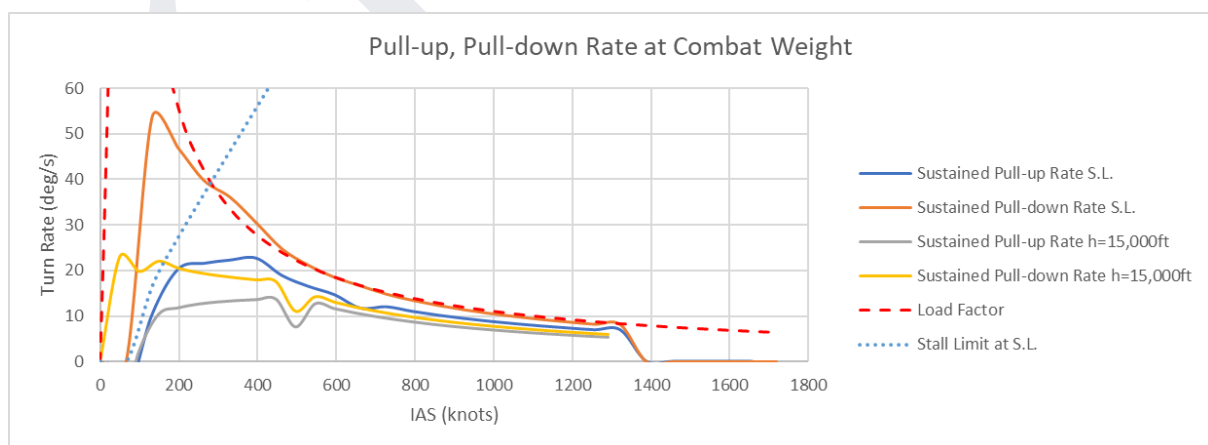


Fig. 188. Sustained Pull-up and Pull-down rate at combat weight.

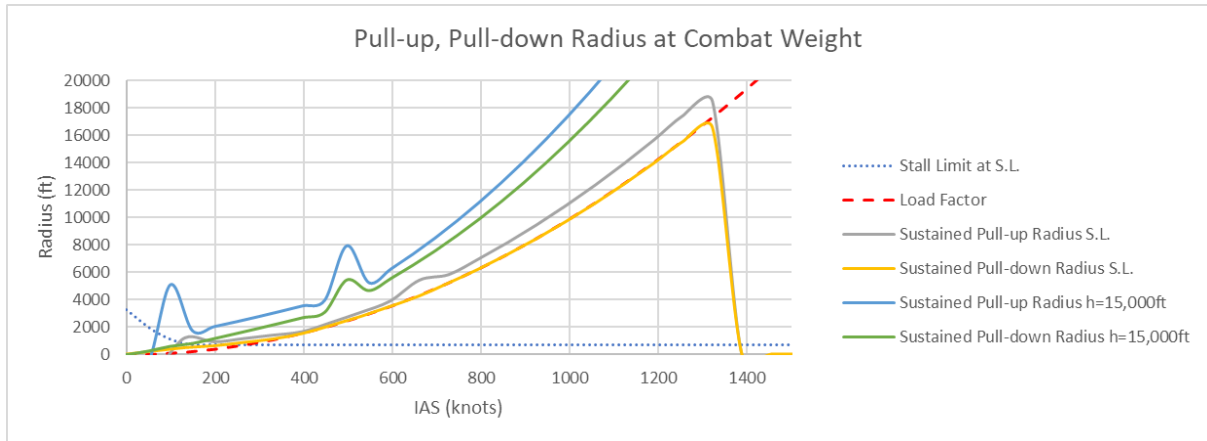


Fig. 189. Sustained Pull-up and Pull-down radius at combat weight.

Notice how pull-down maneuvers can exceed the stall limit of level turns at low speeds due to the nature of the formula governing this maneuver. Unfortunately no public information was found concerning pull-up or pull-down rates for current fighter aircraft.

9.5. Mission Range & Endurance, Payload-Range Diagram

Range, endurance and maximum payload capacity are extremely important metrics in military aircraft. The ability to carry large weapon payloads over long distances is a great added value to Estadea which will demonstrate multirole characteristics although its main mission is air superiority. To compute ranges and endurances for the different missions and configurations it is convenient to determine the landing weight; additionally, the extra drag resulting from externally carried weapons stores/drop tanks must also be taken into account.

Configuration	Ferry	Air Patrol	Combat (Stealth)
Landing Weight (kg)	17793,08	19604,06	17928,66

Table 15: Mission configuration landing weights.

9.5.1. Mission Range & Endurance:

Except for the ferry configuration, it is assumed the aircraft retains 5% of the total fuel capacity as reserves for added safety. In order to simplify the calculation of range and endurance in the different mission configurations an idealized cruise-climb profile to the maximum supercruise speed altitude (FL330) is assumed.

- Range is calculated using the Breguet equation:

$$R = \frac{v}{SFC} \frac{L}{D} \ln\left(\frac{W_o}{W_f}\right) \quad (9.14)$$

- Endurance is calculated using a variation of the previous equation:

$$E = \frac{1}{SFC} \frac{L}{D} \ln\left(\frac{W_o}{W_f}\right) \quad (9.15)$$

- For the air-to-air and ferry configurations the extra drag resulting from the two external drop tanks must be taken into account by adding their parasite drag coefficient to the calculation of aerodynamic efficiency.

By plotting the results over the speed range at FL330, the best cruise speed can be determined by correlation with the maximum values for range and endurance; this speed will then be used in combination with the Breguet range equation to plot the payload-range diagram.

The results were the following:

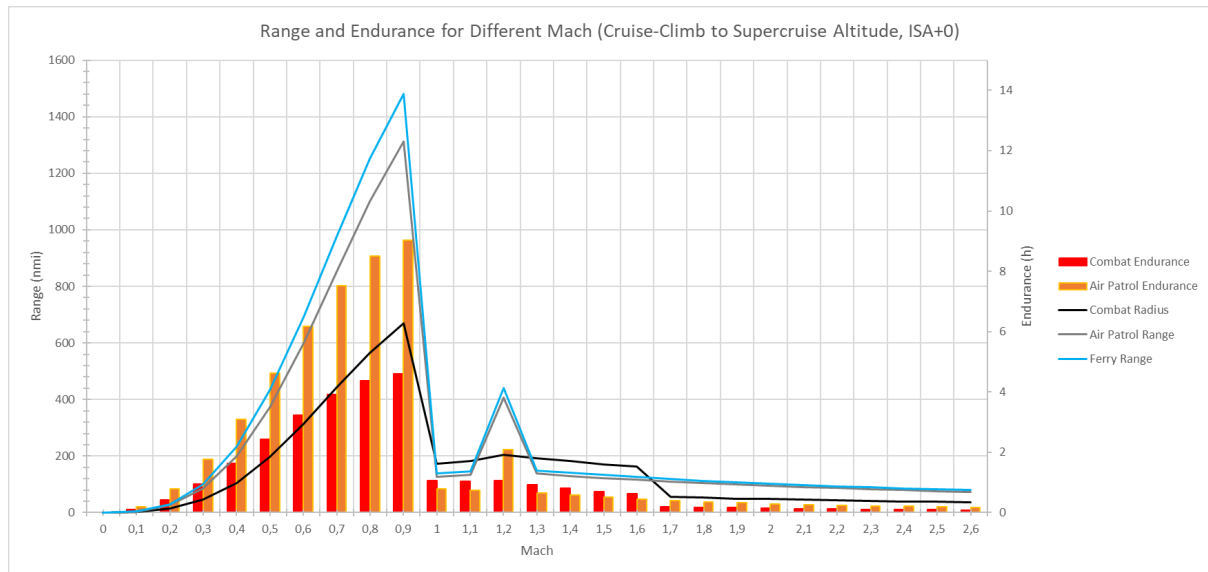


Fig. 190. Range and endurance for mission configuration over the speed range.

Combat range has been halved to determine the combat radius, or how far the aircraft can reach before returning to base in its combat configuration (same for endurance). From the previous results, it is clear that the optimal cruise speed is around Mach 0.9 or 525 knots. For the different mission configurations, the best results were the following:

- **Combat Configuration** (assuming takeoff with full internal fuel and release of all ordinance): 669.30 nmi or 4h 36' @ 525 knots. Notice the better results for both radius and endurance (even when halved) in comparison to the other configurations at supersonic speeds due to Estadea's supercruise abilities in a clean configuration. Taking the spanish air bases as reference, Estadea could effectively establish air superiority over half of the Mediterranean, Morocco, West Africa, Tunisia, Portugal, Italy, France and Switzerland.
- **Air Patrol Configuration** (assuming no release of ordinance): 1313 nmi or 9 h @ 525 knots. In this configuration Estadea can reach without any difficulty all spanish air bases even when taking off from the Gando Air Base on the Canary Islands. Estadea can also land in friendly bases across Europe as far as Poland, Romania and Ukraine
- **Ferry Configuration**: 1481 nmi @ 525 knots, which narrowly misses the target ferry range (1600 nmi); additional external fuel tanks could solve this issue.

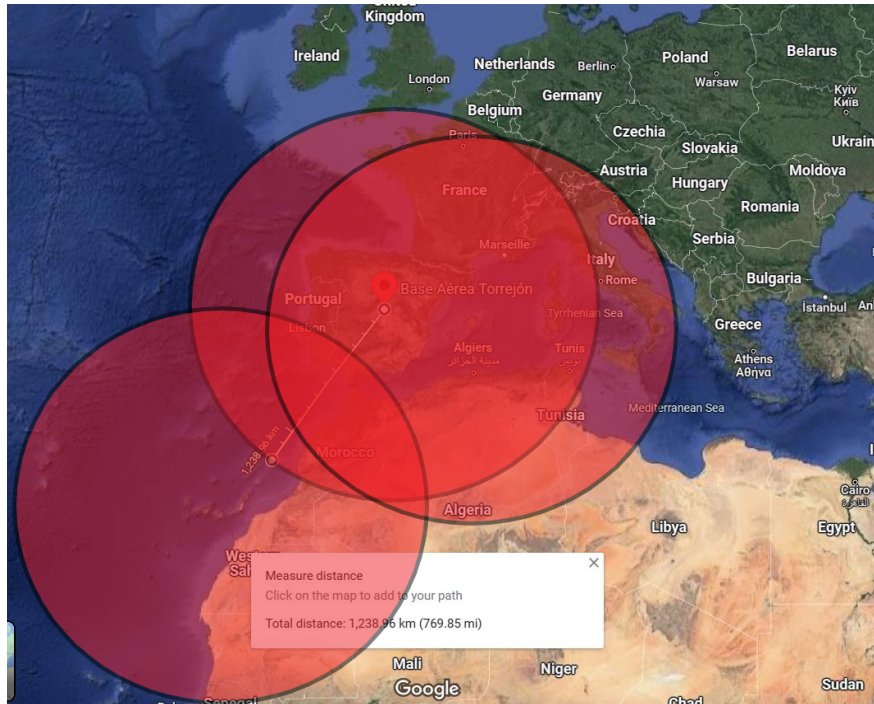


Fig. 191. Estadea’s area of operations (combat radius) from Torrejón, Gando and Son San Juan air bases.

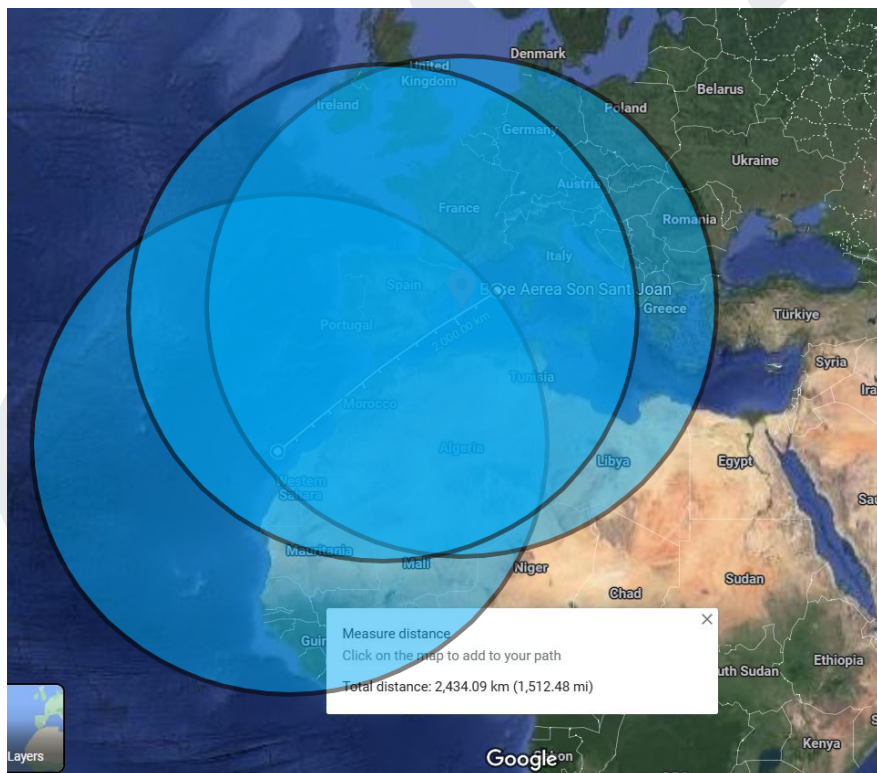


Fig. 192. Estadea’s air patrol range from Torrejón, Gando and Son San Juan air bases.

Accurate information concerning ranges has been difficult to obtain due to the tendency to exaggerate performance figures; for example, the F-22, the closest resemblance to Estadea, claims a ferry range of over 1600 nmi with two external 600 gallon fuel tanks yet it mounts less efficient engines (P&W F-119) and has less internal fuel capacity (15185.44 lbs vs. 19232.73 lbs in Estadea). Nonetheless, an internal presentation from the U.S. Air Force concerning the F-35, the latest stealth fighter, is publicly available, revealing its combat ranges:

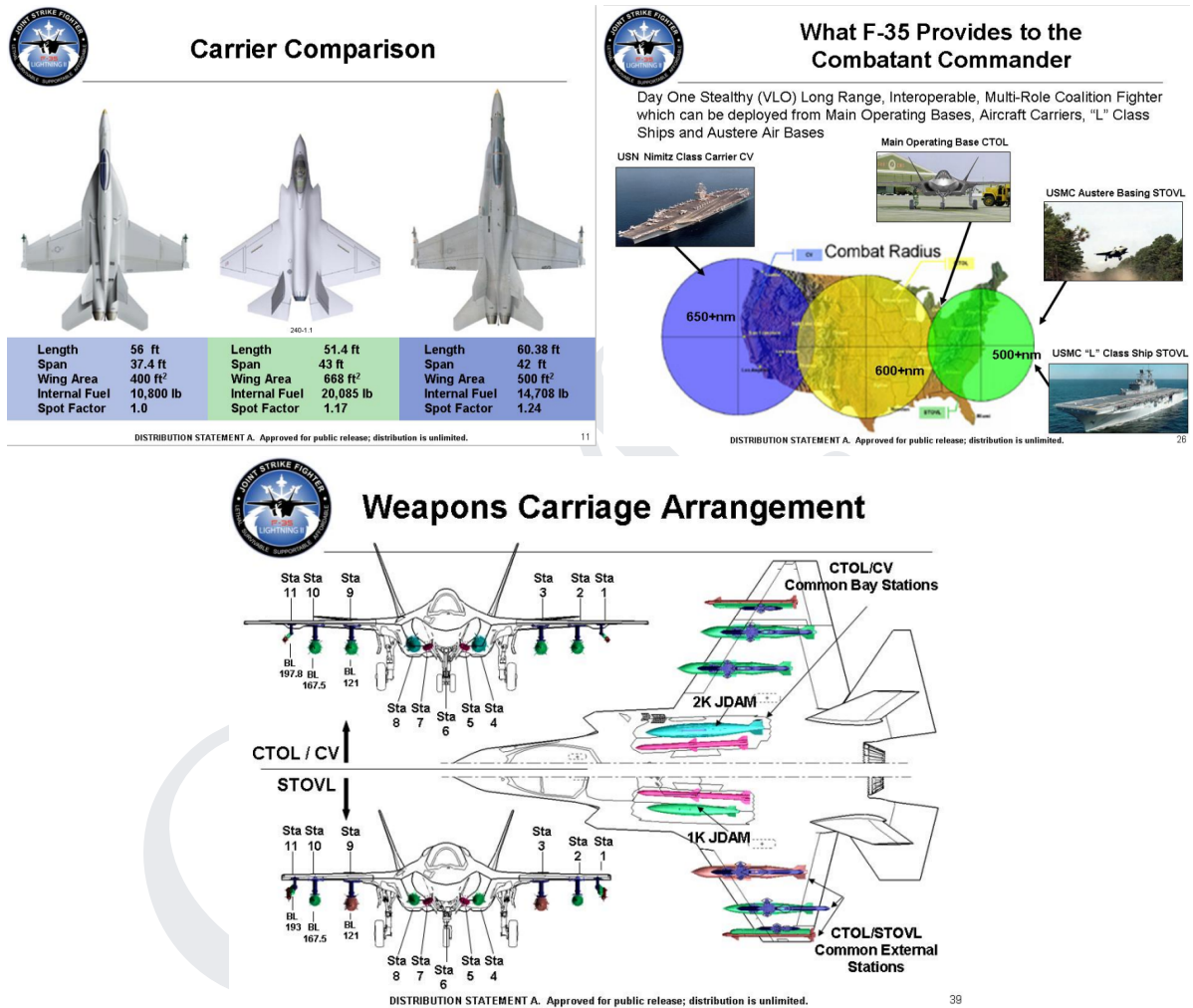


Fig. 193. F-35 internal fuel, ranges and weapons arrangement, extracted from “F-35 Lightning II Program Brief”, courtesy of the USAF.

Estadea can match the F-35C (the most capable in terms of range and fuel capacity) in terms of combat radius while carrying less fuel and more internal weapons than the F-35.

9.5.2. Payload-Range Diagram:

The payload-range diagram is composed of three points: range at maximum payload and MTOW, range at maximum fuel and MTOW and range at maximum fuel and no payload (ferry range). In order to simplify the calculation of range in the different configurations an idealized cruise-climb profile to the maximum supercruise speed altitude (FL330) is assumed. For the maximum payload range calculation it is assumed the external stores produce the same drag penalty as the external fuel tanks. In all three configurations the aircraft flies at its maximum range speed, Mach 0.9 or 525 knots.

	payload (lbs)	Take-off Weight (lbs)	Landing Weight (lbs)
Maximum payload, MTOW	16.836,0	74.633	55400,09
Maximum fuel, MTOW	8423,62	74.633	46987,92
Maximum fuel, no payload	0	66.872	39227,03

Table: 16. Weight configuration take-off and landing weights.

By applying equation 9.14, the results were the following:

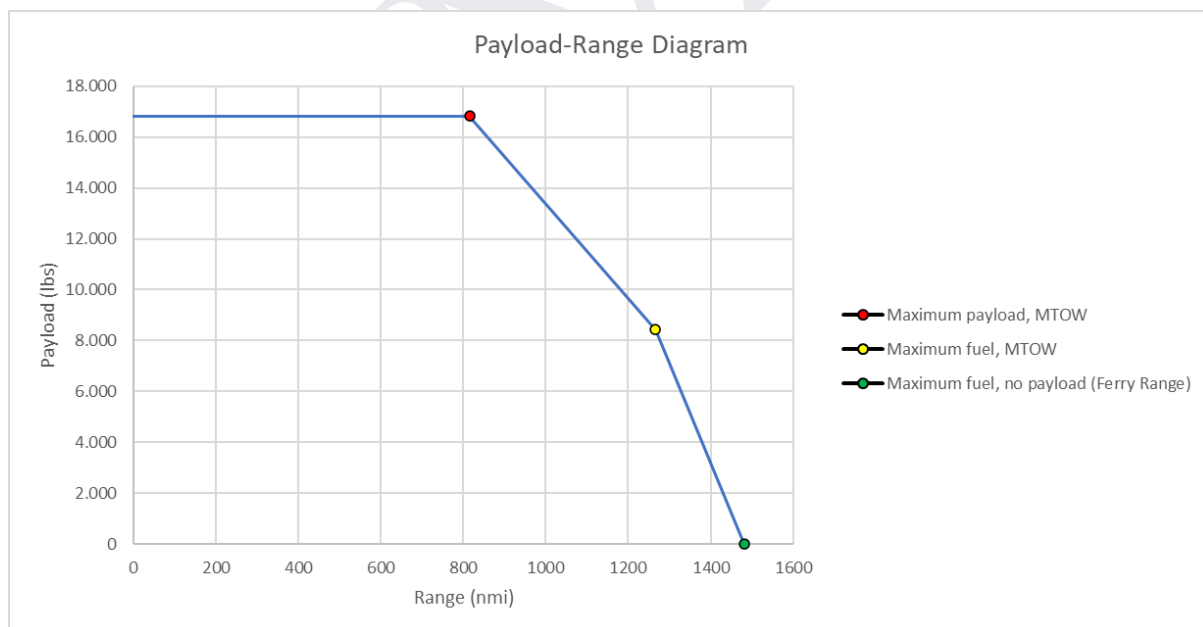


Fig. 194. Estadea’s Payload-Range diagram.

As expected, an increase in payload reduces the range. In terms of payload capacity, Estadea can carry up to 16836.0 lbs, a similar payload to the EF-2000.

9.6. Flight Envelope

A V-n diagram for Estadea will be constructed following the description of the former contained in Chapter 2 adapted for the MTOW at FL330 (ISA+0 conditions), altitude at which the maximum speed is achieved. The components needed for this diagram are the following:

- Upper and Lower Lift Limits, given by equation 9.6.
- Upper and Lower Load Limits, given by n_{pull} for the upper limit and $n_{min} = -3.0 G$.
- Upper and Lower Structural Failure Limits, given by the safety factor (1.50) applied to the upper and lower load limits; therefore $n_{failure} = +9.50 / -4.5 G$ for MTOW.
- Maneuver Speed, given by equation 2.27.
- Never Exceed Speed, assumed to be the maximum speed at FL330, Mach 2.50.
- Cruise Speed, calculated following FAR-23 regulations, $V_c = 36\left(\frac{MTOW}{S_w}\right)$ (9.16).

The results were the following:

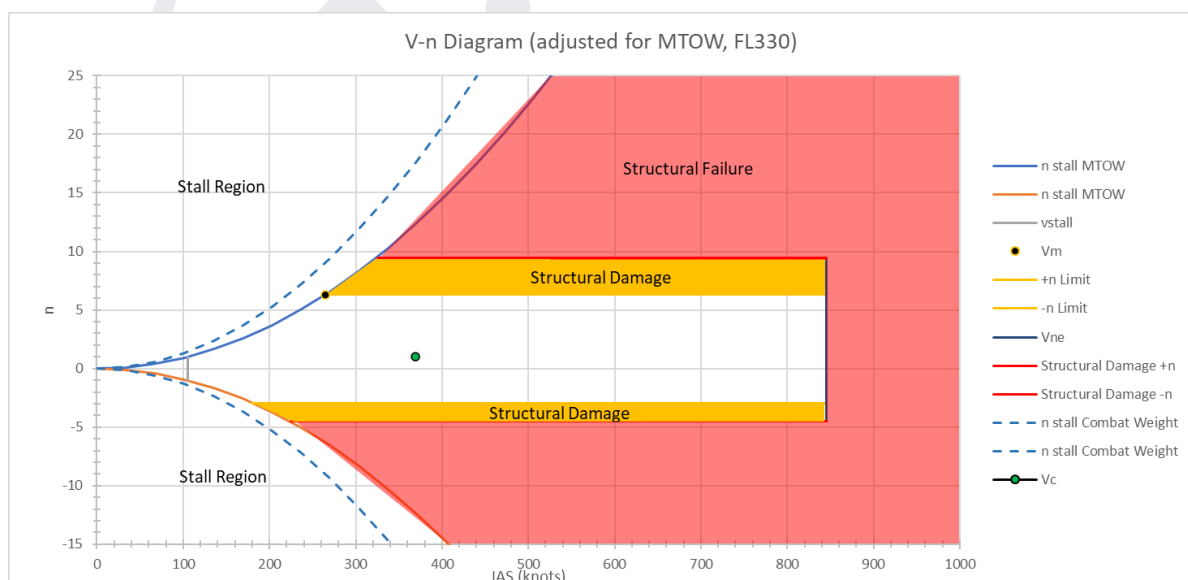


Fig. 195. Estadea’s V-n diagram adjusted for MTOW at 33,000 feet, ISA+0 conditions.

9.7. Ground Interface

In this section the speed for minimum ground control (V_{mcg}), the minimum obstacle clearance radius, the minimum tarmac clearance radius and an approximation for ground roll at MTOW and Combat Weight (50% fuel) will be calculated. Additionally, the ground roll will be compared to the Advanced Tactical Fighter program requirements which stated the fighter aircraft should be able to use a maximum runway length of 2,000 ft (D. P. Raymer, 1996).

9.7.1. Minimum Ground Control Speed (V_{mcg})

The speed for minimum ground control is defined as the minimum speed at which the aircraft can maintain directional control during a takeoff run when an engine suddenly fails by using aerodynamic means only. In the case of Estadea, the ruddervators will be used to counteract the engine yaw moment while being supported by the thrust vectoring of the operational engine to ensure a safe takeoff.

- $M_{z, engine} = 1.5 \cdot T_{av}$ (9.17)
- $M_{ruddervators} = \rho v^2 c_{L, max. rudd.} S_w \sin 40^\circ (X_{CoG} - 16.30)$ (9.18)

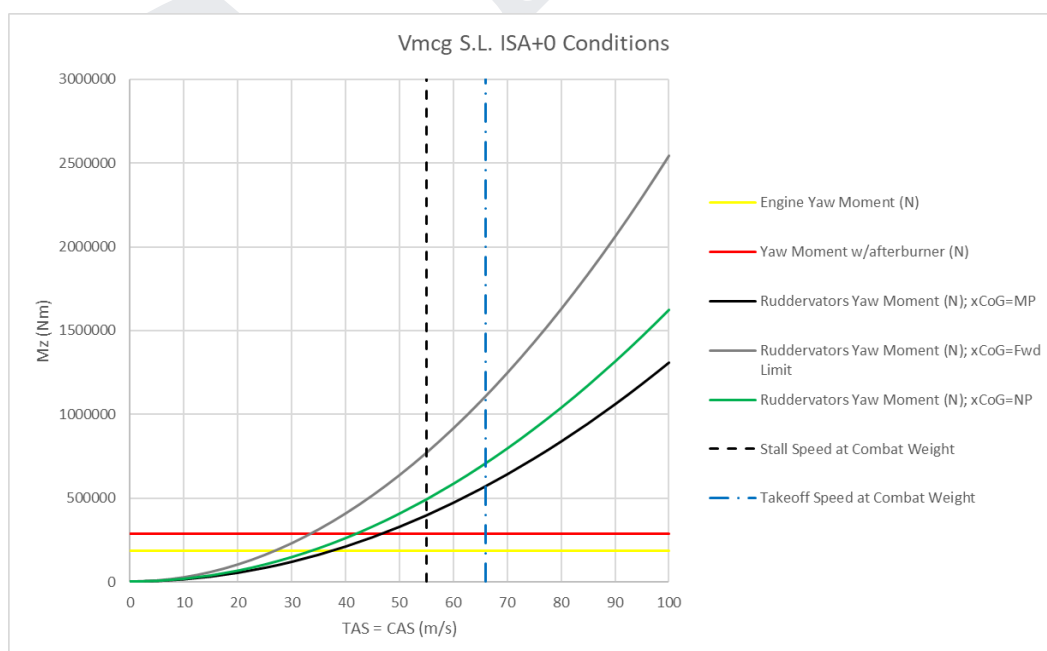


Fig. 196. V_{mcg} determination at S.L., ISA+0 conditions.

Notice how even in the most extreme of cases, that is, combat weight and CoG located at the MP, the minimum velocity for ground control does not exceed the stall speed (taking into account the ground limitations) even when the afterburner is engaged. The decision speed, V_1 , must be located in between the previously mentioned speeds.

9.7.2. Takeoff-Landing Ground Roll Approximation:

Thrust vectoring has another added benefit in the takeoff run, in which the rotation of the aircraft is greatly accelerated, reducing the overall takeoff run:

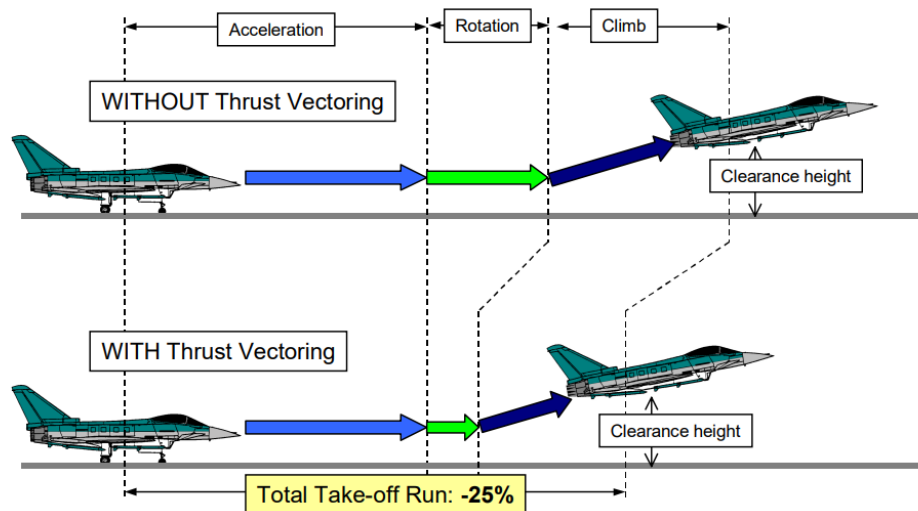


Fig. 197. Effects of thrust vectoring in the take-off run, extracted from “THRUST VECTORING NOZZLE FOR MILITARY AIRCRAFT ENGINES” by Daniel Ikaza, ITP Aero.

In this section the main concern is the approximation of the takeoff and landing ground roll or the minimum runway length necessary for a safe takeoff and landing. It is convenient to evaluate Estadea at various runway conditions and altitudes to determine the variation of the runway minimum length. The following criteria will be used for the calculations:

- ISA+0, ISA+30, ISA-30 conditions.
- $\mu_{dry} = 0.8$, $\mu_{icy} = 0.1$, $\mu_{brakes} = 0.5$ (T. J. Yager, 2013).
- Takeoff Ground Roll: $S_{takeoff} = \frac{1}{2B} \ln\left(\frac{A}{A-BV_{To}}\right)$ (9.19)
 - $A = g\left(\frac{T_{av}}{W} - \mu\right)$ (9.20)
 - $B = \frac{g}{W_{To}} \left(\frac{1}{2} \rho S_w (c_{Dg} - \mu c_{Lg})\right)$ (9.21)

- $c_{Lg} = \frac{\mu}{2K_g}$ (9.22) is the c_L on the ground
- $c_{Dg} = c_{D0} + \frac{c_{Lg}^2}{\pi eAR}$ (9.23) is the c_D on the ground
- $K_g = \frac{1}{\pi eAR} \frac{(16 \frac{h_{wing-ground}}{b})^2}{1+(16 \frac{h_{wing-ground}}{b})^2}$ (9.24) is the induced drag parameter taking into account the ground effects.
- $V_{To} = 1.2V_{stall}$ (9.25) is the takeoff speed. $c_{L,max} = 1.50$ due to tail strike angle limitations.
- Landing Ground Roll: $S_{landing} = S_{braking\ speed} + S_{stop}$ (9.26)
 - $S_{braking\ speed} = \frac{1}{2B} \ln(\frac{A-BV_{TD}^2}{A-BV_B^2})$ (9.27) is the distance to braking speed.
 - $V_{TD} = 1.3V_{stall}$ (9.28) is the touchdown speed.
 - $V_B = 0.8V_{TD}$ (9.29) is the braking speed.
 - $S_{stop} = \frac{1}{2B} \ln(\frac{A-BV_B^2}{A-BV_{stop}^2})$ (9.30) is the distance to stop from the braking speed.
 - It is assumed $c_{Lg} \simeq c_L @ 1.3V_{stall}$ for $S_{braking\ speed}$. $c_{L,max} = 1.50$ due to tail strike angle limitations.
 - For each section, both c_{Lg} and c_{Dg} must be calculated, as well as A and B.

The results were the following:

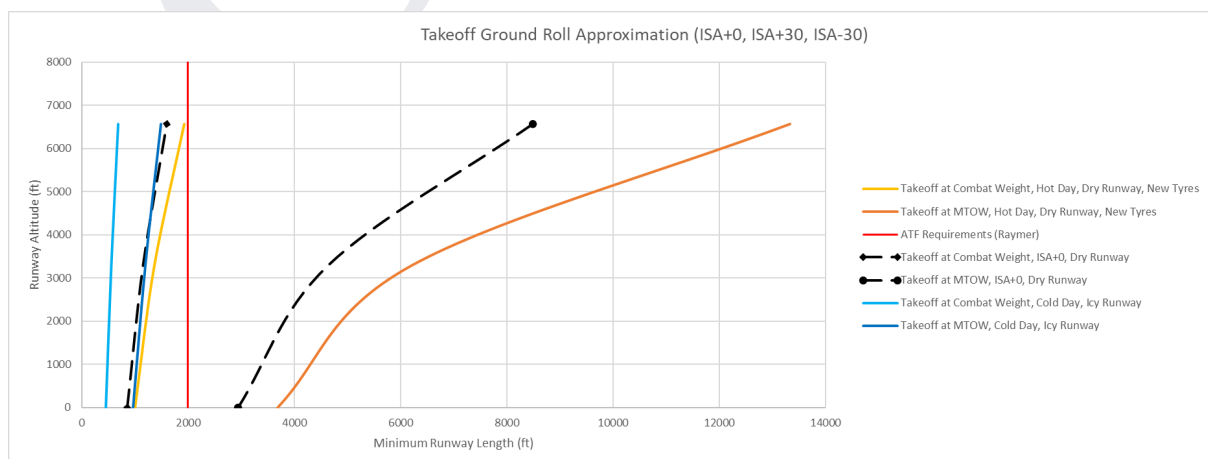


Fig. 198. Estadea’s takeoff ground roll approximation.

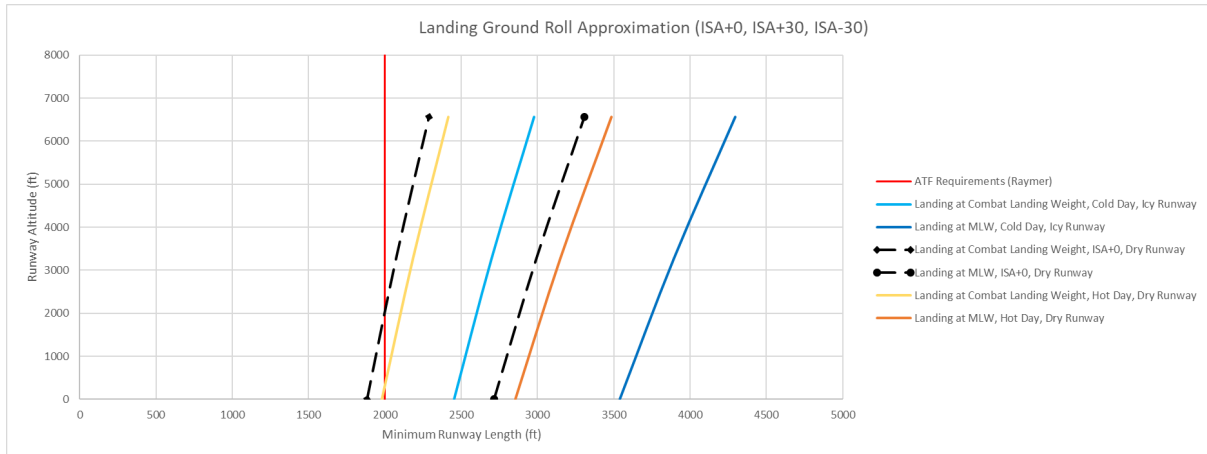


Fig. 199. Estadea’s landing ground roll approximation.

As expected the landing ground roll when compared with the takeoff ground roll is noticeably larger, increasing with decreasing surface friction coefficient and increasing landing weight. Similarly, takeoff ground roll increases with increasing weight, ambient temperature and surface friction coefficient. Notice the increase in both field lengths with increasing altitude due to the reduction in air density (less thrust available and lift for takeoff and less drag for landing). Overall, Estadea complies with the A.T.F. runway length requirements in a standard day at combat weight for both takeoff and landing.

9.7.3. Minimum Clearance Radius and Minimum Pavement Width:

It is convenient to determine Estadea’s minimum clearance radius and minimum pavement width so as to evaluate the possibility of performing turn-arounds in public roads, reducing enormously the aircraft’s dependence on a dedicated airbase, which may be crucial in wartime conditions in which the latter is a prime target.

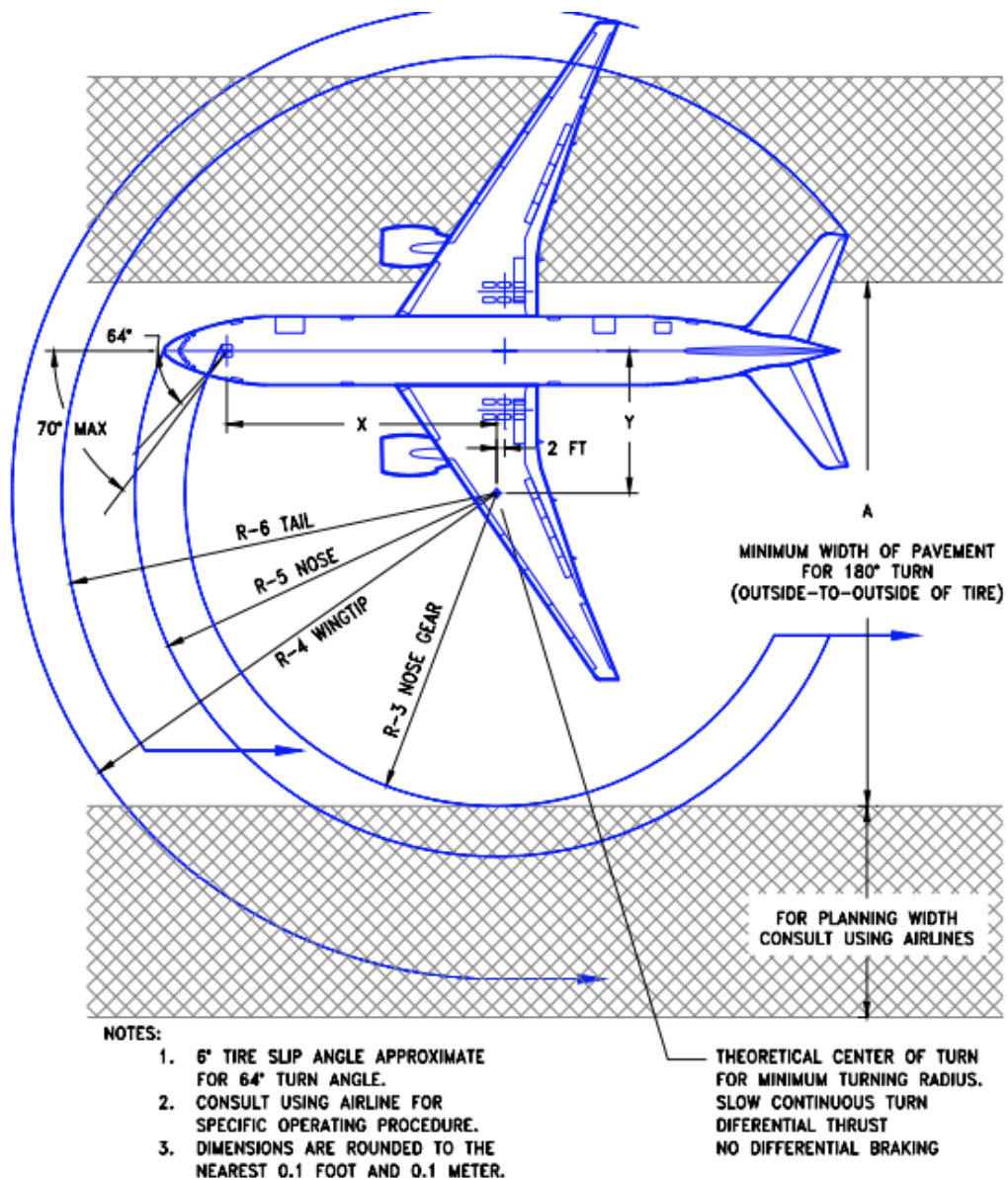


Fig. 200. General aircraft clearance radiuses.

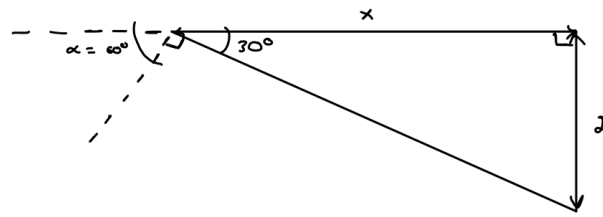


Fig. 201. Center of Rotation calculation.

Assuming a maximum nose wheel deflection angle of 75° , the minimum clearance radius and minimum pavement width can be approximated using the following formulas:

- $R_{min, clearance} = d_{nose\ tyres-main\ tyres} \tan(90 - \alpha_{nose\ wheel}) + d_{nose-main\ tyres}$ (9.31)

- $R_{min, pavement} = \frac{d_{nose\ tyres-main\ tyres}}{\cos(180 - (90 + \alpha_{nose\ wheel}))}$ (9.32)

- The minimum clearance radius is then:

$$R_{min, clearance} = 6.2 \cdot \tan(15^\circ) + 12.2 = 13.86\ m = 45.47\ ft$$

- The minimum pavement width is:

$$R_{min, pavement} = \frac{6.2}{\cos(15^\circ)} = 6.42\ m = 21.06\ ft$$

Taking the spanish roads as reference:

CLASE DE CARRETERA	VELOCIDAD DE PROYECTO (V _p) (km/h)	ANCHO (m)				NIVEL DE SERVICIO MÍNIMO EN LA HORA DE PROYECTO DEL AÑO HORIZONTE
		CARRILES	ARCENES		BERMAS (MÍNIMO)	
			INTERIOR / IZQUIERDO	EXTERIOR / DERECHO		
Autopista y autovía	140, 130 y 120	3,50	1,00 / 1,50	2,50	1,00	C
	110 y 100	3,50	1,00 / 1,50	2,50	1,00	D
	90 y 80	3,50	1,00	2,50	1,00	D
Carretera multicarril	100	3,50	1,00 / 1,50	2,50	1,00	D
	90 y 80	3,50	1,00	2,50	1,00	D
	70 y 60	3,50	0,50 / 1,00	1,50 / 2,50	1,00	E
	50 y 40	3,25 a 3,50	0,50 / 1,00	1,00 / 1,50	0,50	E
Carretera convencional	100	3,50	2,50		1,00	D
	90 y 80	3,50	1,50		1,00	D
	70 y 60	3,50	1,00 / 1,50		0,75	E
	50 y 40	3,00 a 3,50	0,50 / 1,00		0,50	E
Vía colectoras - distribuidora y ramal de enlace de sentido único	100	3,50	1,50	2,50	1,00	D
	90 y 80	3,50	1,00 / 1,50	2,50	1,00	D
	70 y 60	3,50	1,00 / 1,50	2,50	1,00	E
	50 y 40	3,50	0,50 / 1,00	1,50 / 2,50	1,00	E
Ramal de enlace de doble sentido	100	3,50	2,50		1,00	D
	90 y 80	3,50	2,50		1,00	D
	70 y 60	3,50	2,50		1,00	E
	50 y 40	3,50	1,50 / 2,50		1,00	E
Vía de servicio de sentido único	90 y 80	3,50	1,00	1,50	1,00	D
	70 y 60	3,50	1,00	1,00 / 1,50	0,75	E
	50 y 40	3,00 a 3,50	0,50 / 1,00	1,00	0,50	E
Vía de servicio de doble sentido	90 y 80	3,50	1,50		1,00	D
	70 y 60	3,50	1,00 / 1,50		0,75	E
	50 y 40	3,00 a 3,50	0,50 / 1,00		0,50	E

Si los ramales de enlace, los ramales de transferencia, las vías colectoras - distribuidoras, las vías de servicio y las vías laterales solo tuviesen un carril su ancho será de cuatro metros (4,00 m) y, en curvas, tres metros y cincuenta centímetros (3,50 m) más el sobreaño correspondiente (epígrafe 7.3.5) con un valor mínimo de cuatro metros (≥ 4,00 m).

Fig. 202. Spanish roads transversal dimensions according to “Norma de Trazado 2016”, courtesy of historiadecarreteras.com.

The previous figure contains, among others, the nominal lane width of the spanish roads, which stands at 3,50 m of length (approximately 11,50 ft). This means Estadea could theoretically land and takeoff from straight roads of at least 2000 ft in length and four lanes in

width (assuming the road sides have been cleared of any traffic signs, vegetation, etc.). Let's look at some theoretical airfields Estadea could use:

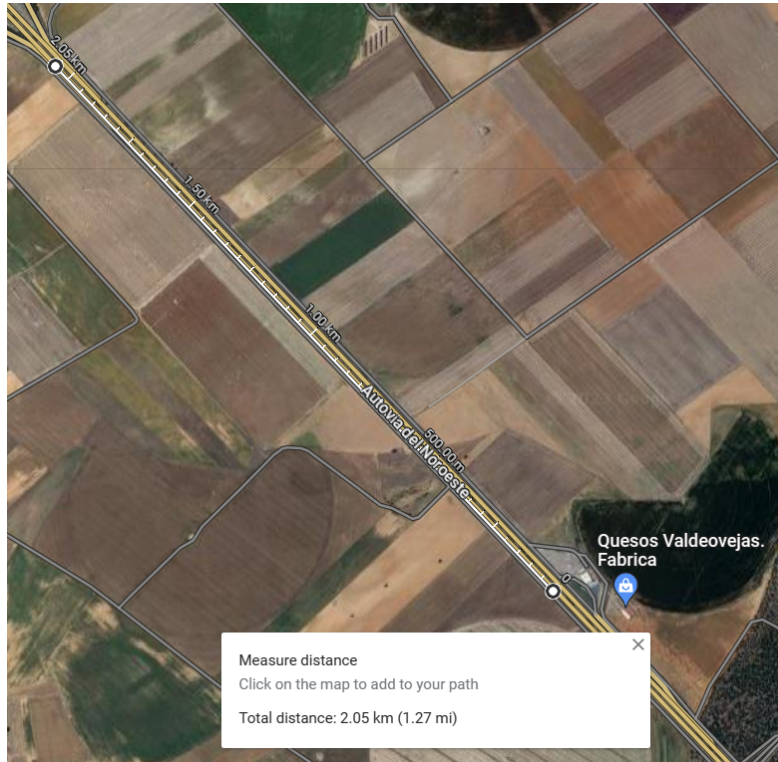


Fig. 203. Autovía del Noroeste Airfield (Castilla y León).

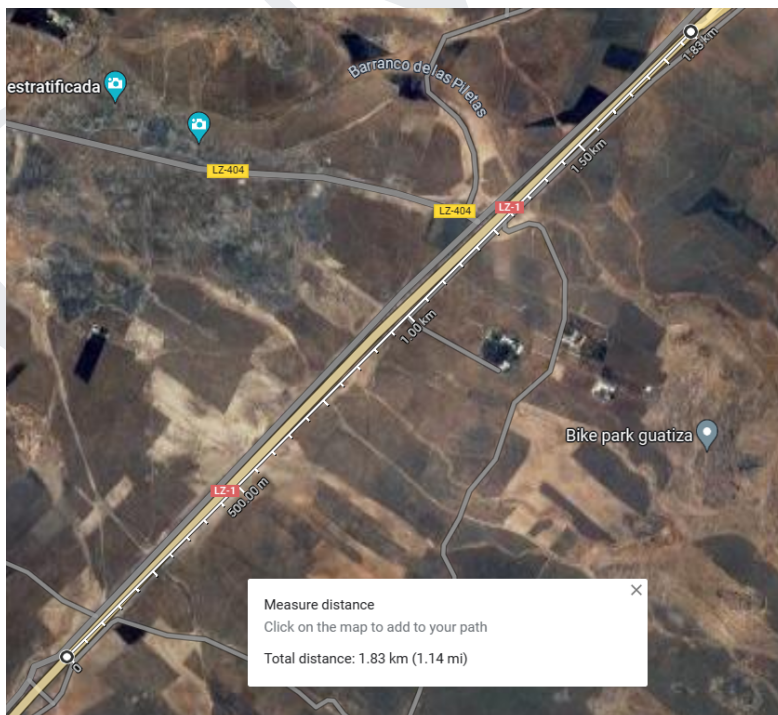


Fig. 204. LZ-1 Airfield (Lanzarote).

9.7.4. Ground Handling:

Several vehicles are involved in the ground service operations, which can be divided into armament reloading, refueling, towing or systems support; they include:

1. Armament Reloading:

- a. General Weapons Loader: for example, the self-propelled BL-3 weapons loader by Advanced Ground Support Systems LTD of dimensions 4.14x3.56 m (Advanced Ground Support Systems LTD, 2023).



Fig. 205. BL-3 weapons loader by Advanced Ground Support Systems LTD.

- b. Linkless Ammunition Loading Vehicle: for example, the USAF’s own by Meggitt Defense Systems of dimensions 1.57x1.03 m (Meggitt Defense Systems, 2023).



Fig. 206. Linkless ammunition loading vehicle by Meggitt Defense Systems.

2. Refueling: for this task the Kovatch R-11-6000 fuel truck was selected due to its capacity, capable of supplying two full internal fuel loads for Estadea thanks to its 23,000 l capacity (Military-Today.com, 2023). Its measurements are 11.58x2.69 m (Military-Today.com, 2023).



Fig. 207. Kovatch R-11-6000 fuel truck.

3. Towing: for this task the Mototok TWIN 6500 remote-controlled towing vehicle has been selected due to its small profile and ease of operation, capable of towing up to 50 tonnes (Mototok, 2023). Its measurements are 2.6x2.14 m (Mototok, 2023).



Fig. 208. Mototok 6500 towing vehicle.

4. Systems Support: since Estadea mounts an APU and its hydraulic systems have been greatly reduced to only handle the landing gear mechanism, the aircraft would only require an air-conditioning unit (ACU) for its day-to-day operations. For this task, the TLD-401 ACU unit has been selected, compatible with aircraft such as the F-14, F-15, F-16 and F-18 (TLD, 2023). Its measurements are 5.16x2.18 m (TLD, 2023).



Fig. 209. TLD 401 ACU unit.

It is required that all these vehicles can develop their tasks in an efficient and safe manner, for that purpose a drawing will be used to show the general disposition of the ground servicing vehicles:

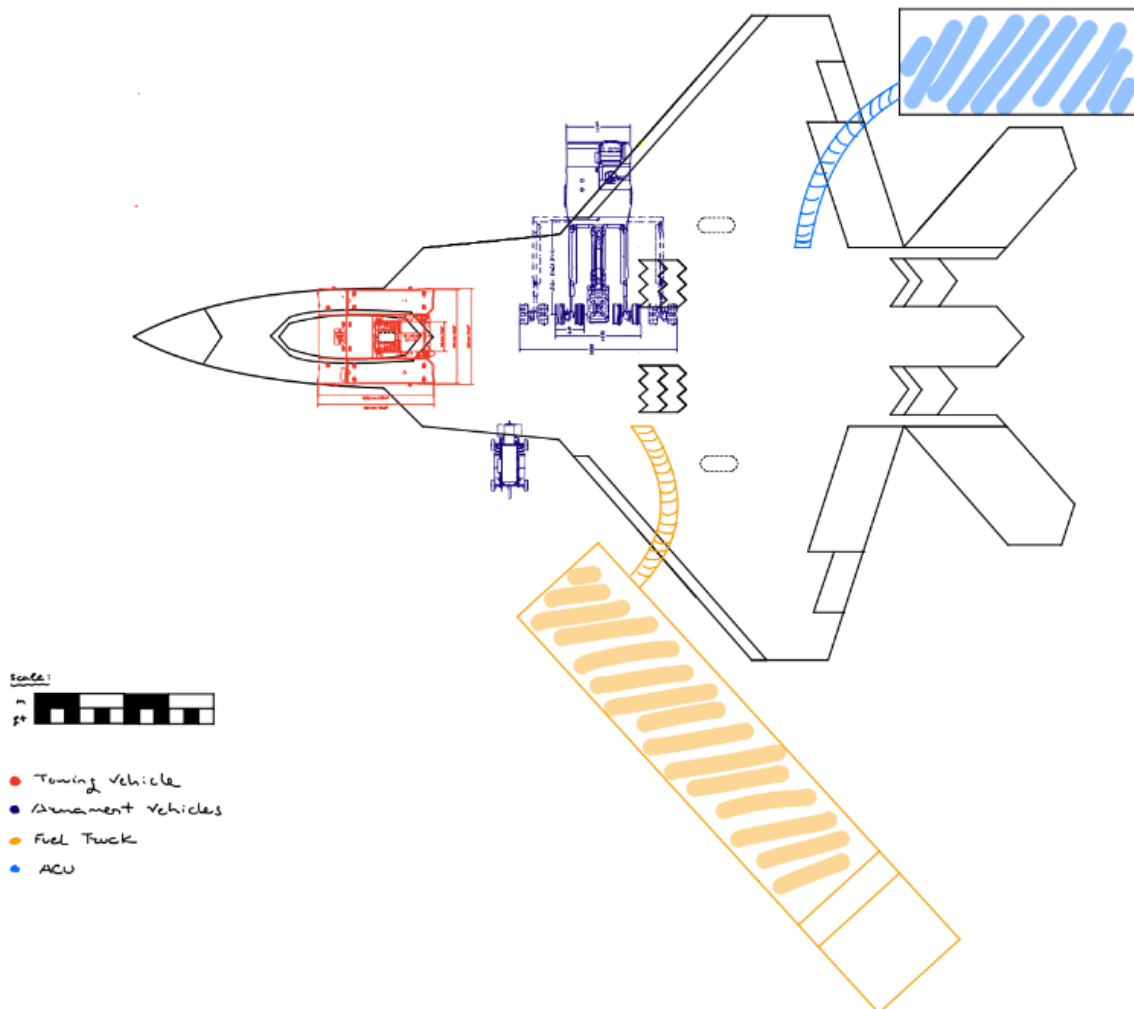


Fig. 210. Estadea ground interface.

9.8. Summary of Estadea’s Specifications

Variable	Value
Empty Weight	38564.30 lbs
Internal Fuel Weight	19232.73 lbs
Max. Fuel Weight	27644.91 lbs
Max. Payload	16836.0 lbs
Combat Weight (50% fuel)	52267.61 lbs
MTOW	74632.83 lbs
Combat Radius	669.30 nmi
Combat Endurance	4h 36'
Mission Range	1313 nmi
Mission Endurance	9 h
Ferry Range	1481 nmi
Max. Speed at Altitude	Mach 2.5
Max. Speed S.L.	Mach 1.2
Max. Supercruise Speed	Mach 1.6
Absolute Ceiling	72,178 ft
Service Ceiling	70,900
Combat Ceiling	35,000 ft
Initial Climb Rate	85,000 ft/min
Wing Loading (Combat Weight)	57.81 lbs/sq ft
Wing Loading (MTOW)	82.54 lbs/sq ft
Max. Sustained Level Turn Rate	28.85°/s
Max. Instantaneous Level Turn Rate	40°/s
Min. Sustained Level Turn Radius	760.81 ft
Min. Runway Length	2000 ft
G Limits	+9.0/-3.0 G
Stealth	Yes

Table 17: Summary of Estadea’s Specifications.

(This page has been intentionally left blank)

G.M.L.

Chapter 10. CONCLUSIONS AND FUTURE WORK

As aerial battlefields become deadlier ever faster due to rapid technological advancements, it is of paramount importance for Europe to count with an effective deterrent against emerging and bellicose powers, this is the core purpose of Estadea. As an air superiority fighter, this design has shown through careful analysis in different metrics (climb rate, maximum speed, turn rate, range, etc.) its potential to surpass the most advanced models in current service and succeed in its mission while being able to utilize standardized armament, equipment and infrastructure, therefore minimizing the economic impact if it was to be widely adopted among militaries with already constrained budgets.

Future work on this aircraft would entail its detailed design phase, in which newer technologies directed to be integrated in 6th generation fighters could be included, making this design a true 6th generation air superiority fighter.



(This page has been intentionally left blank)

G.M.L.

REFERENCES

- [1] Royal Australian Air Force (RAAF, 2012) ‘Five Generations of Jet Aircraft’ by Air Power Development Centre Bulletin. Edited by Dr. C. Clark and Dr. S. Kainikara. Published January 2012.
- [2] Congressional Research Service (CRS, 2022) ‘Air Force Next-Generation Air Dominance Program’. Updated June 23rd, 2022.
- [3] Air Force Research Laboratory (USAF, 2010) ‘Versatile Affordable Advanced Turbine Engines Provide Game Changing Capability with Superior Fuel Efficiency’ by D. E. Thomson. 11th Annual Science & Engineering Technology Conference/DoD Tech Expo. Case Number 88ABW-2010-1467.
- [4] Congressional Research Service (CRS, 2022) ‘Defense Primer: The United States Air Force’. Updated November 14th, 2022.
- [5] European Defense Agency (EDA, 2018) ‘EUROPEAN MILITARY AIRWORTHINESS CERTIFICATION CRITERIA (EMACC)’. Edition 3. Refer to Section 2 “Applicable Documents”.
- [6] UK Ministry of Aviation (UK Ministry of Aviation, 2015) ‘Defence Standard 00-970 Part 1 Section 1’. Issue 13. Refer to “General Requirements” contained in pages 6-14.
- [7] Library of Congress (USAF, 1996) ‘Next-Generation Attack Fighter’ by D. P. Raymer. Published 1996 by RAND. 1700 Main Street, P.O. Box 2138, Santa Monica, CA 90407-2138.
- [8] National Advisory Committee for Aeronautics (NACA, 1956) ‘Theory of Wing-Body Drag at Supersonic Speeds’ by R. T. Jones. Report 1284, 1956.
- [9] National Advisory Committee for Aeronautics (NACA, 1954) ‘Airfoil Section Characteristics at High Angles of Attack’ by L. K. Loftin, Jr. Report TN 3241, 1954.
- [10] J. D. Anderson (J. D. Anderson, 2017) ‘Fundamentals of Aerodynamics’. Sixth edition. New York, NY : McGraw-Hill Education, 2017.
- [11] G. Dimitriadis (G. Dimitriadis, 2017) ‘Fighter Aircraft Design’. Aerospace Design Project 2017-18. Liège Université.

- [12] R. T. Jones (R. T. Jones, 1956) ‘Theory of Wing-Body Drag at Supersonic Speeds’. Report 1284, NACA.
- [13] A. Rajan Iyer & A. Pant (A. Rajan Iyer & A. Pant, 2020) ‘A Review of Nose Cone Design for Different Flight Regimes’. Jain University International Institute of Aerospace Engineering and Management, Bangalore- 560078.
- [14] Lockheed Martin (J. W. Hamstra & B. N. McCallum, 2010) ‘Tactical Aircraft Aerodynamic Integration’ by J. W. Hamstra & B. N. McCallum. Lockheed Martin Aeronautics Company, Fort Worth, TX, USA. DOI: 10.1002/9780470686652.eae490.
- [15] A. F. El-Sayed (A. F. El-Sayed, 2016) ‘Fundamentals of Aircraft and Rocket Propulsion’. Department of Mechanical Engineering, Zagazig University Zagazig, Egypt.
- [16] Georgia Institute of Technology (H. Ran & D. Mavris, 2005) ‘Preliminary Design of a 2D Supersonic Inlet to Maximize Total Pressure Recovery’ by H. Ran & D. Mavris. Aerospace Systems Design Laboratory, School of Aerospace Engineering Georgia Institute of Technology, Atlanta, GA 30332.
- [17] A. M. O. Smith (A. M. O. Smith, 1975) ‘High-Lift Aerodynamics’. VOL. 12, NO. 6. McDonnell Douglas Corporation, Long Beach, Calif.
- [18] R. L. Shaw (R. L. Shaw, 1985) ‘Fighter Combat: Tactics and Maneuvering’. Naval Institute Press Annapolis, Maryland.
- [19] GlobalSecurity.org (Global Security, 2023) ‘F-22 Support System’.
- [20] GlobalSecurity.org (Global Security, 2023) ‘Stealth Aircraft’.
- [21] A. Newman & H. Blenchman (A. Newman & H. Blenchman, 2004) ‘Disruptive Pattern Material: An Encyclopaedia of Camouflage: Nature, Military and Culture’. Published 2004.
- [22] Air Power Australia (Air Power Australia, 2014) ‘Optical Warfare-The New Frontier’ by C. Kopp. First published in November 1989/January 1990. Last updated in January 2014.
- [23] MIT Technology Review (MIT Tech Review, 2011) ‘Nano Paint Could Make Airplanes Invisible to Radar’ by K. Bourzac. Published December 5, 2011.

[24] www.Aircraft101.com (Aircraft 101, 2016) ‘Electronic Countermeasures (ECM)’. Published March 2016.

[25] Goodyear (Goodyear, 2022) ‘Goodyear Aviation Data Book’. The Goodyear Tire & Rubber Company, 200 Innovation Way, Akron, Ohio, 44316.

[26] 2nd International Conference on Energy Systems and Technologies (R. Abdel-Fadil, A. Eid & M. Abdel-Salam, 2013) ‘Electrical Distribution Power Systems in Modern Civil Aircraft’ by Reyad Abdel-Fadil , Ahmad Eid and Mazen Abdel-Salam. 18 – 21 Feb. 2013, Cairo, Egypt.

[27] Aviation Matters (Aviation Matters, 2021) ‘Aircraft Hydraulic Systems (Authoritative Guide)’ by Captain Pete. Published February 9th, 2021.

[28] GlobalSecurity.org (Global Security, 2023) ‘F-22 weapons’.

[29] U. I. Balldin (U. I. Balldin, 2002) ‘Chapter 33: Acceleration effects on fighter pilots’ by U. I. Balldin. In Lounsbury, Dave E. (ed.). Medical conditions of Harsh Environments. Vol. 2. Washington, DC: Office of The Surgeon General, Department of the Army, United States of America.

[30] T. J. Yager (T. J. Yager, 2013) ‘How Best to Determine Runway/Highway Pavement Surface Friction Performance’. Tenth ALACPA Airport Pavement Seminar Mexico City, Mexico; 30 September to 4 October 2013.

[31] Meggitt Defense Systems (Meggitt Defense Systems, 2023) ‘Linkless ammunition loading system US Air Force’. Meggitt Defense Systems, 9801 Muirlands Blvd Irvine, CA 92618, USA.

[32] Advanced Ground Support Systems LTD (Advanced Ground Support Systems LTD, 2023) ‘Product Specification - BL-3’.

[33] Mototok International GmbH (Mototok, 2023) ‘TWIN SERIES 3900 / 6500 / 7500 / WIDE 14’. Hohenzollernstr. 47, 47799, Krefeld, Germany.

[34] www.Military-Today.com (Military-Today.com, 2023) ‘Kovatch R-11-6000’.

[35] Universidad Europea de Madrid (2022) ‘Aircraft Performance - Level Flight’ by R. Llamas. Madrid.

[36] Universidad Europea de Madrid (2022) ‘Aircraft Performance - Climb’ by R. Llamas. Madrid.

[37] Universidad Europea de Madrid (2022) ‘Aerodynamic and Propulsive Forces’ by R. Llamas. Madrid.

[38] Universidad Europea de Madrid (2022) ‘Static Stability and Control’ by R. Llamas. Madrid.

[39] Universidad Europea de Madrid (2022) ‘Aircraft Performance - Range’ by R. Llamas. Madrid.

[40] Kinematic Viscosity Calculator:
<https://www.omnicalculator.com/physics/kinematic-viscosity-of-air>

[41] ISA Model:
<https://www.digitaldutch.com/atmoscalc/>